Integrated Fabrication-Conjugation Approaches for Biomolecular Assembly and Protein Sensing with Biopolymeric–Synthetic Hydrogel Microparticle Platforms and Bioorthogonal Reactions

A dissertation submitted by

Sukwon Jung

in partial fulfillment of the requirements for the degree of

Doctor of Philosophy

in

Chemical Engineering

Tufts University

August 2015

Adviser: Professor Hyunmin Yi

ABSTRACT

Hydrogel microparticles have gained increasing attention as biosensing platforms due to the advantages of hydrogels and particle-based suspension arrays. In this dissertation, I examine facile fabrication–conjugation approaches to construct hydrogel microparticle platforms that can be utilized for biosensing. Specifically, I exploit simple micromolding techniques for fabrication of highly uniform and chemically functional biopolymeric–synthetic hydrogel microparticles, and high yield bioorthogonal conjugation reactions for biomolecule conjugation with the as-prepared microparticles. Two novel approaches allowing for enhanced conjugation capacity and kinetics as well as sensing capability of the microparticle platforms are also examined in this dissertation.

First, facile replica molding (RM) technique is employed to fabricate chitosan–poly(ethylene glycol) (PEG) hydrogel microparticle platforms. The results show that highly uniform and well-defined chitosan–PEG microparticles are readily fabricated via RM. Fluorescence labeling and FTIR microscopy results indicate stable incorporation of chitosan moieties with PEG networks in the microparticles while retaining their chemical reactivity toward amine-reactive chemistries. The utility of these microparticles as biomolecule conjugation platforms is then investigated via conjugation of model biomolecules such as fluorescein-labeled single-stranded (ss) DNAs and red fluorescent proteins (R-phycoerythrin, R-PE) via strain-promoted alkyne–azide cycloaddition (SPAAC) reaction. Fluorescence and confocal microscopy results show highly selective conjugation of biomolecules near the particle surfaces under mild conditions as well as long-term stability of the conjugation scheme using SPAAC reaction. In-depth examination of R-PE conjugation kinetics with the microparticles shows multiple reaction regimes (i.e. rapid initial, intermediate, and steady final stage) owing to steric hindrance arising from the as-conjugated R-PEs and small mesh size of the microparticles. Next, the chitosan–PEG microparticles are enlisted for target protein (R-PE) capture upon anti-R-PE antibody conjugation via SPAAC reaction, and the results show selective and rapid target protein capture with the antibody-conjugated microparticles.

Next, I enlist viral nanotemplates to improve the hindered environment of the chitosan–PEG microparticles, and thus their protein conjugation and kinetics as well as sensing capability. Specifically, tobacco mosaic virus (TMV) templates are assembled with the chitosan–PEG microparticles via nucleic acid hybridization in order to provide abundant conjugation sites with minimal steric hindrance near the particle surfaces. R-PE conjugation results show significantly enhanced protein conjugation capacity of TMV assembled microparticles (TMV-particles) compared to planar substrates and the chitosan–PEG microparticles. In-depth examination of protein conjugation kinetics via SPAAC and tetrazine–*trans*-cyclooctene (Tz–TCO) cycloaddition reaction indicates that the TMV-particles offer less hindered protein conjugation environment over the chitosan–PEG microparticles. Target protein capture results with antibody conjugated TMV-particles also show substantially enhanced capture capacity over the antibody conjugated chitosan–PEG microparticles. In addition, protein and antibody conjugation capacity are readily controlled by simply varying TMV concentrations, with negligible negative impact of densely assembled TMVs on the protein conjugation and capture capability.

Lastly, I examine a simple and robust micromolding-based technique utilizing surface tension-induced droplet formation and polymerization-induced phase separation that allows for fabrication of monodisperse chitosan–PEG microspheres with macroporous and/or intriguing core-shell structures. The utility of these microspheres as platforms for biomolecule conjugation is then thoroughly examined via conjugation of the model biomolecules via SPAAC and Tz–TCO reaction. The results show not only programmable protein conjugation but also enhanced conjugation capacity and kinetics rising from the controlled macroporous structures.

Overall, the results described in this dissertation illustrate facile fabrication–conjugation approaches for construction of biosensing platforms via simple micromolding techniques and efficient bioorthogonal conjugation reactions. I expect that these approaches can be readily enlisted in a wide range of biosensing application areas such as medical diagnostics, bioprocess monitoring, and pathogen detection for biodefense.

LIST OF PUBLICATIONS

Publications for Dissertation

- **Sukwon Jung** and Hyunmin Yi, "Facile Micromolding-based Fabrication of Biopolymeric–Synthetic Hydrogel Microspheres with Controlled Structures for Improved Protein Conjugation", ***Chemistry of Materials***, 2015, 27(11): 3988-3998
- **Sukwon Jung** and Hyunmin Yi, "An Integrated Approach for Enhanced Protein Conjugation and Capture with Viral Nanotemplates and Hydrogel Microparticle Platforms via Rapid Bioorthogonal Reactions", ***Langmuir***, 2014, 30(26): 7762-7770
- **Sukwon Jung** and Hyunmin Yi, "A Facile Strategy for Protein Conjugation with Chitosan–Poly(ethylene glycol) Hybrid Microparticle Platforms via Strain-Promoted Alkyne–Azide Cycloaddition (SPAAC) Reaction", ***Biomacromolecules***, 2013, 14(11): 3892-3902
- **Sukwon Jung** and Hyunmin Yi, "Fabrication of Chitosan–Poly(ethylene glycol) Hybrid Hydrogel Microparticles via Replica Molding and Its Application toward Facile Conjugation of Biomolecules", ***Langmuir***, 2012, 28(49): 17061-17070

Other Publications

- Cuixian Yang, **Sukwon Jung** and Hyunmin Yi, "A Biofabrication Approach for Controlled Synthesis of Silver Nanoparticles with High Catalytic and Antibacterial Activities", ***Biochemical Engineering Journal***, 2014, 89(15): 10-20
- Yader Duenas, Jae Hun Lee, **Sukwon Jung** and Hyunmin Yi, "Multiplexed Hydrogel Microparticle Suspension Arrays for Facile Ribosomal RNA Integrity Assays", *in review*
- **Sukwon Jung** and Hyunmin Yi, "Porosity-tuned Chitosan–Polyacrylamide Hydrogel Microspheres for Improved Protein Conjugation", *in preparation*

TABLE OF CONTENTS

2 FABRICATION OF CHITOSAN-INCORPORATED HYDROGEL MICROPARTICLES VIA REPLICA MOLDING 22

3 PROTEIN CONJUGATION WITH CHITOSAN-INCORPORATED HYDROGEL MICROPARTICLES 53

LIST OF FIGURES

1 INTRODUCTION

Hydrogel microparticles consisting of 3D networks of hydrophilic polymers have gained increasing attention in biosensing[1, 2] and biomedical application areas[3-7] due to the ability to transport small species through the networks in microscopic environments,[8] ease of functionalization,[8, 9] and biocompatibility.[10] While a number of methods for fabrication of the hydrogel microparticles have been established (e.g. traditional and membrane emulsification, photolithography, microfluidics, aerosol polymerization, electrospray),[7-9] there still exist challenges such as lack of uniformity of the microparticles, delicate control of fabrication parameters, and needs for complex devices. In this dissertation, these challenges are addressed by exploiting soft-lithographic micromolding techniques that allow for fabrication of monodisperse hydrogel microparticles in a simple and reliable manner (Chapter 2-5).[11, 12]

To functionalize hydrogel microparticles for specific applications, chemically reactive functional groups (e.g. carboxylic acids and primary amines) are often incorporated with the microparticles as covalent conjugation sites, and functional materials (from small chemicals to large biomolecules) are loaded on these sites via conjugation reactions.[3, 13, 14] However, the functional groups are generally in charged forms under physiological conditions (i.e. neutral pH) due to their own pK_a values,[3, 15, 16] making them less efficient for conjugation reactions[17] and leading to nonspecific binding via electrostatic interaction.[18] Meanwhile, traditional conjugation reactions using crosslinkers (e.g.

carbodiimides, glutaraldehyde and crosslinkers containing *N*-hydroxysuccinimidyl (NHS) ester and/or maleimide) have inherent drawbacks despite recent progress,[17, 19] including limited stability of the crosslinkers, nonselective conjugation, and self-blocking of active conjugation sites by the crosslinkers.[17] In this dissertation, these challenges are addressed by incorporating biopolymer chitosan offering abundant and reactive primary amines with the microparticles (Chapter 2,3 and 5),[20] and by exploiting high yield bioorthogonal conjugation reactions including strain-promoted alkyne–azide cycloaddition (SPAAC) reaction and tetrazine–*trans*-cyclooctene (Tz–TCO) cycloaddition reaction (Chapter 2-5).[21-23]

In the meantime, network (i.e. mesh) structures of the hydrogel microparticles can result in hindered mass transfer particularly for large biomolecules,[24-26] and lead to limitations in biomolecule conjugation and biosensing.[27-30] In this dissertation, I address this challenge by integrating viral nanotemplates with the microparticles (Chapter 4) and by fabricating microparticles with macroporous network structures (Chapter 5).

This introductory chapter describes protein-based biosensing as one of potential applications of the hydrogel microparticles, and general features, utility and benefits of hydrogels. Brief descriptions of chitosan's properties for fabrication, bioorthogonal reactions, and viral nanotemplates are also presented in this chapter. Lastly, an overview of this dissertation is provided at the end of this chapter.

1.1 Protein-based Biosensing

Protein-based biosensing has gained increasing attention in various application areas. For example, in medical diagnostics, detection of characteristic proteins for specific diseases is important in determining disease stages and effective drug treatments.[31] Protein product monitoring in industrial bioprocesses is also crucial to determine optimal harvest time for maximal product yields.[32] Lastly, early detection of pathogens and their toxic protein byproducts has gained attention due to concerns about bioterrorism.[33, 34] While genetic analysis has been also utilized as a biosensing tool, protein analysis can offer more informative and reliable information since proteins are more directly related to physiological functions in biological systems than genes.[30, 35, 36]

Traditionally, enzyme-linked immunosorbent assay (ELISA, Figure 1.1) has been the most widely utilized for protein-based biosensing; target proteins are captured with antibodies anchored on substrate surfaces (capture antibodies), recognized by primary antibodies, and labeled with enzymes via secondary antibodies. Signals are then generated by enzymatic reaction converting enzyme substrates into coloured molecules. While the ELISA remains a central method for protein sensing and quantification, this technique has limitations such as labor intensive and time-consuming nature and requirement of relatively large amount of target samples.[37, 38]

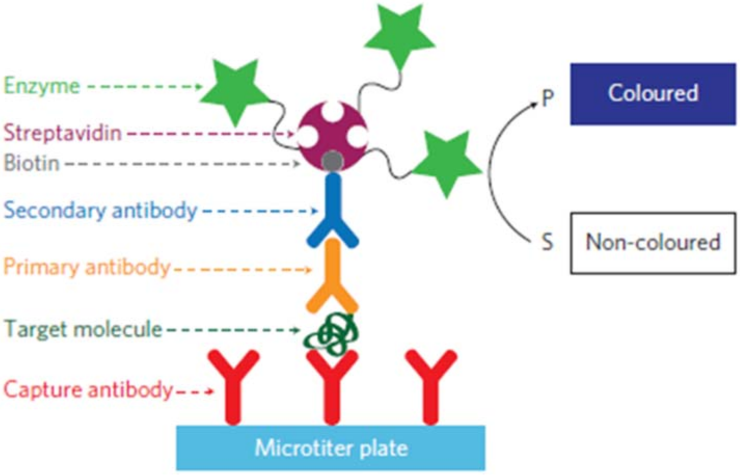

Figure 1.1 Schematic diagram of the conventional sandwich ELISA format. Target molecules are captured by specific antibodies anchored on substrates (capture antibodies), recognized by primary antibodies, and labeled with enzymes by utilizing secondary antibodies. Enzymatic reaction converts enzyme substrates (S) into coloured molecules (P) allowing for quantification of the captured targets. Reproduced from [37].

Meanwhile, previous studies reported that miniaturization of the assays allows for improving detection limits resulting from enhanced signal-to-noise ratios and reducing assay time due to shorter diffusion distance of targets and antibodies.[38, 39] Thus, a variety of planar microarrays[39] and microbead-based suspension arrays[40] have been developed. In these platforms, fluorophores are generally utilized as reporters. As shown in Figure 1.2, the planar microarrays are composed of microspots of capture antibodies with high density on solid substrates, and signals are identified by x-y coordinates. In the meantime, the suspension arrays exploit microbeads as solid supports for capture antibodies, and the microbeads are identified by their size or internally doped fluorophores (i.e. optical encoding). While these technologies have demonstrated varied levels of success in the biosensing field, there still exist challenges such as consistency of the assays, low probe titers and needs for costly equipment.[30, 38, 40]

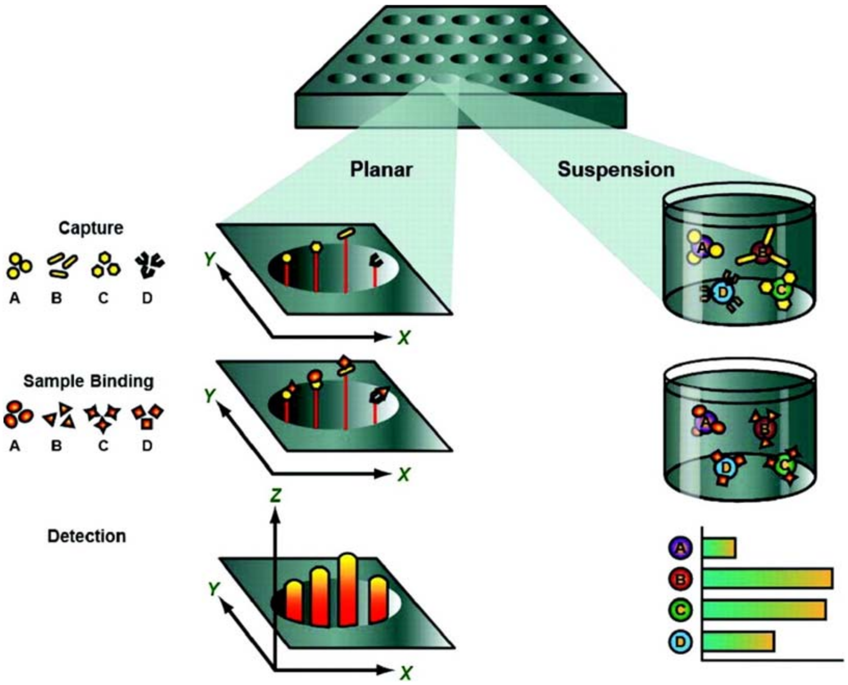

Figure 1.2 Comparison of planar microarrays and microbead-based suspension arrays. In planar microarrays, capture antibodies are immobilized as microspots on solid substrates at spatially discrete locations. In suspension arrays, capture antibodies are immobilized on size- or color-encoded microbeads. Adopted from [38].

1.2 Hydrogels as Biosensing Platforms

1.2.1 Basic Structure and Properties of Hydrogels

Hydrogels, cross-linked three dimensional networks of hydrophilic polymers, have gained increasing attention in a wide range of biological application areas primarily due to their swelling behavior in water or aqueous solutions arising from thermodynamic compatibility of the polymer chains and water molecules.[41] Specifically, degree of swelling at equilibrium plays a critical role in solute diffusion (e.g. drugs, proteins etc.) through the hydrogels as well as in their mechanical properties. Network structures of the hydrogels play a critical role in the swelling behavior, and thus their performance for particular applications. In this dissertation, I examine the network structures of my hydrogel microparticles via protein conjugation and its kinetics (Chapter 3-5).

1.2.2 Photo-induced Radical Polymerization for Hydrogel Fabrication

Among a variety of hydrogel fabrication methods via physical and chemical crosslinking,[41, 42] photo-induced radical polymerization is a widely utilized one due to its convenience and rapid polymerization kinetics.[43-45] Importantly, this method allows for spatial and temporal control of hydrogel fabrication by manipulating UV exposure.[46] As shown in Figure 1.3, the mechanism of photo-induced radical polymerization consists of initiation, propagation and termination.[43, 47] First, the initiation step involves two reactions: formation of radicals ($R^\bullet$) from a initiator (PI) via photolysis, and addition of the radicals to the monomers (M) generating chain-initiating radicals ($RM^\bullet$) During the propagation step, successive addition of monomers takes place resulting in rapid growth and crosslinking of polymer chains. Lastly, at termination step, the growth and crosslinking of polymer chains are stopped by bimolecular interaction between polymer radicals (i.e. bimolecular termination) or radical trapping within polymer networks (i.e. monomolecular termination).[43] With steady-state and bimolecular termination assumptions, the rate of photo-induced radical polymerization (R_p) can be derived as follows:[43, 47]

$$R_p = k_p[\mathrm{F}]\left[\frac{\phi\varepsilon I_0[\mathrm{PI}](10^{-\varepsilon[\mathrm{PI}]z})}{k_t}\right]^{1/2}$$

where k_p and k_t are the rate constants of propagation and termination respectively, $[\mathrm{F}]$ is the concentration of functional groups of the monomer (M), ϕ, ε and $[\mathrm{PI}]$ are the quantum yield, extinction coefficient and concentration of the initiator respectively, I_0 is the incident light intensity at the outer surface of polymerization systems, and z is the penetration depth of the incident light into the polymerization system. Meanwhile, if inhibitors such as oxygen molecules are present during the polymerization, inhibition events should also be considered.

Recent studies reported that network structures determining hydrogel properties can be manipulated by controlling the polymerization kinetics.[12, 48, 49] In other words, the concentrations of the initiator and monomer as well as light intensity play a critical role in control of the hydrogel network structures by controlling polymerization rate R_p. From this perspective, I examine the effect of monomer concentration on network structures of my hydrogel microparticles in Chapter 2 and 5.

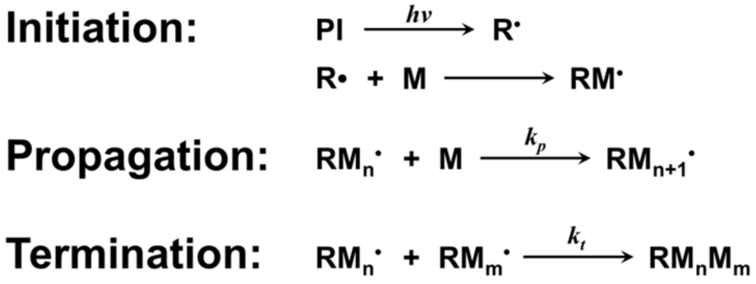

Figure 1.3 General mechanism of photo-induced radical polymerization; initiation by UV exposure, propagation and termination.

1.2.3 Hydrogel-based Biosensing Platforms

Recently, hydrogel-based biosensing techniques have been actively developed due to several advantages of hydrogels as biosensing platforms.[46] These advantages include high water content offering solution-like environment that is favorable to biomolecules, high loading capacity of probe biomolecules (e.g. DNA and antibody), nonfouling nature in biologically complex fluids, readily tunable nature in chemical and physical properties, and mechanical integrity. Specifically, probe biomolecule spots of 2D microarrays were replaced with hydrogels containing the probes (Figure 1.4). A series of studies reported that biosensing performance (i.e. selectivity and sensitivity) of the hydrogel microarrays is superior compared to that of the 2D microarrays, due to thermodynamically better association between targets and probes and/or substantially higher density of the probe biomolecules in the gels.[29, 50, 51] However, both 2D and hydrogel planar microarrays suffer from inherent mass transfer limitation that hampers rapid biosensing.[46] In other words, binding kinetics of target biomolecules on the planar microarrays primarily depends on diffusion rate of the targets rather than binding reaction rate (substantially large Damköhler number, $Da \gg 1$ for typical immunoassay on planar substrates[52]), and characteristic diffusion time for proteins (~10^{-6}-10^{-7} cm^{2}s^{-1} of diffusion coefficients in solution[25]) across even 1 cm length is on the order of days.[46] In the meantime, particle-based suspension arrays (Figure 1.4) can address this limitation by retaining well-mixed conditions via shaking target solutions containing particles. Thus, a variety of biosensing techniques with hydrogel microparticles have been established while adopting the advantages of both suspension arrays and hydrogels.[46]

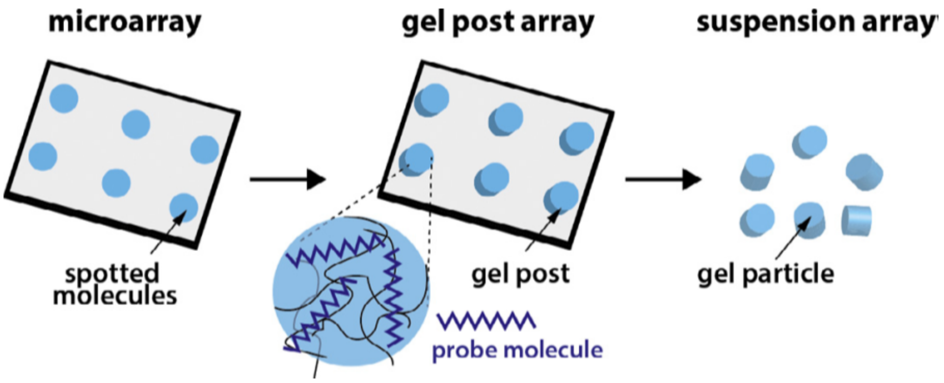

Figure 1.4 Progression of the hydrogel-based biosensing platform. Probe biomolecule spots on planar substrates were replaced with hydrogel posts that are functionalized with probe biomolecules. Hydrogel particle-based biosensing techniques were then established to exploit the advantages of both suspension arrays and hydrogels. Adopted from [46].

1.2.4 Micromolding-based Hydrogel Particle Fabrication

Despite recent progress in fabrication techniques based on photolithography and microfluidics for uniform hydrogel microparticles,[29, 53-58] there still exist several challenges such as delicate control of fabrication parameters and needs of complex devices. Alternatively, micromolding technique based on batch-processing nature (also known as replica molding)[59, 60] allows for simple and robust microparticle fabrication as well as reliable duplication of complex geometries. In typical micromolding technique,[12, 46] preparticle solution consisting of UV-curable monomers and photoinitiators is filled into polymeric micromolds (usually poly(dimethylsiloxane); PDMS). Upon removal of the excess preparticle solution if necessary, the filled molds are exposed to UV light to crosslink the preparticle solution, and to form individual microparticles. Meanwhile, Choi *et al.* recently reported modified micromolding technique that allows for fabrication of monodisperse spherical microparticles via surface tension-induced droplet formation on the micromolds without any delicate control and complex devices.[11] In this dissertation, I examine these micromolding-based fabrication techniques for preparation of highly uniform and well-defined hydrogel microparticles that can be utilized as biosensing platforms.

1.3 Chitosan as a Biomaterial for Fabrication of Conjugation Platforms

Aminopolysaccharide chitosan is a copolymer consisting of glucosamine and *N*-acetylglucosamine, obtained by partial deacetylation of chitin. A unique feature of chitosan compared to other biopolymers is arising from the primary amines at the C-2 position of the glucosamine residues (Figure 1.5).[20] Specifically, the chitosan's primary amines are protonated and positively charged at low pH, allowing the chitosan to be soluble in water. At high pH, these amines are deprotonated and become neutral leading to insoluble form of chitosan via inter-polymer associations. Importantly, this soluble–insoluble transition occurs between pH 6 and pH 6.5 due to near neutral pK_a value of chitosan,[20, 61-63] and allows for platform fabrication via various methods. In addition, the deprotonated amines are chemically reactive under neutral pH conditions, and can be utilized as conjugation and graft sites to functionalize or crosslink chitosan.[20] Meanwhile, chitosan's poor solubility in water and organic solvent,[64] low mechanical strength arising from its rigid crystalline structure,[64] and high viscosity of chitosan solution[65] often pose obstacles toward fabrication processes.

In this dissertation, I exploit short chain chitosan oligosaccharide that can be dissolved in water, and hybrid system with poly(ethylene glycol) to complement chitosan's low mechanical strength.

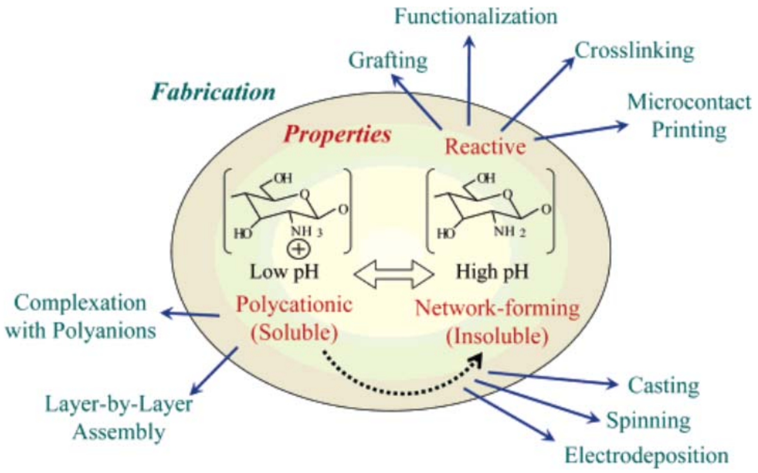

Figure 1.5 Versatility of chitosan as a biomaterial for fabrication. Primary amines of Chitosan are protonated at low pH (< pH 6) conferring polycationic behavior to chitosan. At high pH (> pH 6.5), chitosan's amines are deprotonated being chemically reactive and forming network structures. Adopted from [20].

1.4 Bioorthogonal Reactions: Click Chemistries

In spite of considerable progress in classic bioconjugation techniques for lysine and cystein residues of biomolecules,[66] there still exist inherent drawbacks such as selectivity, stability of functional groups, byproducts and multistep procedures. Recently, "click chemistries" utilizing functional groups that do not exist in nature (i.e. bioorthogonal reactions) have drawn increasing attention as alternative bioconjugation schemes, due to their high selectivity and yield, rapid kinetics, no or harmless byproducts, and stability of their functional groups.[23, 67] These bioorthogonal reactions include azide–alkyne cycloaddition, Diels–Alder addition and thiol–yne reaction as well as oxime formation.[23] The next sections briefly describe the bioorthogonal reactions employed in this dissertation; strain-promoted alkyne–azide cycloaddition (SPAAC) reaction and tetrazine–*trans*-cyclooctene (Tz–TCO) cycloaddition reaction that is one of Diels–Alder addition reactions.

1.4.1 Strain-promoted Alkyne–Azide Cycloaddition Reaction

Alkyne–azide cycloaddition reaction, a representative reaction of click chemistry, requires harsh reaction conditions (i.e. high temperature and pressure) owing to its high activation energy, and is not compatible with biological applications.[66] While Cu(I) catalysts can lower the activation energy allowing the alkyne–azide cycloaddition reaction at ambient conditions,[23, 66] the use of Cu(I) catalyst can lead to severe structural damage of biomolecules by reactive oxygen species.[68] Recently, ring strain structures were introduced into the alkyne group to lower the activation energy (Figure 1.6a), and sufficient reaction rate was achieved without

Cu(I) catalyst under ambient conditions.[66] This reaction is named strain-promoted alkyne–azide cycloaddition (SPAAC) reaction, and has been widely utilized for bioconjugation, targeted drug delivery and cell imaging.[66, 68, 69]

1.4.2 Tetrazine–*trans*-Cyclooctene Cycloaddition Reaction

As shown in Figure 1.6b, tetrazine–*trans*-cyclooctene cycloaddition (Tz–TCO) reaction does not require any harmful catalyst to react under ambient conditions, similar to SPAAC reaction. Yet, the rate of Tz–TCO reaction is significantly faster than that of SPAAC reaction; 2-5 orders of magnitude depending on structure of the tetrazine.[21, 67] This extraordinarily fast reaction rate along with high selectivity allows efficient biomolecule conjugation even at low reactant concentrations.

In this dissertation, I examine protein conjugation with 3D structured microparticle platforms via these two bioorthogonal reactions, and the effect of inherent reaction rates on the protein conjugation kinetics.

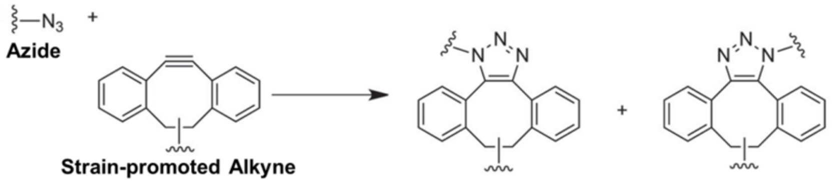

(a) Strain-promoted Alkyne–Azide Cycloaddition Reaction

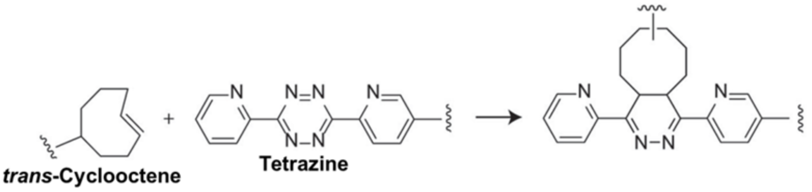

(b) Tetrazine–*trans*-Cyclooctene Cycloaddition Reaction

Figure 1.6 Bioorthogonal reactions; (a) strain-promoted alkyne–azide cycloaddition and (b) tetrazine–trans-cyclooctene cycloaddition reaction. Reproduced from [23].

1.5 Viral Nanotemplates for Sensing Applications

1.5.1 General Structures and Features of Viruses

Viruses are generally composed of coat proteins (capsids) and a nucleic acid such as RNA or DNA that encodes genetic information for their reproduction.[70] The coat proteins assemble together while surrounding the nucleic acid in a highly symmetrical and ordered manner to protect the nucleic acid, and robust and homogenous viral nanoparticles (e.g. spherical, filamentous and rod-like) are formed.[71, 72] As shown in Figure 1.7, these viral nanoparticles can be coupled with a variety of functional materials (e.g. drugs, polymers, fluorophores, quantum dots, oligonucleotides, metals, peptides, proteins, and antibodies) in well-defined spatial arrangements by exploiting their intact or genetically displayed amino acid residues including lysines, cysteines and tyrosines as well as genetically displayed short peptides.[70-73] This feature allows the viruses to be versatile substrates and templates for creation of novel materials toward a wide range of application areas including electronics and construction of biomedical tools.[70, 71, 74, 75] Specifically, in biosensing areas, phages (bacteria-specific filamentous viruses) were widely utilized as sensing platforms[76-79] by exploiting phase display technique that allows for display of target-specific peptides and proteins at the tips and/or surfaces of the phases.[80] In addition, cowpea mosaic viruses (CPMV) were utilized as templates for signal amplification in biosensing.[81, 82]

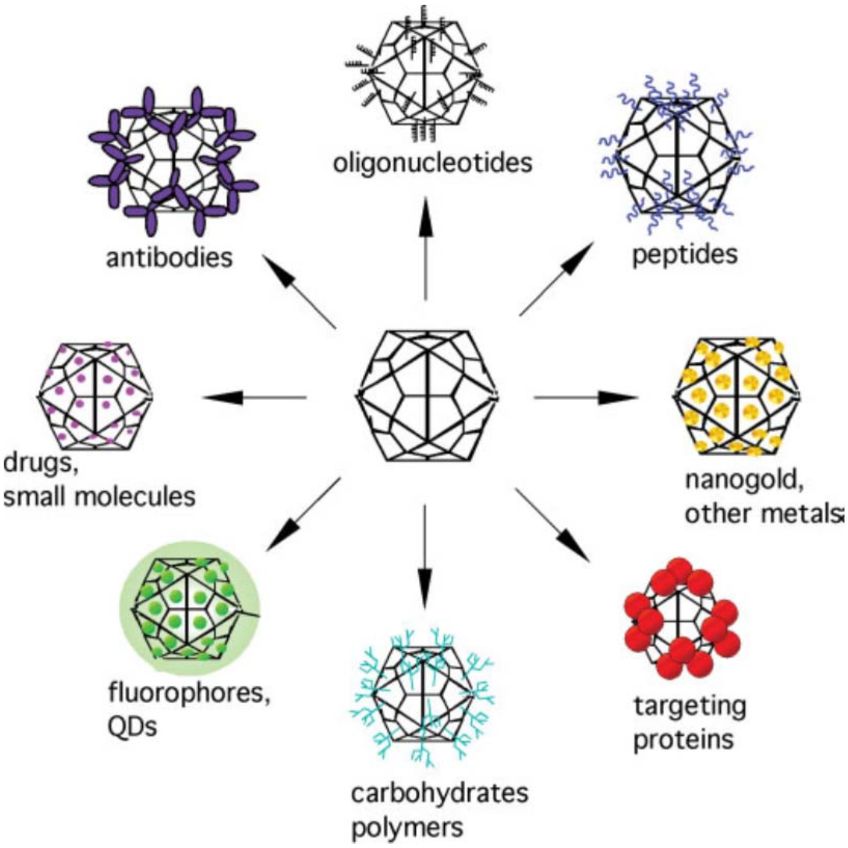

Figure 1.7 Versatility of virus as a nanotemplate. A wide range of functional materials can be attached to the viruses by utilizing their intact or genetically displayed amino acid residues as well as genetically displayed peptides. Adopted from [71].

1.5.2 Properties of Tobacco Mosaic Viruses as Templates for Biosensing

Tobacco mosaic virus (TMV) is a biological nanotube with 300 nm length and 18 nm diameter consisting of over 2000 identical coat proteins wrapped around a 6.4 kb single-strand genomic mRNA (Figure 1.8).[83] In addition to the tyrosine residues on the wild-type TMV,[84, 85] a simple genetic display of one cysteine (i.e. one thiol) on each of the coat proteins (TMV1cys)[85-87] has been shown to provide efficient conjugation handles. Importantly, 5'-end of the TMV can be readily disassembled to expose its mRNA sequence for orientationally controlled assembly onto various platforms via sequence-specific nucleic acid hybridization under mild aqueous conditions (neutral pH and near-room temperature).[86-89] Combined with safety, stability and mass production of the TMV,[90, 91] these two traits make the TMV an ideal candidate as a template for high capacity protein conjugation and sensing platforms. Despite such potential and recent demonstrations with fluorescent labeling,[88, 89, 92] enhanced protein conjugation capacity and improved sensing performance with TMV templates have yet to be realized.

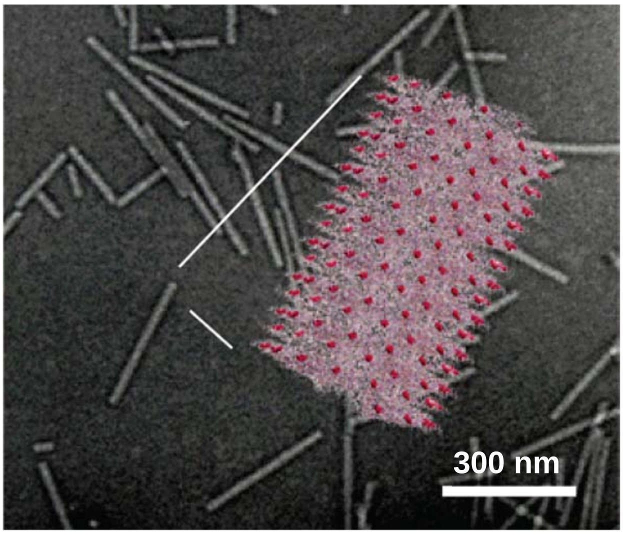

Figure 1.8 Tobacco Mosaic Virus (TMV). Background; electron micrograph of negatively stained TMV. Foreground; structural model for 10% of genetically modified TMV (TMV1cys). Red dots represent the location of the genetically inserted cysteine residues. Adopted from [86].

1.6 Dissertation Outline

The objectives of this dissertation are: i) to examine fabrication of chemically functional biopolymeric–synthetic hydrogel microparticles via simple micromolding techniques, ii) to investigate utility of the microparticles in biomolecular assembly with high yield bioorthogonal conjugation reactions, and iii) to examine approaches for enhancing protein conjugation capacity and kinetics as well as sensing capability of the microparticles. The following dissertation is organized as follows:

Chapter 2 describes a facile fabrication of chitosan–poly(ethylene glycol) (PEG) microparticle platforms for conjugation of biomolecules via replica molding (RM). The works presented in this chapter illustrates that chitosans are incorporated with PEG networks in a stable manner retaining their chemical reactivity, and can be readily utilized as conjugation handles.

Chapter 3 describes protein conjugation with the chitosan–PEG microparticles via SPAAC reaction while thoroughly examining its kinetics. This chapter also illustrates protein capture with the chitosan–PEG microparticles using antibody–antigen interaction.

Chapter 4 describes significantly enhanced protein conjugation and capture capacity by exploiting TMV nanotemplates assembled with the chitosan–PEG microparticles. In-depth examination of protein conjugation kinetics via SPAAC and Tz–TCO reaction illustrates that the TMV-assembled particles provide a less hindered environment for protein conjugation than the chitosan–PEG microparticles.

Chapter 5 describes a simple and robust micromolding-based technique utilizing surface tension-induced droplet formation and polymerization-induced phase separation that allows for fabrication of spherical chitosan-PEG microparticles with macroporous and/or intriguing core-shell structures. The works presented in this chapter illustrate not only programmable protein conjugation but also enhanced conjugation capacity and kinetics due to the controlled macroporous structures.

Chapter 6 summarizes the findings and describes future works that can lead to further improvement of the microparticle platforms for biosensing applications.

2 FABRICATION OF CHITOSAN-INCORPORATED HYDROGEL MICROPARTICLES VIA REPLICA MOLDING

2.1 Introduction

Hydrogel micro- or nano-particles have drawn significant attention as biomolecular conjugation platforms for therapeutic[16, 93] and diagnostic[53, 58] applications due to ease of fabrication into functionalized forms and the ability to transport molecular species through the hydrogel networks in microscopic environments.[8] Traditionally, dispersion and emulsion polymerization methods have been utilized to fabricate various sizes of hydrogel particles with mass quantity. However, the particles produced by these techniques are generally polydisperse, and the shapes are usually limited to spheres or spheroids. In addition, there is a growing need to fabricate non-spherical hydrogel particles for biomedical applications such as multiplexed biosensing using simple shape-encoded methods[12, 53] and controlled drug delivery where the anisotropic particles with different geometries can provide unique drug release profiles.[94]

Recently, microfluidic[95, 96] and photolithographic[55, 56] methods for making various shapes of hydrogel particles with highly uniform size have emerged. However, these techniques have inherent drawbacks including the requirement of rapid polymerization without deformation, harsh process conditions, high equipment costs, and lack of scalability.[12, 97] A facile scheme to fabricate non-spherical hydrogel particles is thus highly desired. Replica molding

(RM) offers a simple, robust, inexpensive and scalable fabrication of polymeric microparticles with reliable replication of small features (Figure 2.1a).[12, 97, 98]

Meanwhile, chitosan offers an attractive matrix for the assembly of biomolecules due to high content of primary amines with low pKa value (~6.5) as shown in Figure 2.1d,[20, 99] which can be enlisted for covalent conjugation or grafting via standard amine group-reactive chemistries. However, chitosan's poor solubility in water or organic solvents and low mechanical strength resulting from its rigid crystalline structure[64] pose obstacles toward fabrication of chitosan-based hydrogel particles with controlled shapes and sizes. One way to overcome these shortcomings of chitosan is the chitosan–poly(ethylene glycol) (PEG) hybrid system where the PEG domain helps improve the mechanical properties.[100]

In addition, standard amine-reactive conjugation chemistries for coupling biomolecules[17] (i.e. using homobifunctional crosslinkers such as glutaraldehyde or homobifunctional *N*-hydroxysuccinimidyl (NHS) ester) have inherent drawbacks; limited stability, non-selective conjugation and self-blocking of active amine sites by the crosslinkers. In the meantime, click chemistry via Cu-catalyzed azide–alkyne cycloaddition has been utilized as a powerful conjugation tool for biomolecules such as proteins and nucleic acids because neither azides nor alkynes usually exist in nature.[17, 68] In other words, the click chemistry can offer selective bio-orthogonal chemistry for conjugation of biomolecules. However, the most critical shortcoming of the Cu-catalyzed click chemistry is the use of Cu catalyst resulting in severe structural damage of biomolecules by reactive oxygen species.[68] Therefore, Cu-free click chemistry utilizing the strain-promoted cyclooctynes (i.e. strain-promoted alkyne–azide cycloaddition (SPAAC) reaction) has been developed due to substantially milder and harmless reaction conditions.[101-103]

In this chapter, I demonstrate a facile scheme to fabricate shape-encoded chitosan–PEG hybrid hydrogel microparticle platforms and to conjugate biomolecules with high surface density. Specifically, I first show that chitosan–PEG microparticles with various non-spherical shapes can be readily fabricated via RM as shown in Figure 2.1a. The preparticle solution containing chitosan, poly(ethylene glycol) diacrylate (PEGDA) (Figure 2.1d) and photoinitiator is placed onto a poly(dimethylsiloxane) (PDMS) mold. Next, the filled mold is exposed to UV light for crosslinking preparticle solution via photo-induced radical polymerization.[47] As shown in the bright-field micrographs of Figure 2.1b,c, the chitosan–PEG particles fabricated by RM are highly uniform and consistent with well-defined shapes. Fluorescent labeling and FTIR analysis verify chemical reactivity of the particles toward amine-reactive chemistries as well as stable incorporation of chitosan molecules within the particles. The as-prepared chitosan–PEG microparticles are then enlisted to anchor single-stranded (ss) DNAs via SPAAC reaction as an example of biomolecular conjugation. Fluorescence and confocal microscopy results clearly illustrate facile conjugation of biomolecules with chitosan–PEG microparticles under mild conditions with high selectivity. Finally, the ssDNA-conjugated chitosan–PEG microparticles are utilized to assemble biological supramolecules (e.g. tobacco mosaic virus, TMV) via nucleic acid hybridization. Fluorescence microscopy and AFM results clearly show controlled supramolecular assembly with high surface density, and indicate substantially high surface DNA density on the particles. Combined, these results demonstrate a facile fabrication and conjugation scheme for robust biomolecular conjugation or assembly platforms. I thus expect that this fabrication-conjugation scheme can be enlisted in a wide array of biomolecular targets and applications.[16, 53, 58, 93]

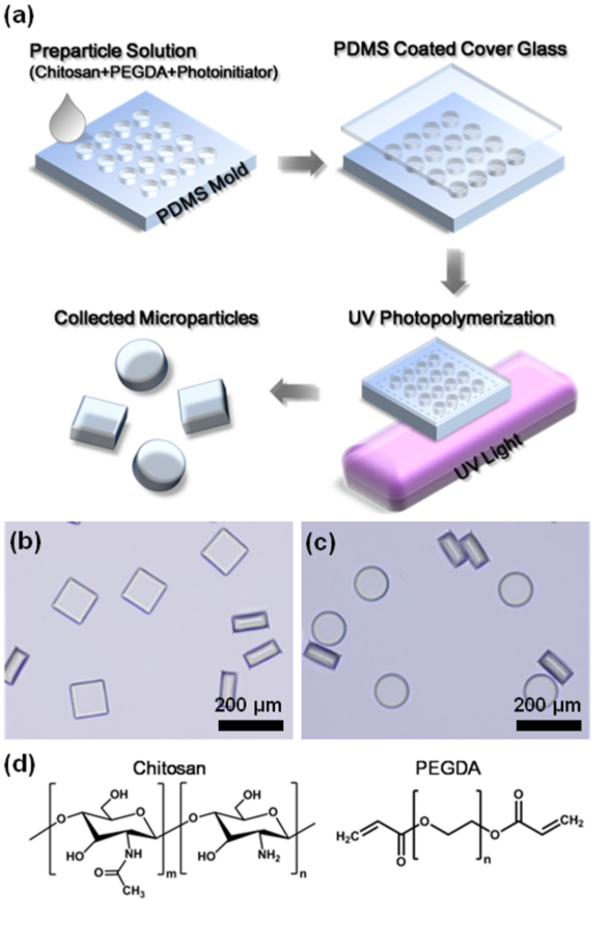

Figure 2.1. Chitosan–PEG microparticle fabrication via replica molding (RM). (a) Schematic diagram of the microparticle fabrication procedure. (b, c) Bright-field images of two different shapes of microparticles with the starting composition of 30% (v/v) PEGDA and 1% (w/v) chitosan. (d) Chemical structures of chitosan and PEGDA.

2.2 Materials and Methods

2.2.1 Materials

Chitosan oligosaccharide lactate (average M_n 5 kDa, > 90% deacetylation), poly(ethylene glycol) diacrylate (PEGDA, average M_n 700 Da), 2-hydroxy-2-methylpropiophenone (Darocur 1173, photoinitiator (PI)), Trizma pre-set crystals (pH 7.5) and saline sodium citrate (SSC) buffer (20×concentrate, molecular biology grade) were purchased from Sigma-Aldrich (St. Louis, MO). 5-(and 6-)carboxyfluorescein succinimidyl ester (NHS–fluorescein) was purchased from Pierce Biotechnology (Rockford, IL). Fluorescein–5-maleimide was purchased from Biotium (Hayward, CA). Azadibenzocyclooctyne (ADIBO)–*sulfo*–*N*-hydroxysuccinimide (NHS) ester (a.k.a. dibenzylcyclooctyne (DBCO)–*sulfo*–NHS ester) was purchased from Click Chemistry Tools (Scottsdale, AZ). Sodium phosphate monobasic anhydrous (99%), sodium phosphate dibasic anhydrous (≥ 99%), Tween 20 (TW20), poly(dimethylsiloxane) (PDMS) elastomer kits (Sylgard 184) and gold-coated glass slides (C09-5076-M20) were purchased from Thermo Fisher Scientific (Waltham, MA). All the chemicals were analytical grade, and used without further purification.

2.2.2 DNA Oligonucleotides

All single-stranded (ss) DNAs used in this study were purchased from Integrated DNA Technologies (Coralville, IA); azide-terminated and fluorescently labeled ssDNA (F–DNA–azide, 5'-/azide/ATGATGATGATGATGATG/FAM/-3'), azide-terminated ssDNA (capture DNA, 5'-/azide/ATGATGATGATGATG

ATG/-3’), and linker DNA (5’-/GTTTGTTGTTGTTGGTAATTGTTG*TTTTTT* CATCATCATCATCATCAT/-3’; TMV 5’end complementary sequence *Spacer* capture DNA complementary sequence).

2.2.3 Fabrication of Chitosan–PEG Microparticles via Replica Molding

PEG and chitosan–PEG microparticles in this study were fabricated according to methods in a recent report with minor modifications.[12] Briefly, the composition of the preparticle solution was as follows: 0-1.2% (w/v) chitosan oligomer, 30-48% (v/v) PEGDA, and 2% (v/v) PI. The chitosan oligomers are dissolved in deionized water, unlike long chain chitosans. As shown in Figure 2.1a, the preparticle solution was placed into a PDMS mold (1600 wells per a mold) which was formed with Sylgard 184 following overnight incubation at 65 °C on a silicon master, and the bubbles in the microwells were removed by rubbing the mold with a disposable plastic pipette tip. The excess preparticle solution was simply taken away by a pipette, then the filled mold was sealed with a PDMS-coated glass slide except for the square region for microwells (roughly 0.7 cm×0.7 cm) to make a small gap between the glass surface and the top portion of the microwells. To prevent rapid evaporation of the preparticle solution, the procedures above were carried out in a humidity chamber with approximately 90% humidity.[12] The sealed mold was then placed on an aluminum mirror (Thorlabs, Newton, NJ) and exposed to 365 nm UV light with an 8 W hand-held UV lamp (Spectronics Corp., Westbury, NY) for 15 min. The polymerized particles were released from the microwells by physically bending the mold, then water containing 0.5% (v/v) TW20 was placed on the top of the mold to collect the particles by pipetting. The microparticles were then transferred to a microcentrifuge tube and rinsed to remove any unreacted chemicals as follows: mixing the particles in 5×SSC buffer solution containing 0.05% (v/v) TW20 by pipetting, allowing them to settle to the tube bottom, and removing the supernatant. The rinsing procedure was repeated at least 5 times.

2.2.4 Fluorescent Labeling of the Microparticles

For fluorescent labeling, the chitosan–PEG microparticles (roughly 200 particles) were incubated in 5×SSC buffer solution containing 0.05% (v/v) TW20 with 10 μM NHS–fluorescein for 1 h on a rotator at room temperature. The unreacted NHS–fluorescein molecules were then removed by rinsing the particles 5 times using the rinsing procedure described above.

2.2.5 Strain-promoted Alkyne–azide Cycloaddition Reaction for Biomolecular Conjugation

The chitosan–PEG microparticles were incubated in 5×SSC buffer solution containing 0.05% (v/v) TW20 with 500 μM ADIBO–*sulfo*–NHS ester for 1 h on a rotator at room temperature. The unreacted ADIBO–*sulfo*–NHS ester molecules were rinsed 5 times using the rinsing procedure. The ADIBO-activated microparticles were then reacted with 10 μM of azide-terminated ssDNAs (i.e. F–DNA–azide or capture DNA) for 1 day at room temperature. The unconjugated DNAs were then rinsed 5 times using the rinsing procedure.

2.2.6 Hybridization-based Assembly of TMV

For TMV assembly with the chitosan–PEG microparticles, I first labeled and partially disassembled TMVs following the previously reported procedure.[89] Briefly, the genetically modified TMVs (TMV1cys) (ranging from 0.06 mg/mL to 6 mg/mL) were reacted with 10-fold molar excess of fluorescein–5-maleimide for 2 h at room temperature in 100 mM sodium phosphate buffer, pH 7.0. The fluorescently labeled TMVs were separated and partially disassembled by ultracentrifugation in a 10-40% sucrose gradient (100 mM Tris buffer, pH 7.5) at 48000g for 2 h. The partially disassembled TMVs were pelleted with 5×SSC buffer solution by ultracentrifugation for 1 h at 90000g and resuspended in 5×SSC buffer solution. Next, the capture DNA-conjugated microparticles were incubated in 5×SSC buffer solution containing 0.05% (v/v) TW20 with 1 μM linker DNA for 5 h on a rotator at room temperature. The extra linker DNAs were rinsed 5 times using the rinsing procedure. Lastly, the microparticles placed in the partially disassembled and fluorescently labeled TMV solution with various concentrations, and incubated for 1 day at 30 ^{o}C. The microparticles were then rinsed 3 times with 5×SSC buffer solution containing 0.05% (v/v) TW20. The TMV concentrations at equilibrium were determined with Evolution 300 UV-vis Spectrophotometer (Thermo Scientific, Waltham, MA) by measuring absorbance at 260 nm and 325 nm (for correction of light scattering) with an extinction coefficient of 3.01 cm^2/mg for TMV.[104]

2.2.7 Imaging Analysis

The fluorescently labeled, ssDNA-conjugated and TMV-assembled chitosan–PEG microparticles were visualized with an Olympus BX51 epifluorescence microscope using a standard green filter set U-N31001 (Chroma Technology Corp., Rockingham, VT), and the fluorescence micrographs were captured with a DP70 microscope digital camera. Fluorescence intensity was evaluated with ImageJ software.[105] Confocal micrographs for the microparticle were acquired on a Leica DMIRE2 microscope (Wetzlar, Germany). The particles were analyzed with a 20×objective (0.7 NA) at 488 nm excitation and 543 nm emission, and the depth scan increment was 1 μm.

2.2.8 FTIR microscopy

FTIR spectra were obtained on a JASCO IRT-5000 FTIR microscope (Easton, MD) with Spectra Manager II software. The samples were prepared as follows. A thin chitosan film was prepared with 2% (w/v) chitosan solution dissolved in deionized water. Specifically, a PDMS well (d = 6 mm & h = 3 mm) was placed on a gold-coated glass slide, and 100 μL of the chitosan solution was added into the well. The chitosan solution in the PDMS well was then dried for 3 h at 65 ^oC and further dried for 2 h in a vacuum chamber at room temperature. A thin liquid PEGDA film was prepared on a gold-coated glass slide; a PDMS well was placed on the gold-coated glass slide, and 5 μL of PEGDA was put into the well. The PEGDA film was then dried for 3 h at 65 ^oC and further dried for 2 h in a vacuum chamber at room temperature. The chitosan–PEG (30% PEGDA with 1% CS) and PEG (30% PEGDA) particles fabricated by RM were thoroughly washed with deionized water, and placed onto the gold-coated glass slide. The particles were then dried for 3 h at 65 ^{o}C and further dried for 2 h in a vacuum chamber at room temperature. The samples were scanned with reflectance mode and resolution of 4.0 cm^{-1}.

2.2.9 AFM

Phase contrast AFM images were taken using a Dimension 3100 atomic force microscope (Digital Instruments, Santa Barbara, CA) with Tap 150 silicon probes with aluminum reflex coating (Budget Sensors, Sofia, Bulgaria) in tapping mode with a scan rate of 0.5 Hz. The AFM images were analyzed using Nanoscope software version 6.00.[89]

2.2.10 Equilibrium Binding Model

To construct the solid curve of Figure 2.6h, the equilibrium binding relationship between the fluorescently labeled TMVs and the binding sites (TMV 5'end complementary sequence) of the chitosan–PEG particles upon capture DNA conjugation and linker DNA hybridization was considered as follows:

$$\mathrm{F\text{-}TMV} + * \leftrightarrow \mathrm{F\text{-}TMV}*$$

where $\mathrm{F\text{-}TMV}$ represents the fluorescently labeled TMV, $*$ represents the binding sites of the particles, and $\mathrm{F\text{-}TMV}*$ represents the TMV-particle complex. At the equilibrium, the equilibrium binding relationship is characterized by the dissociation constant, K_{d}:

$$K_d = \frac{[\mathrm{F\text{-}TMV}][*]}{[\mathrm{F\text{-}TMV}*]}$$

where the concentration of $\mathrm{F\text{-}TMV}$, and the surface concentrations of $*$ and $\mathrm{F\text{-}TMV}*$ at equilibrium are represented as $[\mathrm{F\text{-}TMV}]$, $[*]$, and $[\mathrm{F\text{-}TMV}*]$, respectively. From the equilibrium binding relationship and assuming that the fluorescence intensity of the particles is directly proportional to the TMV-particle complex concentration; $[\mathrm{F\text{-}TMV}*] = \mathrm{k}[\mathrm{F.I.}]$, the following equation is obtained:

$$[\mathrm{F.I.}] = \frac{1}{\mathrm{k}} \cdot \frac{[*]_o[\mathrm{F\text{-}TMV}]}{K_d + [\mathrm{F\text{-}TMV}]} = \frac{\mathrm{k'}[\mathrm{F\text{-}TMV}]}{K_d + [\mathrm{F\text{-}TMV}]}$$

where $[*]_o$ represents initial surface concentration of active binding sites on the particles, $[\mathrm{F.I.}]$ represents fluorescence intensity, and $\mathrm{k'}$ represents maximum fluorescence intensity of particles upon TMV assembly. A double reciprocal plot was utilized to determine the constants K_d and $\mathrm{k'}$ from the linearized equation[106]:

$$\frac{1}{[\mathrm{F.I.}]} = \frac{K_d}{\mathrm{k'}[\mathrm{F\text{-}TMV}]} + \frac{1}{\mathrm{k'}}$$

The solid curve of Figure 2.6h was then drawn with K_d (0.03 mg/mL) and $\mathrm{k'}$ (52.6 AU) obtained by plotting $1/[\mathrm{F.I.}]$ vs. $1/[\mathrm{F\text{-}TMV}]$.

2.3 Results and Discussion

2.3.1 Replica Molding (RM) of Chitosan–PEG Microparticles

As shown in Figure 2.2, I first demonstrate that hydrogel microparticles containing chemically reactive chitosan oligomers can be readily fabricated via replica molding (RM). For this, I fabricated microparticles containing 30% (v/v) poly(ethylene glycol) diacrylate (PEGDA) and varying concentrations of chitosan via RM as shown in Figure 2.1a. These particles were then exposed to identical concentration of 5-(and 6-)carboxyfluorescein succinimidyl ester (NHS–fluorescein), which reacts with the primary amine groups of chitosan via S_N2 (bimolecular nucleophilic substitution) reaction[107] to yield stable amide bonds, as shown in the schematic diagram of Figure 2.2a. The particles were imaged with a fluorescence microscope, and the average fluorescence intensity at the center of particles was measured

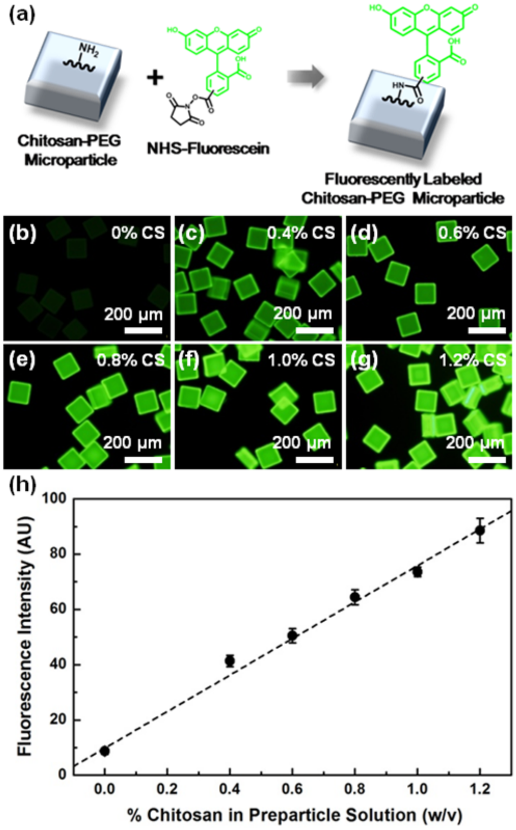

Figure 2.2. Consistency and chemical reactivity of chitosan–PEG microparticles. (a) Schematic diagram of fluorescent labeling of the chitosan–PEG microparticles via NHS ester reaction chemistry. (b-g) Fluorescence micrographs of fluorescently labeled

microparticles with different chitosan contents; 0-1.2% (w/v) chitosan (CS), and 30% (v/v) PEGDA. (h) Average fluorescence intensity plot of microparticles shown in (b-g). Error bars represent standard deviation from at least six particles.

First, the fluorescence micrographs (Figure 2.2c-g) and their corresponding bright-field micrographs (Figure A1.1, Appendices) show the formation of highly uniform and well-defined microparticles via RM under all the chitosan concentrations employed. Second, the fluorescence micrographs of Figure 2.2b-g show that the fluorescence intensity increases with increasing chitosan concentration, while the fluorescence among particles at the same chitosan concentration are highly uniform and consistent. Importantly, Figure 2.2b shows that the particles without chitosan yield negligible fluorescence upon exposure to NHS–fluorescein. This result confirms that most of the fluorescence shown in Figure 2.2c-g results from the specific S_N2 reaction with minimal nonspecific binding or physical adsorption of the fluorescein residues with the microparticles. Next, the average fluorescence intensity plot of Figure 2.2h shows highly linear trend in the fluorescence directly proportional to the chitosan concentration. This further confirms that the fluorescence rises from the S_N2 reaction, and that the added chitosan is readily accessible for reaction with NHS–fluorescein. In addition, the evenly dispersed fluorescence within each microparticle (except for the edge areas) along with very small error bars for all the chitosan concentration ranges in Figure 2.2h clearly illustrate highly uniform and consistent conjugation reaction. These results suggest that the chitosan oligomers are well dispersed on the particles with minimal phase separation (a.k.a.

phase coarsening) during the preparticle solution mixing and photopolymerization steps under the conditions enlisted in this study[17]. Meanwhile, particles with higher chitosan content were not readily fabricated due to high viscosity of the preparticle solution mainly caused by the chitosan moiety[16] (data not shown). In short summary, the results in Figure 2.2 indicate that chitosan oligomers are incorporated with PEG networks in a stable manner (further examined in Figure 2.3) and chemically reactive toward amine group reactive chemistry.

2.3.2 Stable Incorporation of Chitosan Oligomers within the Microparticles

To confirm that the chitosan oligomers are incorporated with the PEG networks of the microparticles in a stable manner, I carried out FTIR analysis on the chitosan–PEG microparticles, and examined the retention of fluorescence and chemical reactivity upon long term storage, as shown in Figure 2.3.

For the FTIR spectra shown in Figure 2.3a, I conducted FTIR microscopy on individual microparticles, allowing for identification of chemical groups on specific locations (i.e. on each microparticle rather than bulk). First as shown in Figure 2.3a(i), the FTIR spectrum of a thin chitosan film shows three characteristic peaks; a broad band at 3420 cm^{-1} attributed to the stretching vibration of O−H and N−H, a peak at 1655 cm^{-1} assigned to the C=O stretching vibration of secondary amide (amide I), and a peak at 1560 cm^{-1} attributed to the N−H bending vibration of secondary amide (amide II).[100, 108] Next, two typical peaks of PEGDA at 2880 cm^{-1} (stretching vibration of methylene, C−H) and 1726 cm^{-1} (stretching vibration of C=O)[109] are shown in the spectrum of a thin PEGDA film (Figure 2.3a(ii)). These two characteristic peaks of PEGDA are also observed for both PEG and chitosan–PEG microparticles as shown in Figure 2.3a(iii) and (iv), while the characteristic peaks for the chitosan are not clearly shown for the chitosan–PEG microparticle in Figure 2.3a(iii), likely due to the low content of chitosan in these particles. Meanwhile, Figure 2.3a(v) shows that subtracting the spectrum of the PEG microparticle from the spectrum of the chitosan–PEG microparticle (i.e. iii – iv) allows the characteristic peaks of chitosan to be clearly observed as indicated by the three small arrows. Therefore, the FTIR microscopy results shown in Figure 2.3a confirm that the chitosan oligomers are incorporated in the PEG-based microparticles.

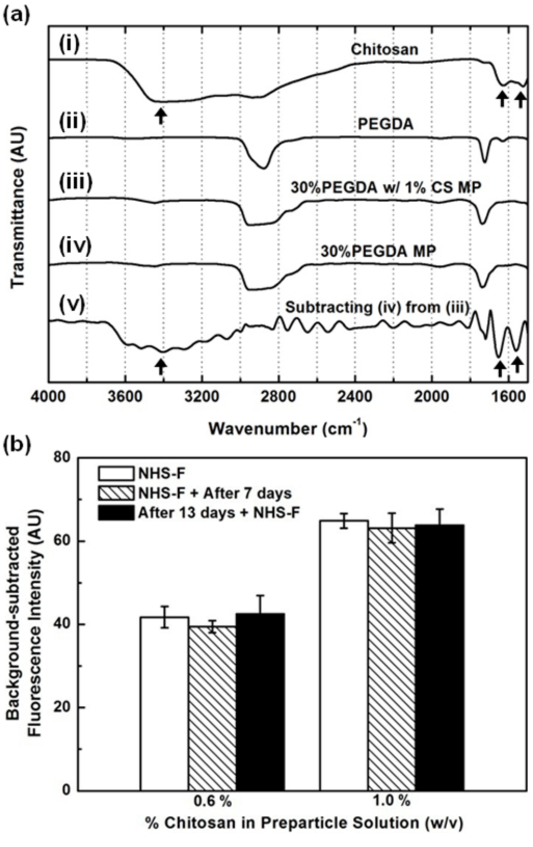

Figure 2.3. Stability of chitosan–PEG microparticles. (a) FTIR spectra of (i) thin chitosan film, (ii) thin PEGDA film, (iii) chitosan–PEG microparticle (MP), (iv) PEG microparticle and (v) subtraction of (iv) from (iii). (b) Background-subtracted average fluorescence intensities of the microparticles immediately upon fluorescent labeling (white columns), upon storage for 7 days in buffer solution after fluorescent labeling (striped columns), and upon fluorescent labeling after 13 days storage of unlabeled particles (black columns). Error bars represent standard deviation from at least seven particles.

I next examined the stability and reactivity of the chitosan moieties in the microparticles upon long term storage as shown in Figure 2.3b. For this, I compared average fluorescence intensities upon background subtraction (i.e. the average fluorescence intensity of PEG microparticles without chitosan) to eliminate fluctuation from any nonspecific binding of the fluorescein dye. First, the average fluorescence intensity of the fluorescently labeled particles stored for 7 days in buffer solution (striped columns in Figure 2.3b) shows negligible difference with that of the particles right upon fluorescent labeling (white columns). This minimal loss of fluorescence indicates that the chitosan oligomers are incorporated with the PEG networks in a stable manner. Second, the average fluorescence intensity of the particles exposed to NHS–fluorescein after 13 days of particle storage in buffer solution (black columns in Figure 2.3b) also shows negligible difference with that of the particles right after exposure to NHS–fluorescein (white columns). This result further demonstrates the stable incorporation of chitosan oligomers with the PEG-based particles as well as the retention of chemical reactivity of the chitosan–PEG particles. In addition, the fluorescence intensities of 0.6% chitosan–PEG particles are approximately 60% of the 1% chitosan particles under all the three conditions, which correlates well with the results shown in Figure 2.2. This result obtained from independent sets of microparticles further confirms reproducibility and consistency of my particle fabrication and chemical conjugation scheme.

I hypothesize that the observed stable incorporation of chitosan with the particles is mainly due to covalent binding between the primary amine groups of chitosan and acrylate groups of PEGDA during the photopolymerization, rather than physical entrapment under the conditions employed in this study (further examined in Figure 2.4). This copolymerization is further supported by previous reports on the free radical-induced graft copolymerization of vinyl group-containing monomers onto chitosan backbone.[110, 111] While the FTIR results in Figure 2.3a do not confirm the covalent bonds between amine groups of chitosan and acrylate groups of PEGDA (such as secondary amine), the results in Figure 2.3b indicate that chitosan–PEG particles possess sufficient stability for further conjugation and applications such as in the development of biosensing platforms.[103, 112, 113] Overall, the results in Figure 2.3 confirm that the chitosan oligomers are incorporated with PEG networks of the microparticles in a stable manner.

2.3.3 Effect of PEGDA Concentration on the Distribution of Chitosan Oligomers within the Microparticles

Next, I examined the effect of PEGDA concentration on the distribution of chitosan available for conjugation within the microparticle structures as shown in Figure 2.4. For this, I fabricated chitosan–PEG particles with fixed chitosan content (1% (w/v)) and varying PEGDA concentrations, which lead to different mesh sizes.[8, 114, 115] These particles were then utilized for fluorescent labeling, and imaged via fluorescence and confocal microscopy.

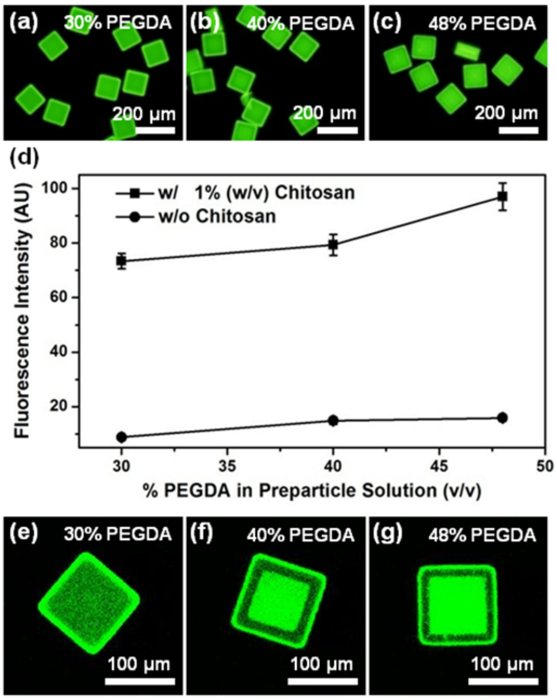

Figure 2.4. Distribution of chitosan within chitosan–PEG microparticles. (a-c) Fluorescence micrographs of the fluorescently labeled microparticles with different PEG contents; 30-48% (v/v) PEGDA and 1% (w/v) chitosan. (d) Average fluorescence intensity plot of the microparticles shown in (a-c); squares, and without chitosan; circles. Error bars represent standard deviation from at least five particles. (e-g) Confocal micrographs of microparticles shown in (a-c).

First, the fluorescence micrographs of Figure 2.4a-c show that the particles are well-formed and uniformly labeled with NHS–fluorescein, and that the total fluorescence appears to be equivalent for the three PEGDA concentrations under the fabrication conditions employed in this study. Second, the average fluorescence intensity analysis at the center of particles shown in Figure 2.4a-c also shows that there is small difference among each case (less than 25%) with slight increase in the fluorescence intensity (Figure 2.4d). Consistently negligible fluorescence of the negative controls (i.e. the particles without chitosan, solid circles in Figure 2.4d) indicates that this slight increase in fluorescence is not due to nonspecific binding of fluorescein dyes from increased PEG contents in the microparticles. Therefore, the result shown in Figure 2.4d confirms that a small rise of fluorescence intensity results from the specific conjugation reaction (S_N2) as mentioned in Figure 2.2, and that there appear to be more chitosan oligomers retained in the particles with higher PEG content. Meanwhile, the small error bars for all the conditions in Figure 2.4d further indicate the consistent and reproducible fabrication and conjugation. Third, confocal micrographs of microparticles with different PEG contents (Figure 2.4e-g) show striking difference in the distribution of fluorescently labeled chitosan moieties within the microparticles. These micrographs were obtained at the center plane of each particle (i.e. the plane at 24-27 μm from the bottom of the approximately 54 μm height particle). Specifically, the chitosan–PEG particle in Figure 2.4e (30% initial PEGDA concentration) shows that most of the labeled chitosans are located along the particle surface, while the center region shows uniform yet weak fluorescence. This also indicates that the fluorescence for all other particles shown in Figure 2.2 mainly comes from surface-labeled ones (9.4 ± 1 μm from the particle surface). Next, particles with higher PEG concentration in Figure 2.4f,g show bright fluorescence at the center region as well as the near-surface regions. This result confirms that the small NHS–fluorescein molecules (MW 473.4 Da) are able to penetrate into the chitosan–PEG microparticles then react with the primary amines of chitosan. In other words, there is minimal diffusion limitation of small molecules (i.e. NHS–fluorescein) in the hydrogel structure. Therefore, the weak fluorescence at the center of the particle shown in Figure 2.4e is not due to diffusion limitation of NHS–fluorescein molecules. The bright fluorescence at the center of particle shown in Figure 2.4f,g suggests that phase separation between chitosan and PEGDA may occur during photopolymerization, and that chitosan oligomers (average M_n 5 kDa) are entrapped within the high concentration (i.e. small mesh size) PEG networks. On the other hand, the evenly dispersed yet weak fluorescence within the 30% PEGDA particle (Figure 2.4e) suggests that not all the chitosan is conjugated, and that unconjugated chitosan oligomers appear to diffuse out from the hydrogel network structure upon extensive washing. Therefore, I hypothesize that the observed slight increase in fluorescence intensity with increasing PEGDA concentration (Figure 2.4d) is mostly due to entrapped chitosans with chemical reactivity. This implies that not all the primary amine groups of chitosan would react with the acrylate groups of PEGDA; that is, chitosan does not act as a crosslinking agent. Rather, only a small number (one in many cases) of amines would conjugate to the hydrogel, and most amine groups should be available for subsequent amine-reactive conjugation reactions. Meanwhile, particles with less PEGDA concentration (below 20% (v/v)) were not readily fabricated (data not shown) regardless of added chitosan concentration, further corroborating my hypothesis that the chitosan does not appear to provide meaningful crosslinking with PEGDA. In addition, previous studies on the photo-induced graft copolymerization of vinyl group-containing monomer or polymeric monomer onto chitosan backbone[116, 117] report that complete graft of chitosan is achieved after approximately 90 min under optimized polymerization conditions. These studies also report that the grafting percentage and efficiency decrease when the excess amount of monomers is used due to more favorable homo-polymerization between the monomers than the copolymerization between chitosans and monomers. In my experimental system, short UV exposure time (15 min) with mild UV radiation (maximum 3 mW/cm^2) is applied to fabricate the chitosan–PEG microparticles. Besides, the chitosan–PEG particles are formed under excess PEGDA condition (more than 16 times in molar excess of PEGDA's acrylates than chitosan's amines). Combined, the previous reports and my experimental system suggest that only small fraction of chitosan is conjugated with PEG networks during the photopolymerization under excess PEGDA condition due to different reaction rates between the homo- (PEGDA–PEGDA) and hetero- (chitosan–PEGDA) polymerization.

In the meantime, long term storage of high PEG content chitosan–PEG particles that were broken did not lead to significant leaching of the fluorescence at the center region (Figure A1.2). This result suggests that these chitosan residues may be covalently bound with PEG networks (due to high PEGDA monomer content), or completely entrapped even without any covalent linkage within PEG networks; hydrogels with high PEG content are known to entirely block diffusion of large biomolecules such as proteins.[24, 25] Thus, the results showing entrapped and chemically reactive chitosan with high PEG concentration in Figure 2.4f,g may indicate potential of such particles for applications in controlled release or delivery of small molecules.[64, 118] In conclusion, the results on the distribution of chitosan within microparticles in Figure 2.4 show that chitosan is present on the particle surfaces, and partially conjugated to the PEG networks with most amine groups remaining for subsequent reactions.

2.3.4 Conjugation of Single-stranded DNA via SPAAC Reaction

As shown in Figure 2.5, I next demonstrate that robust SPAAC reaction can be utilized to anchor biomolecules onto the chitosan–PEG microparticles with high surface density. For this, the schematic diagram of Figure 2.5a shows that the chitosan–PEG microparticles are first activated with azadibenzocyclooctyne (ADIBO) using amine-reactive ADIBO–*sulfo*–NHS ester. These ADIBO-activated particles are then reacted with azide-containing molecules, in this case single-stranded (ss) DNA labeled with a fluorescent marker (F–DNA–azide) to yield stable triazole linkages.[119, 120]

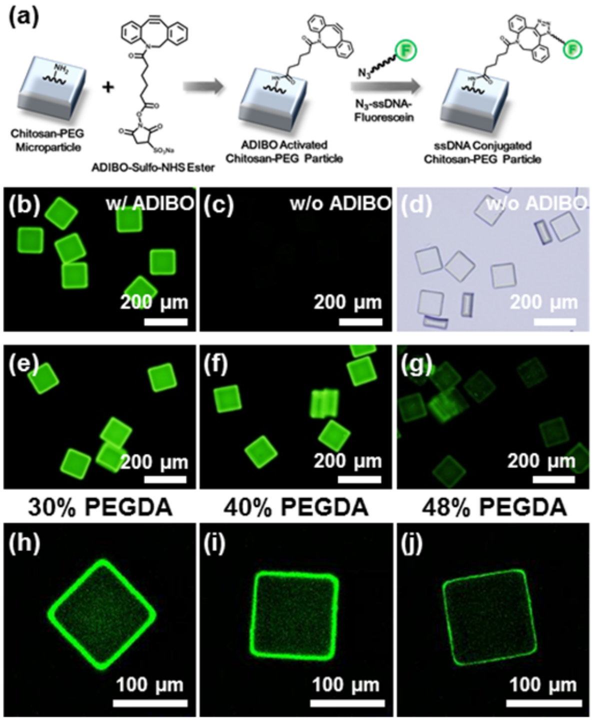

Figure 2.5. Covalent conjugation of ssDNA onto chitosan–PEG microparticles via SPAAC reaction. (a) Schematic diagram showing the ADIBO activation of chitosan–PEG microparticles followed by addition of azide–DNA. Fluorescence micrographs of (b) ADIBO-activated chitosan–PEG microparticles and (c) non-ADIBO-activated ones upon ssDNA conjugation. (d) Bright-field micrograph of the particles corresponding to (c). (e-g) Fluorescence micrographs of ADIBO-activated chitosan–PEG particles with different PEG contents (30-48% PEGDA) upon ssDNA conjugation. (h-j) Confocal micrographs of the particles shown in (e-g).

First, the fluorescence micrograph of Figure 2.5b shows highly uniform and consistent fluorescence of the ADIBO-activated chitosan–PEG particles upon reaction with azide-terminated and fluorescently labeled ssDNA (F–DNA–azide). Figure 2.5c,d shows no fluorescence when the chitosan–PEG particles without ADIBO-activation are reacted with azide–DNA, confirming that the fluorescence of the particles in Figure 2.5b comes from the conjugated DNAs via specific

SPAAC reaction with minimal nonspecific binding. Next, the fluorescence micrographs in Figure 2.5e-g show the effect of PEG contents of the chitosan–PEG particles on the conjugation of fluorescently labeled DNAs via SPAAC reaction. The chitosan–PEG particles with low PEG content shown in Figure 2.5e,f (30-40% PEGDA) yield equivalent fluorescence intensities with the particles reacted with NHS–fluorescein (Figure 2.4a,b) under the same imaging conditions. On the other hand, the fluorescence intensity of the particles with the highest PEG content (48%, Figure 2.5g) is substantially lower, showing low yield of conjugation efficiency. Meanwhile, hybridization assays with fluorescently labeled target DNA onto the capture DNA-conjugated chitosan–PEG particles as shown in Figure A1.3 yield highly sequence-specific binding behavior similar to previous results on the PEG particles with embedded Acrydite™–DNA incorporated by photo-induced copolymerization.[12] Additionally, the negligible decreases in the fluorescence intensity of the particles upon storage for 3 months (Figure A1.3g-l) indicate stable conjugation of capture DNAs with chitosan–PEG microparticles via SPAAC reaction, further confirming the utility of my fabrication-conjugation scheme.

In-depth examination via confocal microscopy in Figure 2.5h-j shows different fluorescence profiles from the conjugated ssDNAs with varying PEG contents. Specifically, the confocal micrographs obtained at the center plane of the particles show that the penetration depth of the ssDNAs decreases with increasing PEG contents (h: 6.5 ± 0.4 μm, i: 5.5 ± 0.4 μm, j: 2.4 ± 0.4 μm). This notable decrease in the penetration depth into the particles with the highest PEG content is consistent with the low fluorescence intensity for the 48% PEGDA particles shown in Figure 2.5g. Furthermore, these images in Figure 2.5h-j show that the fluorescence intensity at the center of particles is negligible, in direct contrast to the fluorescein labeling results in Figure 2.4e-g. These contrasting fluorescence profiles rise from the different size of the marker molecules being conjugated. Compared to the small molecule NHS–fluorescein (MW 473.4 Da), the molecular weight of the 18 base ssDNA used in Figure 2.5 is roughly 6 kDa, with about 2 nm of R_g (radius of gyration) from Kratky–Porod equation.[121] These DNAs thus do not readily penetrate into the particles with small hydrogel mesh size (roughly 1-3 nm[122, 123]) due to their diffusion limitation.[24, 25, 115] Meanwhile, NHS–fluorescein can readily penetrate through the hydrogels with all the PEG contents examined here and react with the available amines of the chitosan. Combined, the results shown in Figure 2.5 demonstrate a facile method for the conjugation of biomolecules onto the chitosan–PEG microparticles via SPAAC reaction.

2.3.5 Hybridization-based Assembly of Viral Supramolecules onto Chitosan–PEG Microparticles

Finally, I demonstrate that my fabrication and conjugation scheme can be utilized to assemble supramolecules (e.g. tobacco mosaic virus, TMV) with high surface density as shown in Figure 2.6. Briefly, the schematic diagram of Figure 2.6a shows that the capture DNA-conjugated chitosan–PEG particles are hybridized with linker DNAs. These linker DNAs consist of two regions, each complementary to the capture DNA and to the 5’ end of TMV’s genomic mRNA respectively. The particles are then assembled with partially disassembled and fluorescently labeled TMVs via nucleic acid hybridization,[87, 89] and analyzed by fluorescence microscopy and AFM.

The fluorescence micrograph in Figure 2.6b shows uniform and consistent assembly of fluorescently labeled TMVs, while low concentration of TMV (Figure 2.6c) yields low fluorescence. Furthermore, negligible fluorescence of negative controls confirms the sequence-specific binding of fluorescently labeled TMVs via nucleic acid hybridization; Figure 2.6d without linker DNA, Figure A1.4b without ADIBO-activation, capture DNA and linker DNA, and Figure A1.4c without capture DNA and linker DNA. These results further indicate the selective nature of the SPAAC reaction utilized here. In addition, a confocal micrograph at the center plane of the TMV-assembled microparticles in Figure A1.5 shows bright fluorescence near the particles surfaces, further confirming that the TMVs are displayed on the particle surfaces in high density. This confocal micrograph result also confirms stable assembly of TMVs on the particles since the confocal microscopy was conducted 1 month after TMV assembly and thorough washing. Next, the phase contrast AFM images of Figure 2.6e-g along with Figure A1.6a-c clearly show dense TMV assembly on the microparticles with minimal non-specific binding, indicating high surface DNA density on the DNA-conjugated chitosan–PEG microparticles.

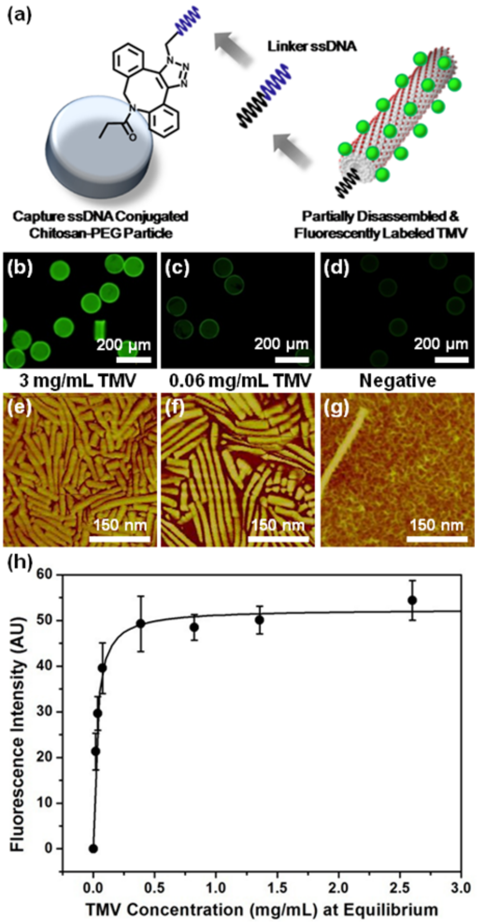

Figure 2.6. Assembly of tobacco mosaic virus (TMV) onto DNA–chitosan–PEG microparticles via nucleic acid hybridization. (a) Schematic diagram for the assembly of partially disassembled and fluorescently labeled TMV with the chitosan–PEG microparticles via nucleic acid hybridization. Fluorescence micrographs of the particles assembled with (b) 3 mg/mL and (c) 0.06 mg/mL TMV solution. (d) Fluorescence micrograph of the particles without linker ssDNA upon TMV (3 mg/mL) assembly. (e-g) Phase contrast AFM images of the particles shown in (b-d). (h) Plot of average fluorescence intensity vs. TMV concentration at equilibrium. The solid curve indicates the equilibrium binding model. Error bars represent standard deviation from at least seven particles per each condition.

Furthermore, I carried out quantitative examination of the TMV assembly with varying initial TMV concentrations (i.e. ranging from 0.06 mg/mL to

6 mg/mL). For this, I plotted the average fluorescence intensities measured at the center of particles (Figure A1.7) and fit the data to an equilibrium binding model with the TMV concentration at equilibrium upon TMV assembly. The significant difference between initial and equilibrium TMV concentrations is likely due to loss of TMV during fluorescent labeling and partial disassembly steps. As shown in Figure 2.6h, the results show typical equilibrium surface binding behavior with linear increase in the fluorescence at low TMV concentrations and reaching saturation at high TMV concentrations. The solid curve in Figure 2.6h represents the equilibrium binding model fit via double reciprocal plot,[12, 106] and indicates a reasonably good fit of the data to the model with 0.03 mg/mL (0.8 nM) of dissociation constant, K_{d} . Thus, the results shown in Figure 2.6h suggest that the TMV assembly with the particles is controllable with varying TMV concentrations, and that the probe DNA sites on the chitosan–PEG particles behave like equally accessible monolayer binding sites similar to the monolayer surface adsorption represented by the Langmuir isotherm.[12]

The results shown in Figure 2.6 are significant, and warrant detailed discussions as below. First, the observed TMV density is substantially higher than the one reported in a previous study on particles fabricated via stop-flow lithography (SFL particles).[89] I attribute this high surface density to more DNAs displayed and accessible to the surfaces for the chitosan–PEG particles, as shown in Figure 2.5. Specifically, DNA-conjugated PEG microparticles fabricated via PDMS-based microfluidic procedures show low DNA surface density due to the inhibition by oxygen,[48] limiting the available DNAs for assembly of supramolecules such as TMV near the particle surfaces. My fabrication and conjugation scheme based on RM and click chemistry utilizing the abundant amine groups thus would have potential for high density and controlled surface assembly or detection of a wide array of supramolecular targets or large biomolecules. In turn, these TMV assembly results suggest that there exist much higher number of DNAs near the surface of the chitosan–PEG particles in nanometer length scales, which may not be readily examined in Figure 2.5, and that the TMVs can be utilized as supramolecular models to examine the surface DNA density at nanoscale. Second, while the AFM results (Figure 2.6e,f) are consistent with the fluorescence results shown in Figure 2.6b,c, the difference in TMV coverage density between high (3 mg/mL) and low TMV concentration (0.6 mg/mL) is not as clear as in fluorescence. I attribute this to both the shrinkage of the particles upon drying for AFM sample preparation (approximately 24% in diameter) and the artifact of size over-estimation in AFM imaging (i.e. tip-induced broadening).[124] Finally, the result shown in Figure 2.6 is significant in that the fabrication and conjugation scheme to produce the assembly platforms in this study are significantly more facile and robust than previous studies on electrodeposited chitosan,[86] planar array platforms[87] and SFL-microparticles.[89] First, the replica molding technique is simple, clean and easy to fabricate the platforms in an economical, reproducible and scalable manner.[12] Second, the click chemistry is robust and selective without the obstacles present in other conjugation chemistries (e.g. rapid NHS ester hydrolysis in the NHS ester reaction chemistry,[17] needs for reduction of disulfide bonds in the maleimide reaction chemistry,[125] and relatively low reactivity in the Staudinger ligation reaction chemistry).[126] These led not only to consistent and reproducible assembly as shown in Figure 2.6b-g, but also to highly controllable assembly as shown in Figure 2.6h. Overall, the results shown in Figure 2.6 illustrate that the chitosan–PEG particles can be utilized as robust platforms for controlled supramolecular assembly with high surface density, and indicate substantially high surface DNA density on the particles.

2.4 Conclusions

In this chapter, I examined a facile method to fabricate non-spherical chitosan–PEG hydrogel microparticles, and to conjugate biomolecules on the particles with high surface density. Specifically, the well-defined and highly uniform chitosan–PEG hydrogel microparticles were readily fabricated via RM up to 1.2% (w/v) of chitosan. Fluorescence micrographs showed that the chitosan–PEG microparticles were chemically reactive to the amine-reactive chemistry. I also confirmed that the chitosan oligomers were incorporated with PEG networks in a stable manner via FTIR microscopy and long term storage studies. In addition, the confocal micrography demonstrated that chitosan oligomers were present near the particle surfaces while some were entrapped within the particles when the PEG contents were high. Next, the SPAAC reaction provided selective and robust routes to conjugation of biomolecules. The results showed that azide-modified ssDNAs were selectively anchored on the chitosan–PEG microparticles under mild conditions. Lastly, I utilized these ssDNA-conjugated chitosan–PEG particles in order to assemble TMV via nucleic acid hybridization as an example of orientationally controlled conjugation of supramolecular targets. AFM and fluorescence microscopy results further revealed sequence-specific and controllable TMV assembly with high surface density. I also carried out quantitative examination for the TMV assembly with the chitosan–PEG microparticles using the equilibrium binding model for the first time. The results showed typical equilibrium surface binding behavior, similar to the monolayer surface adsorption represented by the Langmuir isotherm with 0.8 nM of dissociation constant (K_d). Combined, the results shown in this chapter illustrate a facile fabrication-conjugation scheme for robust biomolecular assembly platforms.

The RM technique presented in this chapter possesses numerous inherent advantages including simple, robust, inexpensive, clean and scalable procedures, in addition to consistent duplication of complex structures with fine resolution. With this RM technique, the chitosan–PEG hybrid microparticles with improved mechanical properties, non-spherical shapes and chemical reactivity can be consistently fabricated. In the meantime, SPAAC reaction allows for utilization of the chitosan's abundant amine groups toward conjugation of biomolecules with the chitosan–PEG microparticles under mild conditions with high selectivity, enabling the high density surface display of biomolecular targets. Thus, I envision that my fabrication-conjugation scheme based on RM and SPAAC reaction can be utilized for a wide array of biomolecular targets (i.e. antibodies or enzymes) and applications (i.e. diagnosis or therapeutics).

3 PROTEIN CONJUGATION WITH CHITOSAN-INCORPORATED HYDROGEL MICROPARTICLES

3.1 Introduction

There exist increasing demands for facile fabrication strategies for protein sensing platforms with rapid and high throughput sensing capability in various application areas such as medical diagnostics,[31] industrial bioprocesses,[32] and pathogen detection.[33] While the enzyme linked immunosorbent assay (ELISA) utilizing antibody–antigen interaction has been established as the standard method for protein detection, it suffers from labor intensive and time consuming nature as well as the requirement for relatively large amount of target protein samples.[38] Alternative protein sensing platforms have been developed such as chip-based microarrays,[127] hydrogel-based planar arrays,[128] and particle-based suspension arrays.[129] However, challenges still remain for facile fabrication of probe biomolecule (i.e. antibody)-conjugated platforms toward rapid biosensing applications; harsh and complex fabrication procedures,[127, 130] nonspecific binding of antibodies and target proteins on substrates,[30] damage of antibodies during conjugation steps[30] and slow target protein (i.e. antigen) binding kinetics due to mass transfer limitation of the target proteins (such as through the hydrogel networks).[28, 30]

In this chapter, I aim to tackle these challenges by utilizing a facile fabrication-conjugation scheme shown in Chapter 2. Specifically, chitosan–PEG hybrid microparticles are fabricated via RM (Figure 3.1a), and the as-prepared chitosan–PEG particles are utilized for protein conjugation via SPAAC reaction (Figure 3.1b). In-depth examination of protein–particle conjugation kinetics is also carried out for further understanding of protein conjugation with hydrogel platforms. For this, I first utilized a red fluorescent protein R-Phycoerythrin (R-PE) as a model protein. Fluorescence and confocal microscopy results on the R-PE-conjugated chitosan–PEG particles demonstrate selective conjugation of the R-PEs near the particle surfaces as well as long term stability. Next, examination of the protein conjugation kinetics indicate multiple reaction regimes comprised of a rapid initial stage, an intermediate stage, and a steady and slow final stage, unlike SPAAC reaction between small molecules. Finally, I demonstrate that antibody-conjugated chitosan–PEG particles are readily fabricated with anti-R-PE antibody – R-PE pair as a model system, and that an antibody–antigen binding kinetics study with these platforms shows rapid antigen binding. Overall, these results illustrate facile fabrication-conjugation strategy via RM and SPAAC reaction for robust protein-conjugated platforms that can be readily extended to a wide range of protein sensing applications.

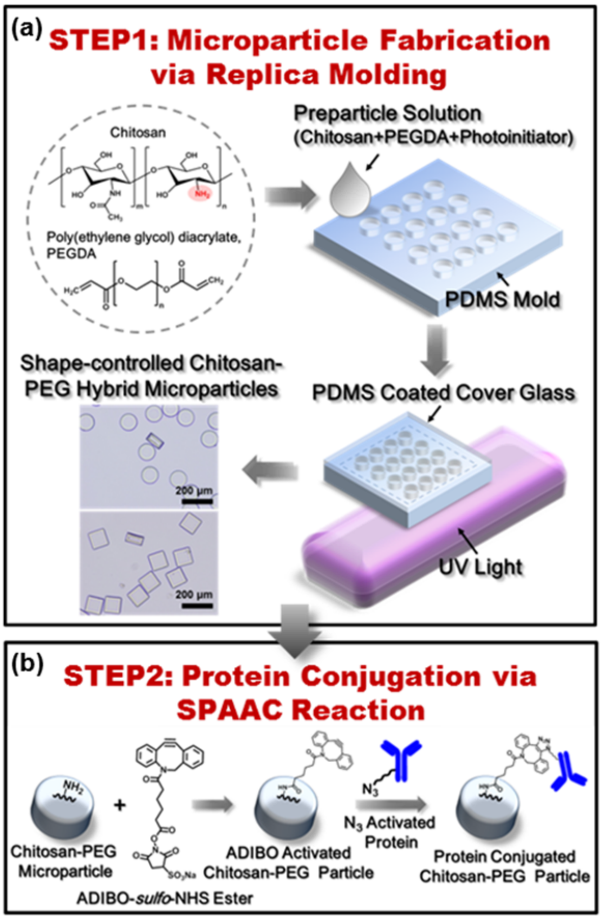

Figure 3.1. Schematic diagram of the fabrication-conjugation scheme via replica molding (RM) and SPAAC reaction for protein–conjugated platforms. (a) Chitosan–PEG hybrid microparticle fabrication procedure via RM. (b) Protein conjugation with the as-prepared chitosan–PEG hybrid microparticle via SPAAC reaction.

3.2 Materials and Methods

3.2.1 Materials

Chitosan oligosaccharide lactate (average M_n 5 kDa, > 90% deacetylation), poly(ethylene glycol) diacrylate (PEGDA, average M_n 700 Da), 2-hydroxy-2-methylpropiophenone (Darocur 1173, photoinitiator (PI)), phosphate buffered saline (PBS) tablets (0.01 M phosphate, 0.0027 M potassium chloride, 0.137 M sodium chloride, pH 7.4), and saline sodium citrate (SSC) buffer (20×concentrate, molecular biology grade) were purchased from Sigma-Aldrich (St. Louis, MO). Azadibenzocyclooctyne (ADIBO)–*sulfo*–*N*-hydroxysuccinimide (NHS) ester (a.k.a. dibenzylcyclooctyne (DBCO)–*sulfo*–NHS ester) and azide–Flour 488 were purchased from Click Chemistry Tools (Scottsdale, AZ). NHS–PEG_{12}–Azide, PBS packs (0.1 M sodium phosphate, 0.15 M sodium chloride, pH 7.2), borate buffer (20×concentrate, 50 mM borate, pH 8.5), Tween 20 (TW20), poly(dimethylsiloxane) (PDMS) elastomer kits (Sylgard 184), and centrifugal filter units (Amicon Ultra 0.5) were purchased from Thermo Fisher Scientific (Waltham, MA). All the chemicals were analytical grade, and used without further purification.

3.2.2 DNA Oligonucleotides

Azide-terminated and fluorescently labeled single-stranded (ss) DNA (5'-/azide/ATGATGATGATGATGATG/FAM/-3') was purchased from Integrated DNA Technologies (Coralville, IA)

3.2.3 Proteins and Antibodies

Red fluorescent protein R-Phycoerythrin (R-PE in sodium phosphate buffer, pH 7.0 with ammonium sulfate) was purchased from AnaSpec (Fremont, CA). Bovine serum albumin (BSA in PBS buffer, pH 7.4 with Kathon preservative) was purchased from Thermo Fisher Scientific (Waltham, MA). Anti-R-PE antibody (R-Ab in 0.02 M potassium phosphate, 0.15 M sodium chloride, pH 7.2 with 0.01% (w/v) Sodium Azide) and anti-green fluorescent protein (GFP) antibody (G-Ab in PBS with 0.01% (w/v) Sodium Azide) were purchased from GenWay Biotech, Inc. (San Diego, CA)

3.2.4 Fabrication of Chitosan–PEG Hybrid Microparticles via Replica Molding

As shown in Figure 3.1a, chitosan–PEG hybrid microparticles utilized in this study were fabricated following procedures shown in Chapter 2. Briefly, preparticle solution consisting of 0.8% (w/v) chitosan, 40% (v/v) PEGDA, and 2% (v/v) PI was placed on a PDMS mold (1600 microwells per a mold), which was made of Sylgard 184 (10% (w/w) crosslinking agent) with overnight incubation at 65 ºC on a silicon master mold. The preparticle solution was then filled into the microwells by rubbing the mold with a disposable pipet tip. Upon taking away the excess preparticle solution with a pipet, the filled mold was sealed with a PDMS-coated glass slide except for the 0.7 cm×0.7 cm microwell section, preventing the glass slide from touching the top portion of the microwells. These procedures were conducted in a humidity chamber with approximately 94%

humidity to avoid evaporation of the preparticle solution.[12] The sealed mold was placed on an aluminum mirror (Thorlabs, Newton, NJ), and exposed to 365 nm UV light with an 8 W hand-held UV lamp (Spectronics Corp., Westbury, NY) for 15 min to crosslink the preparticle solution. The crosslinked chitosan–PEG particles were taken out from the mold by physically bending the mold, and collected by pipetting up upon placing deionized water containing 0.5% (v/v) TW20 on the mold surface. The collected particles were rinsed with washing procedures in a microcentrifuge tube; mixing the particles in 5×SSC buffer solution containing 0.05% (v/v) TW20 by pipetting, letting them to settle to the tube bottom for 1 min, and removing the supernatant. The washing procedure was repeated 5 times.

3.2.5 ADIBO-activation of Chitosan–PEG microparticles

For ADIBO-activation, the as-prepared chitosan–PEG microparticles were incubated with 500 μM ADIBO–*sulfo*–NHS ester in 5×SSC buffer solution containing 0.05% (v/v) TW20 for 1 h on a rotator at room temperature. Then, the unreacted ADIBO–*sulfo*–NHS ester molecules were removed by rinsing the particles 4 times with the washing procedure described above.

3.2.6 Azide-activation of R-PEs and Antibodies

To activate the R-PEs and the antibodies with azide, I first exchanged buffer solution of the R-PE and the antibody solution for borate buffered saline buffer solution (50 mM borate, 300 mM NaCl, pH 8.5) via centrifugal filtration. 450 μL of the R-PE and the antibody solutions (2 mg/mL) were then reacted with

13 µL of NHS–PEG_{12}–Azide solution (20 mM) for 30 min on a rotator at room temperature. The unreacted NHS–PEG_{12}–Azide molecules were separated from the R-PE and the antibody solutions via centrifugal filtration with PBS buffer solution (0.01 M phosphate, 0.0027 M potassium chloride, 0.137 M sodium chloride, pH 7.4). Concentrations of the final R-PE and antibody solutions were determined by UV-vis spectroscopy (Evolution^{TM} 300 UV-vis Spectrophotometer, Thermo scientific, Waltham, MA) with the characteristic absorbance peaks and molar extinction coefficients of the R-PE (1.96×10^6 $M^{-1}cm^{-1}$ at 565 nm)[131] and the antibody (2.1×10^5 $M^{-1}cm^{-1}$ at 280 nm).[132]

3.2.7 SPAAC Reaction for Conjugation with Chitosan–PEG Microparticles

To examine the effect of molecular size on the conjugation, a constant number of the ADIBO-activated chitosan–PEG microparticles (~200) were reacted with 4 µM azide-activated fluorescent dyes, azide-terminated and fluorescently labeled ssDNAs, and the azide-activated R-PEs in 5×SSC buffer solution containing 0.05% (v/v) TW20 for 24 h on a rotator at room temperature. The ADIBO-activated chitosan–PEG microparticles (~200) were also reacted with varying concentrations of azide-activated R-PEs (0-8 µM) for 24 h, and with 4 µM azide-activated R-PE for varying reaction times (0-48 h) in 5×SSC buffer solution containing 0.05% (v/v) TW20 at room temperature to examine the effect of the R-PE concentration on the conjugation and to investigate conjugation kinetics respectively. In order to fabricate antibody-conjugated particles, The

ADIBO-activated chitosan–PEG microparticles were reacted with 4 μM azide-activated antibodies in 5×SSC buffer solution containing 0.05% (v/v) TW20 for 24 h at room temperature. The unconjugated antibodies were separated from the particle solution by rinsing the particles 3 times with the washing procedure described above.

3.2.8 Antibody–antigen Binding

The antibody-conjugated chitosan–PEG microparticles were washed 2 times with blocking buffer solution (PBS pH 7.2 with 2% (w/v) BSA and 0.05% (v/v) TW20), and incubated in the blocking buffer solution for 1 h before antigen binding (i.e. target protein capture). To confirm the antibody conjugation with the chitosan–PEG microparticles, I utilized the anti-R-PE antibody– R-PE pair. For this, the anti-R-PE conjugated chitosan–PEG microparticles were incubated with 1 μM R-PE in blocking buffer solution for 3 h at room temperature. Also, three different shapes of particles; the anti-R-PE antibody-conjugated (circle), anti-GFP antibody-conjugated (square), and bare particles (hexagons) were incubated with 1 μM R-PE in blocking buffer solution for 3 h at room temperature to demonstrate selective antigen binding. Lastly, the anti-R-PE antibody-conjugated particles were incubated with varying concentrations of the R-PE (0.1-1000 nM) in blocking buffer solution for varying incubation times (0-15 h) to examine antigen binding rate. All the particles upon incubation with the R-PEs were rinsed 5 times with washing buffer (PBS pH 7.2 with 0.05% (v/v) TW20).

3.2.8 Imaging Analysis

The fluorescent dye-, fluorescently labeled ssDNA-, and R-PE-conjugated chitosan–PEG particles as well as the anti-R-PE antibody-conjugated chitosan–PEG particles upon incubation with the R-PEs were imaged with an Olympus BX51 microscope equipped with a DP70 microscope digital camera, and standard green (U-N31001) and red (U-N31002) filter sets (Chroma Technology Corp., Rockingham, VT). Confocal micrographs for each particle were obtained via a Leica DMIRE2 microscope equipped with a TCS SP2 scanner (Wetzlar, Germany). The particles were analyzed with a 20× objective (0.7 NA) at 488 nm excitation for the green fluorescent molecules (the fluorescent dyes and fluorescently labeled ssDNAs), and at 543 nm excitation for the R-PEs. Fluorescence intensities of the particles and penetration depths of the conjugated molecules were evaluated with ImageJ software.[105]

3.2.9 AFM

For AFM imaging of the R-PE-conjugated chitosan–PEG particles, the particles were placed on a glass slide, thoroughly washed 3 times with deionized water to remove salts in the buffer solution, and dried in a vacuum chamber for 2 h. 1 μm × 1 μm areas on the dried R-PE-conjugated particles were imaged via Dimension 3100 atomic force microscope (Digital Instruments, Santa Barbara, CA) with a Tap 150 silicon probe (aluminum reflex coating, Budget Sensors, Sofia, Bulgaria) in tapping mode (1.0 Hz scan rate for 512 lines). The AFM images were analyzed with Nanoscope software version 6.00.

3.3 Results and Discussion

3.3.1 Conjugation of Proteins with Chitosan–PEG Microparticles via SPAAC Reaction

As shown in Figure 3.2, I first demonstrate that chitosan–PEG hybrid microparticles fabricated via replica molding (RM) can be readily conjugated with proteins via SPAAC reaction. For this, I fabricated the chitosan–PEG microparticles via RM with a preparticle solution containing 40% (v/v) poly(ethylene glycol) diacrylate (PEGDA) and 0.8% (w/v) chitosan oligomer as shown in Figure 3.1a. The as-prepared particles were then activated with azadibenzocyclooctyne (ADIBO) using amine-reactive ADIBO–*sulfo*–*N*-hydroxysuccinimide (NHS) ester (Figure 3.1b), which then reacts with azide-activated proteins to form stable triazole linkages (SPAAC reaction, Figure 3.1b). To examine biomolecular conjugation of proteins with the particles, I utilized an azide-activated red fluorescent protein R-Phycoerythrin (R-PE, MW 240 kDa) as a model protein. I also utilized small fluorescent dye molecules (Azide-Fluor 488, MW 576 Da) and fluorescently labeled single-stranded (ss) DNAs (F–ssDNA, MW 6 kDa) to examine the effect of the molecular size on the conjugation as shown in the schematic diagrams (top row, Figure 3.2a-c). The particles conjugated with the fluorescent molecules through SPAAC reaction were then imaged via fluorescence and confocal microscopy.

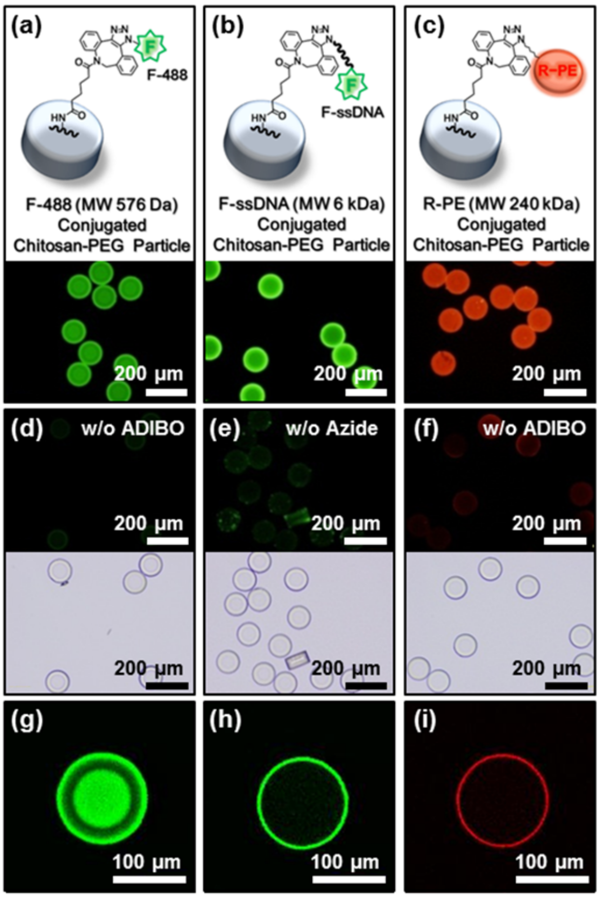

Figure 3.2. Conjugation of fluorescent molecules with different sizes onto chitosan–PEG microparticles via SPAAC reaction. (a-c) Schematic diagrams (top row) and fluorescence micrographs (second row) of (a) fluorescent marker (F-488, 576 Da)-conjugated chitosan–PEG microparticles, (b) fluorescently labeled single-stranded DNA (F–ssDNA, 6 kDa)-conjugated particles, and (c) red fluorescent protein R-Phycoerythrin (R-PE, 240 kDa)-conjugated particles. (d-f) Fluorescent micrographs and bright-field micrographs of negative controls with one of components missing for the SPAAC reaction; (d) azide-activated-fluorescent marker conjugation with non-ADIBO-activated particles, (e) non-azide-activated F–ssDNA conjugation with ADIBO-activated particles, and (f) azide-activated R-PE conjugation with non-ADIBO-activated particles. (g-i) Confocal micrographs at the center plane of the particles conjugated with fluorescent molecules; (g) F-488-, (h) F–ssDNA-, and (i) R-PE-conjugated particle.

First, the fluorescence micrographs in the second row of Figure 3.2a-c demonstrate highly uniform and consistent fluorescence on the ADIBO-activated chitosan–PEG particles with all three azide-modified fluorescent molecules examined. In contrast, fluorescence micrographs of Figure 3.2d-f and Figure A2.1b (Appendices) for negative controls, where one of the conditions for SPAAC reaction was omitted, show negligible fluorescence on the particles; the chitosan–PEG particles in Figure 3.2d,f were not activated with ADIBO, and the fluorescently labeled ssDNAs and the R-PEs used in Figure 3.2e and Figure A2.1b respectively were not activated with azide. These results confirm that the fluorescence of the particles shown in Figure 3.2a-c results from the conjugated fluorescent molecules (i.e. F-488, F–ssDNA and R-PE) via SPAAC reaction with minimal nonspecific binding.

Next, confocal micrographs at the center plane of each particle (Figure 3.2g-i) show different fluorescence profiles upon conjugation of fluorescent molecules with different sizes. Specifically, the confocal micrograph of the particle conjugated with small fluorescent dyes (Figure 3.2g) shows bright fluorescence at the center of particle as well as near the surface. This result is consistent with that in Chapter 2 where direct fluorescent labeling with NHS–fluorescein showed distribution of chitosan moieties within the chitosan–PEG particle; most of the chitosan moieties are located near the surface and at the center of 40% PEG particles. Thus, the fluorescence profile in Figure 3.2g suggests that ADIBO molecules are covalently bound with chitosan moieties near the particle surface and within the particle, and that small fluorescent markers containing azides readily penetrate into polymer networks of the particle and become conjugated with the ADIBO moieties via SPAAC reaction. In contrast, the confocal micrographs of the particles conjugated with biomolecules (Figure 3.2h,i) showed bright fluorescence only near the particle surfaces rising from different sizes of the conjugated molecules. Specifically, the calculated R_g (radius of gyration) of the ssDNA with 18 bases (MW 6 kDa) is about 2 nm,[121] and the reported radius of the R-PE (MW 240 kDa) is 5.54 nm.[133] The ssDNAs and R-PEs thus do not readily penetrate into the particles due to their diffusion limitation[24, 115] through the cross-linked PEG networks with small mesh size (roughly 1-3 nm).[24, 123] In addition, image analysis results for the confocal micrographs of Figure 3.2h,i show that penetration depth of the R-PE (3.08 ± 0.18 μm) is smaller than that of the ssDNAs (5.79 ± 0.16 μm), further confirming the diffusion limitation due to its large size. Combined, the results in Figure 3.2 demonstrate specific conjugation of proteins near the chitosan–PEG microparticle surfaces via SPAAC reaction.

3.3.2 Long-term Stability of ADIBO-activated Microparticles and Azide-activated Proteins.

Next, I examined long-term stability of my overall fabrication-conjugation scheme for protein-conjugated platforms based on the chitosan–PEG hybrid microparticles via RM and SPAAC reaction, as shown in Figure 3.3. For this, the ADIBO-activated chitosan–PEG particles and the azide-activated R-PEs were stored separately for three weeks at 4 ºC and reacted to form the R-PE-conjugated particles, and the resulting fluorescence was directly compared with freshly prepared batches as well as fluorescent dye-conjugated particles (schematic diagrams of Figure 3.3a,d).

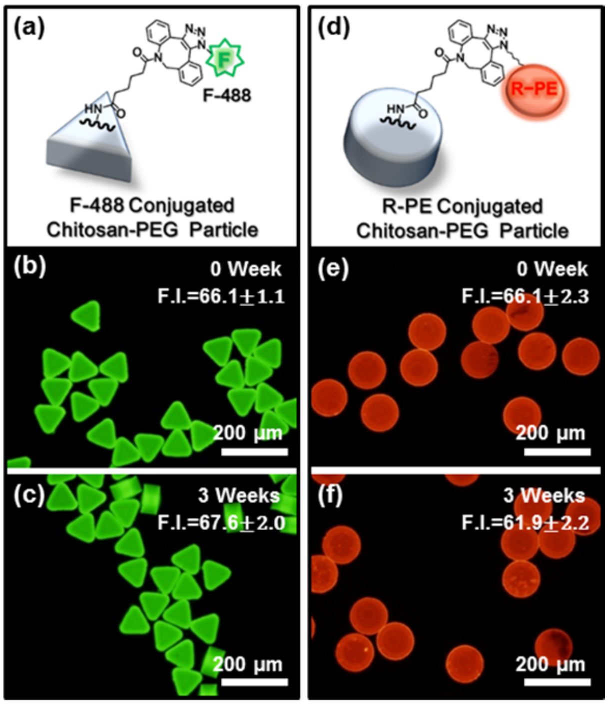

Figure 3.3. Long-term stability of ADIBO-activated chitosan–PEG microparticles and azide-activated proteins with retained chemical reactivity toward SPAAC reaction. (a) Schematic diagram of a fluorescent marker (F-488)-conjugated and triangle-shaped chitosan–PEG particle. (b,c) Fluorescence micrographs of chitosan–PEG particles (b) right upon conjugation with F-488, and (c) conjugated with F-488 upon particle storage for 3 weeks. (d) Schematic diagram of R-PE-conjugated and circle-shaped chitosan–PEG particle. (e,f) Fluorescence micrographs of chitosan–PEG particles (e) right upon conjugation with R-PE and (f) conjugation with R-PE upon particle storage for 3 weeks.

As shown in Figure 3.3b,c, both the freshly prepared and 3-week old ADIBO-activated particles showed highly uniform and consistent fluorescence upon reaction with the azide-modified fluorescent dye with negligible difference in the fluorescence intensity. This result clearly indicates the retention of the chemical reactivity of the ADIBO moieties as well as the stable incorporation of the ADIBO-bound chitosan moieties with the PEG networks of the particles, consistent with the results shown in Chapter 2. Next, the average fluorescence intensity upon reaction between the 3 week-old ADIBO-activated particles and azide-activated R-PEs (Figure 3.3f) showed minimal decrease, compared with that between the freshly prepared pairs (Figure 3.3e). This result shows stability and chemical reactivity of the azide-activated R-PEs under standard aqueous storage conditions, and further confirms the retained chemical reactivity of the ADIBO-activated particles as well as stable incorporation of the chitosan moieties with the particles.

The long term stability and retained chemical reactivity of both ADIBO-activated particles and azide-activated proteins shown here in Figure 3.3 indicates the utility and robust nature of the SPAAC reaction scheme in overcoming the inherent drawbacks of traditional conjugation schemes. For example, hydrolysis of NHS ester[17] prevents functionalized proteins from being stored for extended period until use or from being recycled despite recent advances on their prolonged stability and better formulations.[17, 19] Also, additional reagents (e.g. TCEP; tris(2-carboxyethyl)phosphine hydrochloride) or regeneration steps are required to address disulfide formation or oxidation of thiols,[125, 134] while such treatments may also lead to loss of conjugation efficiency and selectivity.[125] In contrast, the long term stability shown in Figure 3.2c and 3.3e,f suggests potential flexibility in carrying out protein conjugation reactions at points of care or reuse once the proteins are functionalized. In turn, the stability of the azide-activated proteins enable the un-conjugated proteins to be readily reused upon a simple purification step (such as centrifugal filtration), a strong advantage when precious proteins such as antibodies are to be conjugated. Combined with the stable incorporation and chemical reactivity of the chitosan in the chitosan–PEG microparticles via RM[88] and the stable nature of the triazole linkage resulting from SPAAC reaction[17], the results sin Figure 3.3 indicate the overall robust nature of my approach via RM and SPAAC reaction toward facile fabrication of protein-conjugated platforms.

3.3.3 Effect of Azide-activated Protein Concentration

In order to further examine the protein conjugation efficiency and yield at low protein concentrations (~μM) with the chitosan–PEG microparticles via SPAAC reaction, I next investigated the effect of the R-PE concentration as shown in Figure 3.4. For this, the ADIBO-activated chitosan–PEG particles were reacted with varying concentrations of the azide-activated R-PEs (0 to 8 μM) for a 24 h period and imaged with fluorescence microscopy, and the average fluorescence intensities at the center of at least five particles were compared. Atomic force microscopy (AFM) analysis was also performed to physically confirm the conjugated R-PEs on the particles, and the results were correlated with the fluorescence results.

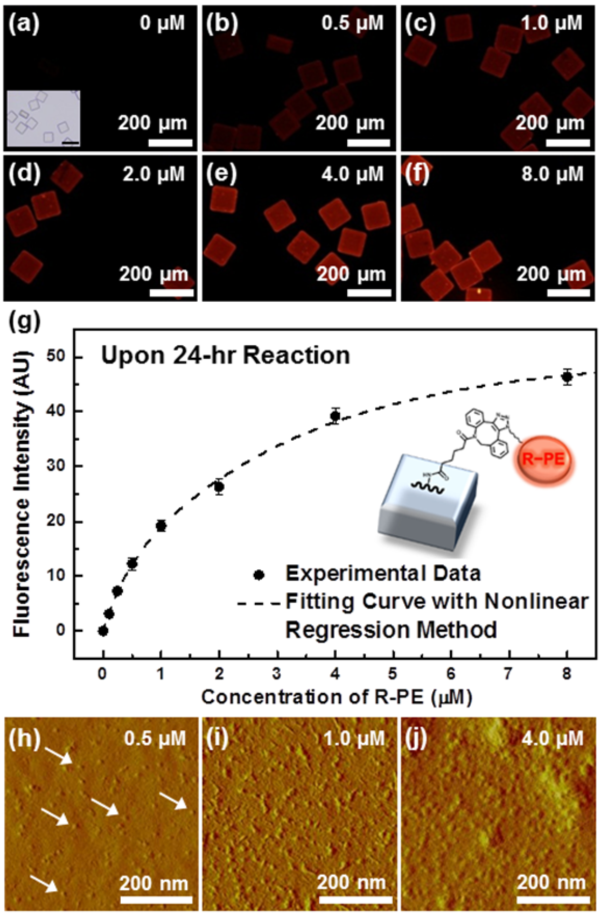

Figure 3.4. Effect of azide-activated protein concentration on protein–particle conjugation via SPAAC reaction. (a-f) Fluorescence micrographs of R-PE-conjugated particles upon reaction with different concentrations of R-PE (0-8 μM) for 24 h. (g) Average fluorescence intensity plot of R-PE conjugated particles shown in (a-f). Error bars represent standard deviation from at least five particles per each condition. (h-j) AFM images of R-PE conjugated particles shown in (b,c, and e). Dashed line represents data fit via a nonlinear regression method.

As shown in Figure 3.4a-f, the fluorescence intensity of the particles increased with increasing concentration of the R-PE. In addition, the fluorescence among the particles at the same R-PE concentration (Figure 3.4b-f) was highly uniform and consistent. This result suggests that the conjugated proteins are evenly dispersed on the particles. Next, the average fluorescence intensity plot (Figure 3.4g) also indicated that the fluorescence intensity increases with increasing R-PE concentration, with the conjugation approaching saturation at 8 μM. Also, the consistently small error bars throughout the concentration range examined indicated uniform and reproducible protein conjugation, and correlated well with the fluorescence images shown in Figure 3.4a-f. Importantly, the fluorescence profile (dashed line in Figure 3.4g, obtained from nonlinear regression method (Figure A2.2)) showed gradual increase in the conjugation, unlike typical saturation behavior observed in Langmuir isotherm-type curves where the binding increases linearly at low concentration and approaches saturation at higher concentration. Recently, Kuzmin *et al.* reported Langmuir isotherm-type profile from the conjugation of azide-modified fluorescent dyes on glass slide surfaces that are modified with strain-promoted alkynes.[135] Compared with this report, the fluorescence profile in Figure 3.4g implies that the R-PE conjugation with the particles doesn't reach completion within 24 h for all concentrations examined here. In addition, Langmuir isotherm-type curve fitting shown in Figure A2.2b yields higher saturation fluorescence intensity (56.82 AU) than that upon 24 h incubation, supporting my hypothesis that 24 h reaction is not sufficient to reach completion. This slow conjugation reaction is possibly due to the slow mass transfer of the R-PEs into the polymer networks of the particles under limited concentration conditions of the R-PEs (i.e. on the order of μM) as well as the inherent rate of the SPAAC reaction (the second-order rate constant of the SPAAC reaction in bulk solution (k) = 3.73 $M^{-1}s^{-1}$, Figure A2.5). Thus, a more in-depth kinetic study on the protein conjugation with the particles is needed, as shown below in Figure 3.5.

Next, AFM images (Figure 3.4h-j and Figure A2.3) confirmed the physical presence of the conjugated R-PEs on the particles. Specifically, circular dots with roughly 10 nm diameter (marked with small arrows in Figure 3.4h and Figure A2.3b) were observed on the R-PE-conjugated particles (Figure 3.4h-j and Figure A2.3b-d) in contrast to the particles before R-PE conjugation (Figure A2.3a). These dots correspond with the reported size of the hydrated R-PE (5.54 nm radius measured via dynamic light scattering[133]), confirming conjugation of the R-PEs on the particles. Of note, AFM results in a previous study also showed an accurate 18 nm diameter of TMV on soft polymeric surfaces unlike on solid surfaces,[89] suggesting that the observed dots here correspond to the R-PEs. Furthermore, the higher coverage density of the small dots with increasing R-PE concentration (Figure 3.4h-j and Figure A2.3a-d) was consistent with the fluorescence results (Figure 3.4a-c,e and insets of Figure A2.3a-d), further confirming that the small dots are the conjugated R-PEs. Meanwhile, the degree of increase in coverage density of the R-PE on the particles at 4 μM R-PE (Figure 3.4j and Figure A2.3d) did not linearly correlate with the increase in fluorescent intensity (Figure 3.4g) when compared with 1 μM

R-PE (Figure 3.4i and Figure A2.3c). Specifically, the fluorescence intensity increased about twice with 4 fold increase in R-PE concentration, yet such higher coverage density of the small dots in the AFM image was not as readily distinguishable. The AFM can probe the R-PEs that are mostly on the particle surfaces, while the confocal microscopy in Figure 3.2i indicates that the R-PE conjugation occurs throughout ~3 μm thickness. Therefore, the higher fluorescence intensity of the particles at 4 μM of R-PE should be due to the R-PEs throughout this 3 μm region. From these results, I hypothesize that the R-PEs are first conjugated near the particle surfaces, then penetrate into the polymer networks below the particle surfaces to find reactive sites to be conjugated. Overall, the results in Figure 3.4 indicate that the protein conjugation via SPAAC reaction is readily controllable by varying concentration of proteins at low μM ranges, and that the conjugated proteins are evenly dispersed on the particles.

3.3.4 Kinetics Study on the Protein Conjugation via SPAAC Reaction

Triggered by the non-ideal conjugation profiles shown in Figure 3.4, I next conducted a more thorough study on conjugation kinetics of R-PE with the chitosan–PEG microparticles via SPAAC reaction as shown in Figure 3.5. For this, a constant number of the ADIBO-activated chitosan–PEG particles (~200 per each reaction) were reacted with a constant concentration of the azide-activated R-PEs for 2 to 48 h. I utilized 4 μM R-PE for this study, since the difference in absorbance spectra of the R-PE before and after SPAAC reaction was negligible

(Figure A2.4), indicating constant concentration of the R-PE during the SPAAC reaction.

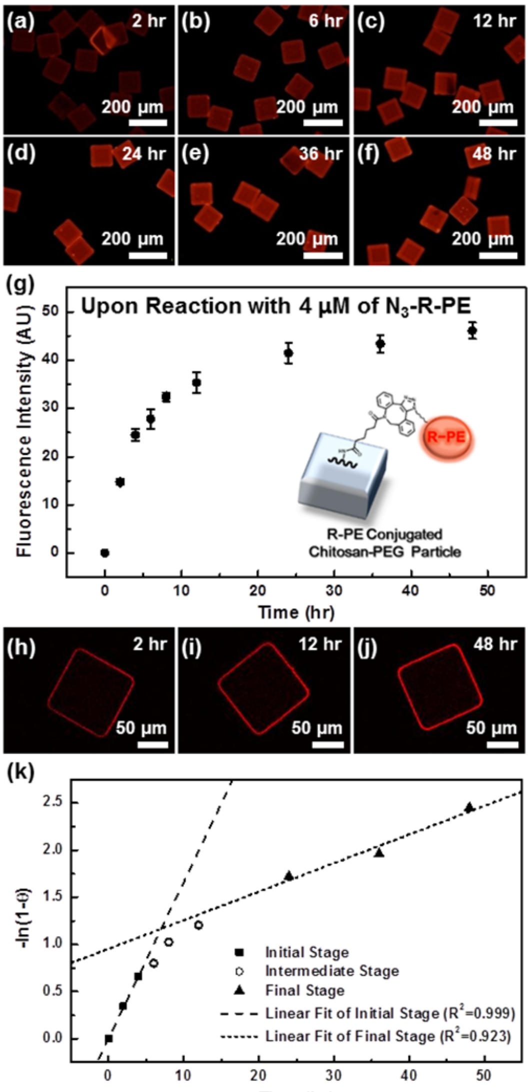

(l)

	k ($M^{-1}s^{-1}$)*	η
2nd Order Reaction Rate Constant of SPAAC Reaction	3.73	1.00
	k_{app} ($M^{-1}s^{-1}$)	η
Initial Stage	11.5	3.08
Final Stage	2.10	0.56

*Measured in aqueous solution (10% (v/v) DMSO and 90% (v/v) 5xSSC buffer solution containing 0.05% (v/v) Tween 20).

Figure 3.5. Protein–particle conjugation kinetics via SPAAC reaction. (a-f) Fluorescence micrographs of R-PE conjugated microparticles upon reaction with 4 µM

R-PE for varying reaction times (2-48 h). (g) Average fluorescence intensity plot of the particles shown in (a-f). Error bars represent standard deviation from at least five particles per each condition. (h-j) Confocal micrographs at the center plane of the particles shown in (a, c, and f). (k) Logarithmic plot of the average fluorescence intensity plot shown in (g) upon normalization with maximum fluorescence intensity of the particles. Slopes represent the apparent pseudo-first order rate constants. (l) Summary of the second-order rate constants (k_{app} and k), and ratios (η) of k_{app} to k.

First, the fluorescence intensity on the particles (Figure 3.5a-f) increased with time until 24 h, then approached saturation. Next, the average fluorescence intensity plot in Figure 3.5g showed that the fluorescence intensity increased rapidly in the first 4 h, then the rate of the increment slowed down. This result suggests that most of the active sites near the particle surfaces are consumed within a few hours, and then the conjugation rate decreases, implying diffusion limitation of the R-PEs into the particles.

Next, the confocal microscopy results in Figure 3.5h,i along with Figure A2.6a,b demonstrated that the penetration depth of the R-PEs upon 12 h reaction (3.1 μm ± 0.2) was deeper than that upon 2 h reaction (2.5 μm ± 0.3), and that the fluorescence intensity near the particle surfaces was also brighter than that of the 2 h reaction (Figure A2.6d,e). Meanwhile, differences in the penetration depth and fluorescence intensity between the particles upon 12 h (3.1 μm ± 0.2) and 48 h reaction (3.1 μm ± 0.2) were minimal (Figure 3.5i,j and Figure A2.6b-e). These results also indicate that the R-PEs are first conjugated near the particle surfaces within a few hours (Figure 3.5h), then penetrate into the polymer networks of the particles to find reactive sites (Figure 3.5i,j). The results on the penetration depth suggest diffusion limitation of the R-PEs into the polymer networks of the particle due to steric hindrance by the as-conjugated R-PEs[136] as well as small mesh size of the polymer networks,[123] leading to slowdown of the conjugation rate after the rapid initial conjugation. Thus, the confocal microscopy results in Figure 3.5h-j along with the fluorescence intensity plot in Figure 3.5g support my hypothesis on the steric hindrance of the protein conjugation mechanism (Figure 3.4).

For further in-depth evaluation of the protein conjugation kinetics under the reaction condition in this study (i.e. constant concentration of the R-PE), I next transformed the fluorescence data (Figure 3.5g) to a logarithmic plot (Figure 3.5k) where a slope represents the pseudo-first order rate constant to the ADIBO bound to the particle (Appendices, Section A2.5). As shown in Figure 3.5k, the transformed data yielded poor fit with the pseudo-first order reaction model (Appendices, Section A2.5), showing varying slopes with time; the slope decreased with time (initial, intermediate, and final stage) unlike the pseudo-first order reaction model with a straight line on the logarithmic plot.[137] This result indicates that the protein conjugation rate slows down over time, and supports my hypothesis that the steric hindrance caused by the as-conjugated R-PEs[136] should lower the conjugation rate further in addition to the diffusion limitation of the R-PEs through the particles with small mesh size.[123]

Lastly, I carried out a quantitative comparison of the rate of SPAAC reaction between the azide-activated R-PEs and the ADIBO-activated particles (protein–particle) with that between small molecules in the bulk solution (i.e.

ADIBO–*sulfo*–NHS (MW 532.5 Da) and NHS–PEG$_{12}$–Azide (MW 740.8 Da)). For this, I first determined the second-order rate constant of SPAAC reaction between the small ADIBO and azide molecules as shown in Figure A2.5. Briefly, I first measured the pseudo-first order rate constants (k') to the ADIBO molecule in the presence of excess azide in an aqueous batch system via UV-vis spectrophotometry (Figure A2.5). Then, the second-order rate constant ($k = 3.73\ M^{-1}s^{-1}$) of the reaction between the small molecules was calculated from the measured pseudo-first order rate constants. Next, I computed the apparent second-order rate constants (k_{app}) of the reaction between the azide–R-PEs and the ADIBO−particles by using the slopes for each stage shown in Figure 3.5k. Based on these rate constants, the ratio (η) of k_{app} to k was calculated as listed in the table of Figure 3.5l.

As shown in Figure 3.5k,l, the protein–particle conjugation at the initial stage (0-4 h, solid square) with 11.5 $M^{-1}s^{-1}$ of k_{app} showed 3.1 times faster conjugation rate than the reaction between small ADIBO and azide molecules in bulk solution ($\eta = 3.08$). Then, k_{app} started to decrease along with the decreasing slope in Figure 3.5k (the intermediate stage, 4-24 h, open circle). Finally, the reaction approached the final stage (after 24 h, solid triangle) with 2.10 $M^{-1}s^{-1}$ of k_{app} where the rate is 44 % lower than the reaction between small molecules ($\eta = 0.56$). The enhanced apparent conjugation rate at the initial stage can be attributed to three factors. First, multiple azide sites on each R-PE may increase the apparent rate (k_{app}). The R-PEs utilized in this study have multiple lysines (maximum 20 lysines on or near each R-PE surface, from crystal structure of R-PE at 2.2 Angstroms),[138, 139] thus multiple azide sites are on or near the surface. Oates *et al.* reported that the rate of antibody conjugation with porous silica supports increased with the number of accessible functional groups on the antibodies.[140] Second, higher density (or accessibility) of the ADIBO sites on the microparticles than bulk solution may also enhance the apparent conjugation rate. Moorthyl *et. al.* also reported that protein interaction (i.e. association) between protein A and IgG in hydrogel platforms was enhanced by "confinement and crowding" environment in the hydrogel.[141] Finally, protein–particle attraction such as the ion-dipole interaction can enhance the apparent conjugation rate. The isoelectric point (p*I*) of the R-PE is around 4.3-4.5, resulting in negatively charged R-PEs under the reaction condition used in this study (pH 7.0).[142] Suh *et al.* reported that negatively-charged magnetic beads were attached to microparticles made from PEGDA due to the ion–dipole interaction.[143] Meanwhile, the decreasing k_{app} after the initial stage further suggests that the as-conjugated R-PEs on the particles incur steric hindrance, preventing un-conjugated R-PEs in the reaction mixture from penetrating into the polymer networks of the particles (i.e. diffusion limitation) and resulting in further decrease in the apparent conjugation rate (24-48 h).

A recent study reported a similar biphasic kinetics behavior for labeling of small fluorescent dyes on ADIBO-attached polymer brush platforms via SPAAC reaction to the results here[137]; rapid initial stage with k'_{app} (the apparent pseudo-first order rate constant) $= 8.01\times10^{-4}$ s^{-1} and slow final stage with $k'_{app} = 1.87\times$

10^{-4} s^{-1}. However, the converted apparent second-order rate constants (k_{app}) of their ADIBO-attached polymer brush platform (1.60 $M^{-1}s^{-1}$ and 0.37 $M^{-1}s^{-1}$ for the initial and final stage, respectively) show slower rate than those of my particle platforms (k_{app} = 11.5 $M^{-1}s^{-1}$ and 2.10 $M^{-1}s^{-1}$ for the initial and final stage respectively, Figure 3.5l). I hypothesize that their slower reaction rate may be attributed to the single azide site on the fluorescent dye vs. multiple sites on azide-activated R-PE used in this study. Oates *et al.* also reported biphasic kinetics behavior for conjugation of aldehyde-activated antibodies on porous hydraizde-activated silica supports[140]; rapid initial stage with k'_{app} =1.9×10^{-5} s^{-1} and slow final stage with k'_{app} =4.0×10^{-6} s^{-1} corresponding to k_{app} =0.48 $M^{-1}s^{-1}$ and 0.10 $M^{-1}s^{-1}$, respectively. Compared with the apparent second-order rate constants of particle platforms used in this study (Figure 3.5l), the rate of antibody conjugation on the silica supports is much slower than that of the protein conjugation with microparticles via SPAAC reaction. This difference in the protein conjugation rate might be due to different reaction schemes.

In short summary, the overall conjugation kinetics of the R-PEs onto the particles shows three-phase behavior including a rapid initial stage (0-4 h) and an intermediate stage (4-24 h), followed by a steady and slow final stage (24-48 h).

3.3.5 Antibody Conjugation on Chitosan–PEG Microparticles

I next demonstrate conjugation of antibodies for selective capture of target proteins via the fabrication-conjugation scheme as shown in Figure 3.6. For this, the ADIBO-activated chitosan–PEG microparticles were reacted with azide-activated anti-R-PE antibodies (R-Ab), and incubated with R-PEs as shown in the schematic diagram of Figure 3.6c. Chitosan–PEG microparticles without ADIBO-activation and R-Ab were utilized as negative controls (schematic diagram in Figure 3.6a,b).

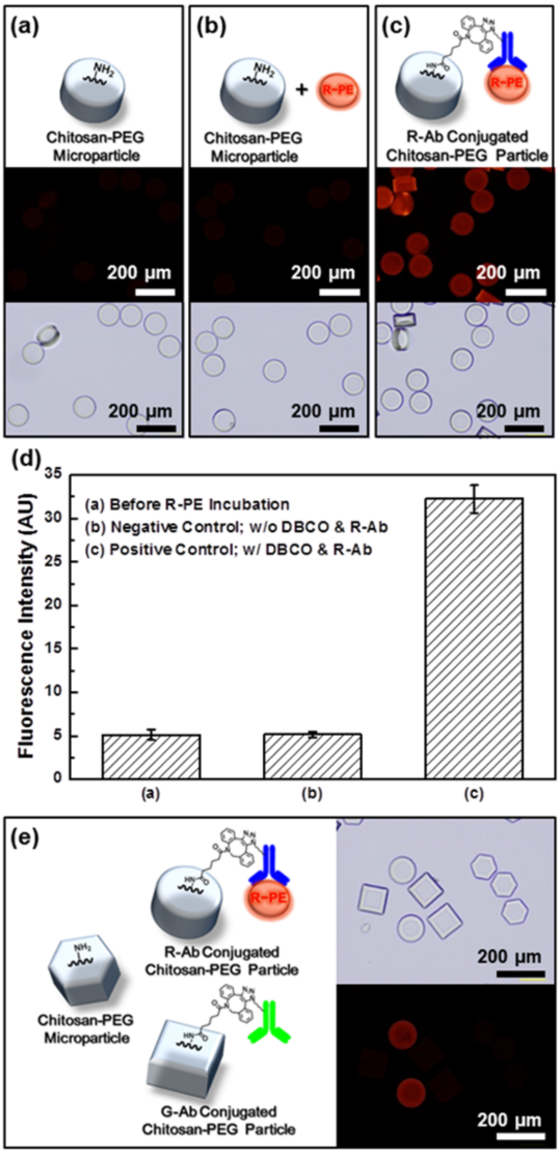

Figure 3.6. Antibody conjugation on chitosan–PEG microparticles and selective target protein capture with antibody-conjugated particles. (a-c) Schematic diagrams (top row), fluorescence micrographs (middle row), and bright-field micrographs

corresponding to the fluorescence micrographs (bottom row) of (a) bare chitosan–PEG particles, (b) non-ADIBO-activated particles upon incubation with 1 μM R-PE, and (c) anti-R-PE antibody-conjugated particles upon incubation with 1 μM R-PE. (d) Average fluorescence intensities of the particles shown in (a-c). Error bars represent standard deviation from at least five particles per each condition. (e) Selective R-PE capture with anti-R-PE antibody-conjugated particles (circle). Negative control particles; anti-GFP antibody-conjugated particles (square) and bare particles (hexagon).

First, the fluorescence micrograph of Figure 3.6a shows that there is minimal auto-fluorescence of the chitosan–PEG microparticles. Upon exposure to the R-PEs, the fluorescence micrograph of the negative control particles (Figure 3.6b) shows negligible fluorescence, while the R-Ab-conjugated particles (Figure 3.6c) show uniform and bright fluorescence. The fluorescence intensity analysis (Figure 3.6d) also clearly shows significant difference in fluorescence intensity between the R-Ab-conjugated particles (the rightmost column in Figure 3.6d) and the negative control ones (the middle and leftmost column in Figure 3.6d). These results indicate that most of the fluorescence on the particles in Figure 3.6c results from the captured R-PEs by the antibodies on the chitosan–PEG particles with minimal nonspecific binding of the R-PEs, confirming successful conjugation of the antibodies with the particles through SPAAC reaction. Importantly, the fluorescence image of the R-PE captured microparticles via antibody binding (Figure 3.6c,d) shows ~50% fluorescence intensity compared to R-PE conjugated microparticles (Figure 3.3e) under identical conjugation and imaging conditions. Considering the large size (240 kDa) of the R-PEs resulting in further steric hindrance (as also indicated by short penetration depth of the R-PEs in Figures 3.2i and 3.5h-j, and slower conjugation reaction rate at the final stage in Figure 3.5k,l), the fluorescence intensity on the R-PE captured microparticles suggests that a significant portion of the conjugated anti-R-PE antibodies retain activity and are available for R-PE recognition. Furthermore, the uniform and consistent fluorescence on the R-Ab-conjugated particles along with the small error bars in Figure 3.6d suggests that the antibodies are evenly conjugated on the particles with retained binding affinity to the antigens, enabling reliable target protein sensing.

Finally, I demonstrate selective antibody-antigen interaction via simple shape-based encoding in Figure 3.6e. For this, I first prepared three different shapes of the chitosan–PEG particles (i.e. circle, square, and hexagon, schematic diagram in Figure 3.6e) via RM, and activated them with ADIBO except for the hexagon particles. The two ADIBO-activated particles (circular and square shapes) were then conjugated with R-Ab and anti-GFP antibodies (G-Ab) respectively via SPAAC reaction. All three types of particles were mixed together, incubated with the R-PEs, then imaged. The bright field micrograph in Figure 3.6e shows three different shapes of particles with and without different antibodies. The fluorescence micrograph in Figure 3.6e shows strong fluorescence only on the R-Ab-conjugated particles (circle) and negligible fluorescence on the G-Ab-conjugated particles (square) and the bare particles (hexagon). This result clearly indicates selective capture of target proteins with the antibody-conjugated particles, along with the readily addressable detection of target antigens via simple shape-based encoding.[12]

The results shown in Figure 3.6 illustrate several advantages of my facile fabrication-conjugation scheme for antibody-conjugated platforms. First, traditional chip-based antibody-conjugated platforms require several harsh cleaning procedures and tedious functionalization steps to obtain well-defined functionalized substrates.[127, 130] Also, hydrophobicity of the functionalized substrates can cause protein denaturation, uneven conjugation and nonspecific binding of proteins.[30] In contrast, my fabrication scheme utilizing RM for the chemically reactive and well-defined platforms (i.e. chitosan–PEG hybrid microparticles) offers a simple, clean, and mild method.[88] In addition, biologically inert and nonfouling nature of PEG of the chitosan–PEG particles allows to retain functionality of the conjugated proteins,[144, 145] while minimizing nonspecific binding[146] as shown in Figure 3.6. My conjugation scheme via SPAAC reaction along with hydrophilic nature of the PEG-based particles[147] allows uniform conjugation of the antibodies on the particle shown in Figure 3.6. Finally, antibody-conjugated hydrogel platforms[53, 148] often suffer from potential antibody damage, lowering the binding affinity of antibodies by active radicals during the polymerization process (i.e. oxidative damage to proteins).[149, 150] In contrast, my post-fabrication antibody conjugation strategy can prevent antibody damage attributed to the mild conjugation conditions.[68]

In the meantime, there exist multiple lysine residues on antibodies, particularly near the recognition sites.[151] Activation of these lysine residues with azides via lysine–NHS ester reaction may lead to reduced binding affinity to antigens,[151] resulting in lower capacity of active antibodies in my system. I note that much progress has been made on the site-specific incorporation of unnatural amino acids on proteins via genetic modification, particularly azidophenylalanines to confer azide functionalities.[152] Combined with the SPAAC reaction-based conjugation schemes and the kinetic considerations reported here, such technologies should open doors for significantly more selective and robust routes to protein conjugation.

In short summary, the results in Figure 3.6 demonstrate that the antibody-conjugated microparticle platforms toward protein sensing applications can be readily fabricated via my fabrication-conjugation method.

3.3.6 Antibody–antigen Binding Kinetics of Antibody-conjugated Chitosan–PEG Microparticles

Finally, I investigated antibody–antigen binding kinetics of the antibody-conjugated chitosan–PEG microparticles as shown in Figure 3.7. For this, I incubated a constant number of the anti-R-PE antibody-conjugated particles (~200) with varying concentrations of the R-PE (0.1-1000 nM) and time periods (0-15 h). The average fluorescence intensity of at least seven particles per each batch was then plotted upon background subtraction.

First, the average fluorescence intensity plot in Figure 3.7 demonstrates that the fluorescence reaches equilibrium within 3 h at high R-PE concentrations (100 and 1000 nM, solid circles and squares in Figure 3.7 respectively), showing rapid antibody–antigen binding. Particularly, the fluorescence reaches above 90% of the equilibrium values within 15 min for these two cases. Next, the average fluorescence intensity at relatively low concentration of the R-PE (1 nM, open squares in Figure 3.7) increased rapidly within 30 min, and the increment of the fluorescence intensity slowed down. Lastly, the average fluorescence intensity at 0.1 nM R-PE (open circles in Figure 3.7) showed relatively linear increase over time, and suggests that femtomolar quantity of the target proteins (i.e. 10 femtomoles at 0.1 nM in 100 µL of total assay volume) can be readily detected under my standard imaging conditions.

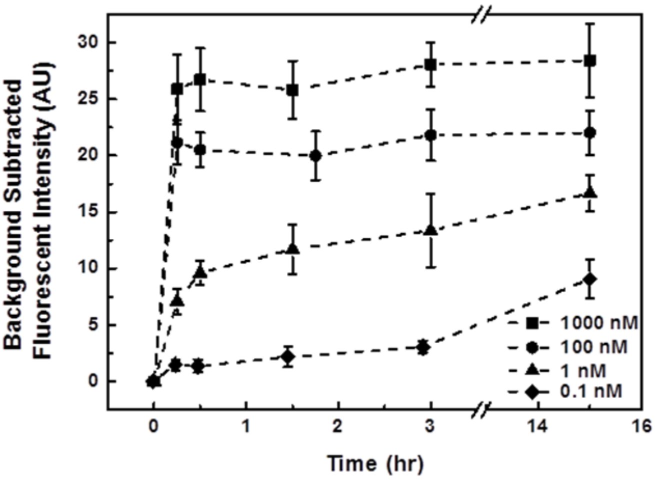

Figure 3.7. Antibody–antigen binding kinetics. Background subtracted average fluorescence intensity plots of anti-R-PE antibody-conjugated chitosan–PEG microparticles upon incubation with varying R-PE concentrations (0.1-1000 nM) and incubation time (0-15 h). Error bars represent standard deviation from at least seven particles per each condition.

This rapid binding within the first 15 min for all R-PE concentration ranges except for 0.1 nM can be attributed to primarily surface binding resulting from the surface-displayed antibodies (within the top 3 µm for R-PE, confocal micrographs in Figure 3.2 and 3.5). Combined with the favorable solution kinetics of the hydrogel microparticle suspension array format,[141] this rapid response illustrates potential for a large number of protein sensing applications[31-33] with improved performances. Meanwhile, the observed difference in the antigen binding trajectory between the high and low R-PE concentrations can be attributed to a combination of several mechanisms, such as the difference in the driving force for diffusion of the R-PEs into the particles and binding rate in a batch system at varying antigen concentrations.[28]

In the meantime, the R-PEs (MW 240 kDa) utilized here for the antibody-antigen binding kinetic study are much larger than typical antigens for clinical applications (MW less than 30 kDa).[53] I thus hypothesize that the model antibody–antigen interaction between the anti-R-PE antibodies on the particles and the R-PEs may suffer from more steric hindrance than that for clinical measurements, slowing down the binding rate. In other words, I anticipate that the antibody–antigen binding rate of my platforms in clinical measurements can be faster than that shown here in Figure 3.7. Overall, the results shown in Figure 3.7 demonstrate the utility of the antibody-conjugated chitosan–PEG microparticles toward rapid protein sensing applications.

3.4 Conclusions

In this chapter, I examined the protein conjugation with the chitosan–PEG hybrid microparticles via SPAAC reaction. First, the fluorescence and confocal microscopy results on the R-PE-conjugated particles showed selective conjugation of the proteins, primarily within top 3 μm of the particles due to the size of the proteins and small mesh size of polymer networks of the particles. My overall fabrication-conjugation scheme via RM and SPAAC reaction showed long-term stability with retained chemical reactivity of each component (ADIBO–particle and azide–protein) under standard aqueous storage conditions. The fluorescence and AFM results for varying R-PE concentration showed controllable protein conjugation. The protein conjugation kinetics results revealed multiple regimes; rapid initial stage, intermediate stage, and steady and slow final stage. Combined with the penetration depth analysis over reaction time, these results suggest that the reduced conjugation rate with time should be due to steric hindrance resulting from the as-conjugated R-PEs as well as the diffusion limitation of the R-PEs through the polymer networks with small mesh size. Lastly, I demonstrated that the antibody (anti-R-PE)-conjugated chitosan–PEG particles were readily fabricated via my fabrication-conjugation scheme, showing selective target protein capture with simple shape-based encoding. In addition, the results on the antibody–antigen binding kinetics demonstrated rapid antigen binding with the antibodies bound to the particles, indicating potential for rapid protein sensing applications. Combined, the results shown in this chapter illustrate facile fabrication-conjugation scheme via RM and SPAAC reaction for robust protein-conjugated platforms.

Meanwhile, the results presented in this chapter demonstrate several advantages of my post-fabrication conjugation strategy via SPAAC reaction along with the RM-based hybrid microparticle fabrication utilizing a versatile biopolymer chitosan; (1) simple, clean, and mild fabrication procedures of RM,

(2) biologically inert and nonfouling characteristic of PEG in the chitosan–PEG particles, (3) highly selective biomolecular conjugation via SPAAC reaction under mild reaction conditions, (4) long-term stability of the conjugation components (ADIBO–particle and azide–protein) for SPAAC reaction, allowing for reuse of precious proteins, and (5) rapid target protein capture through primarily surface-displayed probe biomolecules. These traits should address key challenges in current fabrication techniques for protein-conjugated platforms such as harsh and complex fabrication steps, nonspecific binding of proteins, possible protein damage during protein conjugation with platforms, limited stability of crosslinkers, and slow binding kinetics due to mass transfer limitation of target proteins. I thus envision that my fabrication-conjugation scheme utilizing versatile chitosan, simple RM, and mild and selective SPAAC reaction can be readily expanded to a wide range of protein sensing applications (e.g. disease diagnosis, bioprocess monitoring, bioterrorism detection etc.).[31-33]

4 ENHANCED PROTEIN CONJUGATION WITH VIRAL NANOTEMPLATES ASSEMBLED ON HYDROGEL MICROPARTICLES

4.1 Introduction

There exist increasing demands for protein sensing platforms with high performance in various application areas.[32, 34, 153] Such platforms should offer the ability to properly diagnose disease stages resulting in adequate medical treatments,[153] to accurately determine biopharmaceutical product titer for reliable monitoring in industrial bioprocesses,[32] or to enable early detection of pathogens with their protein byproducts.[34] Planar platforms including enzyme-linked immunosorbent assay (ELISA) and protein microarrays have been typically utilized for quantification of target proteins. However, low conjugation (or loading) capacity of probe antibodies and nonspecific adsorption of target proteins on the planar platforms render accurate quantification challenging.[29, 30, 154] Platforms with 3D structures and nonfouling properties (e.g. polymer brushes[154, 155] and hydrogel-based platforms[27, 29, 53]) have been developed to enhance antibody conjugation capacity and to reduce nonspecific adsorption of proteins. However, there still exist challenges in these 3D platforms; (1) limited enhancement in the antibody conjugation and target protein capture capacity due to diffusion-limited 3D structures of the platforms (i.e. dense or collapsed polymer chains[154, 155] and small mesh size of hydrogel microparticles[27]) and low antibody conjugation efficiency of the hydrogel-based platforms,[29] and (2) potential oxidative damage to antibodies by free radicals and/or oxygen molecules in exited states[150] during formation of polymer networks with antibodies via photo-induced radical polymerization.[29, 53]

In this chapter, I aim to address these challenges via integrated approach with rigid nanotubular virus templates (tobacco mosaic virus; TMV) and hydrogel microparticle platforms, as shown in Figure 4.1. Specifically, genetically modified TMV (TMV1cys) is activated with chemically reactive moieties via thiol–maleimide reaction, partially disassembled at the 5'-end by ultracentrifugation under slightly alkaline pH, and programmed with linker DNAs containing sequences complementary to TMV's 5'-end mRNA and to capture DNA (Figure 4.1a). Particularly, I utilize a rapid and bioorthogonal tetrazine (Tz)–*trans*-cyclooctene (TCO) cycloaddition reaction[21, 22] for protein conjugation in this study due to its high conjugation yield, selectivity and stability of the functional groups.[21] Next, I enlist poly(ethylene glycol) (PEG)-based polymeric hydrogel microparticles containing aminopolysaccharide chitosan (i.e. CS-particles) prepared via simple replica molding as platforms for TMV assembly, as shown in Chapter 2; the as-prepared hydrogel microparticles are first conjugated with capture DNAs, then the activated and programmed TMVs are assembled with the capture DNA-conjugated particles via nucleic acid hybridization as shown in Figure 4.1b. These activated TMV-assembled microparticles (TMV-particles) offer abundant TCO moieties that form stable Tz–TCO linkages upon reaction with Tz-activated proteins.

Protein conjugation results using a model red fluorescent protein R-Phycoerythrin (R-PE) show substantially higher conjugation capacity of the TMV-particles over planar substrates or hydrogel microparticles. Further in-depth comparison in protein conjugation kinetics with a slower conjugation reaction (strain-promoted alkyne–azide cycloaddition (SPAAC) reaction) shows that the TMV-particles provide less hindered environment for protein conjugation over the hydrogel microparticles. Results on protein capture using the anti-R-PE antibody–R-PE pair as a model system also show improved capture capacity for the TMV-particles, while results for controlled TMV assembly density show minimal negative impact on protein conjugation and capture by densely assembled TMV. Combined, these results illustrate a facile post-fabrication protein conjugation approach by integration of viral templates with hydrogel microparticles for improved and controlled protein conjugation and sensing platforms.

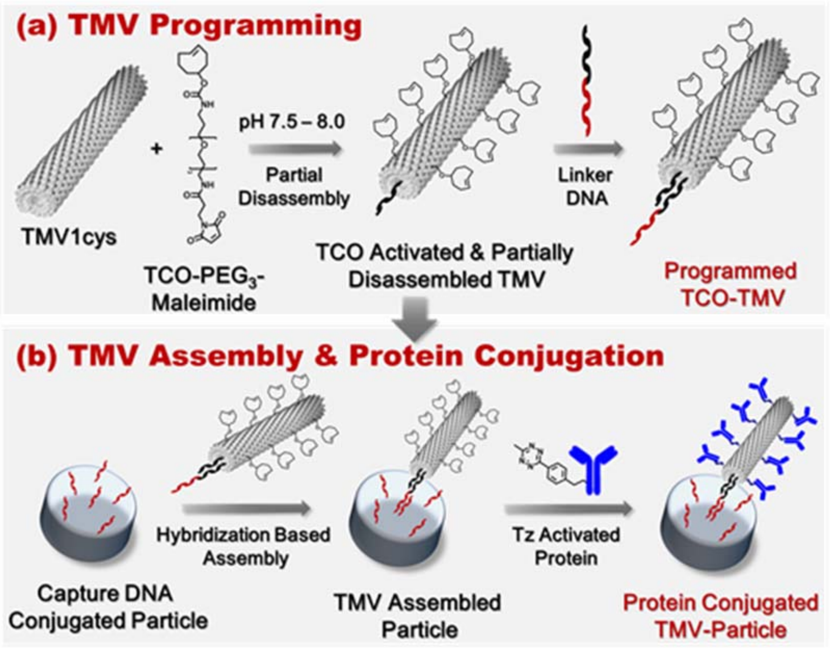

Figure 4.1. TMV assembly with chitosan–PEG hydrogel microparticles followed by protein conjugation. (a) TMV programming with linker DNAs upon TCO activation. (b) TMV assembly via nucleic acid hybridization, and protein conjugation via Tz–TCO cycloaddition reaction.

4.2 Materials and Methods

4.2.1 Materials

Chitosan oligosaccharide lactate (average M_n 5 kDa, > 90% deacetylation), poly(ethylene glycol) diacrylate (PEGDA, average M_n 700 Da), 2-hydroxy-2-methylpropiophenone (Darocur 1173, photoinitiator (PI)), phosphate buffered saline (PBS) tablets (0.01 M phosphate, 0.0027 M potassium chloride, 0.137 M sodium chloride, pH 7.4), Trizma pre-set crystals (pH 7.5) and saline sodium citrate (SSC) buffer (20×concentrate, molecular biology grade) were purchased from Sigma-Aldrich (St. Louis, MO). Fluorescein–5-maleimide was purchased from Biotium (Hayward, CA). *Trans*-cyclooctene (TCO)–PEG_4–*N*-hydroxysuccinimide (NHS) ester, TCO–PEG_3–maleimide, tetrazine (Tz)–PEG_5–NHS ester, azadibenzocyclooctyne (ADIBO)–*sulfo*–NHS ester, and ADIBO–maleimide were purchased from Click Chemistry Tools (Scottsdale, AZ). NHS–PEG_{12}–Azide, D-sucrose (≥ 99.9%), sodium phosphate monobasic anhydrous (99%), sodium phosphate dibasic anhydrous (≥ 99%), PBS packs (0.1 M sodium phosphate, 0.15 M sodium chloride, pH 7.2), borate buffer (20×concentrate, 50 mM borate, pH 8.5), Tween 20 (TW20), poly(dimethylsiloxane) (PDMS) elastomer kits (Sylgard 184), and centrifugal filter units (Amicon Ultra 0.5) were purchased from Thermo Fisher Scientific (Waltham, MA). All the chemicals were analytical grade, and used without further purification.

4.2.2 DNA Oligonucleotides

Single-stranded DNAs used in this study were purchased from Integrated DNA Technologies (Coralville, IA); Capture DNA (5'-/azide/ATGATG ATGATGATGATG/-3') and linker DNA (5'-/GTTTGTTGTTGTTGGTAATTG TTG*TTTTTT*CATCATCATCATCATCAT/-3'; TMV 5'-end complementary sequence *Spacer* capture DNA complementary sequence).

4.2.3 Proteins and Antibodies

Red fluorescent protein R-Phycoerythrin (R-PE in sodium phosphate buffer, pH 7.0 with ammonium sulfate) was purchased from AnaSpec (Fremont, CA). Anti-R-PE antibody (R-Ab in 0.02 M potassium phosphate, 0.15 M sodium chloride, pH 7.2 with 0.01% (w/v) Sodium Azide) was purchased from GenWay Biotech, Inc. (San Diego, CA).

4.2.4 Preparation of Capture DNA-conjugated Chitosan–PEG Microparticles

Capture DNA-conjugated chitosan–PEG microparticles were prepared via replica molding and SPAAC reaction as described in Chapter 2. Briefly, a PDMS mold containing 1600 microwells was made of Sylgard 184 with 10% (w/w) crosslinking agent upon overnight incubation at 65 ºC on a silicon master mold. Microwells of the mold were then filled with preparticle solution (0.8% (w/v) chitosan, 40% (v/v) PEGDA, 2% (v/v) PI, and deionized water) by scratching the mold with a disposable pipet tip. Excess preparticle solution was suctioned up with a pipette, and the filled mold was sealed with a PDMS-coated glass slide except for the microwell area (0.7 cm×0.7 cm). These procedures were carried out in a humidity chamber in order to prevent rapid evaporation of the preparticle solution in the microwell.[12] To crosslink the preparticle solution and form chitosan–PEG microparticles (CS-particles), the sealed mold was exposed to 365 nm UV light with an 8 W hand-held UV lamp (Spectronics Corp., Westbury, NY) on an aluminum mirror (Thorlabs, Newton, NJ) for 15 min. The CS-particles were taken out from the PDMS mold by physically bending the mold, and collected by pipetting up upon placing deionized water containing 0.5% (v/v) TW20 on the mold. The collected CS-particles were then rinsed with washing procedures; mixing the CS-particles with 200 µL of 5×SSC buffer solution containing 0.05% (v/v) TW20 in a microcentrifuge tube by pipetting, and changing the buffer solution for fresh one upon letting them settle to the tube bottom.

To conjugate capture DNAs with the CS-particles via SPAAC reaction, the CS-particles were first activated with ADIBO molecules upon 1 h incubation with 500 µM ADIBO–*sulfo*–NHS ester in 5×SSC buffer solution containing 0.05% (v/v) TW20 at room temperature. The ADIBO-activated CS-particles were then rinsed with the washing procedures, and reacted with 10 µM azide-terminated capture DNA in 5×SSC buffer solution containing 0.05% (v/v) TW20 at room temperature. The capture DNA-conjugated CS-particles were then rinsed with the washing procedures.

4.2.5 TMV Assembly with CS-particles via Nucleic Acid Hybridization

For TMV assembly with the capture DNA-conjugated CS-particles, I first chemically modified and partially disassembled TMVs according to the previously reported procedures with minor modifications.[87-89] Briefly, genetically modified TMVs (TMV1cys) were incubated with 10× molar excess of TCO–PEG$_3$–maleimide, ADIBO–maleimide, or fluorescein–5-maleimide over cysteines displayed on the TMV surfaces separately in 100 mM sodium phosphate buffer (pH 7.0) for 2 h at room temperature. The chemically modified TMVs were then then purified and partially disassembled to expose their 5'-end mRNA sequence by ultracentrifugation in a 10-40 wt% sucrose gradient (100 mM Tris buffer, pH 7.5) at 4 ºC with 48000g. The chemically modified and partially disassembled TMVs were pelleted with ultracentrifugation at 90000g and resuspended in 5× SSC buffer solution. Next, these TMVs were incubated with 10× molar excess of linker DNA overnight at room temperature in order to "program" them for assembly with the capture DNA-conjugated CS-particles via nucleic acid hybridization.[87, 89] The excess linker DNAs were then separated from the TMV solution via centrifugal filtration at 4 ºC with 5×SSC buffer solution containing 0.05% (v/v) TW20. The chemically modified and programmed TMVs were incubated with the capture DNA-conjugated CS-particles in 5×SSC buffer solution containing 0.05% (v/v) TW20 overnight at 30 ºC, and rinsed with washing procedures described above. To control TMV assembly density of the TMV-assembled particles (TMV-particles), I utilized varying TMV concentrations (0-3 mg/mL).

4.2.6 Tetrazine- or Azide-activation of Proteins and Antibodies

In order to activate R-PEs and R-Abs with tetrazine or azide molecules, I first exchanged buffer solution of the R-PE and the R-Ab solution for borate buffered saline buffer solution (50 mM borate, 300 mM NaCl, pH 8.5) via centrifugal filtration at 4 ºC. The R-PEs and the R-Abs (2 mg/mL) were then reacted with 20× molar excess of Tz–PEG_5–NHS ester or NHS–PEG_{12}–Azide for 30 min at room temperature. Unreacted chemicals were separated from the R-PE and the R-Ab solution via centrifugal filtration with PBS buffer solution (pH 7.4). Concentrations of the final R-PE and R-Ab solution were measured by UV-vis spectroscopy (Evolution^{TM} 300 UV-vis Spectrophotometer, Thermo scientific, Waltham, MA) with characteristic absorbance peaks and molar extinction coefficients of the R-PE (1.96×10^6 $M^{-1}cm^{-1}$ at 565 nm)[131] and typical immunoglobulin G (IgG) antibodies (2.1×10^5 $M^{-1}cm^{-1}$ at 280 nm).[132]

4.2.7 Protein Conjugation with Microparticles

To compare protein conjugation capacity between TMV-particles and CS-particles, I conjugated red fluorescent proteins (R-PEs) with both particles via Tz–TCO cycloaddition reaction. As shown in Figure 4.2, the CS-particles were first activated with TCO molecules upon 1 h incubation with 500 μM TCO–PEG_4–NHS ester in 5×SSC buffer solution containing 0.05% (v/v) TW20 at room temperature, and rinsed with the washing procedures described above. Next, TCO-activated CS-particles were reacted with 2 µM Tz-activated R-PEs in 5×SSC buffer solution containing 0.05% (v/v) TW20 for 2 h at room temperature. The as-prepared TCO-activated TMV-particles were also reacted with Tz-activated R-PEs under identical conjugation conditions. The unconjugated R-PEs were separated from the particle solutions with the washing procedures as described above.

Figure 4.2. Schematic diagram for TCO activation of the CS-particle via an amine-reactive chemistry and R-PE conjugation with the TCO-activated CS-particle via Tz–TCO cycloaddition reaction.

To examine the effect of inherent reaction rates of Tz–TCO cycloaddition and SPAAC reaction on protein conjugation kinetics with the TMV- and CS-particles, I conjugated R-PEs with both particles via each conjugation reaction for varying times. Specifically, I conjugated 2 µM Tz-activated R-PEs with the as-prepared TCO-activated TMV- and CS-particles in 5×SSC buffer solution containing 0.05% (v/v) TW20 for 0-17 h at room temperature. I also conjugated 2 µM azide-activated R-PEs with the as-prepared ADIBO-activated TMV- and CS-particles in 5×SSC buffer solution containing 0.05% (v/v) TW20 for 0-18 h at room temperature. The unconjugated R-PEs were then separated from the particle solutions with the washing procedures as described above. The TCO-activated TMV- and CS-particles were also conjugated with 2 μM Tz-activated R-PEs in 5×SSC buffer solution containing 0.05% (v/v) TW20 for 2 h at room temperature to compare R-PE binding between R-Ab conjugated TMV- and CS-particles. The unconjugated R-Abs were separated from the particle solution following the washing procedures with PBS buffer solution (pH 7.2) with 0.05% (v/v) TW20.

4.2.8 Antibody–antigen Binding

To compare R-PE capture capacity between the R-Ab conjugated TMV- and CS-particles, both particles were incubated with 1 and 10 nM R-PEs in PBS buffer solution (pH 7.2) with 0.05% (v/v) TW20 for 3 h at room temperature. Unbound R-PEs were then separated from the particle solution following the washing procedures with PBS buffer solution (pH 7.2) with 0.05% (v/v) TW20.

4.2.9 Imaging Analysis

The fluorescently labeled, R-PE conjugated and R-PE captured TMV- and CS-particles were imaged with an Olympus BX51 microscope equipped with a DP70 microscope digital camera, and standard green (U-N31001) and red (U-N31002) filter sets (Chroma Technology Corp., Rockingham, VT). Fluorescence intensities of the particles (at least 7 particles for each experimental condition) were evaluated with ImageJ software.[105]

4.2.10 Global Fitting Curve for Fluorescence Intensity Plots

As shown in Figure 4.6, I attempted to fit all normalized fluorescence intensity values of the fluorescently labeled, R-PE conjugated and R-PE captured

TMV-particles with a model equation by utilizing a nonlinear regression method provided from OriginPro 8 (OriginLab Corporation, Northampton, MA). Specifically, I examined data fitting for all the normalized fluorescence intensity plots in Figure 4.6 with a Langmuir isotherm-type saturation model,

$$y = \frac{\alpha x}{(\beta + x)}$$

where α (1.09) represents the maximum normalized fluorescence value at saturation, and β (0.299 mg/mL) represents a fitting constant. All the normalized fluorescence data fit well with the Langmuir isotherm-type curve fitting showing R^2=0.984.

4.3 Results and Discussion

4.3.1 Enhanced Protein Conjugation Capacity of TMV-assembled Particles

I first demonstrate that TMV templates assembled with the CS-particles offer more protein conjugation sites than the CS-particles as shown in Figure 4.3. For this, linker DNA programmed- and TCO-activated TMVs (Figure 4.1a) were assembled with capture DNA-conjugated CS-particles via nucleic acid hybridization (Figure 4.1b). TCO-activated TMV-particles were then reacted with 2 μM of Tz-activated R-PEs for 2 h. Next, TCO-activated CS-particles were prepared via S_N2 reaction between primary amines in the CS-particles and NHS-ester derivatives of TCO, and reacted with Tz-activated R-PEs under identical conjugation conditions (Figure 4.2). Fluorescence intensity of the R-PE conjugated TMV-particles (Figure 4.3a) was compared with that of the R-PE conjugated CS-particles (Figure 4.3e).

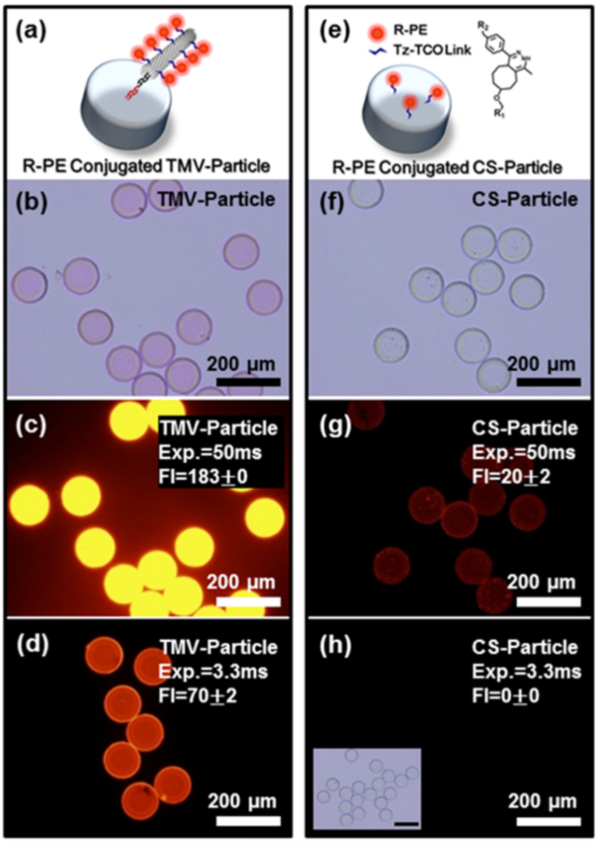

(i)	TMV-Particle	CS-Particle
Fluorescence Intensity at Exp.=50ms (AU)	1060±24*	20±2

*Estimated fluorescence intensity at 50ms exposure time from measured fluorescence intensity at 3.3ms exposure time.

Figure 4.3. Enhanced protein conjugation capacity with assembled TMV templates. (a-d) A schematic diagram (a), a bright-field micrograph (b), and fluorescence micrographs at 50 ms (c) and 3.3 ms exposure time (d) of the R-PE conjugated TMV-particles. (e-h) A schematic diagram (e), a bright-field micrograph (f), and fluorescence micrographs at 50 ms (g) and 3.3 ms exposure time (h) of the R-PE conjugated CS-particles. Inset in (h) is a bright-field image corresponding to the fluorescence micrograph (h). (i) Estimated and measured fluorescence intensity of the R-PE conjugated TMV- and CS-particles at 50 ms exposure time respectively.

First, bright-field images for both TMV- and CS-particles (Figure 4.3b,f) fabricated via replica molding (RM) show uniform and well-defined particle platforms. This result confirms that RM enables facile and reproducible fabrication of particle platforms with complex shapes.[12] Notably, the TMV-particles show red color upon R-PE conjugation, similar to concentrated R-PE solution under a bright-field condition. This red color in direct contrast to the CS-particles indicates that R-PEs are conjugated with significantly high concentration on TMV-particles. Next, fluorescence images of the R-PE conjugated TMV- and CS-particles (Figure 4.3c,g) show bright fluorescence with significant difference in fluorescence intensity (FI) between the two; the TMV-particles (Figure 4.3c) show much brighter fluorescence (FI=183±0) than that on the CS-particles (Figure 4.3g, FI=20±2) under identical imaging condition (i.e. exposure time=50 ms). This result indicates that substantially more R-PEs are conjugated with the TMV-particles than the CS-particles. Meanwhile, all negative control particles show minimal fluorescence (Figure A3.1, Appendices; TMV-particles without TCO or Tz, and CS-particles without TCO), indicating that the observed fluorescence of both the TMV- and CS-particles in Figure 4.3c,g results from specific R-PE conjugation through the Tz–TCO cycloaddition reaction.

Next, another batch of R-PE conjugated TMV-particles was examined with shorter exposure time (3.3 ms) as shown in Figure 4.3d in order to avoid artifacts of saturated fluorescence as in Figure 4.3c. The result shows bright and uniform fluorescence on the particles (FI=70±2), indicating uniform conjugation of R-PEs. In contrast, the R-PE conjugated CS-particles at the same 3.3 ms exposure time (Figure 4.3h) don't show any fluorescence, further confirming the substantial difference in protein conjugation capacity between the TMV- and CS-particles.

To quantitatively compare R-PE conjugation capacity between the TMV- and the CS-particles, I next estimated the fluorescence intensity of the R-PE conjugated TMV-particles at varying exposure times as shown in Figure A3.2. Importantly, the result in Figure A3.2 indicates that measured fluorescence intensity of the R-PE conjugated TMV-particles is linearly proportional to the exposure time in the range up to FI=70 (i.e. up to 3.3 ms). This linearity between the fluorescence intensity and the exposure time is also confirmed over longer exposure time ranges (e.g. R-PE conjugated CS-particles in the range up to FI=70, 25-125 ms; data not shown), indicating that the fluorescence intensity can be quantified with varying exposure time in my imaging setup. The two fluorescence intensity values (i.e. the estimated fluorescence intensity for the R-PE conjugated TMV-particles with the linear correlation shown in Figure A3.2, and the measured fluorescence intensity of the R-PE conjugated CS-particles at 50 ms exposure time) are listed in Figure 4.3i. The result shows that the TMV-particles (FI=1060±24) are 53-fold brighter (i.e. 53-times higher protein conjugation capacity) than the CS-particles (FI=20±2).

Recent studies reported 2-14 times enhanced protein conjugation capacity with polymer brush platforms over reference substrates (i.e. planar substrates or nanoparticle surfaces without polymer brushes for protein conjugation).[154-157] Compared with these reports, the 53-fold enhancement in conjugation capacity with the TMV templates shown in Figure 4.3 is much higher than that with the polymer brushes. In the meantime, the CS-particles already have enhanced R-PE conjugation capacity due to their 3D structure compared to planar substrates (~44 times, Figure A3.3).[27] Combined, the TMV-particles would possess approximately 2400-fold higher R-PE conjugation capacity over planar substrates. I attribute this striking improvement to precisely spaced reactive sites on the rigid nanotubular TMV surfaces along with the 3D structure of chitosan (CS)–PEG hydrogel particle platforms (i.e. CS-particles). Specifically, the TMVs provide ~2000 reactive thiols with 1.8 nm horizontal and 2.3 nm vertical spacing[158] from surface-displayed cysteines on each coat protein via genetic modification.[86] While most of these sites are available for conjugation of small molecules,[159] not all them are expected to be available for protein conjugation due to steric hindrance resulting from the large size of proteins being conjugated. In other words, roughly 287 R-PEs would be conjugated per each TMV at maximum, leading to ~41-fold enhanced R-PE conjugation capacity if R-PE–TMV conjugates were to be assembled as a closely packed monolayer on a planar substrate based on my estimation (Figure A3.4). Compared with this estimation, ~2400-fold enhanced R-PE conjugation capacity of the TMV-particles over the R-PEs conjugated on planar substrates suggests multilayer assembly of the TMVs with the CS-particles. In addition, the confocal micrograph of the R-PE conjugated TMV-particles (Figure A3.5) suggests that 3D polymer networks of the particle platforms enable the TMVs to penetrate a few micrometers (~2 µm) below the particle surfaces, supporting the multilayer assembly of TMV templates.

Combined, the results in Figure 4.3 demonstrate that the assembled TMVs on the CS-particles provide more protein conjugation sites, leading to 53-fold enhancement over the CS-particles and over 2000-fold compared to planar substrates due to abundant surface-displayed thiol groups along with multilayer assembly on 3D scaffolds.

4.3.2 Effect of Inherent Reaction Rates of Conjugation Chemistries on Protein Conjugation

In order to examine the effect of inherent reaction rates of conjugation chemistries on the protein conjugation kinetics through 3D structures, I next carried out a direct comparison of the R-PE conjugation with TMV- and CS-particles as shown in Figure 4.4. Specifically, the second-order rate constant of rapid Tz–TCO cycloaddition reaction for the Tz I employed in this study ($820\ M^{-1}s^{-1}$)[21] is about 410 times higher than that of SPAAC reaction (k=$2.1\ M^{-1}s^{-1}$)[22]. For this, I prepared TCO- and azadibenzocyclooctyne (ADIBO)-activated TMV- and CS-particles, and reacted with Tz- and azide-activated R-PEs respectively for varying times at room temperature (Figure 4.4a). The measured average fluorescence intensity of the R-PE conjugated particles was normalized with maximum fluorescence intensity of each particle platform (i.e. fluorescence intensity of the TMV- and the CS-particles at 9 and 18 h, respectively).

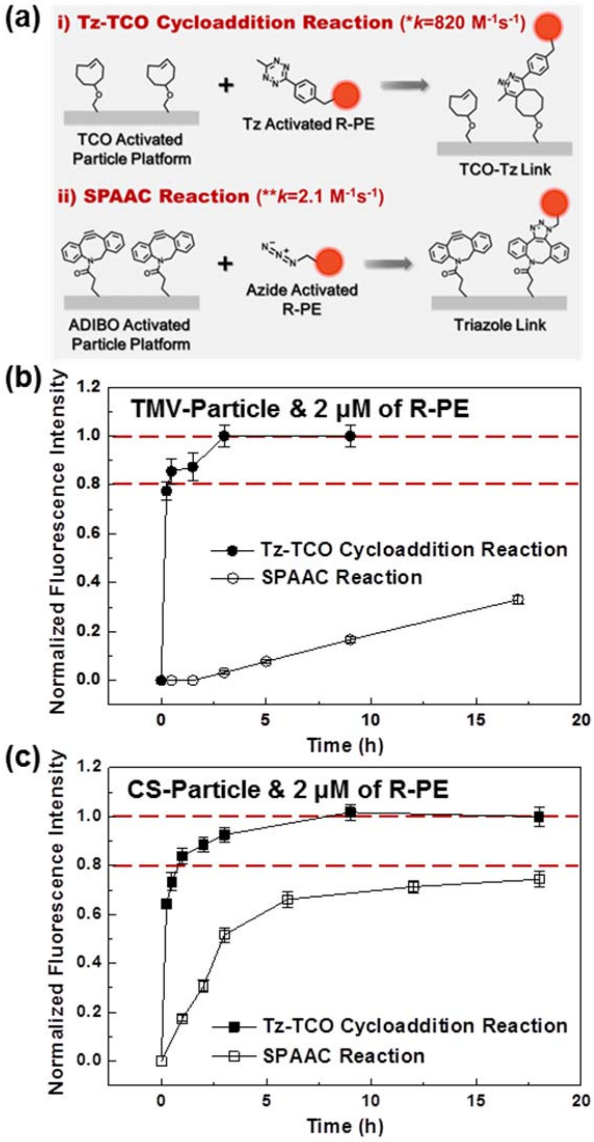

Figure 4.4. Protein conjugation kinetics with the TMV- and CS-particles via Tz–TCO cycloaddition and SPAAC reaction. (a) Schematic diagrams of R-PE conjugation via Tz–TCO cycloaddition and SPAAC reaction. (b,c) Normalized fluorescence intensity plots of (b) the TMV- and (c) CS-particles upon conjugation with 2 µM R-PEs for varying times.

First, the normalized fluorescence plot of the TMV-particles via Tz–TCO cycloaddition reaction (solid circles, Figure 4.4b) shows rapid increase in the fluorescence during the first 15 min (up to roughly 78% of maximum fluorescence), and reaches maximum fluorescence within 3 h. In contrast, the fluorescence of the TMV-particles via SPAAC reaction (open circles, Figure 4.4b) increases with time much slowly; the fluorescence reaches only 33% of maximum fluorescence upon 17 h reaction. This result indicates that the R-PE conjugation with the TMV-particles via Tz–TCO cycloaddition reaction is substantially faster than that via SPAAC reaction, due to the significantly higher reaction rate.[21, 22] Thus, this result suggests that the inherent reaction rates have a critical impact on the protein conjugation kinetics with the TMV-particles.

I next examined the R-PE conjugation kinetics via Tz–TCO cycloaddition and SPAAC reaction with the CS-particles, where diffusion of the R-PEs through the particles was shown to play a critical role in R-PE conjugation kinetics via SPAAC reaction in Chapter 3 (Figure 4.4c). First, the normalized fluorescence of the CS-particles via Tz–TCO cycloaddition reaction (solid squares) rapidly increases during the first 15 min, similar to the TMV-particles. Meanwhile, the rate of increase in fluorescence on the CS-particles gradually decreases after 15 min, taking longer time to reach maximum fluorescence than the TMV-particles. In other words, about 2.5-fold longer time is required to reach the maximum fluorescence (top dashed-line) from 80% of the maximum fluorescence (bottom dashed-line) on the CS-particles, which correlates well with the results in Chapter 3. I attribute this slowdown to the diffusion limitation of the R-PEs through polymer networks of the CS-particles.

Importantly, minimal effect of this diffusion-limited slowdown on the R-PE conjugation with the TMV-particles suggests that the TMV-particles offer less hindered environment for protein conjugation, possibly due to a rigid brush-like structure of the assembled TMVs near the particle surfaces resulting from orientationally controlled assembly at the 5'-end of the TMVs via nucleic acid hybridization (Figure A3.6).[27, 87, 89] In the meantime, several studies on polymer brush platforms reported that density, thickness, solvation and mobility of polymer chains play a crucial role in order to obtain optimal protein conjugation or binding (i.e. less hindered environment) by extending the polymer chains from substrates.[154, 155, 160] Furthermore, a recent study reported significantly lower conjugation rate of small molecules with the polymer brush platforms compared to that in solution.[137] The authors attributed this low conjugation rate to dense polymer chains on substrates resulting in diffusion limitation of target molecules through the polymer chains. While I utilized near-maximum TMV assembly density in this study (i.e. from 3 mg/mL TMV, Figure 4.6a), the densely assembled TMVs appear to have minimal effect of diffusion limitation on the protein conjugation kinetics unlike the polymer brush platforms.

Next, the normalized fluorescence plot of the CS-particles via SPAAC reaction (open squares, Figure 4.4c) is similar to that via Tz–TCO cycloaddition reaction, showing gradually decreasing R-PE conjugation rate due to the diffusion limitation of the R-PEs.[27] In the meantime, the normalized fluorescence plots of the CS-particles (Figure 4.4c) show relatively small difference in the rate of increase in fluorescence between Tz–TCO cycloaddition and SPAAC reaction.

In other words, the difference in the R-PE conjugation rate with the CS-particles between Tz–TCO cycloaddition and SPAAC reactions is not as significant as that in the inherent reaction rate. Compared with the result of the TMV-particles showing substantial difference between Tz–TCO cycloaddition and SPAAC reactions (Figure 4.4b), this result suggests that the effect of the diffusion limitation on the R-PE conjugation kinetics appears to be more pronounced for the CS-particles than the TMV-particles, and further supports the less hindered environment of the TMV-particles for protein conjugation.

In order to directly compare absolute rates of R-PE conjugation between TMV- and CS-particles via SPAAC reaction, I also analyzed the fluorescence intensity shown in Figure 4.4b,c without normalization to each platform (Figure A3.7). The results show that the R-PE conjugation with the TMV-particles is faster than that with the CS-particles, further suggesting favorable environment of the TMV-particles (i.e. less hindered environment) for protein conjugation.

Rapid Cu(I)-catalyzed alkyne–azide cycloaddition (CuAAC) reaction has been widely enlisted for biomolecular conjugation due to its high yield, selectivity and bioorthogonality.[67, 68] In order to circumvent the potential damage to biomacromolecular structures by Cu(I) catalysts in CuAAC reaction,[68] SPAAC reaction has emerged and is being increasingly utilized. While the mild reaction condition and stability of the functional groups of SPAAC reaction are beneficial (also see Chapter 3), its slow reaction rate may pose limitations in the conjugation of labile proteins particularly with hydrogel platforms. Alternatively, Tz–TCO cycloaddition reaction provides a range of high reaction rates and stability depending on various Tz derivatives, while still offering several advantages of the bioorthogonal cycloaddition reactions including high conjugation yield and selectivity in complex biological systems.[21, 161] These traits make Tz–TCO cycloaddition reaction a promising candidate for biomolecular conjugation, and should permit utilization of labile proteins in a wide range of devices and applications beyond cell imaging.[22, 161]

In addition to the effects of significant difference in inherent reaction rates between the Tz–TCO and SPAAC reactions, the results on the R-PE conjugation kinetics in Figure 4.4 show different “effective pore or mesh sizes”[42, 162] of the two platforms examined. That is, the TMV-particles appear to have large pore size resulting in less hindered environment for the diffusion of the large R-PEs (MW 240 kDa, R_h=5.54 nm),[133] and the inherent reaction rate has dominant effect on the R-PE conjugation kinetics. In contrast, the CS-particles appear to have small pore (or mesh) size leading to diffusion limitation of the large R-PEs through the polymer networks, and the diffusion limitation of the R-PEs plays a critical role in the R-PE conjugation kinetics. This difference in effective pore size (i.e. less hindered environment for TMV-particles) is also supported by results in Figure A3.7, where the R-PE conjugation rates are directly compared between TMV- and CS-particles without normalization. Diffusion coefficients of large biomacromolecules such as IgG (MW 150 kDa, R_h=5.45 nm)[163] in polymer networks (calculated mesh size $\xi \approx 2$-3 nm for hydrogels made of 10-30% PEG diacrylate with MW 8 kDa)[24] are known to be as low as 10^{-8}-10^{-9} cm^{2}s^{-1}, substantially smaller than in bulk solution (4.2×10^{-7} cm^2s^{-1}).[25] While conjugation of smaller probe biomolecules (e.g. single-stranded DNAs,[12] short peptide ligands[164] or antibody fragments (Fab),[102] MW<50 kDa) with the CS-particles would be faster than that of R-PEs owing to larger diffusion coefficients of the small molecules,[25] the conjugation would still suffer from diffusion-limited slowdown due to steric hindrance by the as-conjugated biomolecules as well as small pore size of the particles.[27, 136] Meanwhile, less diffusion-limited platforms (e.g. TMV-particles in this study) along with emerging rapid conjugation chemistries (i.e. Tz–TCO cycloaddition reaction)[21] would provide further advantages for more rapid biomolecular conjugation, and allow for preserving activities of labile biomolecules such as antibodies.

In the meantime, target biomolecules also have a range of sizes (e.g. from small miRNAs[165] or cytokines[53] to large mRNAs[166] or aggregated endotoxins[167]); detection of such biomolecular targets with 3D structured platforms (e.g. polymer networks of hydrogels[29, 53] or brush-like scaffolds[154, 155]) would thus be subject to similar diffusion limitation in addition to varying inherent biospecific binding kinetics (e.g. antibody–antigen binding[168] or nucleic acid hybridization[169]) during biomolecular assay procedures. Therefore, one should consider multiple parameters in the design, fabrication and assay procedures with 3D structure-based biosensing platforms. Such parameters include density of conjugation handles (i.e. the TMVs or chitosans in my system) and probe biomolecules, pore sizes of 3D platforms, sizes of both probe and target biomolecules, inherent reaction kinetics of conjugation chemistries, binding kinetics of biomolecules, and diffusion of biomolecules within 3D platforms. In other words, comprehensive understanding of the interplay among the multiple parameters is essential to achieve desired assay times and sensitivities.[162] Meanwhile, conjugation kinetics of probe biomacromolecules such as in Figure 4.4 can also provide estimation of the platforms' structures, thus of the binding/assay kinetics.

Overall, the results in Figure 4.4 show that the protein conjugation kinetics with the TMV-particles depends on the inherent reaction rates of the conjugation chemistries unlike the CS-particles, suggesting that the TMV-particles provide less diffusion-limited environment for the protein conjugation.

4.3.3 Enhanced Target Protein Capture Capacity with TMV-assembled Particles.

I next demonstrate enhanced capacity of target protein capture with antibody-conjugated TMV-particles compared to antibody-conjugated CS-particles, as shown in Figure 4.5. For this, I utilized an anti-R-PE antibody (R-Ab) and R-PE pair as a model system. Specifically, R-Ab conjugated TMV-particles were prepared via Tz–TCO cycloaddition reaction between TCO-activated TMV-particles and Tz-activated R-Abs under identical conjugation conditions as in Figure 4.3, and incubated with R-PEs for a 3 h period (Figure 4.5a). R-Ab conjugated CS-particles were also prepared, and incubated in R-PE solution under identical conjugation and incubation conditions as for the TMV-particles. Both the R-PE captured TMV- and CS-particles were then analyzed with fluorescence microscopy at an identical imaging condition (i.e. at 0.2 s exposure time). In the meantime, the fluorescence intensity of the R-PE captured TMV-particles at 0.2 s exposure time reached pixel saturation showing underestimated fluorescence intensity values (Figure A3.8). In order to avoid this artifact and to quantitatively compare the protein capture capacity, I utilized estimated fluorescence intensity for the R-PE captured TMV-particles as shown in Figure A3.8e.

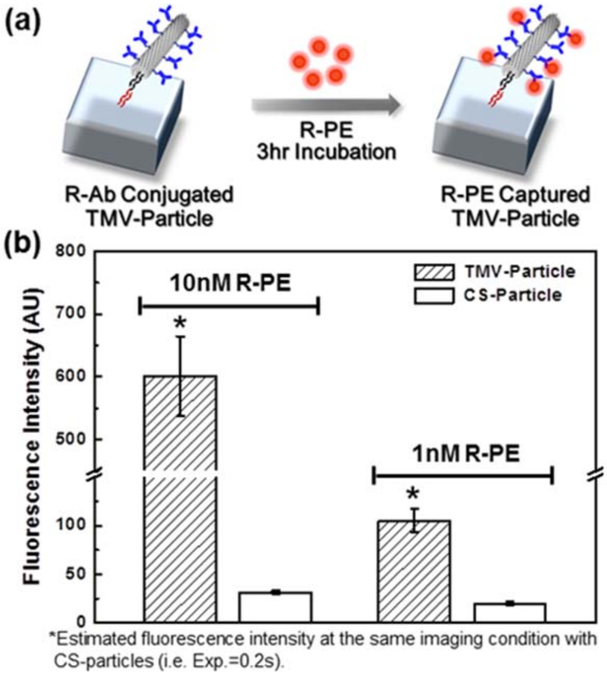

Figure 4.5. Enhanced target protein capture capacity with the assembled TMV templates. (a) A schematic diagram of R-PE capture with the R-Ab conjugated TMV-particles. (b) Estimated fluorescence intensity of the R-Ab conjugated TMV-particles (striped columns) and measured fluorescence intensity of the R-Ab conjugated CS-particles (open columns) at 0.2 s exposure time upon 3 h incubation with 1 or 10 nM R-PEs.

First, both the R-Ab conjugated TMV- and CS-particles show fluorescence upon incubation with 1 and 10 nM R-PEs (Figure 4.5b), while negative control particles show negligible fluorescence (i.e. TMV and CS-particles without R-Ab, data not shown). This result indicates that the fluorescence on the R-Ab conjugated TMV- and CS-particles results from captured R-PEs by antibody–antigen interaction with minimal nonspecific binding of R-PEs. Next, fluorescence intensity of the R-PE captured TMV-particles (striped columns in Figure 4.5b) is substantially higher than that of the R-PE captured CS-particles (open columns in Figure 4.5b) at both 1 and 10 nM R-PE conditions; the fluorescence of the R-PE captured TMV-particles at 1 nM R-PE is 5-fold brighter than that of the R-PE captured CS-particles, and 19-fold brighter at 10 nM R-PE. These results demonstrate significantly enhanced R-PE capture capacity of the R-Ab conjugated TMV-particles over CS-particles due to enhanced antibody conjugation capacity with the TMV templates.

Meanwhile, the enhancement of the R-PE capture capacity was not linearly proportional to the R-PE concentrations examined (i.e. 5-fold at 1 nM and 19-fold at 10 nM over CS-particles), and was lower than enhanced R-PE conjugation capacity (i.e. roughly 53-fold over the CS-particles at 2 μM R-PE concentration, Figure 4.3). Zubtsov *et al.* reported that longer time is required to reach equilibrium of antigen binding on hydrogel platforms with high antibody conjugation capacity under low antigen concentration conditions (i.e. 5-20 nM).[28] The results on antibody–antigen binding kinetics with the R-Ab conjugated TMV-particles also show that 3 h incubation is not sufficient for reaching the equilibrium state (i.e. R-PE binding is increasing with time during 3 h period, Figure A3.9). Taken together, the R-Ab conjugated TMV-particles appear to need longer incubation time to reach equilibrium of R-PE binding possibly due to lower driving force (i.e. concentration gradient) for diffusion of R-PEs and slower binding rate under low R-PE concentration conditions used in this study.[27] Notably, my simple estimation for the number of R-Abs conjugated with roughly 200 TMV-particles (2×10^{-12} moles, Figure A3.10) shows equivalent or one order of magnitude smaller number of R-PEs (10^{-12} and 10^{-13} moles for 10 and 1 nM respectively) in 100 μL assay volume. Under these conditions, the R-PEs in the 100 μL assay solution will be depleted during the R-PE capture, leading to further slowed diffusion and binding rate of the R-PEs. Thus, the observed lower-than-expected R-PE capture capacity can be attributed to target R-PE depletion along with slow binding kinetics. Yet, the substantially enhanced target protein capture capacity of the antibody-conjugated TMV-particles (striped columns in Figure 4.5b) should permit enhanced signals and allow for reliable target protein sensing, compared to the antibody-conjugated CS-particles (open columns in Figure 4.5b).

In the meantime, the R-Ab conjugated CS-particles prepared via Tz–TCO cycloaddition reaction upon 3 h incubation with 1 nM R-PE show brighter fluorescence (FI=20 at 0.2 s exposure time, rightmost open column in Figure 4.5) than those prepared via SPAAC reaction (FI=3 at 0.3 s exposure time in Chapter 3) under identical R-PE capture conditions. I attribute this improved R-PE capture capacity via Tz–TCO cycloaddition reaction to higher reaction rate, leading to higher antibody conjugation capacity in a short period. While relatively rapid and bioorthogonal CuAAC reaction (k=~10^2 $M^{-1}s^{-1}$)[67] has been widely utilized for biomolecular conjugation, Cu(I) catalysts in CuAAC reaction may be toxic to biomolecules.[68] SPAAC reaction has thus been developed to avoid the use of the Cu(I) catalysts.[67, 68] However, the SPAAC reaction is substantially slow,[67] and may not be suitable for rapid conjugation of labile biomolecules. Rapid Tz–TCO cycloaddition reaction under mild reaction conditions should thus be beneficial for conjugation of labile biomolecules in preserving their activity.

Overall, the results in Figure 4.5 illustrate that the antibody-conjugated TMV-particles provide enhanced capacity of target protein capture compared to the antibody-conjugated CS-particles due to enhanced antibody conjugation capacity with the TMV templates.

4.3.4 Effect of TMV Assembly Density on Protein Conjugation and Capture Capacity

Finally, I examined the effect of controllable TMV assembly density of TMV-particles on R-PE conjugation and capture capacity, as shown in Figure 4.6. The TMV assembly density on the particle platforms is readily controlled by simply varying TMV concentrations as in Chapter 2. For this, TMVs were first labeled with fluorescent dyes or activated with TCO molecules separately, and programmed with linker DNAs. Varying concentrations of these programmed TMVs (0-3 mg/mL) were then incubated with capture DNA-conjugated CS-particles. Next, the TCO-activated TMV-particles were conjugated with R-PEs or R-Abs under identical conjugation conditions, and the R-Ab conjugated TMV-particles were incubated with 10 nM R-PEs to examine the R-PE capture. The fluorescently labeled, R-PE conjugated, and R-PE captured TMV-particles were analyzed with fluorescence microscopy, and normalized average fluorescence intensities of the TMV-particles were plotted and fitted with a nonlinear regression method.

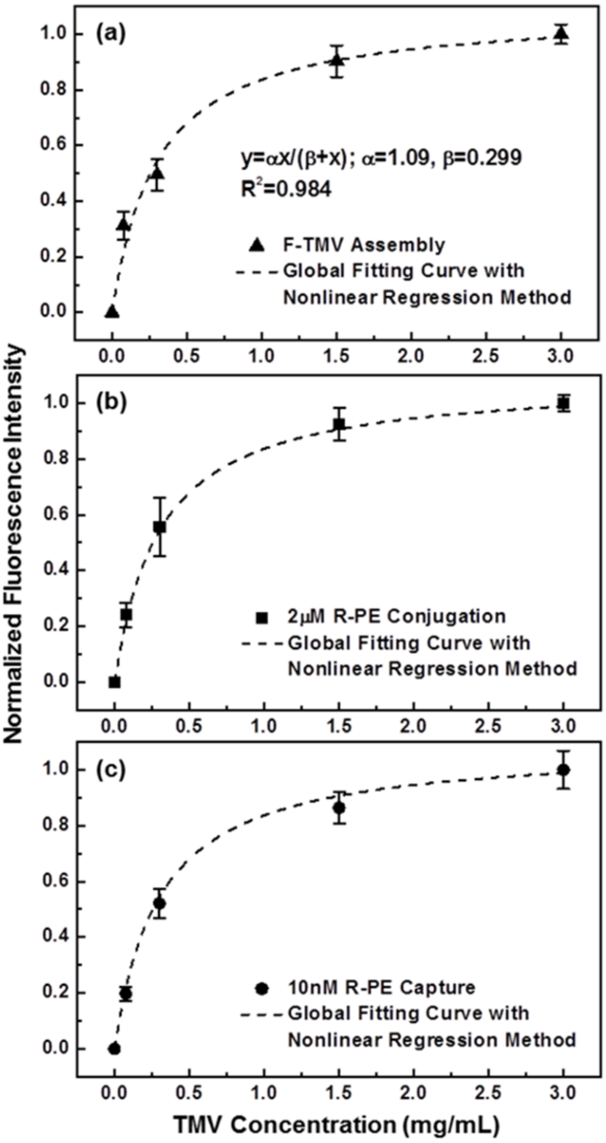

Figure 4.6. Controllable TMV assembly density with varying TMV concentrations and its effect on protein conjugation and target protein capture capacity. (a-c) Normalized average fluorescence intensity plots of (a) fluorescently labeled, (b) R-PE conjugated,

and (c) R-PE captured TMV-particles with varying TMV concentrations. Dashed-lines represent identical global fitting curve with identical fitting parameters (α and β) and R^2 for all fluorescence plots in (a), (b) and (c).

First, each normalized fluorescence plot for three different types of TMV-particles (Figure 4.6) shows uniform fluorescence with small error bars as well as consistent profiles of increasing fluorescence with increasing TMV concentration (dashed-lines in Figure 4.6; identical global fitting curve for all the three different types of TMV-particles with R^2=0.984). This result indicates that each step for fabrication of protein- or antibody-conjugated TMV-particles is highly consistent, robust and controllable. Specifically, normalized fluorescence plot of the fluorescently labeled TMV-particles (F–TMV-particles) shows that fluorescence on the particles increases with increasing TMV concentration, approaching saturation (Figure 4.6a). This result indicates that TMV assembly density is readily controllable with varying TMV concentrations, consistent with the results in Chapter 2. In addition, the maximum normalized fluorescence value close to the unity (α=1.09) suggests that the TMV assembly reached near-saturation level at 3 mg/mL of TMV concentration condition. Next, the normalized fluorescence plot of the R-PE conjugated TMV-particles (Figure 4.6b) shows similar fluorescence increase profile to that of F–TMV-particles, demonstrating that R-PE conjugation capacity also increases along with increasing TMV assembly density. This result indicates that protein conjugation capacity is readily controllable via the TMV assembly density without any negative impact from higher TMV assembly density (i.e. without decreased protein conjugation capacity near maximum TMV assembly density). In contrast, several studies on polymer brush platforms reported that high polymer chain density on substrates results in decreased protein conjugation capacity due to diffusion limitation of target molecules to be conjugated through the dense polymer chains.[154, 155] Thus, the similar profiles in the TMV assembly density and the protein conjugation capacity suggest that the assembled TMVs are sufficiently separated with each other, leading to less diffusion-limited environment for protein conjugation as in Figure 4.4, and provide further indication of multilayer assembly as described above in Figure 4.3. Combined with the enhanced protein conjugation capacity of the TMV-particles shown in Figure 4.3, readily controllable protein conjugation capacity along with less hindered environment for protein conjugation should allow for facile and controllable fabrication of biosensing platforms with desired capacity.

The normalized fluorescence plot of R-PE captured TMV particles (Figure 4.6c) also shows similar fluorescence increase profile to that of the R-PE conjugated TMV-particles with no apparent decrease in R-PE capture capacity with increasing TMV assembly density. Recent studies reported that multiple conjugation sites on antibodies (i.e. lysine residues) cause crosslinking between polymer chains on dense polymer brush platforms, and lead to diffusion-limited environment hindering target protein capture; in other words, target protein capture capacity decreases when the antibody conjugation capacity increases with increasing polymer chain density.[154, 155] In contrast, the results in Figure 4.6 show that the target protein capture capacity proportionally increases with increasing antibody conjugation capacity without any negative effect of high TMV assembly density on the target protein capture. This result further suggests that the assembled TMVs are sufficiently separated from each other, allowing for minimal crosslinking between the TMVs during conjugation reaction.

In short summary, the results in Figure 4.6 indicate that the density of the assembled TMVs on the particles is readily controllable with varying TMV concentrations, allowing for consistently controlling the antibody conjugation and target protein capture capacity.

4.4 Conclusions

In this chapter, I demonstrated substantially improved protein conjugation and capture capacity for TMV templates integrated with hydrogel microparticles under mild aqueous conditions. First, protein conjugation results with R-PEs showed significantly enhanced protein conjugation capacity of TMV-particles; 53-fold and 2400-fold enhancement over CS-particles and planar substrates respectively. Further examination of protein conjugation kinetics via Tz–TCO cycloaddition and SPAAC reaction showed that inherent reaction rates of the conjugation chemistries have a critical impact on protein conjugation kinetics with the TMV-particles, suggesting less diffusion-limited structure of the TMV-particles toward protein conjugation. Next, the R-Ab–R-PE binding study also showed considerably enhanced R-PE capture capacity of R-Ab conjugated TMV-particles compared to R-Ab conjugated CS-particles; 5- and 19-fold enhancement at 1 and 10 nM target R-PE concentration respectively. Lastly, I demonstrated readily controllable TMV assembly density by varying TMV concentrations, and minimal negative effect from densely assembled TMVs on protein conjugation and target protein capture capacity. Combined, the results shown in this chapter demonstrate a facile post-fabrication protein conjugation approach exploiting viral templates assembled with hydrogel microparticles for enhanced and controlled protein conjugation and sensing platforms.

Compared with polymer brush platforms, the results presented in this chapter show advantages of my post-fabrication conjugation approach using rigid nanotubular TMV templates; (1) substantially enhanced protein conjugation capacity (i.e. 2400 times enhancement with the TMVs vs. 2-14 times enhancement with polymer chains[154-157]), and (2) less diffusion-limited environment for protein conjugation and target protein capture. Meanwhile, protein sensing for low concentration targets is generally carried out in combination with signal amplification methods such as sandwich assays utilizing secondary antibodies bearing signal-enhancing entities.[170] I expect that combination of TMV templates and hydrogel microparticle-based high capacity platforms with such signal amplification methods should provide further improvement for a wide range of protein sensing applications.

5 MICROMOLDING-BASED FABRICATION OF CHITOSAN-INCORPORATED HYDROGEL MICROSPHERES WITH CONTROLLED MACROPOROUS STRUCTURES FOR IMPROVED PROTEIN CONJUGATION

5.1 Introduction

Desired performances of hydrogel microparticles toward specific needs in biomedical application areas can be achieved by controlling their structures such as morphologies and mesh sizes.[8, 10] Emerging microfluidics-based techniques have been utilized to fabricate highly uniform hydrogel microspheres with complex 3D structures (i.e. multicompartmental)[13, 54] and shape-encoded nonspherical particles.[1] However, these techniques have limitations in precise control of fabrication parameters, needs for complex devices and lack of scalability.[97] Sequential layer deposition approaches[171-173] allow for fabrication of multilayered hydrogel microspheres, yet these approaches have limitations of arduous multistep procedures. Recently, a micromolding-based technique exploiting surface tension-induced droplet formation has emerged, which allows highly uniform microspheres to be readily fabricated with fine tuning of their sizes by simple change of mold volume without any delicate controls or complex devices.[11] Furthermore, the convenience of batch processing of this technique allows a wide range of fabrication parameters to be readily tuned, and ease of mass production via parallelization.

Meanwhile, network structures of the hydrogel particles can pose mass transfer limitation (i.e. hindered diffusion) particularly for large biomolecules.[24, 25] While the network structures (i.e. mesh sizes) can be tuned by their crosslinking density,[10] it remains challenging to lower the crosslinking density while retaining mechanical integrity and well-defined shapes.[88, 115] Various porogens are also utilized to increase the mesh sizes,[9] yet such approaches can lead to nonuniform network structures and/or compromised mechanical integrity. Therefore, there exist critical needs for facile fabrication strategies for uniform and macroporous hydrogel microparticles with controlled structures.

In this chapter, I demonstrate a facile fabrication scheme for chemically functional and macroporous hydrogel microspheres with controlled structures. For this, I enlisted a chitosan–poly(ethylene glycol) (PEG) hybrid system and a simple micromolding-based method utilizing surface tension-induced droplet formation and polymerization-induced phase separation (PIPS), as shown in the schematic diagram of Figure 5.1a. Briefly, aqueous prepolymer solution made by simple mixing of chitosan and PEG diacrylate (PEGDA) is filled into cross-shaped PDMS micromolds. Upon addition of hydrophobic wetting fluid (*N*-hexadecane with photoinitiator, PI) on the filled molds, prepolymer droplets are readily formed (bright-field micrograph, inset of Figure 5.1a) by surface tension at the interface between the prepolymer solution and the wetting fluid.[11] The droplets are then exposed to UV light to crosslink the prepolymer solution via photoinduced radical polymerization,[43] leading to PIPS-based core-shell structure formation within monodisperse chitosan–PEG microspheres. I also examine utility of these microspheres as biomolecular conjugation platforms by exploiting high yield bioorthogonal conjugation reactions (“click chemistries”; strain-promoted alkyne–azide cycloaddition (SPAAC) and tetrazine–*trans*-cyclooctene (Tz–TCO) cycloaddition reactions).[21-23]

The results show that my simple micromolding-based fabrication approach allows consistent fabrication of monodisperse microspheres with mechanical integrity for a wide range of PEGDA contents. Morphology of the microspheres (i.e. uniform or core-shell) is controlled via PIPS occurring at specific PEGDA concentration ranges, without any delicate controls, complex devices or multistep procedures. Fluorescent labeling of the microspheres via an amine-reactive chemistry confirms that chitosan moieties are incorporated with PEG networks in a stable manner with retained chemical reactivity. Next, biomolecular conjugation results with fluorescein-labeled single-stranded (ss) DNAs (F–ssDNA) and red fluorescent protein R-phycoerythrin (R-PE) confirm well-defined and macroporous network structures of the microspheres, permitting programmable conjugation of the biomolecules and improved protein conjugation capacity as well as kinetics.

Combined, these results demonstrate a facile micromolding-based fabrication approach for highly uniform microspheres with controlled macroporous structures and their utility in biomolecular conjugation. I thus expect that my facile fabrication-conjugation approach can be readily enlisted to manufacture potent microscale materials with programmable functionalities for various biomedical applications[1-7] in a consistent and scalable manner.

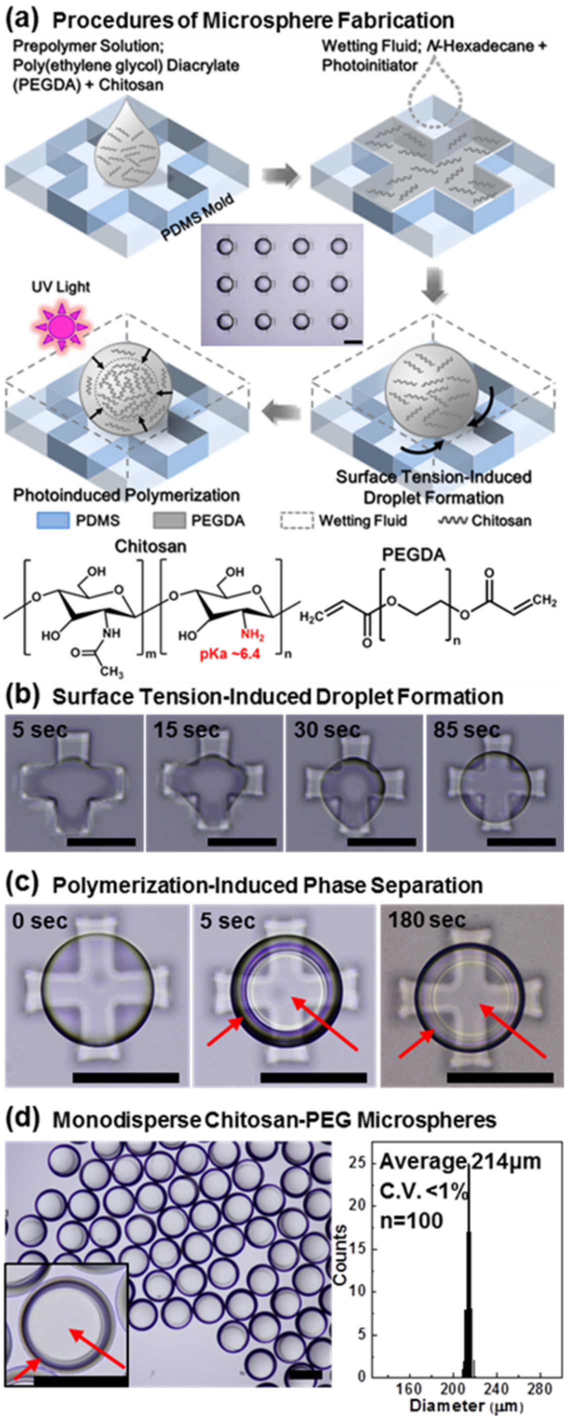

Figure 5.1. Micromolding-based fabrication of chitosan–PEG microspheres. (a) Schematic diagram of the microsphere fabrication procedure, and chemical structures of chitosan and PEGDA. (b) Bright-field micrographs showing the progress of surface tension-induced droplet formation. (c) Micrographs showing core-shell structure

formation. (d) As-prepared chitosan–PEG microspheres in aqueous solution and their size distribution. Long and short arrows indicate core and shell regions respectively. All scale bars represent 200 μm.

5.2 Materials and Methods

5.2.1 Materials

Chitosan oligosaccharide lactate (average M_n 5 kDa, > 90% deacetylation), poly(ethylene glycol) diacrylate (PEGDA, average M_n 700 Da), 2-hydroxy-2-methylpropiophenone (photoinitiator, PI), red fluorescent dye (sulforhodamine B), phosphate buffered saline (PBS) tablets (10 mM phosphate, 2.7 mM potassium chloride, 137 mM sodium chloride, pH 7.4), and saline sodium citrate (SSC) buffer (20× concentrate, molecular biology grade) were purchased from Sigma-Aldrich (St. Louis, MO). 5-(and 6-)carboxyfluorescein succinimidyl ester (NHS–fluorescein) was purchased from Pierce Biotechnology (Rockford, IL). *Trans*-cyclooctene (TCO)–PEG_4–*N*-hydroxysuccinimide (NHS) ester, Tetrazine (Tz)–PEG_5–NHS ester, azadibenzocyclooctyne (ADIBO)–*sulfo*–NHS ester, and azide–Fluor 488 (F-488) were purchased from Click Chemistry Tools (Scottsdale, AZ). Acrylate–PEG–succinimidyl valerate (SVA) with average MW 1 kDa was purchased from Laysan Bio, Inc. (Arab, AL). NHS–PEG_{12}–azide, borate buffer (20× concentrate, 50 mM borate, pH 8.5), Tween 20 (TW20), poly(dimethylsiloxane) (PDMS) elastomer kits (Sylgard 184), and centrifugal filter units (Amicon Ultra 0.5) were purchased from Thermo Fisher Scientific (Waltham, MA). Dimethyl sulfoxide (DMSO, extra dry) and *N*-hexadecane (99%)

were purchased from ACROS Organics$^{\mathrm{TM}}$. 2-propanol (> 99.7%) was purchased from J.T.Baker®. All the chemicals were analytical grade, and used without further purification.

5.2.2 DNA Oligonucleotides and Proteins

All single-stranded (ss) DNAs used in this study were purchased from Integrated DNA Technologies (Coralville, IA); azide-terminated and fluorescein-labeled ssDNA (F–ssDNA, 5’-/azide/ATGATGATGATGATGATG/FAM/-3’), capture ssDNA (5’-/azide/ATGATGATGATGATGATG/-3’), and linker ssDNA (5’-/GTTTGTTGTTGTTGGTAATTGTTG*TTTTTT*CATCATCATCATCATCAT /-3’; TMV 5’ end complementary sequence *Spacer* capture ssDNA complementary sequence). Red fluorescent protein R-Phycoerythrin (R-PE in sodium phosphate buffer, pH 7.0 with ammonium sulfate) was purchased from AnaSpec (Fremont, CA).

5.2.3 Fabrication of Chitosan–PEG Microspheres

As shown in Figure 5.1a, chitosan–PEG microspheres were fabricated via a simple micromolding-based approach as in a recent study[11] with minor modifications. I first prepared a PDMS mold consisting of cross-shaped microwells with 5.14 nL of volume for large microspheres and with 1.20 nL for small ones via thermal curing (overnight at 65 °C) of Sylgard 184 elastomer (9:1 weight ratio of elastomer to curing agent) on a photolithographically patterned silicon master mold. Next, I prepared aqueous prepolymer solutions by mixing chitosan (0.5% w/v), PEGDA (5-70% v/v) and deionized (DI) water, and hydrophobic wetting fluid by mixing *N*-hexadecane and PI (1% v/v). The prepolymer solution was placed on the PDMS mold, and filled into the microwells by rubbing the mold with a disposable pipet tip. The excess prepolymer solution was taken away by pipetting, and the filled mold was covered with the wetting fluid. These procedures were conducted in a humidity chamber with ~94% humidity to avoid rapid evaporation of water in the prepolymer solution.[12] The mold covered with the wetting fluid was left on an aluminum mirror (Thorlabs, Newton, NJ) for at least 2 min in order to form prepolymer droplets via surface tension at the interface between the prepolymer solution and the wetting fluid. Then, the droplets were exposed to 365 nm UV light with an 8 W hand-held UV lamp (Spectronics Corp., Westbury, NY) for 3 min in order to polymerize the droplets (i.e. crosslinking). The crosslinked droplets (i.e. microspheres) were collected by pipetting then washed 5 times with 2-propanol, 3 times with DI water containing 0.5% (v/v) TW20, and 2 times with 5× SSC buffer solution containing 0.05% (v/v) TW20 (SSC–TW20 buffer solution).

5.2.4 Swelling Ratio and Water Content of Chitosan–PEG Microspheres

The chitosan–PEG microspheres with varying PEG contents were immersed in SSC–TW20 buffer solution for at least 1 day to reach equilibrium swelling (i.e. wet state). The microspheres were then dried in a vacuum chamber at room temperature for at least 1 day upon washing 5 times with deionized water. The microspheres were imaged under a bright-field mode, and sphere diameters were analyzed with an image analysis software ImageJ[105] in order to compute the volumetric swelling ratio (γ):

$$\gamma = V_{wet}/V_{dry}$$

and water content:

$$\text{Water Content} = \frac{V_{wet} - V_{dry}}{V_{wet}} \times 100\%$$

where V_{wet} and V_{dry} represent sphere volumes under wet and dry states, respectively.

5.2.5 Preparation of Acrylate-modified Chitosans

To prepare acrylate-modified chitosans, some of chitosan's primary amines were replaced with acrylates by reacting 250 μL of 20 mg/mL chitosan in DI water with 20 μL of 100 mg/mL acrylate–PEG–SVA in DMSO (i.e. 2-fold molar excess over chitosan; ~7.4% molar ratio to the chitosan's amines) for 2 h at room temperature. To separate the acrylate-modified chitosans from unreacted acrylate residues, the chitosans were precipitated by adding SSC–TW20 buffer solution (pH 7.0), then washed 3 times via centrifugation at 9000g for 30s with 500 μL of SSC–TW20 buffer solution. Note, soluble-insoluble transition of typical chitosans in aqueous solution arises between pH 6 and pH 6.5 due to their unique pKa value (~6.4).[20] Lastly, the pelleted acrylate-modified chitosans were dissolved in 250 μL of 0.1N HCl solution to prepare acrylate-modified chitosan solution (~2% w/v).

5.2.6 Fluorescent Labeling of Chitosan–PEG Microspheres

For fluorescent labeling of the chitosan–PEG microspheres prepared with acrylate-modified or unmodified chitosans, a constant number (~40) of the microspheres were incubated in SSC–TW20 buffer solution with 5 μM of NHS–fluorescein for 1 h at room temperature. The unreacted fluorescein residues were removed by washing the microspheres 3 times with aqueous solution containing 2-propanol (50% v/v).

5.2.7 TCO- or Azide-activation of Proteins

In order to activate R-PEs with TCO or azide molecules, I first exchanged buffer solution of the R-PE solution for borate buffered saline buffer solution (50 mM borate, 300 mM NaCl, pH 8.5) via centrifugal filtration at 4 ºC. The R-PEs (2 mg/mL) were then reacted with 20-fold molar excess of TCO–PEG_4–NHS ester or NHS–PEG_{12}–azide for 30 min at room temperature. Unreacted chemicals were separated from the R-PE solution via centrifugal filtration (Amicon Ultra 0.5) with PBS buffer solution (pH 7.4). Concentrations of the final R-PE solutions were measured by UV-vis spectrophotometry (Evolution^{TM} 300 UV-vis Spectrophotometer, Thermo scientific, Waltham, MA) with the characteristic absorbance peaks and molar extinction coefficients of the R-PE (1.96×10^{6} $M^{-1}cm^{-1}$ at 565 nm[131]).

5.2.8 Biomolecular Conjugation with Chitosan–PEG Microspheres

For biomolecular conjugation with the chitosan–PEG microspheres, I utilized Tz–TCO cycloaddition and strain-promoted alkyne–azide cycloaddition

(SPAAC) reaction. First, the as-prepared chitosan–PEG microspheres were activated with Tz and ADIBO molecules upon incubation with 500 μM of Tz–PEG_5–NHS ester and ADIBO–*sulfo*–NHS ester in SSC–TW20 buffer solution for 1 h at room temperature, respectively. The unreacted chemicals were removed by washing the microspheres 4 times with SSC–TW20 buffer solution. To examine 3D network structures of the microspheres, the ADIBO-activated microspheres (~40 large-sized spheres) were reacted with 2 μM of azide-terminated F–ssDNAs and azide-activated R-PEs for 24 h in SSC–TW20 buffer solution at room temperature, separately. To examine the effect of sphere size on protein conjugation capacity, a constant number (~120) of small ADIBO-activated microspheres were also reacted with 2 μM of azide-activated R-PEs for 24 h in SSC–TW20 buffer solution at room temperature. To examine protein conjugation kinetics with the microspheres, a constant number of (~120) small Tz- and ADIBO-activated microspheres were reacted with 2 μM of TCO- and azide-activated R-PEs for varying reaction times (0-48 h) in SSC–TW20 buffer solution at room temperature, respectively. The unconjugated biomolecules were separated from the microsphere solution by washing the microspheres 5 times with SSC–TW20 buffer solution.

5.2.9 Imaging Analysis

The fluorescently labeled, and F–ssDNA and R-PE conjugated microspheres were imaged with an epifluorescence microscope (Olympus BX51 equipped with a DP70 microscope digital camera, Center Valley, PA) and a confocal microscope (Leica DMIRE2 equipped with a TCS SP2 scanner, Wetzlar, Germany) in SSC–TW20 buffer solution (pH 7.0). Epifluorescence micrographs of the microspheres were obtained with a 10× objective under standard green (U-N31001) and red (U-N31002) filter sets (Chroma Technology Corp., Rockingham, VT) for the green fluorescent molecules (fluorescein and F–ssDNA) and the R-PEs, respectively. Confocal micrographs of the microspheres were obtained with a 20× objective at 488 nm and 543 nm excitation for the green fluorescent molecules and the R-PEs, respectively. Diameters and fluorescence intensities of the microspheres were analyzed with the image analysis software ImageJ.[105]

5.3 Results and Discussion

5.3.1 Simple Micromolding-based Fabrication of Highly Uniform and Core-shell Structured Chitosan–PEG Microspheres

As shown in Figure 5.1, I first demonstrate that highly uniform and core-shell structured chitosan–PEG microspheres are readily fabricated via surface tension-induced droplet formation followed by photoinduced radical polymerization from aqueous mixture of short-chain chitosan (M_n 5 kDa, 0.5% w/v) and PEGDA (M_n 700 Da, 30% v/v) as the prepolymer solution.

The bright-field micrographs in Figure 5.1b show progress of the droplet formation; the prepolymer solution starts to move from the edge of the molds toward the center upon addition of the wetting fluid (*N*-hexadecane with photoinitiator, PI), and the spherical droplets are formed within 2 min. This result is consistent with a recent study by Choi *et al.*,[11] where the authors attributed the droplet formation of 100% PEGDA prepolymer to pressure difference between the edge and the center of the molds, caused by surface tension at the interface between the prepolymer and the wetting fluid. Meanwhile, more hydrophilic, aqueous prepolymer solution (70% water) in my system should lead to higher pressure difference allowing for more reliable droplet formation.

Next, Figure 5.1c shows that UV exposure leads to two different phases in a droplet within 5 sec (i.e. core-shell structure marked with long and short arrows), and that the droplet is polymerized while retaining the core-shell structure (i.e. minimal difference in morphology of the crosslinked droplets upon 3 min UV exposure with an 8 W hand-held UV lamp). I attribute this core-shell structure in the crosslinked droplets (i.e. microspheres) to the polymerization-induced phase separation (PIPS).[174, 175] To confirm my hypothesis, I examined the microsphere fabrication procedure with non-polymerizable and polymerizable systems, as shown in Figure A4.1 (Appendices). First, non-polymerizable systems (e.g. no PI or acrylates) show no two distinct phases upon UV exposure. In contrast, the polymerizable systems both with and without chitosan clearly show core-shell structure. These results indicate that crosslinking of the PEGDAs during the polymerization results in phase separation within the droplets, leading to formation of the core-shell structure. To further examine morphology of the microspheres, I utilized binding affinity of red fluorescent dyes (sulforhodamine B) to PEG networks[176] as shown in Figure A4.2. Upon incubation of the microspheres in sulforhodamine B solution, the confocal micrograph of Figure A4.2 at the center plane of a microsphere shows that the core area is significantly brighter than the shell, suggesting that the microsphere consists of PEG-rich core and PEG-poor shell domains. In short summary, the results in Figure 5.1c, A4.1 and A4.2 demonstrate PIPS-based formation of core-shell (PEG rich & poor respectively) structure in the droplets composed of 30% PEGDA.

Next, Figure 5.1d shows highly uniform microspheres with 214 μm diameter (coefficient of variation, C.V. < 1%) in aqueous solution (i.e. swollen state), consistent with the results by Choi *et al.*[11] Meanwhile, Figure 5.1d inset shows that the core-shell structure of the microsphere (marked with long and short arrows respectively) still remains upon swelling in aqueous solution.

The results in Figure 5.1 demonstrate that my approach for the fabrication of highly uniform and core-shell structured microspheres is simple and robust. Specifically, my fabrication scheme utilizing one step droplet formation and spontaneous PIPS-based core-shell structure formation is simple and robust, compared to other microfluidics-based methods requiring complex devices and delicate fluid controls.[13, 54] Furthermore, no surfactants are utilized in my fabrication system unlike conventional emulsion polymerization[177] and microfluidics-based methods,[13, 54] owing to localization of the droplets on the molds (Figure 5.1a inset and Figure 5.1b). Overall, the results in Figure 5.1 show that monodisperse and core-shell structured chitosan–PEG microspheres are readily fabricated in my simple micromolding scheme.

5.3.2 Effect of PEGDA Concentration on Swelling Ratio and Water Content of Chitosan–PEG Microspheres

As shown in Figure 5.2, I next examined the effect of PEGDA concentration on swelling ratio and water content of the chitosan–PEG hydrogel microspheres. For this, I fabricated microspheres with prepolymer solutions containing varying concentrations of PEGDA (10-50% v/v) and fixed amount of chitosan (0.5% w/v), and sphere diameters were measured under wet and dry states. Sphere volumes were then calculated with the diameters, and utilized to compute swelling ratio and water content.

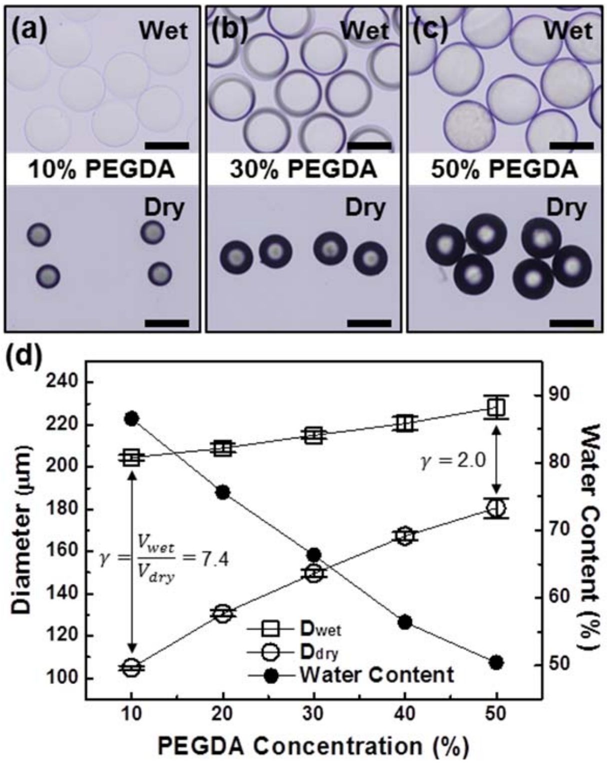

Figure 5.2. Effect of PEGDA concentration on swelling ratio and water content of chitosan–PEG microspheres. (a-c) Representative bright-field micrographs of the microspheres fabricated with varying PEGDA concentrations under wet (top row) and

dry states (bottom row). Scale bars represent 200 μm. (d) Sphere diameter and water content plots with varying PEGDA concentrations; sphere diameters under wet (open squares) and dry states (open circles), and water contents of microspheres (solid circles). Error bars represent standard deviation from twelve microspheres per each condition.

First, the bright-field micrographs in Figure 5.2a-c show representative microspheres prepared with varying PEGDA concentrations under wet (swollen, top) and dry (shrunken, bottom) states. The results show that both wet and dry microspheres are highly uniform for all PEGDA concentrations examined, indicating consistent microsphere fabrication with my simple micromolding-based technique. The difference in sphere size between wet and dry states (i.e. swelling ratio) decreases with increasing PEGDA concentration due to varying crosslinking densities and polymer contents resulting from the PEGDA concentrations.[178, 179] Note that the wet 10% PEGDA spheres are more transparent than the 30% and 50% PEGDA ones, due to lower PEG content.

Next, I further analyzed average diameters of the microspheres as shown in Figure 5.2d. First, the wet microspheres (curve with open squares) show minimal difference in diameter for the entire range of PEGDA concentrations (less than 15%) as shown in Figure 5.2a-c. In contrast, the dry microspheres (curve with open circles) show significant decrease in diameter with decreasing PEGDA concentration. Thus, the difference in diameter between wet and dry states increases with decreasing PEGDA concentration, leading to substantial difference in volumetric swelling ratio (γ) between spheres fabricated with 10% (γ=7.4) and 50% (γ=2.0) PEGDA. Accordingly, the water content of wet microspheres (curve with solid circles) increases with decreasing PEGDA concentration, up to 87% in the case of 10% PEGDA microspheres. In short summary, the results in Figure 5.2d demonstrate that lower PEGDA content in the prepolymer solution leads to higher swelling ratio and water content due to lower PEG content and crosslinking density in the polymerized microspheres. Meanwhile, consistently small error bars (obtained from 12 randomly selected microspheres in each case) for all the conditions examined in Figure 5.2d further indicate highly uniform microspheres and robustness of my fabrication scheme.

Importantly, results in Figure 5.2 indicate that my micromolding method allows substantially low polymer content microstructures to be readily fabricated with retained mechanical integrity and uniform shape (down to 5% PEGDA microspheres, data not shown), which is challenging to achieve with other methods (e.g. PDMS-based replica molding technique[88] and stop-flow lithography[115]). I attribute this to less oxygen-inhibited environment for the radical polymerization (i.e. less severe radical scavenging by oxygen) in my system than the PDMS-based ones; dissolved oxygen in the wetting fluid (one order of magnitude smaller amount than the dissolved PIs, based on solubility of oxygen in *N*-hexadecane[180]) will be rapidly consumed by radicals generated from UV-exposed PIs with the high consumption rate constant (~10^8 $M^{-1}s^{-1}$),[48] allowing for prevention of oxygen supply to the droplets during the polymerization. In contrast, the dissolved oxygen in the PDMS-based systems continuously diffuse in through the permeable PDMS layers, and inhibit the polymerization by scavenging the radicals.[48] Additionally, the abundant PIs in the wetting fluid along with long UV exposure time (i.e. several minutes versus milliseconds in the stop-flow lithography[115]) should allow the microspheres to be fully polymerized, leading to well-defined microstructures with low polymer content. Meanwhile, convenience of my simple batch processing-based micromolding setup allows for a wide range of polymerization reaction parameters (e.g. UV exposure time and PI concentration) to be readily employed and tuned. Combined, the results in Figure 5.2 demonstrate that my simple micromolding-based technique allows consistent fabrication of microspheres with a wide range of PEG contents, with low PEG content conditions showing high swelling ratio and water content.

5.3.3 Chemical Reactivity and Distribution of Chitosan in Microspheres with Varying PEG Contents

I next examined the effect of PEGDA concentration on chitosan distribution in the chitosan–PEG microspheres via fluorescent labeling, as shown in Figure 5.3. For this, microspheres were fabricated with prepolymer solutions composed of varying concentrations of PEGDA (10-70%) and fixed amount of chitosan (0.5%), then incubated in aqueous solutions of carboxyfluorescein succinimidyl ester (NHS–fluorescein). As shown in the schematic diagram of Figure 5.3a, the unshared electron pairs of primary amine groups on the chitosan backbone attack the electron-deficient carbon in the ester linkage of NHS–fluorescein (i.e. bimolecular nucleophilic substitution (S_N2) reaction[109]) to rapidly form stable amide linkages (i.e. amidation),[17] resulting in fluorescent labeling of the microspheres. The fluorescently labeled microspheres were imaged with epifluorescence and confocal microscopy.

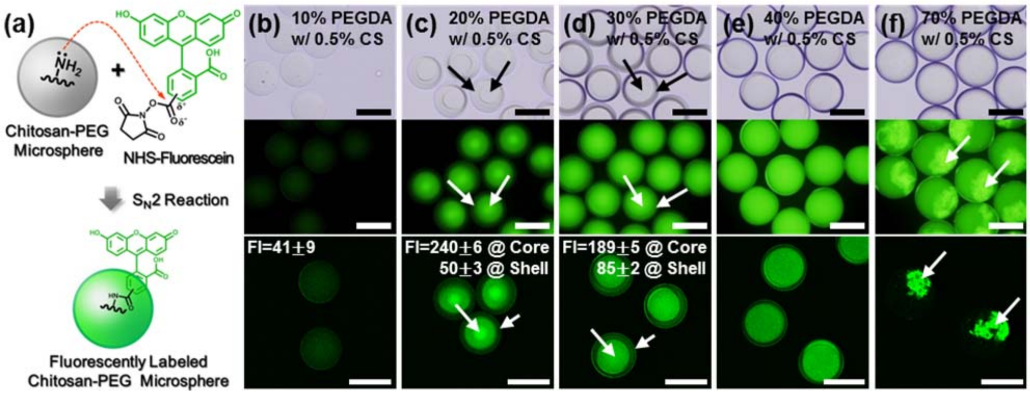

Figure 5.3. Fluorescent labeling and distribution of chitosan within chitosan–PEG microspheres. (a) Schematic diagram for fluorescent labeling of the microspheres with NHS–fluorescein. (b-f) Bright-field (top row), fluorescence (middle row), and confocal (bottom row) micrographs of the fluorescently labeled microspheres fabricated with varying PEGDA concentrations (10-70% v/v) and fixed chitosan content (0.5% w/v). The confocal micrographs were imaged at the center plane of the microspheres. Average fluorescence intensities (FI) in panel b-d (bottom row) were obtained from 5 randomly selected circular areas with 22 μm diameter for core and shell regions. All scale bars represent 200 μm.

First, the bright-field micrographs (Figure 5.3b-f, top row) show uniform chitosan–PEG microspheres for all the PEGDA content conditions examined, consistent with the results in Figure 5.2. Meanwhile, the apparent two different phases in the microspheres (i.e. core-shell structure shown in Figure 5.1) are observed only at 20% and 30% PEGDA conditions (arrows in the top row of Figure 5.3c,d). This result indicates that the PIPS-based core-shell structure formation occurs at specific PEGDA concentration ranges (further discussed below). Next, the fluorescence micrographs corresponding to the bright-field ones (Figure 5.3b-f, middle row) show distinguishable fluorescence on all the chitosan–PEG microspheres, in contrast to no or minimal fluorescence for negative controls (i.e. microspheres without chitosan, Figure A4.3). This result indicates that most of the fluorescence on the chitosan–PEG microspheres results from the specific S_N2 reaction between the NHS–fluorescein and chitosan's amines with minimal nonspecific binding, confirming stable incorporation of chitosan with retained chemical reactivity in the microspheres for all PEGDA concentrations employed as in Chapter 2. I hypothesize that this stable incorporation of chitosan is mainly due to copolymerization between chitosan and PEGDA at chitosan's amines during radical polymerization (i.e. amine–radical reaction),[110, 111] whose efficiency is lower than that of the reaction between acrylates themselves.[116] In addition, average total fluorescence of the microspheres appears to increase with increasing PEGDA concentration, indicating increase in chitosan incorporation (further quantified in Figure 5.4). Meanwhile, microspheres fabricated with long-chain chitosan (MW ~200 kDa) showed equivalent fluorescence intensity to the ones with the unmodified short-chain chitosan (M_n 5 kDa) used throughout this study (data not shown). Long-chain chitosan should be more likely to be incorporated via the amine–radical reaction due to higher number of amines per chitosan chain. This equivalent fluorescence thus suggests that major portion of the short-chain chitosan used throughout this study is incorporated with retained chemical reactivity. Note, the chitosan's primary amines with uniquely low pKa value (~6.4) can be readily enlisted for covalent conjugation via standard amine-reactive reactions (e.g. using isothiocyanates, NHS esters and sulfonyl chlorides etc.[17]) under neutral pH conditions.[20] In contrast, the pKa values of common amine-containing components are above 9 (10.5 for lysine,[181] ≥ 9 for *N*-terminal groups of amino acids[181] and 9-10 for aminosilane[182]), making them heavily protonated and much less efficient for amine-reactive reactions under neutral pH.[17]

Next, the middle row of Figure 5.3b-f show different types of fluorescence (i.e. chitosan) distribution on the microspheres with varying PEGDA concentrations. First, the microspheres fabricated with 10% PEGDA show significantly low yet uniform fluorescence. Next, the microspheres fabricated with 20% and 30% PEGDA show bright and dim fluorescence at the core and the shell regions respectively, indicating core-shell like chitosan distribution (marked with arrows). Meanwhile, the core region appears to expand with increasing PEGDA concentration in the fluorescence micrographs as well as in the bright-field ones, reaching uniform morphology throughout the microspheres for the 40% PEGDA condition (also in 50% PEGDA, data not shown). Lastly, uniform fluorescence with some regions showing substantially bright yet irregular fluorescence (arrows in the middle row of Figure 5.3f) is observed on the microspheres fabricated with 70% PEGDA (also with 60% PEGDA, data not shown), suggesting aggregated forms of chitosan.

To further investigate the chitosan distribution within the microspheres in detail, I next examined the center plane of the fluorescently labeled microspheres via confocal microscopy in the bottom row of Figure 5.3b-f. First, the confocal micrographs show distinguishable fluorescence on the center plane of all the microspheres examined, confirming that small NHS–fluorescein molecules (MW 473.4 Da) readily penetrate into the polymer networks of the microspheres and react with the chitosan's primary amines (i.e. minimal mass transfer limitation of small molecules into the microspheres). Next, the 10% PEGDA microspheres (Figure 5.3b, bottom) show weak yet uniform fluorescence (FI=41±9) throughout the center plane of the microspheres, indicating low degree of chitosan incorporation. This result also suggests minimal phase separation between chitosan and PEGDA during the mixing step of the prepolymer solution and the radical polymerization. I attribute this low chitosan incorporation at 10% PEGDA condition to low polymerization efficiency.[115] Also, large mesh size of the polymerized PEG networks at 10% PEGDA condition should allow unconjugated and relatively small chitosan molecules (M_n 5 kDa) to diffuse out of the PEG networks upon extensive washing (supported by the mesh size examination in Figure 5.5). Next, the 20% and 30% PEGDA microspheres (Figure 5.3c,d, bottom row) clearly show lower fluorescence at the shell of the microspheres (marked with short arrows, FI=50±3 and 85±2 for 20% and 30% PEGDA respectively) than around the core (marked with long arrows, FI=240±6 and 189±5 for 20% and 30% PEGDA respectively), indicating relatively lower chitosan incorporation at the shell regions, comparable with that in the 10% PEGDA microspheres (FI=41±9). Note that these chitosan-rich core and the chitosan-poor shell regions in Figure 5.3d correspond well with the PEG-rich core and the PEG-poor shell domains from noncovalent adsorption of sulforhodamine B in Figure A4.2. This result suggests that the core-shell like chitosan distribution should result from the PIPS-based core-shell structure formation. In other words, the polymerization initiated at the surfaces of droplets should lead to crosslinked and immobile PEG networks, occupying volume of the polymerizing droplets from the surfaces. At the same time, the short polymeric mobile components (i.e. uncrosslinked PEGDAs and unconjugated chitosans) should be simply pushed into the core area possibly due to volume exclusion and poor compatibility with the crosslinked PEG networks (i.e. PIPS). This localization of chitosan moieties migrating with PEGDAs should lead to incorporation with the locally concentrated PEGDAs around the core of the droplets via chemical binding and/or physical entrapment.[88] Meanwhile, the bottom row of Figure 5.3c-e clearly show that the chitosan-rich core region expands with increasing PEGDA concentration, then finally occupies most of the center plane of the microsphere (Figure 5.3e, bottom; 40% PEGDA), resulting in relatively uniform chitosan distribution as shown in the middle row of Figure 5.3e. Combined with the results shown in the top row of Figure 5.3c-e (i.e. broadening core region with increasing PEGDA concentration), I attribute the relatively uniform chitosan distribution and morphology of the microspheres at higher PEGDA concentration to rapid polymerization rate[43] leading to immediate formation of the PEG networks with small mesh sizes (less than 1 nm[122]), allowing for minimal migration of chitosans and PEGDAs toward the core region of the droplets. Lastly, 70% PEGDA microspheres clearly show irregular fluorescence regions (arrows in Figure 5.3f, bottom), suggesting aggregated chitosan. I attribute this aggregation to incompatibility in

70% PEGDA solution (i.e. aqueous two-phase system[183] of 70% PEGDA and 0.5% chitosan), shown in a phase diagram of the prepolymer solution based on the turbidity measured via UV-vis spectrophotometry (Figure A4.4).

In short summary, the results in Figure 5.3 show retained chemical reactivity of chitosan's primary amines in chitosan–PEG microspheres via fluorescent labeling, which then allows examination of chitosan distribution in the microspheres confirming core-shell structure formation, as well as chitosan incorporation in a semi-quantitative manner.

5.3.4 Distribution and Incorporation of Acrylate-modified Chitosan in Microspheres

As shown in Figure 5.4, I further examined the distribution of chitosan and the PIPS using acrylate-modified chitosan. I hypothesized that the acrylate–chitosan should be more efficiently copolymerized with PEGDA than the unmodified chitosan, enhancing the incorporation ratio and suppressing the mobility of chitosan moieties during the PIPS. To prepare the acrylate–chitosan, small portions of the chitosan's amines were replaced with acrylates via S_N2 reaction using 2-fold molar excess of amine-reactive acrylate–PEG–succinimidyl valerate over chitosan (i.e. ~7.4% molar ratio to chitosan's amines). The microspheres fabricated with the acrylate–chitosan and PEGDA were analyzed under identical fabrication and imaging conditions as in Figure 5.3.

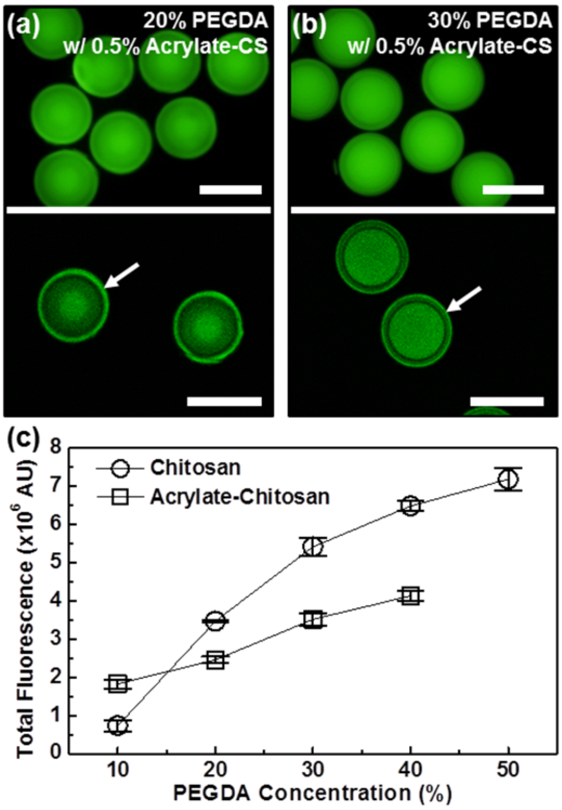

(d) Apparent Chitosan Incorporation Ratio (η)

PEGDA [%]	10	20	30	40	50
Chitosan	0.10	0.48	0.75	0.90	1.0
Acrylate-Chitosan	0.26	0.34	0.49	0.58	-

Figure 5.4. Chitosan distribution and incorporation in microspheres fabricated with acrylate–chitosan. (a,b) Fluorescence (top row) and confocal micrographs (bottom row) of (a) 20% and (b) 30% PEGDA microspheres fabricated with acrylate–chitosan. All scale bars represent 200 µm. (c) Average total fluorescence intensity plots of the microspheres with unmodified chitosan (open circles) and acrylate–chitosan (open squares). Error bars represent standard deviation from five microspheres per each condition. (d) Table for summary of calculated apparent chitosan incorporation ratios based on total fluorescence intensities in (c).

First, the fluorescence micrographs of the microspheres fabricated with the acrylate–chitosan (Figure 5.4a,b, top row) show relatively uniform fluorescence throughout the microspheres in contrast to those with the unmodified chitosan showing core-shell like fluorescence distribution (Figure 5.3c,d), suggesting suppressed migration of chitosan moieties during polymerization. Next, the confocal micrographs at the particle centers (Figure 5.4a,b, bottom row) show a bright fluorescent layer near the sphere surfaces (marked with arrows) as well as core-shell like fluorescence distribution, unlike the results in Figure 5.3c,d (i.e. dim fluorescence near the surface). This result suggests that the acrylate–chitosan is copolymerized with the PEGDA near the droplet surfaces at the onset of the polymerization, then subsequently localized and copolymerized with the PEGDA that is pushed into the core area via the PIPS.

As shown in Figure 5.4c, I next carried out total fluorescence intensity analysis to compare the incorporation of the unmodified chitosan with that of the acrylate–chitosan for a range of PEGDA concentrations. For this, the average total fluorescence intensity was analyzed via an image analysis software (ImageJ)[105] with four randomly selected microspheres for each case. First, the total fluorescence intensity plot for both types of microspheres (with unmodified chitosan, open circles & with acrylate–chitosan, open squares) show increase in fluorescence intensity (i.e. chitosan incorporation) with increasing PEGDA concentration, presumably due to combination of higher polymerization efficiency (i.e. more number of acrylates) and small mesh size at higher PEGDA content conditions.[88, 115] Particularly, the acrylate–chitosan particles at 10% PEGDA show higher fluorescence intensity than those with the unmodified chitosan, indicating improved chitosan incorporation due to more efficient copolymerization of the acrylate–chitosan with the PEGDA. In the meantime, the acrylate–chitosan particles for 20-40% PEGDA range show lower fluorescence intensity values than those with unmodified chitosan, presumably due to the reduced number of chitosan's reactive amines from the acrylate modification step (i.e. NHS ester reaction with amines), rather than to lower chitosan incorporation. Meanwhile, irregular fluorescence on the microspheres with the acrylate–chitosan (i.e. aggregated chitosan, similar to Figure 5.3f; 60-70% PEGDA) is observed at 50% PEGDA composition resulting from incompatibility of chitosan and PEGDA in the prepolymer solution (possibly due to higher polymer contents from the PEG–acrylate chains on the chitosan backbone, data not shown).

Finally, I evaluated apparent chitosan incorporation ratio (η, table of Figure 5.4d) by normalization with the fluorescence intensity of 50% PEGDA microspheres, where the chitosan incorporation should be maximal among the conditions examined due to sufficient number of PEGDA's acrylates for the amine–radical reaction.[88] First, 10% PEGDA condition shows 2.6-fold enhancement in the apparent chitosan incorporation for the acrylate–chitosan. Next, assuming that all the acrylate–chitosan moieties in the droplets at 40% PEGDA are incorporated due to covalent linkage and/or physical entrapment,[115] the apparent chitosan incorporation ratio with the acrylate–chitosan (η=0.58) suggests that ~42% of the amines on the chitosan backbone are unavailable for further amine-reactive reactions presumably due to reduced accessibility of the amines by grafted chains as well as their consumption in the acrylate modification step (max. ~7.4% based on molar ratio employed here).

Accounting for this reduced amine titer, the maximum incorporation ratio of the acrylate–chitosan at 10% PEGDA should be ~45% (corrected $\eta \approx 0.45$); i.e. 4.5-fold enhanced incorporation with the acrylate–chitosan over that with the unmodified chitosan.

Overall, the results with acrylate-modified chitosan in Figure 5.4 show that copolymerization of chitosan moieties with PEGDAs suppresses migration of the chitosan moieties, further supporting PIPS-based formation of core-shell structures.

5.3.5 Conjugation of Biomolecules with Chitosan–PEG Microspheres via SPAAC Reaction

In order to further evaluate the 3D network structures and utility of the chitosan–PEG microspheres in the conjugation of biomacromolecules, I next enlisted strain-promoted alkyne–azide cycloaddition (SPAAC) reaction, as shown in Figure 5.5. Specifically, the microspheres with varying PEG contents (10-30% PEGDA) were activated with azadibenzocyclooctyne (ADIBO) molecules using ADIBO–*sulfo*–NHS ester that reacts with chitosan's amines via S_N2 reaction[34] as shown in the schematic diagram of Figure 5.5a. These ADIBO-activated microspheres were then reacted with 2 μM of azide-modified biomolecules with different sizes for 24 h; azide-terminated and fluorescein-labeled single-stranded (ss) DNA (F–ssDNA, MW 6 kDa) and azide-activated red fluorescent protein (R-phycoerythrin; R-PE, MW 240 kDa). The microspheres missing ADIBO-activation were utilized as negative controls.

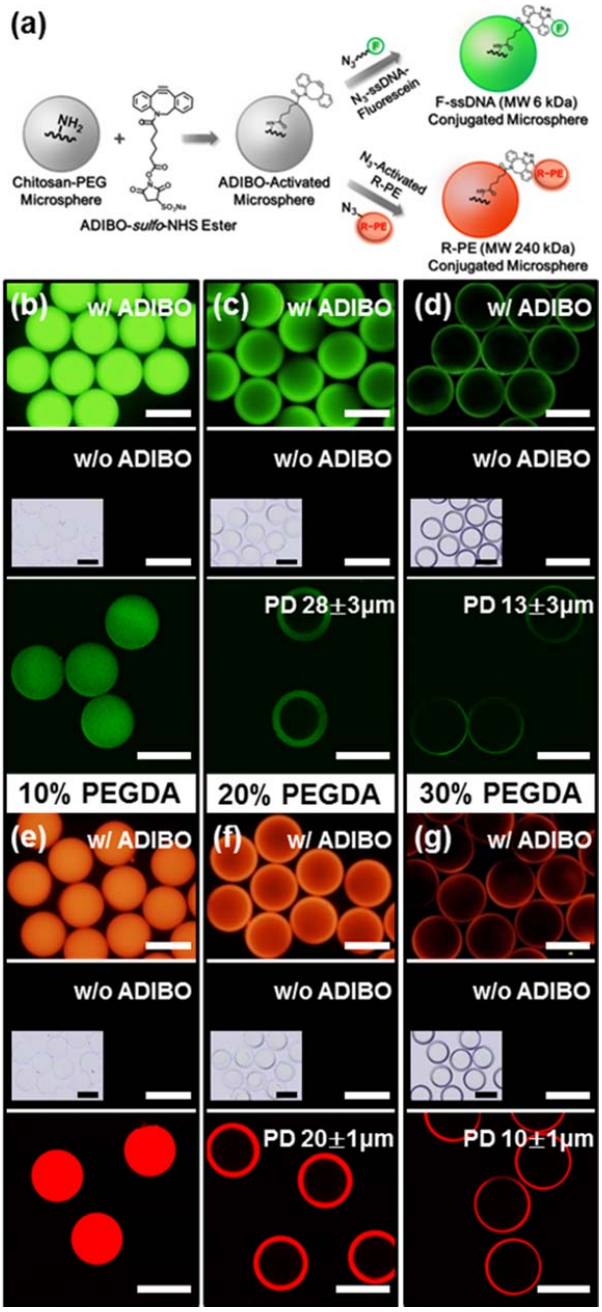

Figure 5.5. Conjugation of biomolecules with chitosan–PEG microspheres via SPAAC reaction. (a) Schematic diagram for ADIBO-activation of the microspheres followed by conjugation with two different azide-modified biomolecules separately. (b-g) Fluorescence (top rows) and confocal (bottom rows) micrographs of biomolecule-conjugated microspheres with different PEG contents (10-30% PEGDA); (b-d) F–ssDNAs and (e-g) R-PEs. Fluorescence micrographs of negative controls (middle rows)

missing ADIBO-activation upon incubation with each azide-modified biomolecule. Insets in the middle rows are bright-field micrographs corresponding to the fluorescence micrographs of the negative controls. All scale bars represent 200 μm.

First, the fluorescence micrographs (Figure 5.5b-g, top rows) show distinguishable fluorescence on the ADIBO-activated microspheres for all PEGDA concentrations examined, in contrast to negligible fluorescence on the negative controls (Figure 5.5b-g, middle rows). This result confirms selective conjugation of both biomolecules (F–ssDNA and R-PE) with the microspheres via SPAAC reaction without any nonspecific binding, consistent with the results in Chapter 3. Next, the microspheres fabricated with 10% PEGDA show uniform fluorescence throughout the microspheres for both F–ssDNA and R-PE, while the microspheres fabricated with 20-30% PEGDA show higher fluorescence near the surfaces. The total fluorescence on these microspheres decreases with increasing PEGDA concentration. Meanwhile, the ADIBO-activated 40% PEGDA microspheres show negligible fluorescence upon the conjugation reaction (Figure A4.5). These results indicate that the number of conjugated biomolecules decreases with increasing PEGDA concentration despite increase in the number of conjugation sites (i.e. ADIBO molecules) resulting from higher chitosan incorporation at high PEGDA content conditions (Figure 5.3). I attribute this reduced number of conjugated biomolecules to small mesh size of the high PEG content microspheres (< 1 nm),[122] leading to mass transfer limitation of the relatively large biomolecules into the microspheres.[24, 27]

Next, confocal microscopy results (bottom rows, Figure 5.5b-g) revealed clear structural features of the microspheres fabricated with varying PEGDA concentrations. First, the 10% PEGDA microspheres (Figure 5.5b,e, bottom rows) show uniform fluorescence throughout the microspheres, consistent with the fluorescence results in the top rows of Figure 5.5b,e. This result indicates that the mesh size of the 10% PEGDA microspheres is large enough for both biomolecules (i.e. F–ssDNA, radius of gyration $R_g \approx 2$ nm[121] & R-PE, hydrodynamic radius $R_h \approx 5.6$ nm[184]) to readily penetrate into the microspheres during the 24 h conjugation reaction. Thus, the effective mesh size of the 10% PEGDA microspheres should be substantially larger than the size of hydrated R-PEs (i.e. macroporous structure). This should allow most of the conjugation sites in the microspheres to be readily accessible, leading to the highest capacity for the biomolecular conjugation of both F–ssDNA and R-PE among the microspheres examined here (detailed conjugation capacity analysis in Figure 5.6). Next, the 20% and 30% PEGDA microspheres (bottom rows in Figure 5.5c,f & d,g) show bright fluorescence layers along the sphere surfaces, again consistent with the fluorescence results in the top rows of Figure 5.5c,f & d,g. This result indicates that both biomolecules can penetrate and are conjugated only in the shell layers with well-defined thicknesses in contrast to small NHS–fluorescein (Figure 5.3); penetration depth PD=28±3 μm for the F–ssDNA and 20±1 μm for the R-PE. Note, the penetration depth of the F–ssDNA in the 20% PEGDA microspheres corresponds well to the thickness of PEG-poor shell region in these microspheres (26±1 μm, Figure 5.3c). I thus attribute this penetration depth of the F–ssDNA to small mesh size at the PEG-rich core region and macroporous (i.e. large mesh size) shell layer, also in support of the discussion in Figure 5.3. Next, the penetration depth of the R-PE in the same microspheres (PD=20±1 μm, bottom row of Figure 5.5f) is smaller than that for the F–ssDNA (PD=28±3 μm) due to R-PE's larger size,[27] further supported by gradually increasing penetration depth over time during conjugation (data not shown). Meanwhile, small standard deviation (5%) of the penetration depth for the R-PE indicates uniform mesh size of the shell layer and its thickness. Next, the bottom rows of Figure 5.5d,g for 30% PEGDA microspheres show smaller penetration depth of each biomolecule (PD≈10 μm) than 20% PEGDA ones, yielding the lowest conjugation among the microspheres examined. Importantly, these confocal microscopy results in Figure 5.5 show that there exist sufficient sites for the biomolecular conjugation in the entire 10% PEGDA microspheres and the shell layers of the 20-30% PEGDA ones, while the chitosan incorporation appears low for fluorescent labeling in these regions (Figure 5.3). The macroporous regions in the microspheres should offer favorable environment for the conjugation of large biomolecules (e.g. proteins), leading to enhanced conjugation capacity and kinetics (further discussed in Figure 5.6 and 5.7). I also examined the mesh size of the 10% and 20% PEGDA microspheres with substantially larger supramolecules, i.e. nanotubular tobacco mosaic virus (TMV, 18×300 nm dimension and R_h≈55 nm[185]) by exploiting hybridization-based TMV-assembly approach[89, 186] (Figure A4.6). The confocal micrographs of the microspheres assembled with fluorescein-labeled TMVs show a very thin fluorescence layer (thickness≈1 μm) along the sphere surfaces, indicating that the mesh size of both microspheres is not large enough for the penetration of TMVs. This result suggests that the mesh sizes of the microspheres are uniform throughout the macroporous regions; substantially larger than R-PE (R_h≈5.6 nm) yet smaller than TMV (R_h≈55 nm). Meanwhile, the assembled TMVs on the surface of the microspheres indicate that conjugated ssDNAs with the microspheres are available for targeting large biomacromolecules.

The well-defined core-shell structures shown in Figure 5.5 can allow programmable functionalization of the microspheres via size-selective conjugation, as shown in Figure A4.7. Specifically, sequential conjugation of the R-PE and a small fluorescent marker (F-488, MW 576 Da) via SPAAC reaction led to localization of the R-PEs in the shell region while the remaining ADIBO-activated chitosans were conjugated with F-488 molecules throughout the microspheres, particularly with high titer in the core region. In other words, functional molecules with varying sizes can be selectively localized with spatial control (i.e. core and shell) in the microspheres even with the same conjugation scheme. For example, cell- or surface ligand-targeting macromolecules such as antibodies (150-160 kDa)[39] and aptamers (8-25 kDa)[40] can be placed at the shell layers, and the remaining abundant conjugation sites around the cores can be loaded with small therapeutic molecules such as doxorubicin (MW 544 Da)[41] for targeted delivery applications.[42]

Notably, results in Figure 5.5 indicate that my simple one-step micromolding approach enables fabrication of chemically functional microstructures with controlled macroporous polymer networks without delicate flow control[7], arduous multistep procedures,[9] and/or, inert porogens.[5, 43] The microspheres with uniform macroporous or well-defined shell layers shown in Figure 5.5 should thus have significant potential for size-selective biosensing applications[44] where rapid and specific binding of biomacromolecular targets in hydrophilic platforms are highly desired.

Overall, the results in Figure 5.5 show well-defined and macroporous network structures of the microspheres, suitable for controlled biomacromolecular conjugation.

5.3.6 Protein Conjugation Capacity of Chitosan–PEG Microspheres

Next, I further examined consistency of the macropore structure formation and protein conjugation capacity via fluorescence microscopy and total fluorescence analysis, as shown in Figure 5.6. For this, I fabricated smaller 10-20% PEGDA microspheres than those shown in Figure 5.5 by utilizing micromolds with smaller volume. These microspheres were then conjugated with the R-PEs via SPAAC reaction for 24 h under identical conjugation conditions as in Figure 5.5. Total fluorescence intensity of the protein-conjugated microspheres were also compared with shape-encoded particle platforms shown in Chapter 4 in order to examine the effect of macroporous microsphere structures on protein conjugation capacity.

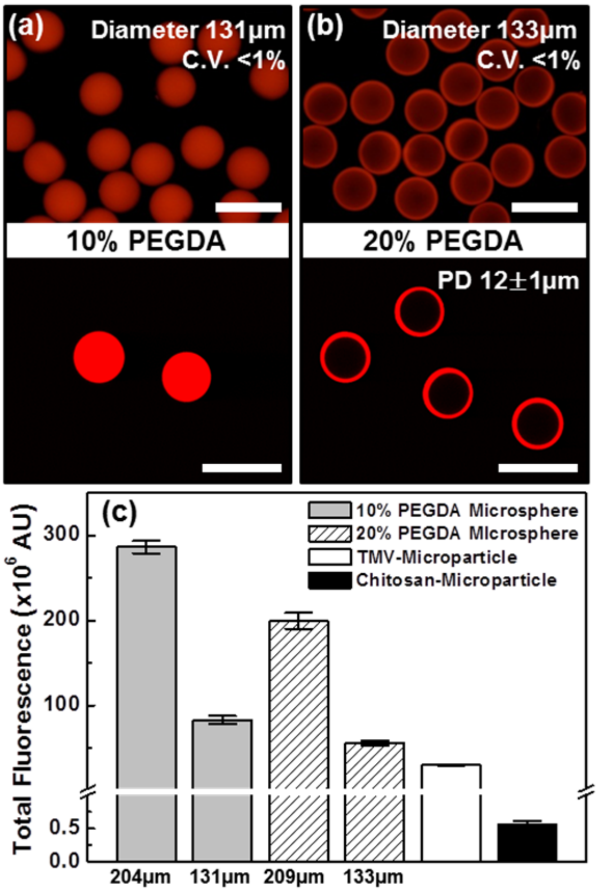

Figure 5.6. Protein conjugation capacity of chitosan–PEG microspheres. (a,b) Fluorescence (top row) and confocal (bottom row) micrographs of R-PE conjugated small (a) 10% and (b) 20% PEGDA microspheres. All scale bars represent 200 µm. (c) Total fluorescence intensity of R-PE conjugated platforms; 10% (gray columns) and 20% PEGDA (striped columns) microspheres with large (shown in Figure 5.5e,f) and small (shown in Figure 5.6a,b) sizes, and TMV- (white column) and chitosan-microparticles (black column) shown in Chapter 4. Error bars represent standard deviation from five microspheres per each condition.

First, the fluorescence (Figure 5.6a,b, top row) and bright-field micrographs (data not shown) reveal highly monodisperse microspheres (C.V. < 1%) with minimal difference in diameter (131 µm and 133 µm for 10% and 20% PEGDA, respectively). This result for the microspheres with roughly 4-

fold smaller volume is similar to that for the large microspheres (204 µm and 209 µm diameter) in Figure 5.2, illustrating consistency of droplet and microsphere formation in my simple fabrication scheme. Next, the top row of Figure 5.6a,b show uniform fluorescence throughout the 10% PEGDA microspheres and brighter fluorescence near the surfaces of the 20% PEGDA ones, consistent with the result for large microspheres in Figure 5.5. This result indicates that the formation of macroporous and well-defined 3D structures of the microspheres in Figure 5.5 is consistent for various sizes. The confocal micrographs (Figure 5.6a,b, bottom row) confirm these structural features; R-PEs readily penetrate and are conjugated throughout the 10% PEGDA microspheres and in the shell layers of the 20% PEGDA ones. Meanwhile, penetration depth of the R-PEs in the small 20% PEGDA microspheres (PD=12±1 µm) is smaller than that in the large-sized ones (PD=20±3 µm), suggesting controllable thickness of the macroporous shell layers based on microsphere size. Structures of the shell layers such as thickness and mesh size may be further tuned via use of inert PEG porogens and/or PEGDAs with longer chain lengths.[24, 187]

To quantitatively evaluate R-PE conjugation capacity of the microspheres, I next compared total fluorescence intensity from identical imaging condition (i.e. 50 ms exposure time) by utilizing linearity between fluorescence intensity and exposure time,[186] as shown in Figure 5.6c. First, the total fluorescence intensity of both large and small 10% PEGDA microspheres (gray columns) is higher (1.3-1.5 times) than that of 20% PEGDA microspheres (striped columns). This indicates higher protein conjugation capacity of the 10% PEGDA microspheres due to their larger macroporous regions spanning the entire sphere volume versus the shell layers of the 20% PEGDA ones (Figure 5.6a,b, bottom row). Next, the conjugation capacity of large microspheres (~207 μm) is ~3.5 times higher than that of the small ones (~132 μm). Meanwhile, R-PE conjugation kinetics with the large microspheres (Figure A4.8) showed incomplete R-PE conjugation upon 24 h incubation (i.e. gradual increase for 48 h) unlike the small microspheres reaching near-saturation upon 24 h incubation. Thus, the actual difference in the conjugation capacity between the large and small microspheres is larger than the one shown here in Figure 5.6c; roughly 4-fold difference in conjugation capacity between them upon 48 h reaction (Figure A4.8), similar to the difference in the microsphere volume. Next, I compared the conjugation capacity of these small microspheres to shape-encoded chitosan-microparticles (fabricated without droplet formation) with and without TMV templates shown in Chapter 3 and 4. Briefly, chitosan-particles with similar dimensions to the small microspheres have 44-fold enhanced conjugation capacity over planar substrates due to their 3D structure, with ~3 μm of R-PE penetration below their surfaces.[186] chitosan-particles with surface-assembled TMV templates (TMV-particles) via nucleic acid hybridization-based approach as in Figure A4.6 show 53-fold enhancement in capacity over the chitosan-particles due to the TMV templates providing abundant and precisely spaced sites for protein conjugation.[186] As shown in Figure 5.6c, the protein conjugation capacity of the small microspheres (gray and striped columns) is two orders of magnitude higher than that of the chitosan-particles (black column). I attribute this substantially enhanced conjugation capacity to macroporous structures of the microspheres leading to much deeper R-PE penetration (Figure 5.6a,b, bottom row) than that into the chitosan-particles (only 3 μm). Next, conjugation capacity of the microspheres is higher (~3 and 2-fold for 10% and 20% PEGDA microspheres, respectively) than that of the TMV-particles (white column), suggesting abundant conjugation sites that are readily accessible in the macroporous regions of the microspheres. My simple estimation for the number of protein conjugation sites in the small 10% PEGDA microspheres (Figure A4.9) also supports this hypothesis on abundant sites for protein conjugation in the microspheres. In short summary, the results in Figure 5.6c clearly show significantly enhanced protein conjugation capacity of my microspheres due to their macroporous structures with abundant conjugation sites (i.e. over 4400 times higher conjugation capacity than that of the planar substrates).

Other 3D structured platforms such as polymer brush-grafted substrates have been reported in several studies,[154-157] yet the enhancement in the conjugation capacity of such platforms (2-14 times) over reference substrates (without polymer brushes) is substantially lower than that of the microspheres shown here. This substantially improved conjugation capacity of the microspheres demonstrates benefits of my micromolding-based technique leading to well-defined macroporous structures. In addition, for optimal protein conjugation with the polymer brush-based platforms, several fabrication and reaction parameters (e.g. density, thickness and solvation of the polymer brushes) should be carefully chosen and maintained to prevent collapse and aggregation of the polymer brushes.[154, 155] In contrast, the well-defined macroporous 3D structures of my microspheres are retained through various pH and ionic strength conditions due to crosslinked polymer networks providing mechanical integrity (data not shown). In turn, these macroporous structures should provide further benefits in biosensing applications in terms of target binding kinetics with minimal mass transfer limitation. Finally, my post-fabrication protein conjugation approach can preserve the activity of labile proteins such as antibodies unlike other copolymerization-based strategies,[1, 29] which potentially lead to protein damage by reactive radicals generated during polymerization.[150]

Combined, the results in Figure 5.6 show consistency of my micromolding-based approach for fabrication of well-defined and macroporous microspheres with varying sizes. In addition, the total fluorescence analysis results show substantially enhanced protein conjugation capacity of the microspheres due to their macroporous structures, suggesting their potential as attractive platforms for biosensing applications.

5.3.7 Protein Conjugation Kinetics of Microspheres

Finally, I examined the effect of inherent reaction rates on "apparent" protein conjugation kinetics as shown in Figure 5.7. For this, I directly compared the conjugation kinetics behavior of R-PE with the microspheres via rapid tetrazine–*trans*-cyclooctene (Tz–TCO) cycloaddition reaction (k=820 $M^{-1}s^{-1}$)[21] vs. that via SPAAC reaction (k=2.1 $M^{-1}s^{-1}$)[22]; ~400 times difference in the inherent reaction rate. Specifically, small 10-20% PEGDA microspheres were activated with Tz and ADIBO molecules separately, then reacted with 2 μM of TCO- and azide-activated R-PEs for varying times (0-48 h) respectively (Figure 5.7a). Total fluorescence intensity of the R-PE conjugated microspheres were compared upon normalization with maximum fluorescence of the 10% PEGDA microspheres (i.e. at 48 h Tz–TCO reaction).

First, the normalized fluorescence plot of the 10% PEGDA microspheres via Tz–TCO reaction (Figure 5.7b, open squares) shows gradual increase in fluorescence with time, reaching maximum (i.e. completion of R-PE conjugation) within 24 h; 55% and 80% of the maximum upon 2 h (dashed line) and ~8 h reaction (dash-dot line), respectively. The fluorescence of the 10% PEGDA microspheres via SPAAC reaction (open circles) also gradually increases over time, showing minimal difference in the conjugation kinetics behavior with that via Tz–TCO reaction; 31% and 80% of the maximum upon 2 h (dashed line) and ~11 h reaction (dash-dot-dot line). These results indicate minimal difference in the rate of R-PE conjugation between Tz–TCO and SPAAC reaction despite significant difference (~400 times) in their inherent reaction rates. This suggests that the conjugation kinetics is mainly governed by mass transfer (i.e. diffusion) of the R-PEs through the 10% PEGDA microspheres under the reaction conditions enlisted here. Importantly, reaching ~50% of the conjugation completion within 2 h via Tz–TCO reaction suggests rapid diffusion of the R-PEs through the microspheres due to their macroporous structure.

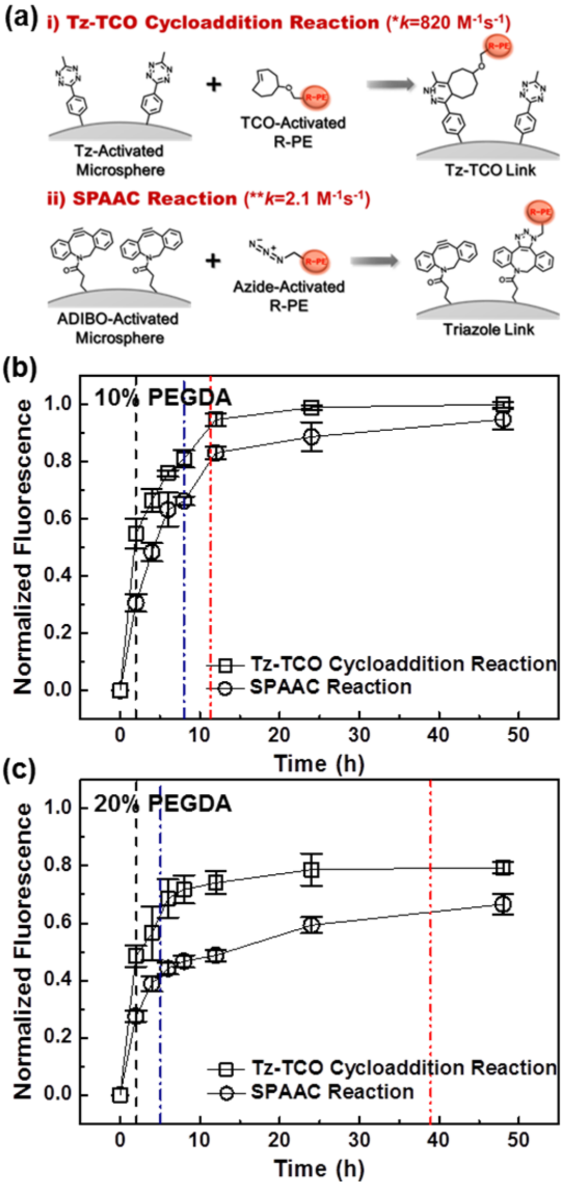

Figure 5.7. Apparent protein conjugation kinetics with the small microspheres fabricated with 10% and 20% PEGDA via rapid Tz–TCO cycloaddition and slow SPAAC reaction. (a) Schematic diagrams of R-PE conjugation via Tz–TCO cycloaddition and SPAAC reaction. (b,c) Normalized fluorescence intensity plots of (b) the 10% and (c) 20% PEGDA microspheres upon conjugation with R-PEs for varying times via Tz–TCO cycloaddition (open squares) and SPAAC (open circles) reaction. Error bars represent standard deviation from five microspheres per each condition.

Next, the 20% PEGDA microspheres via Tz–TCO reaction (Figure 5.7c, open squares) show similar gradual increase in fluorescence to that with the 10% PEGDA microspheres, reaching conjugation completion (~80% of the maximum fluorescence on the 10% PEGDA microspheres) within 24 h. Specifically, the conjugation reaches 61% and 80% of the completion upon 2 h (dashed line) and ~5 h reaction (dash-dot line) respectively, showing rapid diffusion of the R-PEs through the macroporous shell layers of the microspheres. Note, the difference in fluorescence at the conjugation completion between 10% and 20% PEGDA microspheres is due to the difference in their conjugation capacity (i.e. chitosan's amine groups available for conjugation, Figure 5.6c). The fluorescence of the 20% PEGDA microspheres via SPAAC reaction also gradually increases, yet much slowly; longer reaction time (~39 h) is required to reach 80% of the completion (dash-dot-dot line). This result indicates that the inherent conjugation reaction rates have impact on the conjugation kinetics behavior with the 20% PEGDA microspheres to some extent unlike the 10% PEGDA microspheres, and implies smaller mesh size of the shell layers in the 20% PEGDA microspheres than that of the entire 10% PEGDA ones. In other words, combination of small mesh size and slow inherent rate of SPAAC reaction should lead to considerable decrease in driving force (i.e. protein concentration gradient within the microspheres) for the proteins to diffuse into the microspheres resulting in slower conjugation.

Next, the 20% PEGDA microspheres with Tz–TCO reaction take shorter reaction time (~5 h) to reach 80% of the conjugation completion than the 10% PEGDA ones (~8 h); Figure 5.7b,c, dash-dot lines. I attribute this faster approach toward the completion for the 20% PEGDA microspheres to smaller thickness of their macroporous region (i.e. shorter diffusion length). That is, the 20% PEGDA microspheres reach the conjugation completion once the R-PEs penetrate only 12 μm below the sphere surfaces (corresponding to thickness of their shell layers) unlike the 10% PEGDA microspheres (PD≈65 μm, corresponding to radius of the microspheres). This suggests that the apparent conjugation kinetics is controllable with thickness of the macroporous regions in the microspheres, which is further supported by the results in Figure A4.8 (i.e. smaller microspheres take shorter time to reach saturation due to shorter diffusion length resulting from smaller thickness of the macroporous regions). In short summary, the results in Figure 5.7 show that conjugation kinetics behavior with the microspheres is rapid, and controllable by tuning their structures (i.e. mesh size and thickness of macroporous regions).

Meanwhile, the microspheres' mesh structures should also affect target protein binding kinetics (e.g. antibody–antigen (Ab–Ag) binding) in a similar manner to the conjugation kinetics with rapid Tz–TCO reaction, since the inherent biospecific binding for such events also are often rapid ($k \approx 10^4$-10^6 $M^{-1}s^{-1}$ for Ab–Ag binding[168]). Combined with tunable probe conjugation capacity of the microspheres (Figure 5.6c), biosensing performance parameters (e.g. assay time and sensitivity) can be readily controlled by tuning the microsphere structures. My simple micromolding-based technique should enable such control of structures by simple parameters such as PEGDA contents (Figure 5.5) and sphere sizes (Figure 5.6), and also via use of PEGDAs with different lengths and PEG porogens.[24, 187]

Compared with the chitosan-particles shown in Chapter 4, the conjugation kinetics with the macroporous microspheres appears to be somewhat slower; conjugation completion via Tz–TCO reaction within 24 h for the microspheres vs. 18 h for the chitosan-particles, partially due to much longer diffusion length and higher conjugation capacity (Figure 5.6). Yet, the macroporous structure of the microspheres should benefit the conjugation kinetics given their significantly enhanced conjugation capacity over the chitosan-particles (Figure 5.6c); minimal increase in reaction time to reach two orders of magnitude higher maximum conjugation (i.e. much faster protein conjugation rate based on the number of conjugated proteins per hour). Meanwhile, Chapter 4 showed that the conjugation kinetics as well as capacity of the chitosan-particles was improved via high density surface-assembly of TMV templates with abundant protein conjugation sites (TMV-particles), yet this approach has limitations rising from multistep procedures (Figure A4.6). In contrast, my approach for fabrication of the microspheres with controlled macroporous structures and high conjugation capacity provides much simpler routes to improved conjugation and biosensing performances.

In summary, the results in Figure 5.7 show rapid protein conjugation kinetics behavior with microspheres due to their macroporous structures. In addition, the conjugation kinetics can be readily tuned with simple parameters.

5.4 Conclusions

In this chapter, I demonstrated a facile approach to fabricate highly uniform and chemically functional chitosan–PEG microspheres with controlled macroporous structures, and their utility in biomolecular conjugation via bioorthogonal SPAAC and Tz–TCO cycloaddition reactions. First, highly monodisperse (C.V. < 1%) chitosan–PEG microspheres with a wide range of PEGDA contents (5-70%) were readily fabricated via a simple micromolding-based technique utilizing surface tension-induced droplet formation of aqueous chitosan–PEGDA prepolymer solution followed by photopolymerization. At 20-30% PEGDA content conditions, PIPS led to formation of core-shell (PEG-rich and PEG-poor respectively) structures. Fluorescent labeling results revealed stable incorporation of chitosan in the microspheres with retained chemical reactivity toward amine-reactive chemistries. Lastly, biomolecular conjugation results with F–ssDNAs and R-PEs showed well-defined macroporous regions of the microspheres (i.e. entire 10% PEGDA microspheres and shell layers of 20% PEGDA ones), allowing for rapid protein conjugation and significantly enhanced capacity (e.g. ~4400 times over planar substrates) as well as programmable and size-selective conjugation. I envision that my integrated fabrication-conjugation approach can be readily enlisted to manufacture microspheres with controlled macroporous structures and programmable functionalities for various biomedical applications.[1-7]

6 CONCLUSIONS AND FUTURE PROSPECTS

In Chapter 2, I presented a facile method to fabricate nonspherical chitosan−PEG microparticle platforms for conjugation of biomolecules with high surface density. Specifically, I demonstrated that PEG microparticles containing short chitosan oligomers are readily fabricated via replica molding (RM). Fluorescence and FTIR microscopy results illustrated that the chitosan moieties are incorporated with PEG networks in a stable manner while retaining their chemical reactivity toward amine-reactive chemistries (e.g. bimolecular nucleophilic substitution (S_N2) reaction with NHS ester). The chitosan−PEG microparticles were then conjugated with single-stranded (ss) DNAs via SPAAC reaction. Fluorescence and confocal microscopy results showed facile conjugation of biomolecules with the chitosan−PEG particles under mild conditions with high selectivity. These ssDNA-conjugated chitosan−PEG particles were then enlisted to assemble TMV via nucleic acid hybridization as an example of orientationally controlled conjugation of supramolecular targets. Results clearly showed controllable TMV assembly with high surface density, indicating high surface DNA density on the particles. Combined, these results demonstrated a facile fabrication–conjugation scheme for robust biomolecular conjugation or assembly platforms.

In Chapter 3, I thoroughly examined protein conjugation with the chitosan–PEG microparticles via SPAAC reaction between azide-activated proteins and ADIBO-activated microparticles. Upon conjugation of a model red fluorescent protein (R-PE), fluorescence and confocal micrographs showed selective protein conjugation, yet only near the particle surfaces (primarily within top 3 µm of the microparticles), owing to the size of R-PEs and small mesh size of the microparticles. The R-PE conjugation results also showed long-term stability of the conjugation scheme via SPAAC reaction (more than 3 weeks). Fluorescence and AFM results upon conjugation with varying protein concentrations indicated controllable protein conjugation. In-depth examination of protein–particle conjugation kinetics showed multiple reaction regimes; rapid initial (k_{app}=11.5 $M^{-1}s^{-1}$), intermediate and steady final stage (k_{app}=2.10 $M^{-1}s^{-1}$). Lastly, I demonstrated anti-R-PE antibody (R-Ab) conjugation with the microparticles, and rapid target protein (R-PE) capture with the antibody-conjugated microparticles (i.e. up to femtomolar quantity within 3 h). Combined, these results illustrate a facile fabrication–conjugation scheme for robust protein-conjugated platforms that can be readily enlisted in various protein sensing applications.

In Chapter 4, I demonstrated significantly enhanced protein conjugation and target protein capture capacity by exploiting TMV templates assembled with hydrogel microparticles. Protein conjugation results with R-PEs showed significantly enhanced protein conjugation capacity of TMV assembled particles (TMV-particles) compared to planar substrates (2400-fold) or chitosan–PEG microparticles (53-fold). In-depth examination of protein conjugation kinetics via Tz−TCO and SPAAC reaction demonstrated that TMV-particles provide a less hindered environment for protein conjugation. R-PE capture results using R-Ab conjugated TMV-particles also showed substantially improved capture capacity of the TMV-particles over the chitosan–PEG microparticles. I further demonstrated readily controlled protein and antibody conjugation capacity by simply varying TMV concentrations, which shows negligible negative impact of densely assembled TMVs on protein conjugation and capture capacity. Combined, these results illustrated a facile post-fabrication protein conjugation approach with TMV templates assembled onto hydrogel microparticles for improved and controlled protein conjugation and sensing platforms.

In Chapter 5, I presented a simple approach for fabrication of highly uniform spherical chitosan–PEG microparticles (C.V. < 1%) with controlled macroporous structures. For this, I exploited a micromolding-based technique utilizing surface tension-induced droplet formation followed by photo-induced radical polymerization. The as-prepared microspheres showed macroporous and/or intriguing core-shell (PEG-rich and PEG-poor) structures by polymerization-induced phase separation (PIPS). Fluorescent labeling studies indicated stable incorporation of chitosan with retained chemical reactivity in the microspheres, similar to the results of nonspherical chitosan–PEG particles fabricated via RM in Chapter 2. The controlled macroporous structures of the chitosan–PEG microspheres and their utility in programmable biomacromolecular assembly were thoroughly examined with conjugation of model biomolecules such as fluorescein-labeled ssDNA and R-PE via SPAAC and Tz–TCO reaction. The conjugation results confirmed well-defined and macroporous network structures of the microspheres, which lead to improved protein conjugation capacity (~4400 times over planar substrates) and kinetics. Combined, these results illustrated a simple and robust micromolding-based fabrication approach for highly uniform microspheres with controlled macroporous structures, and their utility as platforms for biomolecule conjugation.

Overall, the works presented in this dissertation illustrate facile fabrication–conjugation approaches for construction of biomolecule conjugation and biosensing platforms via integration of simple micromolding-based techniques and high yield bioorthogonal conjugation reactions. Table 6.1 is a brief summary of comparison between current fabrication techniques for protein-based biosensing platforms and the micromolding-based approaches presented in this dissertation. This comparison illustrates convenience and merits of the integrated approaches with micromolding techniques and post-fabrication conjugation. For example, the micromolding-based techniques allow for well-defined and uniform platform fabrication in a simple manner without any delicate control and complex devices unlike microfluidics-based techniques, and without any harsh washing and functionalization steps that are required in the fabrication process of microarrays and polymer brush platforms. Next, the post-fabrication conjugation approach allows for minimal damage of biomolecules unlike copolymerization-based approaches generally utilized in fabrication of polymer brush platforms and microfluidics systems.

Meanwhile, I examined biosensing performance (i.e. sensitivity and assay time) of the antibody-conjugated microparticle platforms via capture of the red fluorescent protein (R-PE) as a model target in my study, unlike other existing studies shown in Table 6.1. In other words, most of target proteins in biosensing barely generate fluorescence signals by themselves unlike the R-PE, and a signal conversion step for the captured targets is required; the captured targets are generally converted to amplified signals by utilizing secondary antibodies bearing signal-enhancing entities[37, 170, 188] (i.e. ‘sandwich’ assays as shown in Figure 1.1). Therefore, the biosensing performance of the microparticle platforms should be further evaluated with target proteins relevant to real applications and the signal amplification for direct comparison with the existing platforms. Combined with the signal amplification, substantially improved probe loading capacity and less hindered environment of the microparticle platforms would allow for highly sensitive and rapid biosensing. I thus believe that the integrated fabrication–conjugation approaches presented in this dissertation can be readily enlisted in a wide range of biosensing application areas including medical diagnostics,[31] industrial bioprocess monitoring,[32] and pathogen detection.[33, 34]

	Planar Array			Suspension Array		
	ELISA^{A}	Microarray^{B}	Polymer Brush^{C}	Microbead^{D}	Hydrogel Microparticle	
					Microfluidics^{E}	Micromolding
Substrate Material	96-well polystyrene plates	Glass slides	Poly(ethylene glycol)-based Polymer brushes on glass slides	Polystyrene	Poly(ethylene glycol)	Poly(ethylene glycol) with chitosan
Platform Fabrication Methods +Strength −Weakness	N/A	Automatic spotting −Harsh glass slide washing and functionalization steps −Needs of specialized spotting solution and humidity control	Polymerization on functionalized glass slides −Harsh glass slide washing and functionalization steps −Needs for delicate control of fabrication parameters to retain relaxed polymer chains	Dispersion and emulsion Polymerization +Scalability −Polydisperse particles	Polymerization in PDMS microfluidic devices +Capability to fabricate highly uniform particles with complex shapes −Needs for complex devices −Delicate control of fabrication parameters	Polymerization in PDMS micromolds +Simple fabrication steps for monodisperse particles with complex shapes +Flexible control of fabrication parameters −Needs of high humidity conditions to prevent rapid evaporation
Antibody Immobilization +Strength −Weakness	Physical adsorption +No chemical modification steps −Unstable immobilization −Possible damage of antibodies owing to hydrophobic substrates −Reduced activity owing to blocked recognition sites −Needs of additional blocking steps to prevent nonspecific adsorption of target proteins	Physical adsorption or covalent conjugation +Concentrated antibodies in a spot leading to enhanced signal and reduced sample volume −The same weaknesses as ELISA's	Covalent conjugation during polymer brush formation +Enhanced antibody loading capacity −Possible damage of antibodies during polymerization	Physical adsorption or covalent conjugation upon particle fabrication −Low antibody loading capacity −Nonspecific binding	Covalent conjugation during particle fabrication +Enhanced antibody loading capacity −Possible damage of antibodies during polymerization	Covalent conjugation upon particle fabrication +Enhanced antibody loading capacity +Minimal damage of antibodies +Specific conjugation
Sensitivity* (Limit of Detection)	~2-100 pg/mL	~5-1000 pg/mL	~3-4 pg/mL	~1-8 pg/mL	~1-9 pg/mL	~20 ng/mL (w/o signal amplification)
Total Assay Time*	>5 h	~1-2 h	~15 min	~30 min	~3 h	<3 h (w/o signal amplification)

Table 6.1. Comparison of current fabrication techniques for protein-based biosensing platforms with the integrated micromolding and bioorthogonal conjugation approaches. ^{A}[53, 189], ^{B}[189], ^{C}[160, 190], ^{D}[191] and ^{E}[53]. *Evaluated with signal amplification

In the meantime, several future works should be carried out to further improve the performances presented in this dissertation. First, the mesh size of hydrogel microparticles can be further tuned via use of long chain polymeric monomers (i.e. PEGDA) and/or inert porogens (i.e. PEG). Several studies reported that the mesh size of hydrogels, directly relevant to solute diffusion, depends to a great extent on chain length of the polymeric monomers.[24, 25, 42] In addition, recent studies reported that addition of inert PEG porogens in pre-hydrogel solutions leads to increase in the mesh size via phase separation of the PEG during polymerization, and enables large molecules to more readily penetrate into the hydrogels compared to those fabricated without PEG porogens.[136, 187] I thus expect that the use of PEGDA with longer chain lengths and/or inert PEG porogens will further increase mesh sizes of the hydrogel microparticles presented in this dissertation, and thus improve mass transfer of large biomolecules through the hydrogel microparticles resulting in rapid conjugation and biosensing. In addition, polymerization systems consisting of monomers rather than crosslinking monomers (PEGDA) and small amount of crosslinkers (e.g. an acrylamide and bisacrylamide system) would allow for fabrication of hydrogel microparticles with readily tunable mesh sizes by simply adjusting the concentrations and/or ratios of the monomers and crosslinkers.[192, 193] Along with the low-fouling feature of polyacrylamide,[194-196] the mesh size-tuned polyacrylamide microparticles could be also a suitable candidate as a biosensing platform. Next, recent studies reported that polymerization kinetics also affect network structures of hydrogels.[48, 49] As described in Chapter 1, the key parameters determining kinetics of photo-induced radical polymerization are UV intensity and photoinitiator concentration, as well as monomer concentration already examined in this dissertation. I expect that further investigation of the effect of polymerization kinetics on hydrogel network structures with UV intensity and photoinitiator concentration would lead to better understanding of hydrogel network formation allowing for fine control of the network structures. Meanwhile, advanced microscopy techniques for soft materials such as cryo-SEM (scanning electron microscopy)[197] along with microtome[198] or beam milling[199] techniques would assist in examination of intact network structures of the hydrogel microparticles under hydrated conditions.

Furthermore, one important future study is in-depth examination and quantitative understanding of mass transfer of solutes (i.e. biomolecules) in the hydrogel microparticles where diffusion of the solutes and conjugation reaction are coupled. First, Renkin equation[26] can be exploited to quantitatively investigate the relation between mesh sizes and diffusion of the solutes in the hydrogel microparticles (without conjugation reaction), along with estimated diffusion coefficients of the solutes in bulk solution from Stokes–Einstein equation.[200]

<u>Renkin Equation</u>

$$\frac{D_m}{D_0} = \left(1 - \frac{d_s}{d_m}\right)^2 \times \left[1 - 2.10\left(\frac{d_s}{d_m}\right) + 2.09\left(\frac{d_s}{d_m}\right)^2 - 0.95\left(\frac{d_s}{d_m}\right)^5\right]$$

<u>Stokes–Einstein Equation</u>

$$D_0 = \frac{k_B T}{3\pi\eta d_s}$$

where D_m and D_0 represent diffusion coefficients of solutes in hydrogels and solution, respectively. d_s and d_m represent hydrodynamic diameter of solutes and mesh size of hydrogels, respectively. T and η represent temperature and viscosity of solution, respectively. k_B is Boltzmann constant.

Next, Damköhler number (*Da*), the ratio of reaction rate to diffusion rate in a system can be exploited to determine diffusion-limited ($Da \gg 1$) or reaction-limited ($Da \ll 1$) mass transfer of the solutes in the hydrogel microparticle systems.[29, 115]

Damköhler number

$$Da = \frac{Reaction\ Rate}{Diffusion\ Rate} = \frac{kC_0R^2}{D_m}$$

where k represents the second-order rate constant of conjugation reactions, R is radius of microspheres, and C_0 represents concentration of conjugation (or binding) sites.

As an example, the R-PE conjugation with small 10% PEGDA microspheres (R=65.6 μm) via Tz–TCO reaction shown in Chapter 5 (Figure 5.7b) was examined with Renkin and Stokes–Einstein equation as well as *Da*. The results in Chapter 5 showed that mesh size of the 10% PEGDA microspheres is larger than the size of R-PEs (11 nm) yet smaller than that of TMVs (110 nm).

Thus, I first estimated diffusion coefficients of the R-PEs in the microspheres (D_m) with Renkin equation for mesh sizes (d_m) ranging from 13 to 100 nm, along with Stokes–Einstein equation (D_0=4.0×10^{-7} cm^{2}s^{-1}). By utilizing these estimated diffusion coefficients, Damköhler numbers (Da) were then computed with the second-order rate constant of Tz–TCO reaction (k=820 M^{-1}s^{-1}) and estimated concentration of the accessible conjugation site in the 10% PEGDA microspheres (C_0~10^{-3} M, see Section A4.9). The estimated D_m and computed Da values are summarized in Table 6.2, and the Da values (i.e. $Da \gg 1$) suggest that mass transfer of the R-PEs during the conjugation is governed by the diffusion rather than the conjugation reaction for the range of mesh sizes examined.

d_m		D_m		Da
13 nm	> R-PE Diameter	7.3×10^{-10}	cm^{2}s^{-1}	48290
35 nm	≈ 3×R-PE Diameter	7.6×10^{-8}	cm^{2}s^{-1}	467
100 nm	< TMV Diameter	2.5×10^{-7}	cm^{2}s^{-1}	144

Table 6.2. Summary of estimated diffusion coefficients of the R-PEs in the 10% PEGDA microspheres (D_m) for varying mesh sizes, and computed Damköhler numbers (Da) with the estimated D_m, 820 M^{-1}s^{-1} of k for Tz–TCO reaction and ~10^{-3} M of C_0 for the 10% PEGDA microspheres.

Based on this result, the progress of R-PE conjugation with the microspheres could be considered as R-PE diffusion through the microspheres with time; non-steady state diffusion in a sphere[201] described with the equation,

$$\frac{C}{C_0} = 1 + \frac{2R}{\pi r}\sum_{n=1}^{\infty}\frac{(-1)^n}{n}\sin\frac{n\pi r}{R}e^{-(D_m n^2 t/R^2)}$$

where C represents concentration of solutes at a location in a sphere (r) and transient time (t). C_0 represents constant surface concentration (i.e. maximum concentration). By utilizing this equation, the time required to reach completion (i.e. $C/C_0 > 0.99$) for specific D_m can be estimated as shown in Figure 6.1. For D_m=7.3×10^{-10} cm^{2}s^{-1}, the estimated completion time is ~10 h, comparable to the experimental results shown in Figure 5.7b (i.e. conjugation completion within 12 h). Combined, the R-PEs during the conjugation appear to diffuse into the microspheres with 13 nm pores, corresponding to 7.3×10^{-10} cm^{2}s^{-1} of D_m. Note that, the 13 nm pore size should represent narrowed diffusion paths by the as-conjugated R-PEs, and thus the real mesh size of the 10% PEGDA microspheres should be ~35 nm.

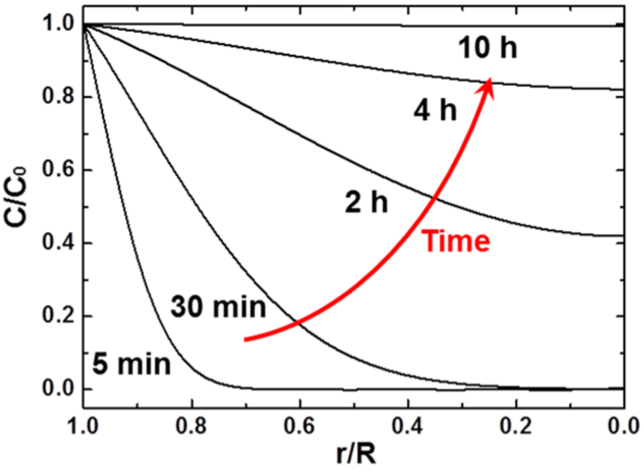

Figure 6.1. Simulated concentration distributions of the R-PE at various times in a microsphere for D_m=7.3×10^{-10} cm^{2}s^{-1}.

In short summary, this initial attempt shows potential of the analysis approach using Renkin and Stokes–Einstein equation as well as *Da* toward in-depth and quantitative examination of mass transfer of biomacromolecules in the diffusion–reaction coupled systems. I thus anticipate that this approach should allow for more profound understanding on the interplay between mesh sizes of hydrogel microparticles, inherent rates of conjugation reactions (or biospecific bindings) and diffusion coefficients of biomolecules, and should lead to rational design principles for construction of biosensing platforms.

Lastly, from the perspective of antibody conjugation, the conjugation scheme using lysine residues often found in hypervariable or recognition sites (shown in Chapter 2 and 3) potentially leads to decrease in recognition capability of the antibodies. Meanwhile, there has been substantial progress on the genetic modification of proteins with unnatural amino acids to confer additional functionalities, particularly azidophenylalanine offering azide groups on specific sites of protein surfaces.[102, 152] Combined with the bioorthogonal reaction-based conjugation scheme shown in this dissertation, such technologies should allow for significantly more selective and robust antibody conjugation (i.e. site specific conjugation retaining the recognition capability).

APPENDICES

A1 Fabrication of Chitosan-incorporated Hydrogel Microparticles via Replica Molding

A1.1 Consistent Fabrication of Chitosan–PEG Microparticles

The bright-field micrographs of Figure A1.1 show that the chitosan–PEG microparticles are fabricated with consistent and reproducible dimensions via replica molding (RM) under all the chitosan concentration conditions examined. For this, I prepared preparticle solutions consisting of 30% (v/v) PEGDA, 2% (v/v) 2-hydroxy-2-methylpropiophenone (photoinitiator) and varying concentrations of chitosan (from 0 to 1.2% (w/v)). These preparticle solutions were added to a PDMS-based micromold under controlled humidity (~90% RH), and the particles were formed via photopolymerization with UV light (365 nm). The results show the formation of highly uniform and well-defined microparticles with consistent heights and shapes via RM under all the chitosan concentrations employed.

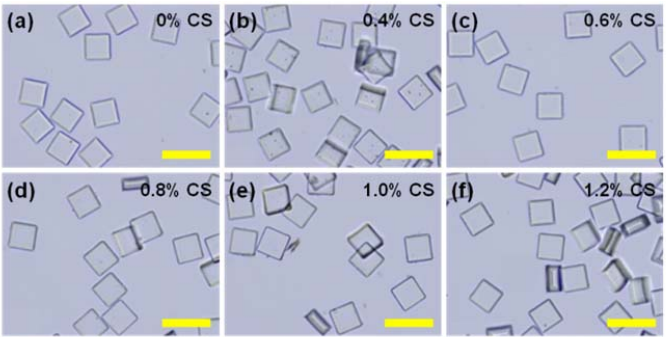

Figure A1.1. Bright-field micrographs of the chitosan–PEG microparticles with (a) 0% (w/v), (b) 0.4% (w/v), (c) 0.6% (w/v), (d) 0.8% (w/v), (e) 1.0% (w/v) and (f) 1.2% (w/v) of chitosan (CS). Scale bars represent 200 µm.

A1.2 Effluence of Fluorescently Labeled Chitosan from Broken Chitosan–PEG Particles: Stable Incorporation

The fluorescence micrographs of Figure A1.2 show that the chitosan oligomers are incorporated within the PEG networks of the microparticles in a stable manner. For this, the high PEG content particles (40% PEGDA and 48% PEGDA) are first fluorescently labeled with 10 µM of NHS–fluorescein. The labeled particles were then broken with a small blade, and stored for 5 days in the buffer solution (5×SSC with 0.05% (v/v) Tween 20), with exchanging the buffer solution every day. Upon extensive washing, I observed no significant leaching of the fluorescence at the center region (small arrows). Thus, the chitosan oligomers appear to be incorporated within the particles in a stable manner, and I hypothesize that this stable incorporation of chitosan results from either covalent binding[116] as shown in Figure A1.2c or physical entrapment within the particles.

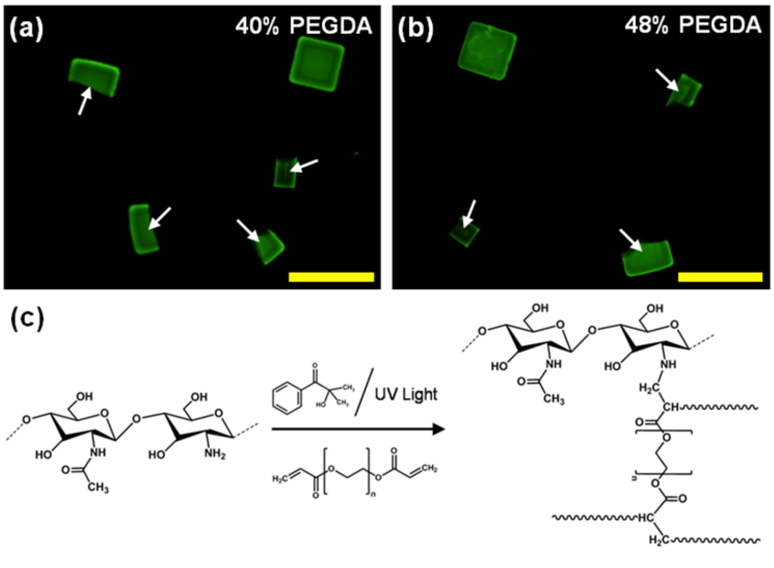

Figure A1.2. Fluorescence micrographs of the fluorescently labeled chitosan–PEG microparticles upon breaking; (a) 40% PEGDA and (b) 48% PEGDA. Scale bars represent 200 μm. (c) Suggested covalent reaction scheme between primary amines of the chitosan and acrylate groups of the PEGDA during photopolymerization.[116]

A1.3 Sequence-specific DNA–DNA Hybridization and Stable Conjugation of Capture DNAs with Chitosan–PEG Microparticles

The bright-field and fluorescence micrographs of Figure A1.3 show sequence-specific hybridization using different shapes of chitosan–PEG microparticles conjugated with different capture DNA sequences. For this, I prepared three shapes of chitosan–PEG particles from 1% (w/v) chitosan and 30% (v/v) PEGDA preparticle solution via RM and activated them with ADIBO. The as-prepared particles were then conjugated with different capture DNA sequences (Table A1.1). All three types of particles were mixed and then hybridized with one of three fluorescently labeled target DNAs (1 μM) for 3 h at room temperature. The micrographs of Figure A1.3a-f were taken upon 4 times washing with 5×SSC buffer containing 0.05% Tween 20. Furthermore, the micrographs shown in Figure A1.3g-l demonstrate stable conjugation of capture DNAs with chitosan–PEG microparticles via SPAAC reaction. For this, thoroughly washed and target DNA-hybridized microparticles were stored in 5×SSC buffer containing 0.05% Tween 20 for three months, then examined via fluorescence microscopy as shown in Figure A1.3g-l.

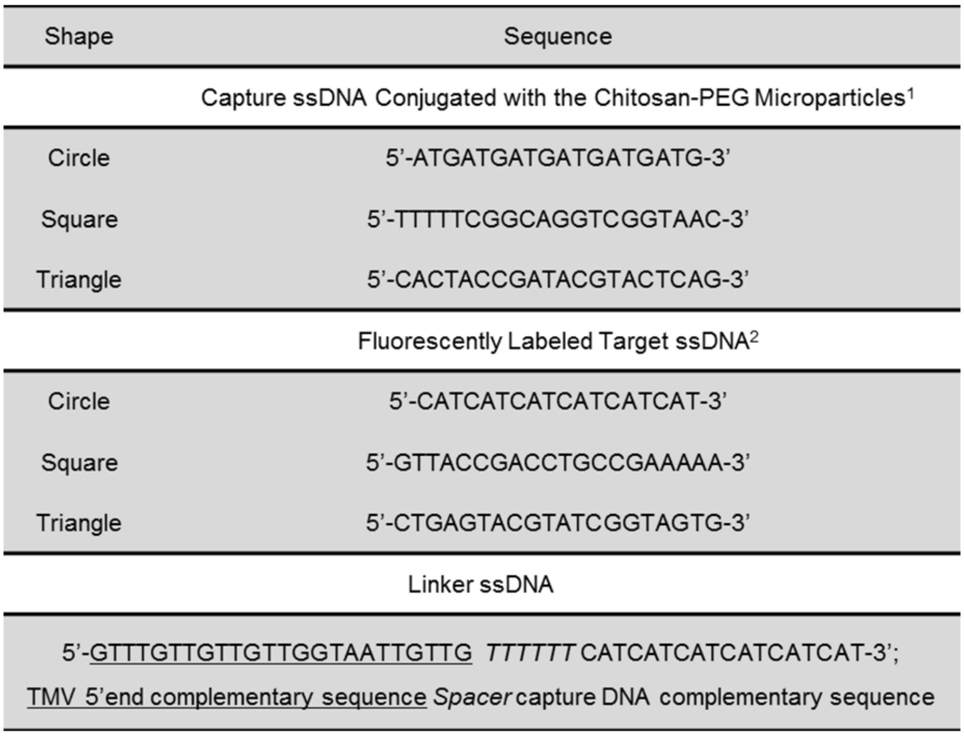

Shape	Sequence
	Capture ssDNA Conjugated with the Chitosan-PEG Microparticles[1]
Circle	5'-ATGATGATGATGATGATG-3'
Square	5'-TTTTTCGGCAGGTCGGTAAC-3'
Triangle	5'-CACTACCGATACGTACTCAG-3'
	Fluorescently Labeled Target ssDNA[2]
Circle	5'-CATCATCATCATCATCAT-3'
Square	5'-GTTACCGACCTGCCGAAAAA-3'
Triangle	5'-CTGAGTACGTATCGGTAGTG-3'
	Linker ssDNA
5'-GTTTGTTGTTGTTGGTAATTGTTG *TTTTTT* CATCATCATCATCATCAT-3'; TMV 5'end complementary sequence *Spacer* capture DNA complementary sequence	

[1] Capture ssDNA sequences are all modified with Azide at the 5'end.
[2] Target ssDNA sequences are all modified with 5-(and 6-)carboxyfluorescein (5(6)-FAM) at the 5'end.

Table A1.1. List of capture, target and linker ssDNA sequences

The bright-field micrographs of Figure A1.3a-c show three different shapes of highly uniform microparticles with different capture DNA sequences. The fluorescence micrographs of Figure A1.3d-f show that nucleic acid hybridization occurs only between the complementary target and capture DNA pairs, and that negligible fluorescence from the particles with non-complementary sequences clearly illustrates highly sequence-specific hybridization. Next, the fluorescence micrographs of Figure A1.3j-l show minimal decrease in the fluorescence intensity of the particles after three month storage in the buffer solution. Therefore, this result clearly indicates that the capture DNAs are conjugated with chitosan–PEG particles in a stable manner via SPAAC reaction. In short summary, the results shown in Figure A1.3 indicate the robust and selective nature of my fabrication-conjugation scheme.

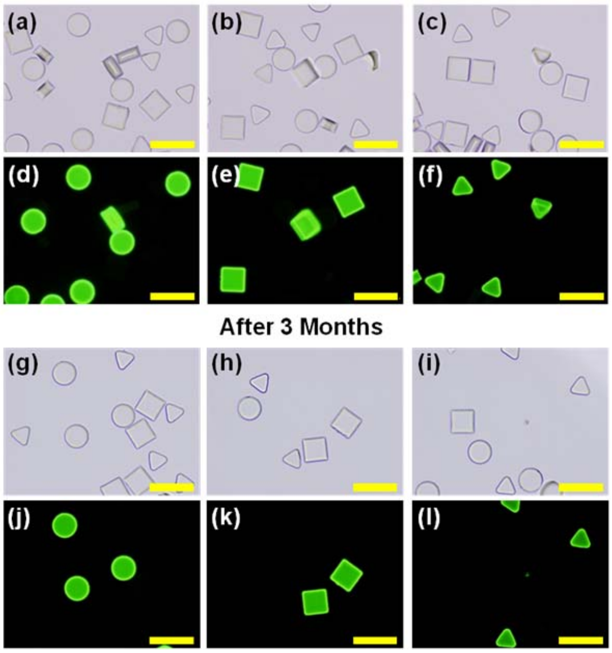

Figure A1.3. Sequence specific hybridization using capture ssDNA-conjugated chitosan–PEG microparticles and stable conjugation of the capture DNAs with the chitosan–PEG particles. Bright-field micrographs (a-c) of three types of microparticles. Fluorescence micrographs (d-f) upon hybridization with fluorescently labeled target ssDNAs (1 μM) which are complementary to each type of particles. Bright-field (g-i) and fluorescence micrographs (j-l) of the particles hybridized with the target DNAs after three month storage in 5×SSC buffer containing 0.05% Tween 20. Scale bars represent 200 μm.

A1.4 Sequence-specific Assembly of TMV with Chitosan–PEG Microparticles

The results shown in Figure A1.4 indicate that the TMV assembly with chitosan–PEG microparticles is achieved by sequence-specific binding via nucleic acid hybridization. For this, the chitosan–PEG microparticles (30% PEGDA and 1%

chitosan) were fully activated or un-activated with missing components; (a) with ADIBO-activation, capture azide–DNA conjugation and linker DNA hybridization, (b) without ADIBO-activation, capture azide–DNA and linker DNA, (c) without capture and linker DNA, and (d) without linker DNA. The particles were then incubated with fluorescently labeled TMVs (3 mg/mL) for overnight at 30 °C.

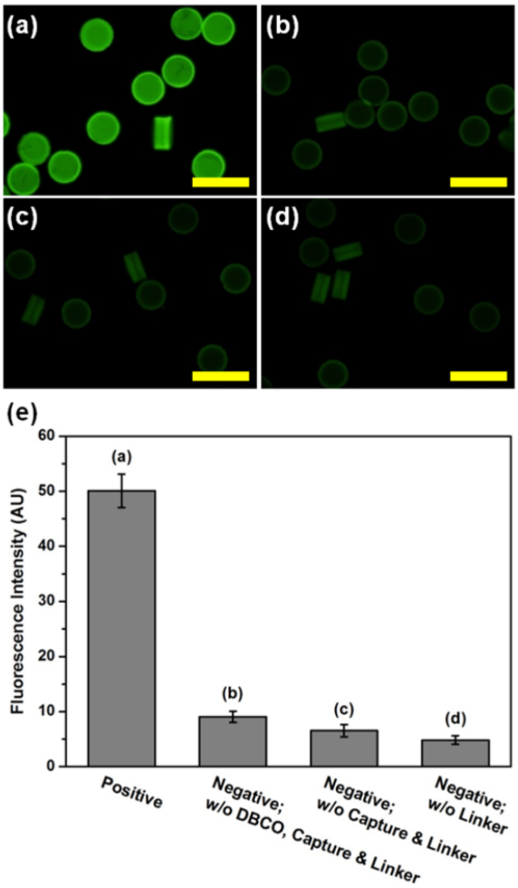

Figure A1.4. Fluorescence micrographs of the chitosan–PEG microparticles upon assembly with fluorescently labeled TMVs (3 mg/mL); (a) with ADIBO-activation, capture azide–DNA conjugation and linker DNA hybridization, (b) without ADIBO-activation, capture azide–DNA and linker DNA (c) without capture and linker DNA, and (d) without linker DNA. Scale bars represent 200 μm. (e) Average fluorescence intensities of the particles shown in (a-d). Error bars represent standard deviation from at least five particles.

The fluorescence micrograph in Figure A1.4a shows uniformly and consistently assembled fluorescent TMVs onto the particles. Meanwhile, all the negative control particles (Figure A1.4b-c) show negligible fluorescence. The significant difference in the fluorescence intensity between the positive and negative controls is also observed in the average fluorescence intensity analysis plot (Figure A1.4e). Combined, the results shown in Figure A1.4 confirm the selective nature of the SPAAC reaction as well as sequence-specific assembly of TMVs with the particles.

A1.5 A Confocal Micrograph of TMV-assembled Microparticles: Stable TMV Assembly on the Particle Surfaces

To demonstrate that TMVs are displayed on the microparticle surfaces via nucleic acid hybridization in a stable manner, the microparticles assembled with fluorescently labeled TMVs were characterized via confocal microscopy. For this, the capture DNA-conjugated chitosan–PEG particles were hybridized with linker DNAs (Table A1.1). The particles were then assembled with partially disassembled and fluorescently labeled TMVs via nucleic acid hybridization. Upon 3 times washing with 5×SSC buffer containing 0.05% Tween 20, the TMV-assembled microparticles were further stored in the buffer solution for one month until examination with Leica DMIRE2 microscope (Wetzlar, Germany).

The confocal micrograph at the center plane of the TMV assembled particles (Figure A1.5) shows bright fluorescence near the particle surfaces, confirming that the TMVs are displayed on the particle surfaces. This result also indicates that TMVs are assembled on the particle surfaces in a stable manner since the confocal microscopy was conducted one month later upon TMV assembly and thorough washing.

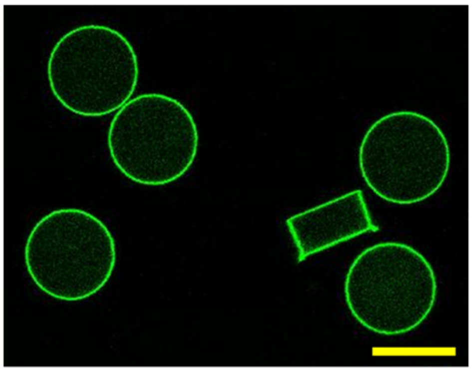

Figure A1.5. The confocal micrograph at the center plane of the chitosan–PEG microparticles upon assembly with fluorescently labeled TMVs (3 mg/mL). Scale bar represents 100 μm.

A1.6 Full Scan Area AFM Images of TMV-assembled Microparticles

The phase contrast AFM images of the entire scanned area in Figure A1.6e-g show densely assembled TMV on the chitosan–PEG microparticles with minimal non-specific binding via nucleic acid hybridization throughout the particles. For this, the chitosan–PEG microparticles (30% PEGDA and 1% chitosan) were activated (i.e. with ADIBO-activation, capture ssDNA conjugation and linker ssDNA hybridization) or missing one or more components (i.e. without ADIBO-activation, capture DNA and linker DNA). The activated particles were incubated with fluorescently labeled TMVs (3 mg/mL or 0.6

mg/mL) for overnight at 30 ^{o}C, and the negative control particles were incubated with 3 mg/mL of fluorescent TMVs for overnight at 30 ^{o}C. Before AFM imaging, the TMV-assembled particles were placed on a glass slide, and thoroughly washed with deionized water to remove salts in the buffer solution. The particles were then dried in a vacuum chamber at room temperature for 2 h.

The phase contrast AFM images of Figure A1.6a,b show different TMV coverage density resulting from TMV concentration, and the AFM image of negative control (Figure A1.6c) shows negligible non-specifically bound TMV. Therefore, the AFM results in Figure A1.6 illustrate that the TMVs are specifically bound onto the chitosan–PEG particles via nucleic acid hybridization with high surface coverage density over the entire scan area.

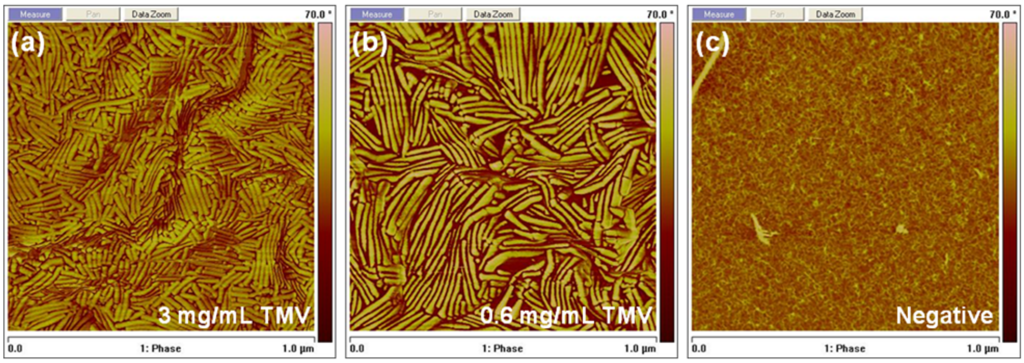

Figure A1.6. Full scan area AFM images of TMV-assembled microparticles. Phase contrast AFM images of the chitosan–PEG microparticles upon assembly with (a) 3 mg/mL of TMV and (b) 0.6 mg/mL of TMV. (c) Phase contrast AFM image of the particles without liker ssDNA upon TMV (3 mg/mL) assembly.

A1.7 Fluorescence Micrographs of TMV-assembled Microparticles: Controllable TMV Assembly

In Figure A1.7, I provide the fluorescence micrographs of the TMV-assembled chitosan–PEG microparticles utilized to construct the equilibrium binding plot in Figure 2.6h. For this, the chitosan–PEG microparticles (30% PEGDA and 1% chitosan) were activated (i.e. with ADIBO-activation, capture ssDNA conjugation and linker ssDNA hybridization), then incubated with various initial concentrations of TMV solution ranging from 0.06 mg/mL to 6 mg/mL overnight at 30 °C. The fluorescence images clearly show that the assembly is consistent and reproducible, as all microparticles show equivalent and relatively uniform fluorescence, as further indicated by the consistently small error bars in Figure 2.6h. Furthermore, the fluorescence images illustrate that the TMV assembly is controllable simply by varying the TMV concentration.

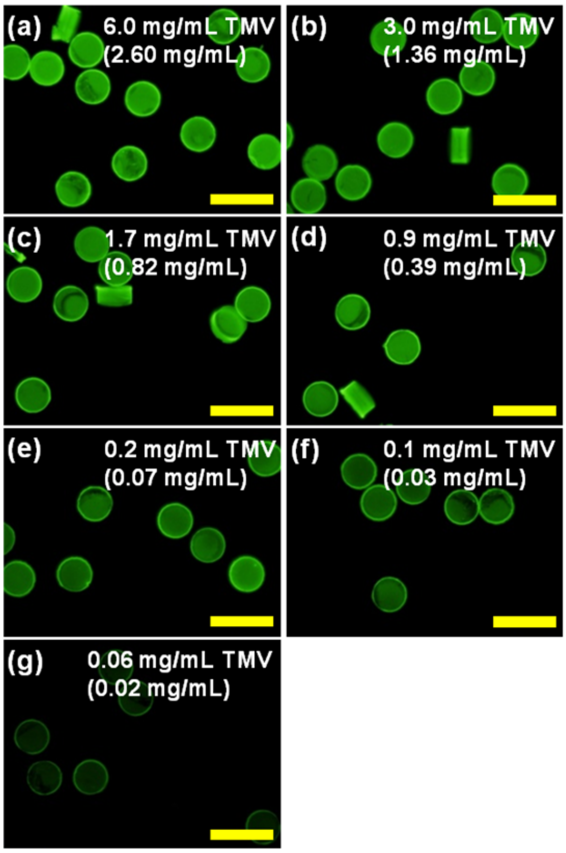

Figure A1.7. Fluorescence micrographs of the chitosan–PEG microparticles upon assembly with different concentrations of fluorescently labeled TMV; (a) 6 mg/mL (2.60 mg/mL), (b) 3 mg/mL (1.36 mg/mL), (c) 1.7 mg/mL (0.82 mg/mL), (d) 0.9 mg/mL (0.39 mg/mL), (e) 0.2 mg/mL (0.07 mg/mL), (f) 0.1 mg/mL (0.03 mg/mL) and (g) 0.06 mg/mL (0.02 mg/mL). The concentrations in the parentheses represent TMV concentrations at equilibrium. Scale bars represent 200 μm.

A2 Protein Conjugation with Chitosan-incorporated Hydrogel Microparticles via Strain-promoted Alkyne–Azide Cycloaddition (SPAAC) Reaction

A2.1 Specific Conjugation of R-PEs with Chitosan–PEG Microparticles via SPAAC Reaction

To further confirm specific conjugation of the R-Phycoerythrin (R-PE) with chitosan–PEG microparticles via strain-promoted alkyne–azide cycloaddition (SPAAC) reaction in addition to what is shown in Figure 3.2c,f (i.e. with and without azadibenzocyclooctyne (ADIBO) activation respectively), I conducted a negative control experiment where the azide molecule for SPAAC reaction was omitted. For this, I first prepared ADIBO-activated chitosan-poly (ethylene glycol) (PEG) particles, and the as-prepared particles were incubated with 4 μM of azide-activated R-PEs and non-azide-activated R-PEs for 24 h as the positive and negative control respectively.

As shown in Figure A2.1 above, bright and uniform fluorescence (fluorescence intensity, FI 76.05±2.39) is observed on the positive control particles (Figure A2.1a), while the fluorescence image for negative control particles (i.e. the ADIBO-activated particles upon incubation with non-azide-activated R-PEs, Figure A2.1b) shows negligible fluorescence (FI 10.34±2.21). This result indicates that the fluorescence on the particles shown in Figure 3.2c result from specific conjugation of R-PEs through SPAAC reaction with minimal nonspecific binding.

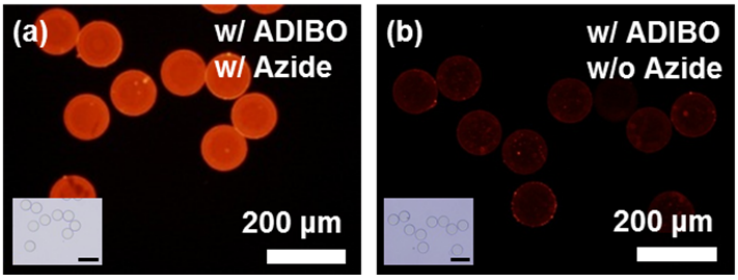

Figure A2.1. Fluorescence images of ADIBO-activated chitosan–PEG microparticles upon incubation with (a) azide-activated R-PEs and (b) non-azide-activated R-PEs. Insets are bright-field images corresponding to the fluorescence images.

A2.2 Fitting Curves of Fluorescence Intensity Plot; Uncompleted Conjugation Reaction

As shown in Figure A2.2, I attempted to fit the fluorescence data shown in Figure 3.4 to two different equations. For this, I utilized a nonlinear regression method (Figure A2.2a, OriginPro 8, OriginLab Corporation, Northampton, MA), and a Langmuir isotherm-type saturation model (Figure A2.2b). I assume that the azide-activated R-PEs are in excess of the ADIBO molecules bound to the particles in a reaction mixture, and the concentration of the R-PE remains constant in a batch system during the reaction as indicated in the UV-vis absorbance study in Figure A2.4.

First, the fluorescence intensity plot in Figure A2.2 (solid circles) fits well with an equation (red-dash line in Figure A2.2a):

$$y = \alpha_1 e^{-\beta_1 x} + \alpha_2 e^{-\beta_2 x} + \alpha$$

where y represents fluorescence intensity on the particle, x represents the concentration of the R-PE in the reaction mixture, α_1 (-8.10 AU), α_2 (-41.88 AU), β_1 (2.75 μM^{-1}) and β_2 (0.32 μM^{-1}) represent fitting constants, and α (49.98 AU) represents the maximum fluorescence intensity. The fluorescence profile in Figure A2.2a (red-dash line) shows gradual increase in the fluorescence intensity with increasing R-PE concentration, suggesting that the protein–particle conjugation is not completed within 24 h for all concentrations examined here.

Next, I examined the data fitting for the fluorescence intensity to the Langmuir isotherm-type saturation model,

$$y = \frac{\alpha x}{(\beta + x)}$$

where α (56.82 AU) represents the maximum fluorescence value at saturation, and β (1.87 μM) represents a fitting constant similar to the dissociation constant of the Langmuir isotherm curve. For this, I transformed the fluorescence data with Hanes–Woolf plot, which tends to provide more accurate estimation of the maximum value (α) than the double-reciprocal (a.k.a. Lineweaver–Burk) plot or Eadie–Hofstee plot as follows[106]:

$$\frac{x}{y} = \frac{\beta}{\alpha} + \frac{1}{\alpha} x$$

The fluorescence data fit well with the Langmuir isotherm-type curve fitting (red-dash line in Figure A2.2b), yet do not appear to reach saturation (α=56.82 AU) within the 24 h reaction period for all concentrations examined here. While I initially hypothesized that 24 h reaction time should be sufficient to reach completion based on the reported rate constants of the SPAAC reaction,[202] the fluorescence data and their fitting curves (red-dash lines in Figure A2.2a,b) show gradually increasing fluorescence, suggesting mass transfer limited reaction as further described in Figure 3.5.

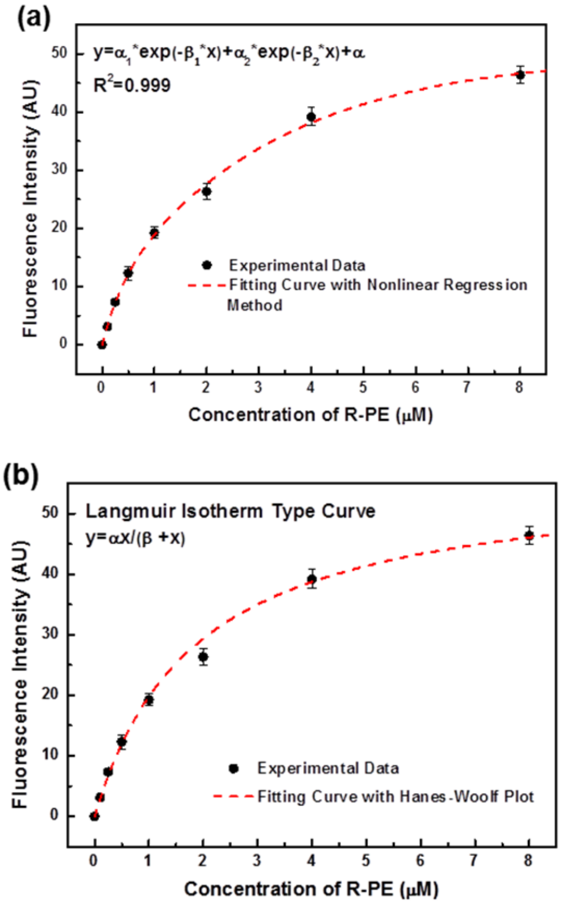

Figure A2.2. Fitting curves of fluorescence intensity plot shown in Figure 3.4 via (a) nonlinear regression method, and (b) Langmuir isotherm-type saturation model using Hanes–Woolf plot.

A2.3 Full Scan Area AFM Images of R-PE-conjugated Chitosan–PEG Microparticles; Physical Confirmation of Conjugated R-PEs

The AFM images shown in the Figure A2.3 provide further physical evidence of the uniformly conjugated R-PEs on the chitosan–PEG microparticles via SPAAC reaction. For this, a constant number of the ADIBO-activated chitosan–PEG microparticles (~200) were reacted with varying concentrations of the azide-activated R-PEs (0 to 4 μM) for 24 h. Before AFM imaging, the R-PE-conjugated particles were placed on a glass slide, thoroughly washed with deionized water to remove salts in the buffer solution, and dried in a vacuum chamber for 2 h. The dried R-PE-conjugated microparticles were then imaged with an atomic force microscope (Dimension 3100, Digital Instruments) in tapping mode.

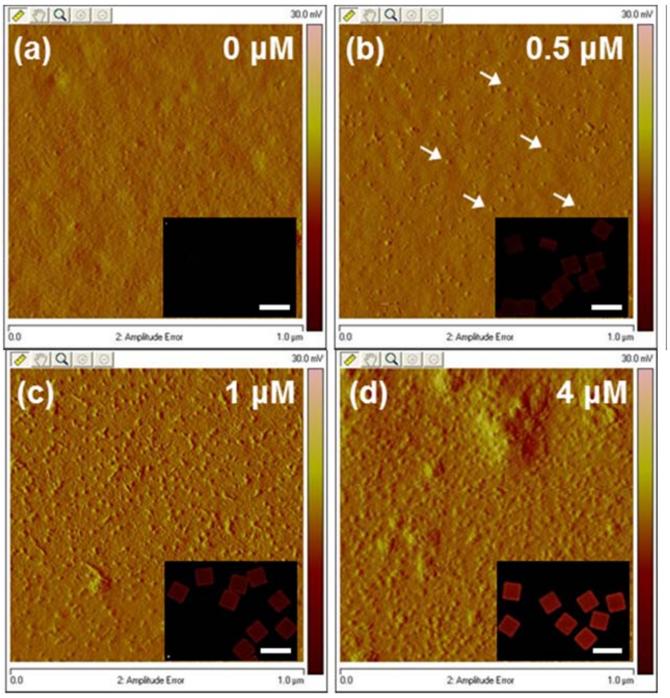

Figure A2.3. AFM images of chitosan–PEG microparticles (a) before reaction with R-PE, (b) upon reaction with 0.5 μM R-PE, (c) 1 μM R-PE, and (d) 4 μM R-PE. Insets are fluorescence micrographs corresponding to (a-d).

The AFM image of the ADIBO-activated microparticles before conjugation with the R-PEs (Figure A2.3a) shows a smooth surface, corresponding to the minimal fluorescence in the fluorescence micrograph (inset of Figure A2.3a). In contrast, circular dots with roughly 10 nm diameter (marked with small arrows in Figure A2.3b) are observed on the R-PE conjugated microparticles (Figure A2.3b-d), of which the surface coverage density increases with increasing R-PE concentration (roughly 212/μm^2, 528/μm^2, and 616/μm^2 at 0.5 μM, 1 μM, and 4 μM respectively), consistent with the fluorescence results shown in the insets of Figure A2.3b-d. Consistent with the reported size of the R-PE (5.54 nm radius),[133] these results indicate that the small dots on the microparticle are the conjugated R-PEs.

A2.4 Constant Concentration of Azide-activated R-PE in Reaction Medium during SPAAC Reaction

To confirm that 4 μM azide-activated R-PE remains constant during the SPAAC reaction, I examined the reaction medium before and after the reaction via UV-vis spectrophotometry, as shown in Figure A2.4. For this, azide-activated R-PE solution at 4 μM final concentration was added into the reaction medium containing a constant number of the ADIBO-activated chitosan–PEG microparticles (~200), and the UV-vis spectra were recorded right upon mixing and upon 24 h reaction with Evolution^{TM} 300 UV-vis Spectrophotometer (Thermo scientific, Waltham, MA). As shown in Figure A2.4, the spectra of the reaction medium before and after reaction (black and red line respectively) show characteristic absorbance peaks for the R-PE (absorption maxima at 498, 538, and 565 nm)[131] and negligible difference in the absorption intensity, indicating constant concentration of the R-PE throughout the reaction. Therefore, I can treat the conjugation reaction between 4 µM R-PE and the ADIBO-activated microparticles via SPAAC reaction as a pseudo-first order batch reaction, as further described in Section A2.5 and Figure 3.5.

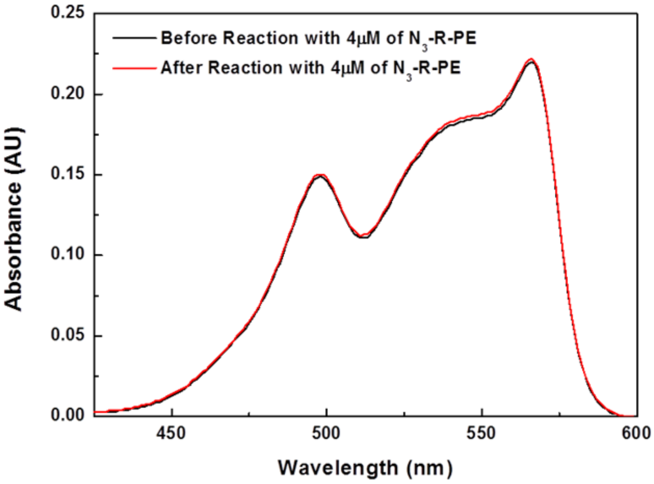

Figure A2.4. UV-vis spectra of reaction medium containing 4 µM of azide-activated R-PE right upon mixing with particles (black line) and upon 24 h reaction (red line).

A2.5 Pseudo-first Order Reaction Model

To evaluate the kinetics of the protein–particle conjugation via SPAAC reaction as shown in Figure 3.5, I utilized the pseudo-first order batch reaction model. I first considered SPAAC reaction between the azide-activated R-PEs (reactant A) and the ADIBO molecules bound to the particle (reactant $*$) as the second-order reaction[202-204] as follows:

$$\frac{\mathrm{d}[\mathrm{A}*]}{\mathrm{dt}} = k_{app}[\mathrm{A}][*]$$

where k_{app} ($M^{-1}s^{-1}$) represents the apparent second-order rate constant, t represents reaction time, [A] represents the concentration of the azide-activated R-PEs in the reaction mixture, $[*]$ represents surface concentration of the ADIBO molecules bound to the particles, and $[\mathrm{A}*]$ represents concentration of the conjugated R-PEs on the particles. When the azide-activated R-PE (reactant A) is present in excess and its concentration remains constant until the completion of the reaction in a batch system (i.e. $[\mathrm{A}]_0 \gg [*]_0$, and $[\mathrm{A}] \approx [\mathrm{A}]_0 \approx$ constant where $[\mathrm{A}]_0$ and $[*]_0$ represent initial concentrations of A and surface concentration of $*$ respectively), the rate constant of the ADIBO molecule bound to the particles (reactant $*$) and reacting with the azide-activated R-PEs in the SPAAC reaction can be determined from the pseudo-first order batch reaction:

$$\frac{\mathrm{d}[\mathrm{A}*]}{\mathrm{dt}} = k'_{app}[*], \qquad k'_{app} = k_{app}[\mathrm{A}]_0$$

where k'_{app} (s^{-1}) represents the apparent pseudo-first order rate constant. With the relationships $[*] = [\mathrm{A}*]_{\max} - [\mathrm{A}*]$ fluorescence intensity (FI) $\propto [\mathrm{A}*]$, and normalization of the fluorescence intensity with the maximum fluorescence intensity (50.51 AU, obtained from the fitting curve of fluorescence intensity plot shown in Figure 3.5g), the above equation is solved as follows:

$$-\ln(1-\theta) = k'_{app}\mathrm{t}$$

where θ represents normalized fluorescence intensity, and this relationship is plotted in the manuscript (Figure 3.5k)

A2.6 The Second-order Rate Constant of SPAAC Reaction between ADIBO and Azide Molecules in Bulk Solution

As shown in Figure A2.5, I determined the pseudo-first order rate constant to the ADIBO molecule in the SPAAC reaction between the ADIBO (ADIBO–*sulfo*–NHS, MW 532.5 Da) and the short chain PEG derivative of azide (NHS–PEG_{12}–Azide, MW 740.8 Da) in the presence of excess azide in a bulk batch reaction system. In other words, the SPAAC reaction is reported to follow second order reaction (first order to the ADIBO molecule (reactant A) and first order to the azide molecule (reactant B)) as follows[202-204]:

$$-\frac{\mathrm{d[A]}}{\mathrm{dt}} = \mathrm{k[A][B]}$$

where $\mathrm{k}\,(\mathrm{M^{-1}s^{-1}})$ represents the second-order rate constant, and $\mathrm{[A]}$ and $\mathrm{[B]}$ represent concentration of reactant A (ADIBO) and B (azide), respectively. When one reactant is present in excess and its concentration remains constant until the completion of the reaction in a batch system (i.e. $\mathrm{[B]_0} \gg \mathrm{[A]_0}$ and $\mathrm{[B]} \approx \mathrm{[B]_0} \approx \mathrm{constant}$, where $\mathrm{[A]_0}$ and $\mathrm{[B]_0}$ represent initial concentration of A and B, respectively), the rate constant of the other reactant can be determined as the pseudo-first order rate constant as follows:

$$-\frac{\mathrm{d[A]}}{\mathrm{dt}} = \mathrm{k'[A]}, \qquad \mathrm{k'} = \mathrm{k[B]_0}$$

where $\mathrm{k'}(\mathrm{s^{-1}})$ represents the pseudo-first order rate constant.

For this, I reacted excess azide molecules (reactant B, 202.5, 405.0, 607.5, 810.0, and 1012.4 μM of NHS–PEG$_{12}$-Azide with MW 740.8 Da) with ADIBO molecules (reactant A, 18.8 μM of ADIBO–*sulfo*–NHS with MW 532.5 Da) in an aqueous solution (10% (v/v) DMSO and 90% (v/v) 5×SSC buffer containing 0.05% (v/v) Tween 20) at room temperature. Even though the aqueous solution used in this experiment contains a small amount of organic solvent (DMSO) to dissolve A and B, I assume that the 90% water content should be sufficiently close to the aqueous condition used in the protein–microparticle conjugation reactions (as in Figure 3.2-3.5).

Before monitoring the SPAAC reaction with the UV-vis spectrometry, I first investigated characteristic peaks of UV spectra for the reactant A (18.8 μM, Figure A2.5a) and B (202.5 μM, Figure A2.5b) in aqueous solution. First, a broad absorbance peak in the wavelength range of 250 nm to 280 nm in both Figure A2.5a,b is observed, and increases with time. This increasing absorbance indicates hydrolysis of *N*-hydroxysuccinimide (NHS) ester group in both of the reactant A and B[205]. Meanwhile, the UV spectra of the reactant A (Figure A2.5a) show two distinguishable absorbance peaks at 290 nm and 309 nm, which are not observed in the UV spectra of the reactant B (Figure A2.5b). Thus, the two characteristic UV absorbance peaks at 290 nm and 309 nm indicate strain-promoted cyclooctyne in the reactant A[206], and I monitored the peak at 309 nm during the SPAAC reaction. As shown in Figure A2.5c, the absorbance at 309 nm decreases with time, indicating consumption of ADIBO molecules during the SPAAC reaction.

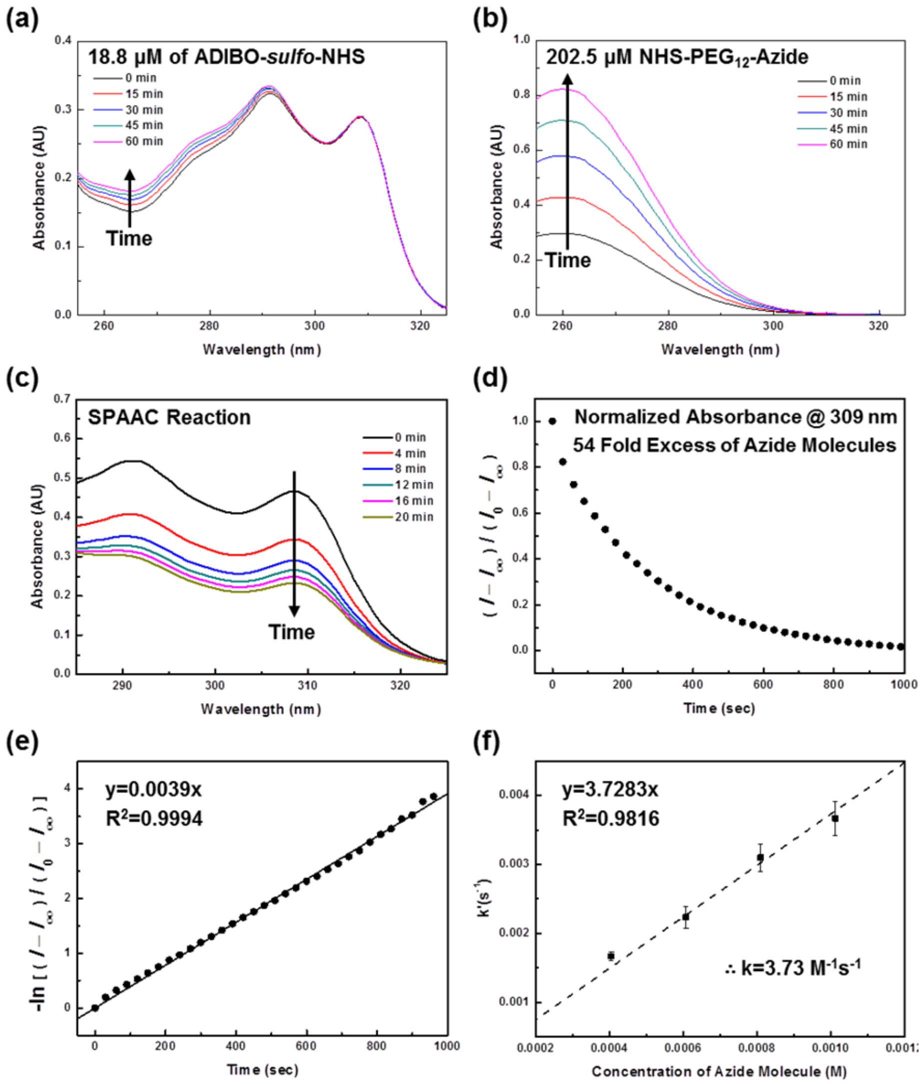

Figure A2.5. The second-order rate constant of SPAAC reaction between ADIBO and azide molecules in bulk solution. UV-vis spectra of (a) 18.8 μM of ADIBO–*sulfo*–NHS, (b) 202.5 μM of NHS–PEG$_{12}$–Azide in aqueous buffer solution, and (c) SPAAC reaction between 202.5 μM of NHS–PEG$_{12}$–Azide and 18.8 μM of ADIBO–*sulfo*–NHS at room temperature. (d) Plot of normalized absorbance at 309 nm during SPAAC reaction between 1012.4 μM of NHS–PEG$_{12}$–Azide and 18.8 μM of ADIBO–*sulfo*–NHS. (e) Logarithmic plot of the normalized absorbance plot shown in (d). The slope represents the pseudo-first order rate constant (k′). (f) Plot of the pseudo-first order rate constant with concentration of the azide molecule. Slope represents the second-order rate constant (k).

To analyze the rate of the SPAAC reaction, I first normalized the monitored absorbance at 309 nm as follows:

$$\text{Nomalized Absorbance at 309 nm} = \frac{\mathrm{I} - \mathrm{I}_\infty}{\mathrm{I}_0 - \mathrm{I}_\infty}$$

where I represents absorbance at specific time (t), I_0 represents absorbance at initial state of the reaction, and I_∞ represents absorbance upon completion of the reaction. Figure A2.5d shows a representative result of the normalized absorbance, showing consumption of ADIBO molecules during the reaction. These absorbance data were then fit into the pseudo-first order reaction model with a relationship that the concentration of the ADIBO molecules is proportional to the absorbance at 309 nm[137]:

$$-\ln\frac{[\mathrm{A}]}{[\mathrm{A}]_0} = -\ln\frac{\mathrm{I} - \mathrm{I}_\infty}{\mathrm{I}_0 - \mathrm{I}_\infty} = \mathrm{k}'\mathrm{t}$$

Figure A2.5e shows a representative result of the transformed data, which fit well with the pseudo-first order batch reaction model showing the pseudo-first order rate constant (k') as a slope. From the measured pseudo-first order rate constants of ADIBO with varying excess azide concentrations (405.0, 607.5, 810.0, and 1012.4 μM, Figure A2.5f), I calculated 3.73 $M^{-1}s^{-1}$ as the second-order rate constant for the SPAAC reaction in aqueous solution. In the meantime, the calculated second-order rate constant is much greater than a reported value (0.31 $M^{-1}s^{-1}$) measured in deuterated methanol (CD_3OD).[202] McNitt and Popik recently reported that presence of water in the reaction mixture for the SPAAC reaction using strain-promoted cyclooctynes significantly affects the reaction rate.[204] Specifically, the second-order rate constant increased with increasing water content in the reaction solvent mixture, and the reaction was ~10 fold faster in aqueous solution containing 95% water than in pure methanol, supporting the validity of my second-order rate constant obtained under the primarily aqueous reaction conditions relevant to the protein–microparticle conjugation in Chapter 3 (Figure 3.2-3.5) as well as to other protein conjugation reaction conditions in general. Another reported rate constant (0.36 $M^{-1}s^{-1}$) measured in deuterium oxide (D_2O)[202] is also much smaller than my observed rate constant (3.73 $M^{-1}s^{-1}$). I note that this difference may be due to different reaction conditions; the rate constant of 0.36 $M^{-1}s^{-1}$ was measured in D_2O with basic condition (specific pH not indicated in their study) in contrast to the neutral condition (pH 7.0) in my study. In summary, I obtained 3.73 $M^{-1}s^{-1}$ as the second-order rate constant for the SPAAC reaction between ADIBO and azide molecules under similar reaction conditions to the protein–microparticle conjugation via SPAAC reaction.

A2.7 Confocal Micrographs of R-PE-conjugated Chitosan–PEG Microparticles; Penetration Depth of R-PE

To analyze the penetration depth of the R-PEs into the microparticles during protein–microparticle conjugation, I conducted confocal microscopy for the R-PE-conjugated microparticles over time as shown in Figure A2.6. For this, a constant number of the ADIBO-activated microparticles (~200) were reacted with the azide-activated R-PEs at 4 μM concentration for 2 to 48 h. The R-PE-conjugated microparticles were then imaged at the center plane of the particles (i.e. the plane at 25-28 μm from the bottom of the approximately 55 μm height particles) with a confocal microscope (Leica DMIRE2, Wetzlar, Germany), and the penetration depths of the R-PEs were evaluated with an image analysis software (ImageJ, U. S. National Institutes of Health).[105]

All the confocal micrographs in Figure A2.6a-c show uniform and consistent fluorescence near the particle surfaces for all the particles examined regardless of the reaction time, suggesting evenly conjugated R-PEs on the particles. Furthermore, fluorescence intensity profiles across the R-PE conjugated regions near the particle surfaces (Figure A2.6d,e) show that the fluorescence intensity rapidly approach near saturation point in the first 2 h, while the increase in the fluorescence intensity is minimal upon 12 h reaction. In the meantime, the fluorescence profiles slightly broaden with increasing conjugation time. These results imply that most of the reactive conjugation sites near the particle surfaces are rapidly consumed, and that un-conjugated R-PEs diffuse into the polymer network with as-conjugated R-PEs to find reactive sites. Next, the penetration depth analysis results show that the penetration depth of the R-PEs slightly increases from 2.47 μm ± 0.27 (Figure A2.6a) to 3.10 μm ± 0.24 (Figure A2.6b) between 2 h and 12 h reaction, and that difference in the penetration depth is minimal between 12 h (3.10 μm ± 0.24, Figure A2.6b) and 48 h reaction (3.09 μm ± 0.22, Figure A2.6c) consistent with fluorescence profile results (Figure A2.6d,e). These results further suggest that the R-PEs are rapidly conjugated near the particle surfaces within a few hours (Figure A2.6a), then penetrate into the polymer network of the particles to find reactive sites and to be conjugated (Figure A2.6b), followed by saturation (Figure A2.6c). I thus hypothesize that diffusion limitation of the R-PEs into polymer networks of the particles resulting from steric hindrance by the already-conjugated R-PEs[136] as well as small mesh size of the polymer networks (1-3 nm)[24, 123] slows the conjugation rate after the rapid initial conjugation.

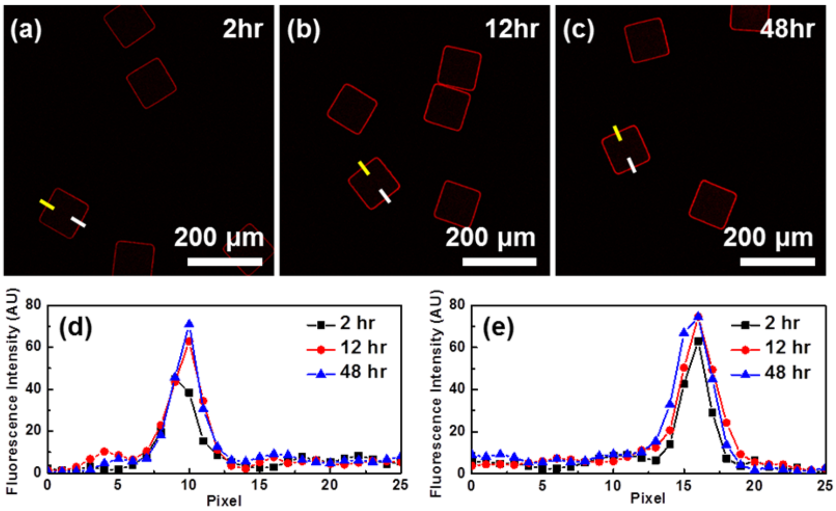

Figure A2.6. Confocal micrographs at the center plane of R-PE-conjugated particles upon (a) 2 h, (b) 12 h, and (c) 48 h reaction with 4 μM R-PE. Representative fluorescence intensity profiles across R-PE conjugated regions indicated by (d) yellow and (e) white lines in the confocal micrographs.

A3 Enhanced Protein Conjugation with Viral Nanotemplates assembled on Hydrogel Microparticles

A3.1 Negligible Nonspecific Binding of Proteins on Particle Platforms

As shown in Figure A3.1, I carried out four different negative control experiments in order to confirm that the fluorescence on the particles in Figure 4.3 results from specific R-PE conjugation via tetrazine (Tz)–*trans*-cyclooctene (TCO) cycloaddition reaction. Specifically, I first prepared TMV-assembled particles (TMV-particles) with or without TCO, chitosan–PEG particles (CS-particles), and capture DNA-conjugated CS-particles. The TMV-particles without TCO were then incubated with Tz-activated R-PEs (top row in Figure A3.1a), and those with TCO were incubated with R-PEs without Tz (top row in Figure A3.1b). Next, the CS-particles and the capture DNA-conjugated CS-particles were incubated with the Tz-activated R-PEs (top row in Figure A3.1c,d). For all cases, roughly 200 particles were incubated with 2 μM of R-PEs for 2 h at room temperature, which is the identical conjugation condition with that used in Figure 4.3. The particles were then imaged with a fluorescence microscope under the identical imaging condition as in Figure 4.3c,g (i.e. 50 ms of exposure time). The fluorescence images of the TMV-particles and the capture DNA-conjugated particles (bottom row in Figure A3.1a,b and d) clearly show minimal fluorescence, indicating that the bright fluorescence of the TMV particles in Figure 4.3c is due to specific R-PE conjugation through the Tz–TCO cycloaddition reaction with minimal non-specific binding. In addition, the fluorescence image of the CS-particles (bottom row in Figure A3.1c) clearly shows minimal fluorescence, confirming that the observed fluorescence of the CS-particles in Figure 4.3g results from specific conjugation of the R-PEs via the Tz–TCO cycloaddition reaction.

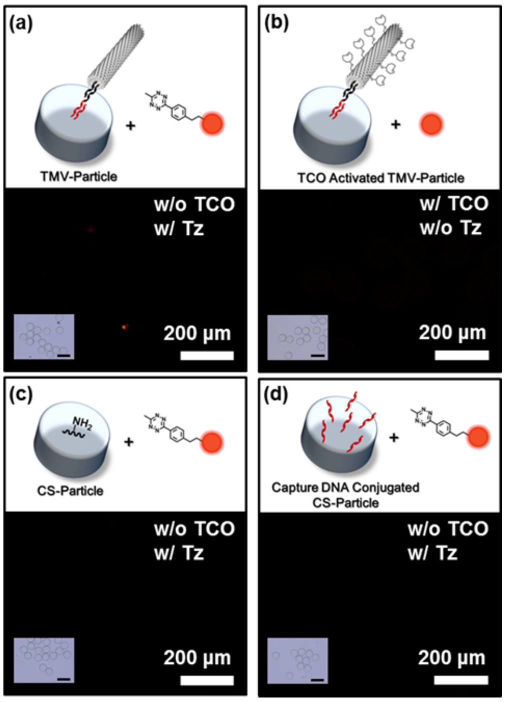

Figure A3.1. Fluorescence micrographs of negative controls; (a) TMV-particles without TCO upon incubation with Tz-activated R-PEs, (b) TCO-activated TMV-particles upon incubation with R-PEs without Tz, (c) CS-particles upon incubation with Tz-activated R-PEs, and (d) capture DNA-conjugated CS-particles upon incubation with Tz-activated R-PEs. Insets are bright-field micrographs corresponding to each fluorescence micrograph. All fluorescence micrographs were imaged at 50 ms exposure time.

A3.2 Linear Correlation between Fluorescence Intensity and Exposure Time

As shown in Figure A3.2, I examined average fluorescence intensity of R-PE conjugated TMV-particles at varying exposure times in order to estimate the fluorescence intensity from longer exposure time where pixel saturation was observed (e.g. Figure 4.3e; FI=183±0 at 50 ms). For this, the R-PE conjugated TMV-particles, prepared under identical fabrication and conjugation conditions as used in Figure 4.3, were imaged with a fluorescence microscope at varying exposure times ranging from 0.83 ms to 100 ms. The average fluorescence intensity for at least 7 particles at each exposure time was then plotted as shown in Figure A3.2 (solid-circles).

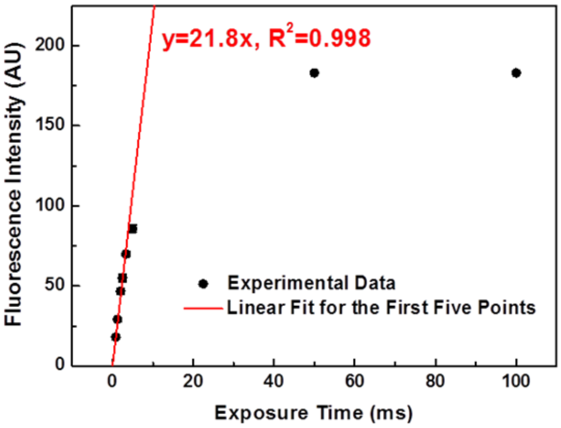

Figure A3.2. Average fluorescence intensity plot of the R-PE conjugated TMV-particles with varying exposure times. The red-line represents linear fit for the first five data points.

The result demonstrates that the fluorescence intensity linearly increases with increasing exposure time, then deviates from the linearity approaching limited maximum fluorescence intensity (i.e. FI=183) due to pixel saturation of the digital microscope camera (Olympus DP70). A calibration curve (red-line in Figure A3.2) obtained upon linear fitting for the first five points shows that the fluorescence intensity linearly increases with increasing exposure time in the range up to FI=70 with very high coefficient of variation (R^2=0.998). This linear correlation between the exposure time and the fluorescence intensity (up to FI=70) is also confirmed over longer exposure time ranges (i.e. 25-125 ms) with R-PE conjugated CS-particles (data not shown). These results indicate that the fluorescence intensity of the R-PE conjugated TMV-particles at longer exposure time (e.g. 50 ms) can be estimated by imaging with shorter exposure time where the measured fluorescence intensity is within a linear range (FI≤70) under the equipment (i.e. Olympus BX51 with DP70 digital camera) and imaging setup used in my study. Thus, the fluorescence intensity of the R-PE conjugated TMV-particles shown in Figure 4.3c at 50 ms exposure time is estimated to be 1060±24.

A3.3 Protein Conjugation with Planar Substrates

As shown in Figure A3.3, I examined R-PE conjugated planar substrates to compare their R-PE conjugation capacity with that of the TMV- and CS-particles. For this, I first prepared TCO-activated glass substrates from amine-functionalized glass substrates (Erie Scientific Company, Portsmouth, NH). Specifically, the amine-glass substrate was washed with acetone, methanol and DI water, and dried with ultrapure nitrogen gas. The cleaned amine-glass substrate was then activated with TCO molecules via amine-reactive chemistry. Specifically, the amine-glass substrate was incubated with a 1 μL drop of 500 μM TCO–PEG$_4$–NHS ester in 5×SSC buffer with 0.05% Tween 20 for 1 h in a humidified petri dish at room temperature, and thoroughly washed with methanol and DI water. Next, the TCO-glass substrate was incubated with a 1 μL drop of 2 μM Tz-activated R-PE in 5×SSC buffer with 0.05% Tween 20 for 2 h in the humidified petri dish at room temperature, in order to conjugate the R-PEs via Tz–TCO cycloaddition reaction. The R-PE conjugated glass substrate was imaged with a fluorescence microscope in 5×SSC buffer at 1 s exposure time. Atomic force microscopy (AFM) was also carried out for the R-PE conjugated glass substrates; 1 μm^2 of the R-PE conjugated glass substrate was imaged with an atomic force microscope (Dimension 3100, Digital Instruments, Santa Barbara, CA) in tapping mode (1.0 Hz scan rate for 512 lines). The fluorescence and AFM images were then analyzed with an image analysis software (ImageJ, U. S. National Institutes of Health).[105]

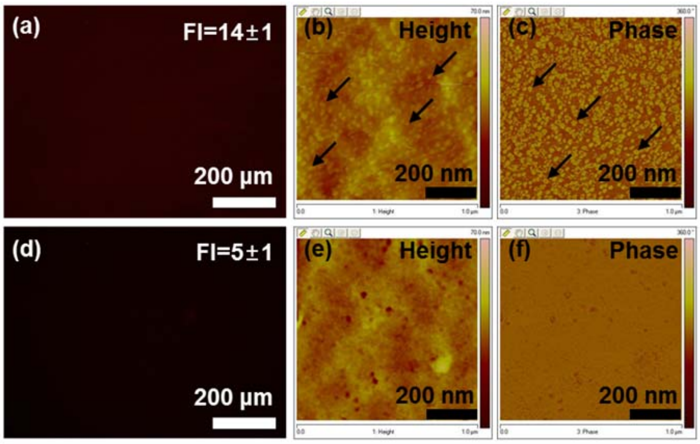

(g)	TMV-Particle	CS-Particle	Glass
Fluorescence Intensity at Exp.=1s (AU)	21200[a]	400[a]	9[b]

[a] Estimated fluorescence intensity from linear correlation between fluorescence intensity and exposure time.

[b] Measured fluorescence intensity upon background subtraction (i.e. (a)-(d)).

Figure A3.3. Protein conjugation with planar substrates. Fluorescence (a) and AFM images (b,c) of the R-PE conjugated planar substrates. Fluorescence (d) and AFM images (e,f) of the cleaned amine-glass substrates. (g) Summary of fluorescence intensities of the R-PE conjugated TMV-particles, CS-particles, and planar substrates at 1 s exposure time.

The fluorescence micrograph of the R-PE conjugated glass substrate shows red fluorescence (Figure A3.3a) in contrast to the amine-glass substrate without TCO-activation (Figure A3.3d). In addition, circular dots with 19.6±2.6 nm diameter are observed on the TCO-glass substrate as shown in height and phase contrast AFM images (small arrows in Figure A3.3b,c) with high density, while those dots are not observed on the amine-glass substrate (Figure A3.3e,f). Taking into account artifacts of AFM on solid substrates (i.e. overestimated width),[124] these circular dots are considered as the R-PEs (11.1 nm diameter).[133] Combined, the results shown in Figure A3.3a-f confirm that the red fluorescence on the TCO-glass substrate results from the conjugated R-PEs.

To quantitatively compare the R-PE conjugation capacity of the planar substrates (i.e. the TCO-glass) with that of the TMV- and CS-particles, I next estimated fluorescence intensity of the R-PE conjugated TMV- and CS-particles at 1 s exposure time with the linear correlation between fluorescence intensity and exposure time shown in Figure A3.2. To offset auto-fluorescence from the glass substrate itself at 1 s exposure time, I subtracted the fluorescence intensity of the amine-glass substrate (FI=5, Figure A3.3d) from the measured fluorescence intensity of the R-PE conjugated glass substrate (FI=14, Figure A3.3a). The estimated and measured fluorescence intensity values are listed in Figure A3.3g. The results show that the CS-particles are roughly 44-fold brighter than the planar substrates. I attribute this enhancement in R-PE conjugation to multilayer conjugation of the R-PE with the 3D network structure of the CS-particles (3 μm thickness of the conjugated R-PE layer near the particle surfaces).[27]

Furthermore, the results show that the TMV-particles are roughly 2400-times brighter than the planar substrates. I attribute this substantial enhancement in R-PE conjugation to the TMV templates along with the 3D network structure of the CS-particles. I further discuss this substantially enhanced R-PE conjugation capacity with the TMV-particles in Figure 4.3, A3.4, and A3.5.

A3.4 Estimation of Maximum Number of Proteins Conjugated on a TMV Template

To compare R-PE conjugation capacity of TMV-particles with surface-monolayered R-PEs, I first estimate maximum number of R-PEs conjugated on a TMV template via Tz–TCO cycloaddition reaction through cysteine residues genetically displayed near the outer surface of each TMV coat protein,[86] as shown in Figure A3.4. Specifically, I draw an imaginary cylinder (bold dashed line) consisting of the TMV rod (diameter D=18 nm and length L=300 nm)[83] fully coated with a layer of R-PE (diameter d=11 nm)[133] with its diameter 29 nm corresponding to the sum of those of the TMV and R-PE diameter.

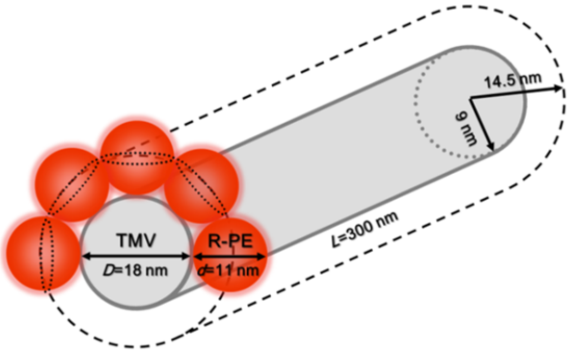

Figure A3.4. Schematic diagram of the R-PE conjugated TMV template.

The area of the imaginary cylinder is:

$$A_{\mathrm{TMV}'} = \pi(D + d) \times L$$

The cross-sectional area of the R-PE is:

$$A_{\mathrm{R-PE}} = \frac{\pi}{4} d^2$$

The maximum number of R-PEs conjugated per the TMV ($n_{\mathrm{R-PE}}$) is then estimated to be:

$$n_{\mathrm{R-PE}} = \frac{A_{\mathrm{TMV}'}}{A_{\mathrm{R-PE}}} = \frac{\pi \times (18 + 11) \times 300}{\pi \times \frac{11^2}{4}} \approx 287$$

Next, I estimate maximum number of surface-monolayered R-PEs on 1 μm^2 planar surface (n_1), and maximum number of R-PEs conjugated on TMV templates (n_2) vertically oriented as a monolayer on 1 μm^2 surface, in order to evaluate enhancement in R-PE conjugation capacity.

The maximum number of the surface-monolayered R-PEs on the 1 μm^2 planar surface is:

$$n_1 = \frac{1000 \times 1000}{A_{\mathrm{R-PE}}} = \frac{1000 \times 1000}{\pi \times \frac{11^2}{4}} \approx 10522$$

The maximum number of the surface-monolayered TMVs taking into account spaces for the R-PE conjugation (i.e. 29 nm diameter of R-PE–TMV complexes) on the 1 μm^2 planar surface (N_{TMV}) is:

$$N_{\mathrm{TMV}} = \frac{1000 \times 1000}{\pi \times \frac{(D + d)^2}{4}} = \frac{1000 \times 1000}{\pi \times \frac{29^2}{4}} \approx 1513$$

The maximum number of R-PEs on the 1 μm^2 of surface-monolayered TMV is then:

$$n_2 = N_{\mathrm{TMV}} \times n_{\mathrm{R-PE}} \approx 434231$$

These estimated values show roughly 41-fold enhanced R-PE conjugation capacity (i.e. n_2/n_1) of TMV templates over surface monolayer of R-PEs. Compared with this estimation, ~2400-fold enhancement in R-PE conjugation capacity for the TMV-particles over the planar surfaces (Figure A3.3) suggests that TMVs are assembled as a multi-layer format near the TMV-particle surfaces (further examined in Figure A3.5).

A3.5 A Confocal Micrograph of R-PE Conjugated TMV-particles; Multilayer Assembly of TMVs with CS-particles

As shown in Figure A3.5, confocal microscopy was utilized to evaluate thickness of TMV layers near the surface of R-PE conjugated TMV-particles. For this, the R-PE conjugated TMV-particles prepared under the identical fabrication and conjugation conditions as in Figure 4.3 were imaged with a confocal microscope (Leica DMIRE2, Wetzlar, Germany). Specifically, the center plane of the particles (i.e. the plane at ~25 μm from the bottom of the particles, inset in Figure A3.5a) was imaged with a 20× objective at 543 nm excitation. The thickness of the R-PE conjugated TMV layers was then evaluated with ImageJ (U. S. National Institutes of Health).[105]

The confocal micrograph of the R-PE conjugated TMV-particles (Figure A3.5a) shows bright red rings near the circular particle surfaces, and thickness of the ring is 2.1±0.5 μm from fluorescence intensity profiles across the R-PE conjugated TMV-particles (1.5 μm/pixel resolution, Figure A3.5b). While the bright fluorescence may lead to artifacts (i.e. overestimated thickness), this result suggests that the TMVs can penetrate a few micrometers below the surface of chitosan–PEG hydrogel microparticles through their polymer networks allowing for a multilayer assembly of the TMVs near the particle surfaces.

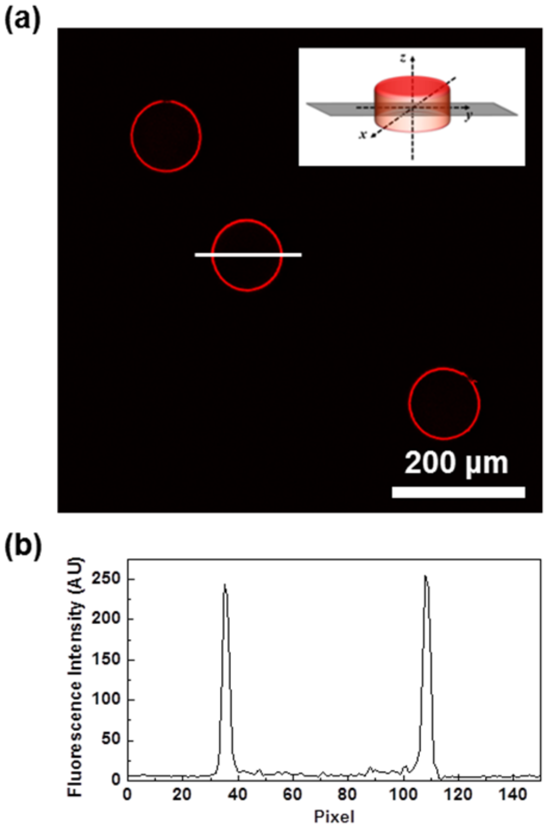

Figure A3.5. (a) Confocal micrograph at the center plane of the R-PE conjugated TMV-particles and (b) representative fluorescence intensity profile across the R-PE conjugated TMV-particle indicated by a white line in the confocal micrograph (a).

A3.6 Sequence Specific and Orientationally Controlled Assembly of TMVs with CS-particles

As shown in Figure A3.6, I demonstrate sequence-specific assembly of TMVs with CS-particles via nucleic acid hybridization in order to confirm orientationally controlled assembly at 5’-end of the TMVs. For this, I first fabricated capture DNA-conjugated CS-particles via strain-promoted alkyne–azide cycloaddition (SPAAC) reaction.[88] Specifically, shape-encoded CS-particles (circle, square and triangle) were activated with azadibenzocyclooctyne (ADIBO) molecules separately, and reacted with three different azide-modified capture DNAs overnight at room temperature (Table A3.1). Genetically modified TMVs (TMV1cys)[86] were activated with *trans*-cyclooctene (TCO) molecules (TCO–TMVs) via reaction with 10× molar excess of TCO–PEG$_3$–maleimide over cysteines displayed on the TMV surfaces for 2 h at room temperature. Fluorescently labeled TMVs (F–TMVs) were also prepared with the identical reaction conditions (i.e. 10× excess of fluorescein–maleimide for 2 h at room temperature). The TCO– and F–TMVs were then purified and partially disassembled to expose their 5’-end mRNA sequence by ultracentrifugation in a 10-40 wt% sucrose gradient at pH 7.5-8.0 with 48000g,[86] pelleted at 90000g and resuspended in 5×SSC buffer solution. The TMVs were then incubated with 10× excess of linker DNAs complementary to TMV mRNA’s 5’-end sequence and capture DNAs (Table A3.1) overnight at room temperature in order to “program” them for assembly with capture DNA-conjugated particles via DNA–DNA hybridization.[87] The excess linker DNAs were then separated via centrifugal filtration (Amicon Ultra 0.5, Waltham, MA). For the sequence-specific assembly, all three types of capture DNA-conjugated particles (i.e. circle, square and triangle) were mixed together in a microcentrifuge tube, and the TCO– and F–TMVs were added sequentially; the TCO–TMVs were incubated in the particle solution overnight at 30 ºC, then the F–TMVs were incubated overnight at 30 ºC following incubation with 2 μM tetrazine (Tz)-activated R-PEs for 2 h at room temperature. Upon thorough washing, the particles were imaged with a fluorescence microscope.

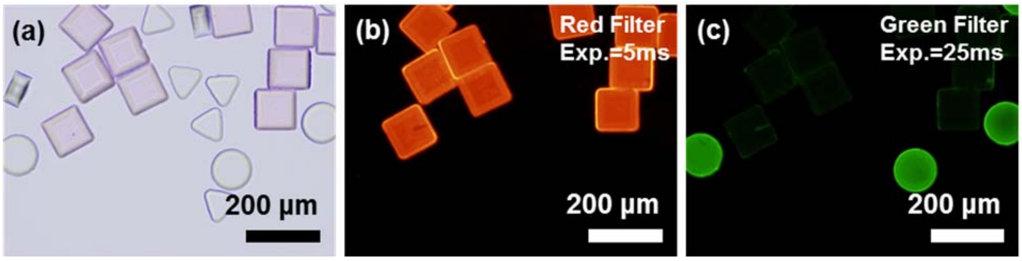

Figure A3.6. Sequence-specific assembly of TMVs with capture DNA-conjugated CS-particles. (a) A bright-field micrograph of all three types of capture DNA-conjugated CS-particles upon TMV assembly and R-PE conjugation. (b,c) Fluorescence micrographs of the particles shown in the bright-field micrograph with (b) a red filter set at 5 ms exposure time and (c) a green filter set at 25 ms exposure time.

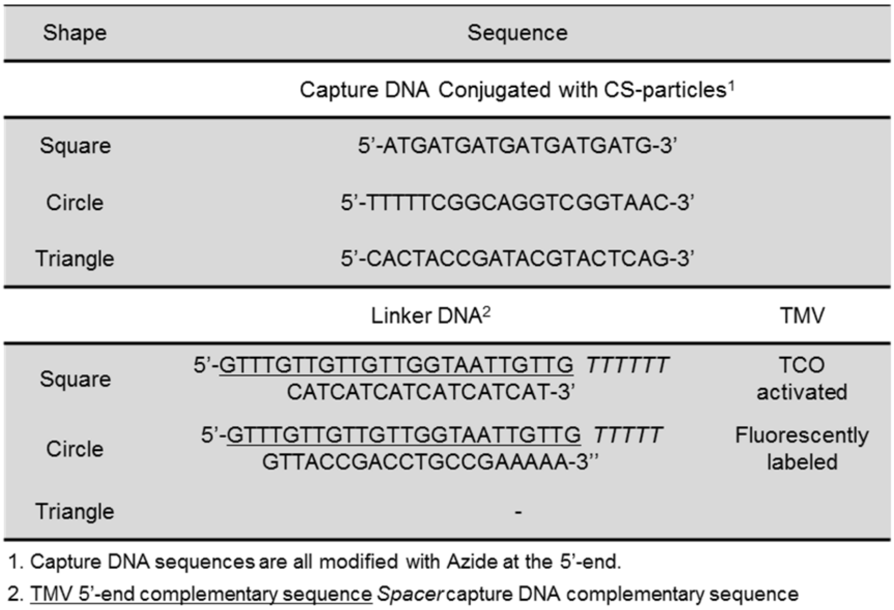

Shape	Sequence	
	Capture DNA Conjugated with CS-particles[1]	
Square	5’-ATGATGATGATGATGATG-3’	
Circle	5’-TTTTTCGGCAGGTCGGTAAC-3’	
Triangle	5’-CACTACCGATACGTACTCAG-3’	
	Linker DNA[2]	TMV
Square	5’-GTTTGTTGTTGTTGGTAATTGTTG *TTTTTT* CATCATCATCATCATCAT-3’	TCO activated
Circle	5’-GTTTGTTGTTGTTGGTAATTGTTG *TTTTT* GTTACCGACCTGCCGAAAAA-3’’	Fluorescently labeled
Triangle	-	

1. Capture DNA sequences are all modified with Azide at the 5’-end.
2. TMV 5’-end complementary sequence *Spacer* capture DNA complementary sequence

Table A3.1. List of capture and linker DNA sequences

First, the bright-field micrograph of the mixed particles (Figure A3.6a) shows well-defined and uniform particles with different shapes, confirming reliable fabrication of shape-encoded particles via replica molding.[12] Importantly, this image shows red color only on the square particles, similar to the result shown in Figure 4.3b. This result indicates selective conjugation of Tz-activated red-fluorescent R-PEs on the square particles with high density via Tz–TCO cycloaddition reaction; the reaction between the Tz-activated R-PEs and the TCO–TMVs that were assembled to the square particles via nucleic acid hybridization in a sequence-specific manner under a mild aqueous condition (Table A3.1). Next, the fluorescence micrograph with a red filter set (Figure A3.6b) shows bright red fluorescence on the square particles and negligible fluorescence on the circle and triangle particles, further confirming selective conjugation of the R-PEs along with sequence-specific assembly of the TCO–TMVs on the square particles. In addition, the fluorescence micrographs with a green filter set (Figure A3.6c) shows bright green fluorescence only on the circle particles containing complementary capture DNAs to the programmed F–TMVs (Table A3.1), further confirming the sequence-specific assembly of the TMVs. The sequence-specific assembly of the TMVs via nucleic acid hybridization takes place at the 5'-end of TMVs (i.e. orientationally controlled assembly of TMVs), and the TMV-assembled particles should have a brush-like structure. Meanwhile, the result for the sequence-specific assembly of chemically functionalized or activated TMVs (i.e. TCO–and F–TMVs) and selective conjugation of the R-PEs via Tz–TCO cycloaddition reaction suggests that the hybridization-based TMV assembly scheme along with an array of emerging bioorthogonal reactions (such as Tz–TCO cycloaddition and SPAAC reaction)[67, 161, 207] should enable simultaneous and high-throughput assembly of multifunctional TMV templates with multiple particle arrays in one pot. Also, mild reaction conditions of Tz–TCO cycloaddition[161] and SPAAC reaction[207] (i.e. physiological conditions without biologically toxic catalyst such as Cu(I)) can allow for preserving activity of labile biomolecules such as antibodies during conjugation. In short summary, the results in Figure A3.6 show sequence-specific assembly of chemically functionalized and fluorescently tagged TMVs, that further indicate orientationally controlled assembly at the 5'-end of the TMV, as well as suggest the potential for high-throughput one-pot assembly of multifunctional TMV templates toward multiplexed biosensing platforms.

A3.7 R-PE Conjugation Kinetics with TMV- and CS-particles via SPAAC Reaction; Rate of Increase in Fluorescence on the Particles

In order to directly compare R-PE conjugation rates between TMV- and CS-particles via SPAAC reaction, the raw fluorescence data shown in Figure 4.4b,c were analyzed without normalization for each platform as shown in Figure A3.7. Meanwhile, the R-PE conjugated TMV-particles showed pixel saturation at 0.1 s exposure time, identical imaging condition with the R-PE conjugated CS-particles (data not shown). To avoid this artifact, I estimated fluorescence intensity of the R-PE conjugated TMV-particles at 0.1 s exposure time by utilizing measured fluorescence intensity at 1.25 ms exposure time and linear correlation between fluorescence intensity and exposure time shown in Figure A3.2. The estimated fluorescence intensity was marked with an asterisk star in Figure A3.7.

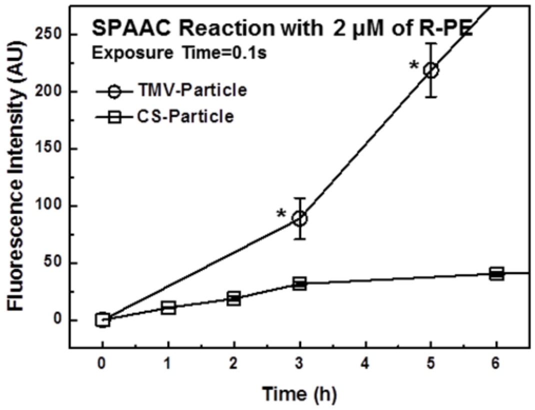

*Estimated fluorescence intensity at 0.1s exposure time from measured fluorescence intensity at 1.25ms exposure time

Figure A3.7. Average fluorescence intensity plots of TMV- and CS-particles upon conjugation with 2 μM R-PE via SPAAC reaction for varying times (0-6 h).

The average fluorescence intensity plot of the R-PE conjugated TMV-particles shows rapid increase in fluorescence (open circles in Figure A3.7) unlike that of the R-PE conjugated CS-particles (open squares in Figure A3.7). These results clearly indicate that R-PE conjugation with the TMV-particles via SPAAC reaction is faster than that with the CS-particles, suggesting more favorable environment of the TMV-particles for protein conjugation than the CS-particles.

A3.8 Fluorescence Micrographs of R-PE captured TMV-particles at Short Exposure Time

In order to quantitatively compare the R-PE capture on TMV- and CS-particles conjugated with anti-R-PE antibodies (R-Ab), I carried out imaging at short exposure times for the R-PE captured TMV-particles and utilized the linear correlation (Figure A3.2) to estimate fluorescence intensity at long exposure time, as shown in Figure A3.8.

Specifically, Figure A3.8a,b show that the fluorescence intensity of the R-Ab conjugated TMV-particles upon 3 h incubation with 1 and 10 nM R-PEs reach pixel saturation (i.e. FI>70) at 0.2 s exposure time under identical imaging condition with the R-PE captured CS-particles in Figure 4.5. In order to avoid artifacts from this pixel saturation (i.e. underestimated fluorescence), another batch of the R-PE captured TMV-particles was imaged at short exposure time (i.e. 50 and 20 ms exposure time at 1 and 10 nM R-PE respectively), where the measured fluorescence intensity values of these particles are below pixel saturation level; FI=26±3 at 1 nM R-PE (Figure A3.8c) and FI=60±6 at 10 nM R-PE (Figure A3.8d). Using the linear correlation, fluorescence intensity values of R-PE captured R-Ab TMV-particles at 0.2 s were estimated to be FI=105±12 and 601±64 at 1 and 10 nM R-PE respectively (Figure A3.8e). These values are then compared with measured values of the R-PE captured CS-particles in Figure 4.5, in order to compare capacity of target protein capture between the R-Ab conjugated TMV- and CS-particles.

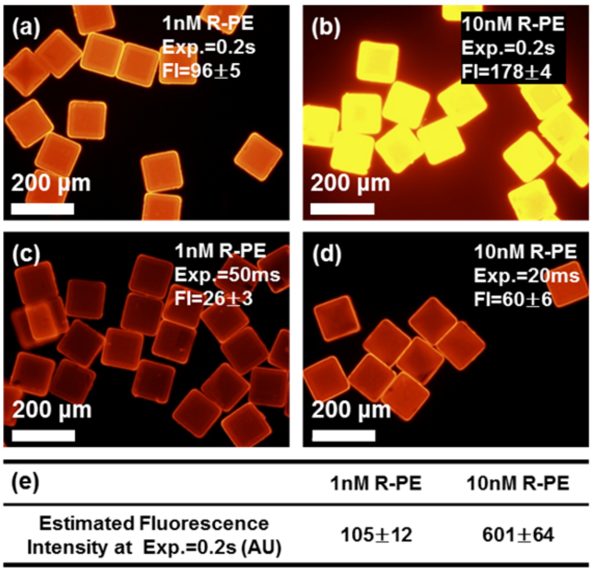

	1nM R-PE	10nM R-PE
Estimated Fluorescence Intensity at Exp.=0.2s (AU)	105±12	601±64

Figure A3.8. Fluorescence micrographs of the R-Ab conjugated TMV particles upon 3 h incubation with (a,c) 1 and (b,d) 10 nM R-PEs. The fluorescence micrographs were imaged at (a,b) 0.2 s or (c,d) 50 ms exposure time. (e) Summary of estimated fluorescence intensities of the R-PE captured TMV-particles at 0.2 s exposure time.

A3.9 Antibody–antigen Binding Kinetics with Antibody Conjugated TMV- and CS-particles

As shown in Figure A3.9, I carried out a study on antibody–antigen binding kinetics with R-Ab conjugated on TMV- and CS-particles for a 3 h period, similar to standard assay time for clinical applications.[53, 153] For this, the R-Ab conjugated TMV- and CS-particles were separately incubated in 1 and 10 nM R-PE solution for 0-3 h at room temperature. Upon thorough washing, R-PE captured TMV- and CS-particles were imaged with a fluorescence microscope at 0.1 s exposure time, and average fluorescence intensity for at least 8 particles was plotted as shown in Figure A3.9. Meanwhile, the R-PE captured TMV-particles at 10 nM R-PE showed pixel saturation under 0.1 s exposure time, leading to underestimated fluorescence intensity (data not shown). To avoid this artifact, I estimated fluorescence intensity at 0.1 s exposure time by utilizing measured fluorescence intensity at low exposure time (i.e. 25 ms) and linear correlation between fluorescence intensity and exposure time shown in Figure A3.2. The estimated fluorescence intensity was plotted, and marked with an asterisk star as shown in Figure A3.9a.

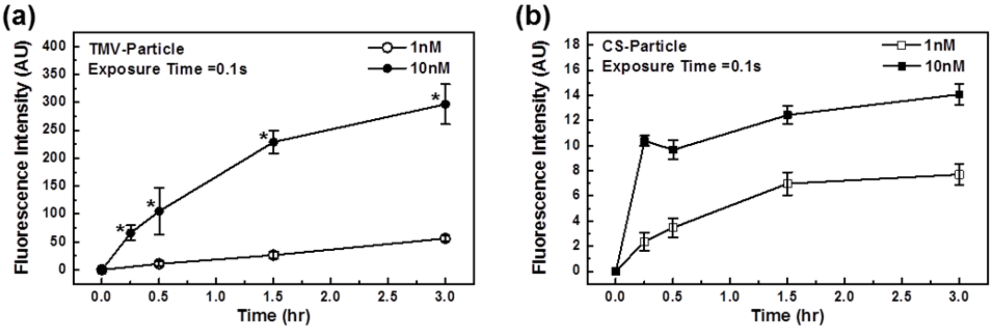

*Estimated fluorescence intensity at 0.1s exposure time from measured fluorescence intensity at 25ms exposure time

Figure A3.9. Average fluorescence intensity plots of (a) the R-Ab conjugated TMV- and (b) CS-particles upon incubation with 1 and 10 nM R-PEs for varying times (0-3 h).

The average fluorescence intensity plots of the R-PE captured TMV-particles at both 1 and 10 nM conditions (Figure A3.9a) show gradually increasing fluorescence with time during the 3 h period. These results suggest that 3 h incubation is not sufficient for reaching equilibrium R-PE binding on the R-Ab conjugated TMV-particles under low R-PE concentrations. In contrast, the fluorescence plots of the R-PE captured CS-particles at both 1 and 10 nM conditions (Figure A3.9b) show that the fluorescence intensity appears to reach saturation upon 3 h incubation (i.e. equilibrium binding of the R-PEs). A recent study on antibody-antigen binding kinetics with hydrogel platforms reported that considerably longer time is required to reach equilibrium of antigen binding on the hydrogel platforms with higher antibody conjugation capacity under low antigen concentration conditions (i.e. 5-20 nM).[28] Combined with this result, significantly enhanced antibody conjugation capacity of the R-Ab conjugated TMV-particles may require substantially longer time to reach equilibrium R-PE binding under 1 and 10 nM R-PE concentrations. Meanwhile, the results in Figure A3.9 show bright fluorescence upon binding of low concentration R-PE targets, indicating significantly enhanced R-PE capture capacity of the R-Ab conjugated TMV-particles upon 3 h incubation.

In short summary, the results in Figure A3.9 demonstrate that the R-Ab conjugated TMV-particles need longer incubation time to reach equilibrium R-PE binding under low R-PE concentrations, while the TMV-particles show considerably enhanced R-PE capture capacity compared to the CS-particles.

A3.10 Comparison of Total Number of Antibodies and Antigens in 100 μL Assay Volume

To compare the amount of anti-R-PE antibodies (R-Ab) with that of R-PEs in my 100 μL assay volume, I estimated total number of R-Abs conjugated with TMV-particles (Figure A3.10). For this, I first estimated the number of R-Ab conjugated TMV-templates on a CS-particle (Figure A3.10a) with an assumption that the R-Ab conjugated TMV templates are assembled as monolayers on all surfaces of the CS-particle.

The surface area of the CS-particle is:

$$A_{\mathrm{MP}} = [(W \times L) + (W \times H) + (L \times H)] \times 2 = 4 \times 10^{10}\ \mathrm{nm}^2$$

The maximum cross-sectional area of the R-Ab conjugated TMV (Figure A3.10b) is:

$$A_{\mathrm{TMV}'} = \frac{\pi}{4}(D + 2d)^2 \approx 1257\ \mathrm{nm}^2$$

The maximum number of the R-Ab conjugated TMVs assembled as a surface-monolayer on each CS-particle is then estimated to be:

$$n_{\mathrm{TMV/MP}} = \frac{A_{\mathrm{MP}}}{A_{\mathrm{TMV}'}} \approx 3.2 \times 10^7\ \text{molecules} \approx 5.3 \times 10^{-17}\ \text{moles}$$

In order to estimate total number of R-Abs in 100 μL assay volume, I next assumed that there exist 200 particles (n_{MP}=200) in 100 μL assay volume, and that 200 R-Abs are conjugated with each TMV template ($n_{\mathrm{R-Ab/TMV}}$=200).

Total number of R-Abs in 100 μL assay volume is then estimated to be:

$$n_{\mathrm{R-Ab}} = n_{\mathrm{MP}} \times n_{\mathrm{TMV/MP}} \times n_{\mathrm{R-Ab/TMV}} = 200 \times 5.3 \times 10^{-17} \times 200$$

$$\approx 2 \times 10^{-12}\ \text{moles}$$

Meanwhile, this estimated number of R-Abs should be lower than the actual value due to the assumption that TMVs are assembled as monolayers on the CS-particles. As discussed in Figure 4.3, several-fold more TMVs appear to be assembled as a multilayer. Thus, the total number of R-Abs should be larger than 2×10^{-12} moles in 100 μL assay volume.

Calculated numbers of 1 and 10 nM R-PEs in 100 μL assay volume are 10^{-13} and 10^{-12} moles respectively. Compared with these values of the R-PE, there should exist at least equivalent or one order of magnitude larger number of R-Abs conjugated with TMV-particles in 100 μL assay volume.

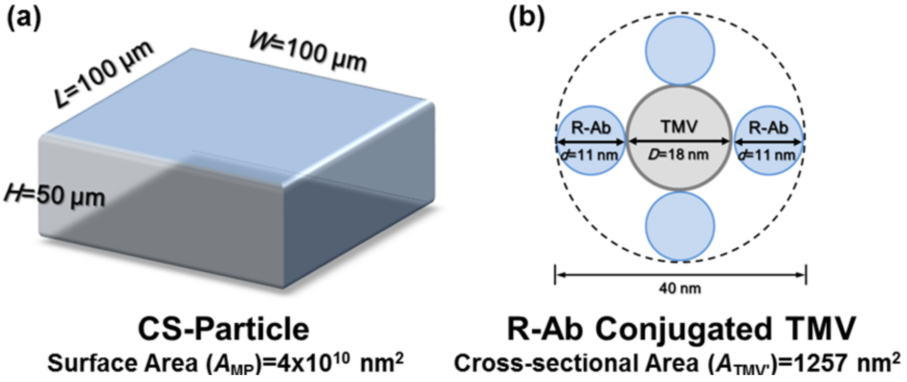

Figure A3.10. Schematic diagrams of (a) CS-particles with dimensions and (b) the maximum cross-section of the R-Ab conjugated TMV template.

A4 Micromolding-based Fabrication of Chitosan-incorporated Hydrogel Microspheres with Controlled Macroporous Structures for Improved Protein Conjugation

A4.1 Core-shell Structure via Polymerization-induced Phase Separation

To confirm that the core-shell structure within microspheres in Figure 5.1c results from polymerization-induced phase separation (PIPS), I carried out comparison of apparent phase behavior with non-polymerizable system and that with polymerizable one, as shown in Figure A4.1. For the non-polymerizable systems, one of the components for polymerization is missing under identical fabrication conditions with that used in Figure 5.1; no photoinitiator (PI) in the wetting fluid (Figure A4.1a) and no acrylate in prepolymer solution (PEG200 instead of PEGDA, Figure A4.1b). For the polymerizable system, I utilized 30% PEGDA aqueous solution without chitosan as prepolymer solution (Figure A4.1c) to examine the effect of chitosan on the phase separation shown in Figure 5.1c.

First, the bright-field micrographs in the top row of Figure A4.1 show uniform and transparent spherical droplets in both non-polymerizable and polymerizable systems upon surface tension-induced droplet formation, indicating no phase separation in the droplets before UV exposure. Next, UV-exposed droplets in the polymerizable system (Figure A4.1c, bottom) clearly show two different phases (i.e. core-shell structure marked with long and short arrows) as shown in Figure 5.1c, while no core-shell structure is observed in the non-polymerizable systems upon UV exposure (Figure A4.1a,b bottom). These results indicate that polymerization of PEGDAs within the droplets, regardless of the chitosan, results in phase separation leading to formation of the core-shell structure in microspheres.

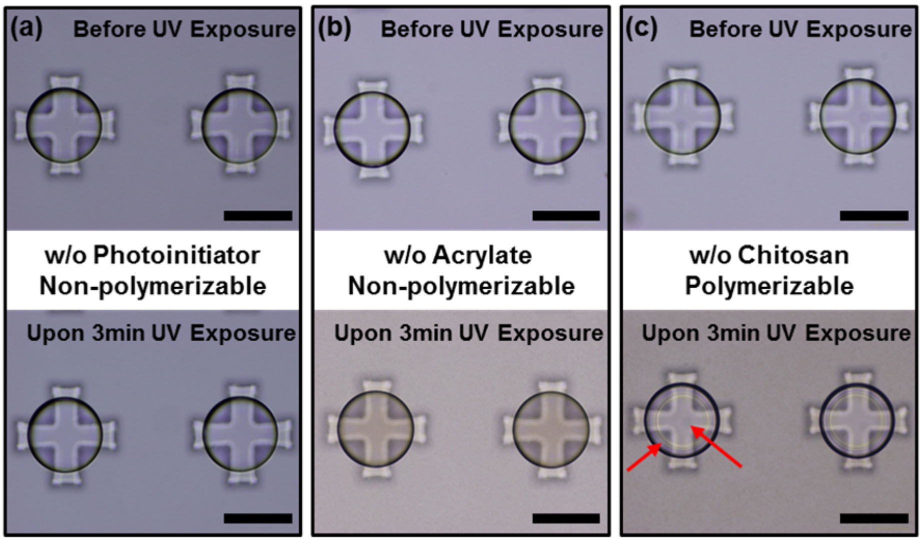

Figure A4.1. Bright-field micrographs of droplets before (top) and upon UV exposure (bottom). (a,b) Non-polymerizable systems; (a) without photoinitiators in the wetting fluid and (b) without acrylates in the prepolymer solution. (c) Polymerizable system without chitosans in the prepolymer solution. Long and short arrows indicate core and shell regions respectively. Scale bars represent 200 µm.

A4.2 PEG-rich Core and PEG-poor Shell domains in Microspheres

I next examined the core-shell structure within microspheres shown in Figure 5.1 by utilizing binding affinity of a red fluorescent dye (sulforhodamine B, Sigma-Aldrich, St. Louis, MO) to PEG networks by hydrophobic adsorption,[176] as shown in Figure A4.2. For this, microspheres were fabricated with identical fabrication procedure and conditions as in Figure 5.1; surface tension-induced droplet formation of prepolymer solution consisting of 30% PEGDA and 0.5%

chitosan upon addition of wetting fluid containing 1% PI, and 3 min UV exposure for polymerization. The microspheres were then washed with isopropanol (5 times), DI water with 0.5% TW20 (3 times) and 5xSSC buffer with 0.05% TW20 (2 times) sequentially, and incubated in an aqueous solution of sulforhodamine B (5 mg/mL in 5xSSC buffer with 0.05% TW20) for 3 h. Upon 3 times washing with the 5xSSC buffer with 0.05% TW20, the sulforhodamine B-adsorbed microspheres were analyzed with a confocal microscope (Leica DMIRE2, Wetzlar, Germany). Specifically, the center plane of the microsphere was imaged with a 20× objective under transmitted light imaging mode (Figure A4.2a) and under 543 nm excitation (Figure A4.2b).

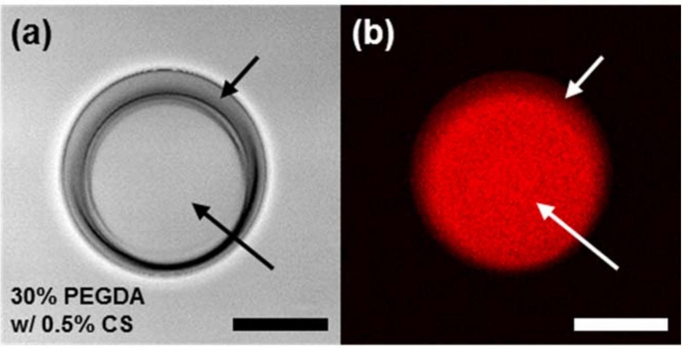

Figure A4.2. Confocal micrographs at the center plane of the sulforhodamine B-adsorbed microsphere under (a) transmitted light imaging mode and (b) 543 nm excitation. Long and short arrows indicate core and shell regions respectively. Scale bars represent 100 μm.

First, the transmission mode (i.e. bright-field) confocal micrograph in Figure A4.2a clearly shows two different phases in the microsphere (i.e. core and shell regions marked with long and short arrows, respectively). Next, its corresponding fluorescence confocal micrograph (Figure A4.2b) shows significantly brighter fluorescence at the core region than the shell, indicating more dyes adsorbed to the core due to higher PEG content. In comparison, the shell region shows non-negligible yet much lower fluorescence, indicating lighter PEG content. This result suggests that the microspheres in Figure 5.1 are composed of PEG-rich core and PEG-poor shell domains.

A4.3 Minimal Fluorescence of Microspheres without Chitosan

In order to confirm that the observed fluorescence on the chitosan–PEG microspheres in Figure 5.3 is due to the specific S_N2 reaction between NHS–fluorescein molecules and chitosan's primary amines, I carried out negative control experiments with microspheres where chitosan is missing, as shown in Figure A4.3. Specifically, the microspheres were fabricated with prepolymer solutions consisting of 10-70% PEGDA without chitosan, and incubated in aqueous solutions containing 5μM of NHS–fluorescein for 1 h. Upon 3 times washing, the microspheres were imaged with epifluorescence microscopy under identical imaging conditions as in Figure 5.3. As shown in the bright-field micrographs (Figure A4.3a-e, top row), the microspheres are uniform for all the PEGDA concentrations employed as in Figure 5.3, indicating consistency and robustness of my simple micromolding-based fabrication method. Next, the fluorescence micrographs corresponding to the bright-field ones (Figure A4.3a-e, bottom row) show no fluorescence on the microspheres prepared with 10-20% PEGDA, indicating minimal nonspecific binding of fluorescein with the microspheres. While microspheres prepared with 30-70% PEGDA show some fluorescence that increases with the PEGDA concentration, the average total fluorescence is substantially lower than the microspheres with chitosan shown in Figure 5.3; one order of magnitude lower average total fluorescence on the microspheres without chitosan (total FI=10^5-10^6) than that with chitosan (total FI=10^6-10^7) for every PEGDA condition examined. I attribute this fluorescence on higher PEG content microspheres to hydrophobic adsorption of the fluorescein to the PEG residues, similar to the binding of sulforhodamine B to the PEG networks shown in Figure A4.2. In the meantime, highly hydrophilic nature of chitosan leads to negligible nonspecific binding with fluorescein,[208] supporting specific conjugation of the fluorescein molecules with the chitosan's amines via the S_N2 reaction. The low fluorescence on the microspheres without chitosan shown in Figure A4.3 confirms that most of the fluorescence on the chitosan–PEG microspheres in Figure 5.3 results from covalently conjugated fluorescein molecules via the specific S_N2 reaction.

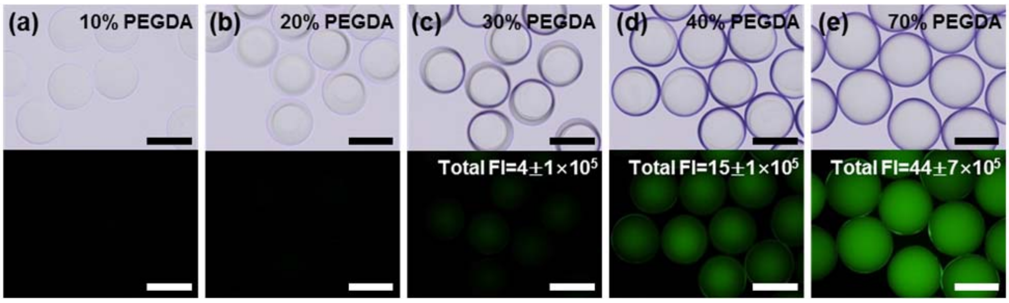

Figure A4.3. Bright-field (top row) and fluorescence micrographs (bottom row) of microspheres without chitosan upon incubation in an aqueous solution of NHS–fluorescein; microspheres fabricated with prepolymer solution containing (a) 10% (v/v), (b) 20% (v/v), (c) 30% (v/v), (d) 40% (v/v) and (e) 70% (v/v) PEGDA without chitosan. Scale bars represent 200 μm.

A4.4 Compatibility of Chitosan with PEGDA in Aqueous Solution

Figure A4.4 shows the effect of PEGDA concentration on compatibility of chitosan with PEGDA in aqueous prepolymer solutions. For this, I prepared 500 µL of aqueous prepolymer solutions by mixing fixed amount of chitosan (0.5% w/v) with varying concentrations of PEGDA (10-70% v/v), and examined turbidity of the prepolymer solution's absorbance at 450 nm (Abs_{450}) with an Evolution^{TM} 300 UV-vis Spectrophotometer (Thermo scientific, Waltham, MA) at room temperature.

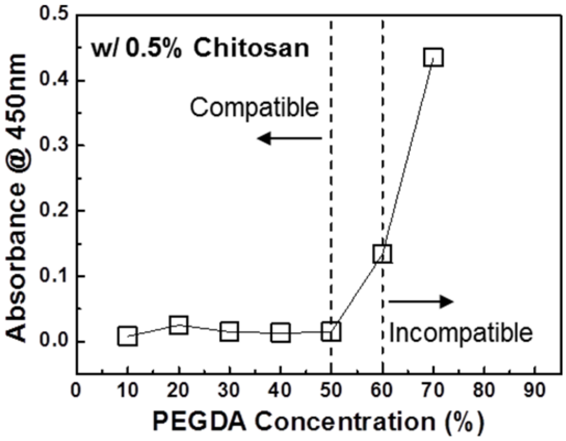

Figure A4.4. Phase diagram of the aqueous prepolymer solution composed of varying concentrations of PEGDA (10-70% v/v) and fixed amount of chitosan (0.5% w/v).

As shown in Figure A4.4, the prepolymer solutions containing up to 50% PEGDA are clear (i.e. $Abs_{450} \approx 0$), indicating compatible composition of the prepolymer solutions (i.e. one-phase). The prepolymer solutions then become turbid above 60% PEGDA composition, showing increasing Abs_{450} with increasing PEGDA concentration. This result indicates that the chitosan is incompatible with PEGDA in the prepolymer solutions containing PEGDA above

60%, forming aqueous two-phase system with the hydrophilic chitosan undergoing phase separation from more hydrophobic PEGDA-rich phase.[209] This phase behavior likely leads to the observed uniform fluorescence of chitosan–PEG microspheres with lower PEG content (Figure 5.3b-e), and the bright fluorescence of the aggregated chitosan and minimal fluorescence elsewhere for the high PEG content microspheres (Figure 5.3f). In other words, the bright fluorescence of the aggregated phase in high PEG content microspheres in Figure 5.3f likely resulted from the phase-separation of chitosan in the prepolymer solution that remains chemically active for labeling with NHS–fluorescein

A4.5 Negligible Biomolecular Conjugation with High PEG Content Microspheres

As shown in Figure A4.5, I also carried out biomolecular conjugation with high PEG content (40% PEGDA) microspheres via SPAAC reaction as in Figure 5.5. Upon ADIBO activation and conjugation reaction with azide-modified biomolecules (i.e. F–ssDNA and R-PE) via SPAAC reaction, the fluorescence micrographs of the microspheres (Figure A4.5a,b, top row) show negligible fluorescence, similar to non-fluorescence on the microspheres missing ADIBO-activation (Figure A4.5a,b, bottom row). This result indicates that both F–ssDNA and R-PE are minimally conjugated with the microspheres due to small mesh size of the high PEG content microspheres despite high chitosan incorporation

(Figure 5.4), leading to mass transfer limitation of the relatively large biomolecules into the microspheres.[27, 88]

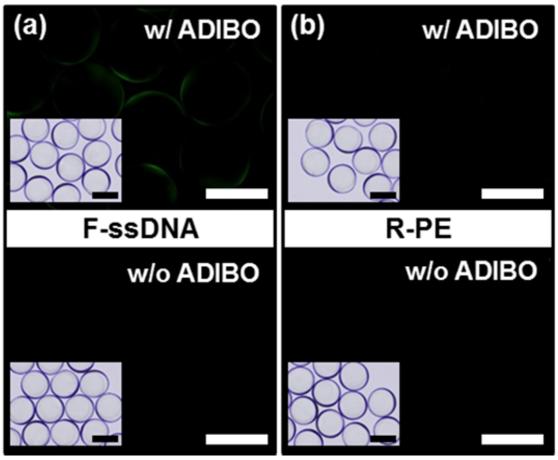

Figure A4.5. Fluorescence micrographs of 40% PEGDA microspheres with and without ADIBO-activation (top and bottom rows respectively) upon incubation with (a) F–ssDNAs and (b) R-PEs. Insets are bright-field micrographs corresponding to each fluorescence micrograph. All scale bars represent 200 μm.

A4.6 TMV Assembly with Microspheres

As shown in Figure A4.6, I further examined the mesh size of the 10-20% PEGDA microspheres (i.e. entire 10% PEGDA microspheres and the shell layers of 20% PEGDA ones, Figure 5.5) by utilizing significantly large supramolecules, nanotubular tobacco mosaic virus (TMV, 18×300 nm dimension and hydrodynamic radius R_h≈55 nm[185]). For this, I exploited hybridization-based TMV-assembly approach,[86] following the procedures described in Chapter 4 (schematic diagram of Figure A4.6a). Briefly, 300 μg/mL of genetically modified TMV (TMV1cys)[86] was fluorescently labeled; 2 h incubation at room temperature in an aqueous solution (100 mM sodium phosphate buffer, pH 7.0) containing 10-times molar excess of fluorescein–5-maleimide over the cysteines that are genetically displayed on the surface of the TMV1cys. The TMVs were then purified from unreacted fluorescein residues and partially disassembled to expose their 5’-end mRNA sequence via ultracentrifugation (at 48000g for 2 h) in a 10-40% sucrose gradient (100 mM Tris buffer, pH 7.5). Next, the fluorescently labeled and partially disassembled TMVs were purified (i.e. pelleted with ultracentrifugation at 90000g for 1 h, then resuspended in 5×SSC buffer solution), and hybridized with linker single-stranded (ss) DNAs (10:1 molar ratio to the TMV) whose sequence consists of two different regions complementary to TMV’s 5′-end mRNA and to the capture ssDNA (conjugated with the microspheres via SPAAC reaction). Lastly, these TMVs were incubated with the capture ssDNA-conjugated microspheres for 24 h at 30 ºC to assemble the TMVs with the microspheres via nucleic acid hybridization. The TMV-assembled microspheres were then analyzed via epifluorescence and confocal microscopy.

First, the epifluorescence micrographs (Figure A4.6b,c, top row) show distinguishable fluorescence (brighter fluorescence near surfaces) on both 10% and 20% PEGDA microspheres indicating assembled TMVs, similar to the results in Chapter 2. Total fluorescence on the 20% PEGDA microspheres is brighter than that on the 10% PEGDA ones. Next, the confocal micrographs (Figure A4.6b,c, bottom row) show very thin fluorescence layers (roughly 1 μm) at the surfaces of both microspheres, consistent with the epifluorescence results. This result illustrates that the mesh size of the macroporous regions in the 10-20% PEGDA microspheres are not large enough for penetration of the TMVs (R_h≈55 nm), and the TMVs are assembled only at the sphere surfaces.

Meanwhile, brightness of the fluorescence layer on the 20% PEGDA microspheres is higher than that on the 10% PEGDA ones, consistent with the epifluorescence results (Figure A4.6b,c, top row). I attribute this brighter fluorescence to higher surface density of the capture ssDNAs on the 20% PEGDA microspheres, enabling the TMVs to be assembled at the sphere surfaces in higher density. In short summary, the results in Figure A4.6 combined with the penetration results for R-PEs (R_h≈5.6 nm) in Figure 5.5 suggest quite uniform mesh size through macroporous regions in 10-20% PEGDA microspheres; larger than the size of R-PE (R_h≈5.6 nm) and smaller than the size of TMV (R_h≈55 nm).

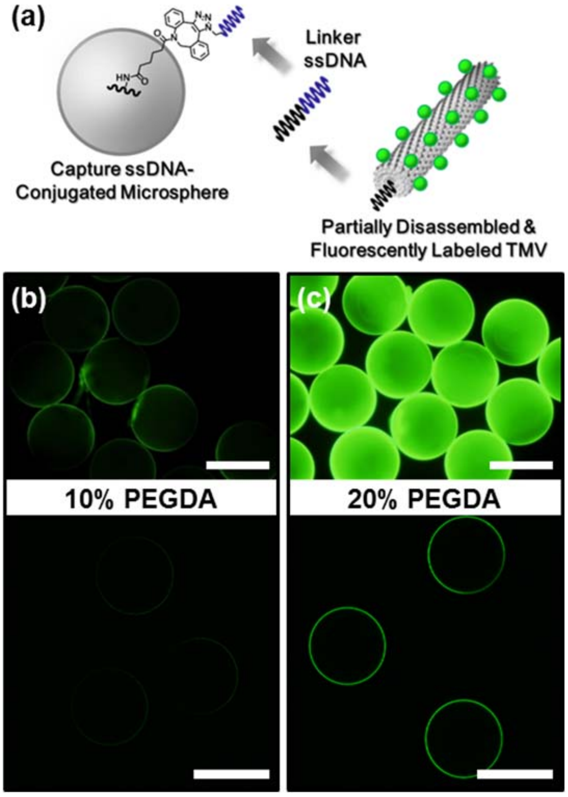

Figure A4.6. Assembly of tobacco mosaic virus (TMV) with the chitosan–PEG microspheres via nucleic acid hybridization. (a) Schematic diagram for hybridization-based assembly of fluorescein-labeled and partially disassembled TMV with capture ssDNA-conjugated microspheres. (b,c) Fluorescence (top row) and confocal (bottom row) micrographs of TMV-assembled microspheres fabricated with (b) 10% PEGDA and (c) 20% PEGDA. All scale bars represent 200 μm.

A4.7 Size-selective Dual Conjugation with Core-shell Structured Microspheres

As shown in Figure A4.7, I demonstrate size-selective conjugation of red fluorescent protein (R-PE, MW 240 kDa) and green fluorescent marker (F-488, MW 576 Da) with core-shell structured chitosan–PEG microspheres via SPAAC reaction. Specifically, the core-shell structured microspheres were fabricated with 20% PEGDA as in Figure 5.3c and 5.5c,f, and activated with ADIBO molecules (500 μM of ADIBO–*sulfo*–NHS ester) for 30 min at room temperature. The ADIBO-activated microspheres were then incubated with 2 μM of azide-activated R-PE in 5× SSC buffer solution with 0.05% (v/v) TW20 (SSC–TW20) for 6 h. Upon washing, the R-PE conjugated microspheres were incubated with 2 μM of azide-containing F-488 for 12 h in aqueous solution (SSC–TW20 with 4% (v/v) DMSO) at room temperature. The microspheres conjugated with both fluorescent molecules were imaged at the center plane with a confocal microscope under 543 nm and 488 nm excitation for the R-PE and the F-488, respectively. The confocal micrographs show red fluorescence near the sphere surfaces (Figure A4.7a), and bright green fluorescence around the cores (Figure A4.7b). This result indicates that the large R-PEs are conjugated only at the well-defined macroporous shell layers (consistent with the result in Figure 5.5f), and that the small F-488 molecules pass through the R-PE conjugated shell layers then are conjugated around the cores. The overlay image (Figure A4.7c) of the confocal micrographs more clearly shows distinct R-PE conjugated shell and F-488 conjugated core regions. Combined, the results in Figure A4.7 show size-selective conjugation that allows different molecules to be placed with spatial control (i.e. core and shell) in the microspheres even using the same conjugation reaction (i.e. SPAAC). This suggests potential for programmable functionalization of my core-shell microspheres by utilizing multiple functionalities of varying sizes. For example, large antibodies with cell- or surface ligand-specificity can be conjugated at and near the sphere surfaces for targeting, while the remaining and abundant (ADIBO-activated) chitosan sites can be loaded with small therapeutic drug molecules for targeted drug delivery applications.[210]

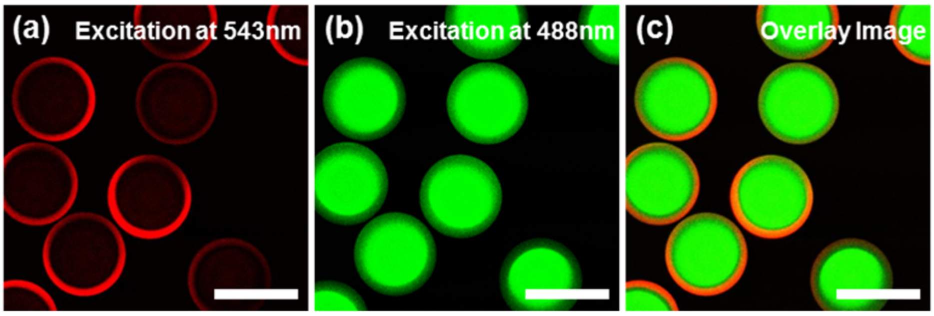

Figure A4.7. Size-selective conjugation of red fluorescent protein R-phycoerythrin (R-PE, MW 240 kDa) and green fluorescent marker (F-488, MW 576 Da) with core-shell structured chitosan–PEG microspheres. (a,b) Confocal micrographs of the core-shell microspheres conjugated with the R-PE and F-488; excitation at (a) 543 nm and (b) 488 nm. (c) Overlay image of (a) and (b). All scale bars represent 200 μm.

A4.8 Effect of Sphere Size on Protein Conjugation Kinetics

As shown in Figure A4.8, I compared protein conjugation kinetics behavior between the large and small microspheres via SPAAC reaction. For this, I prepared large (204 µm and 209 µm diameter) and small (131 µm and 133 µm diameter) 10-20% PEGDA microspheres, and activated them with ADIBO molecules via S_N2 reaction with 500 µM of ADIBO–*sulfo*–NHS ester for 1 h at room temperature. These microspheres were then reacted with 2 µM of azide-activated R-PEs for 0-48 h at room temperature. Average total fluorescence intensity of the R-PE conjugated microspheres were analyzed with an image analysis software ImageJ. First, the total fluorescence plots of the large microspheres (open squares and circles) show gradual increase in fluorescence with time, approaching saturation toward the end of the 48 h reaction period. Total fluorescence intensity of the small microspheres (solid squares and circles) also gradually increases with time, yet reaches near-saturation upon 24 h reaction. These results indicate that larger microspheres take longer time to be fully conjugated with the R-PEs resulting from longer diffusion length. In other words, the protein conjugation kinetics behavior with the microspheres appears to be governed by diffusion of the proteins through the microspheres under the reaction conditions enlisted here (further discussed in Figure 5.7). Meanwhile, the difference in protein conjugation capacity between the large and small microspheres upon 48 h reaction (~4 times larger capacity of the large microspheres) is equivalent to their difference in volume (roughly 4-fold larger volume). Assuming that the reaction approaches completion in the 48 h period, this result suggests that maximum protein conjugation capacity of the microspheres is directly proportional to their volume, and that the 3D network structures of the microspheres (i.e. chitosan incorporation ratio and mesh size) and the availability of reactive ADIBO sites (thus chitosan) should be consistent for various sphere sizes.

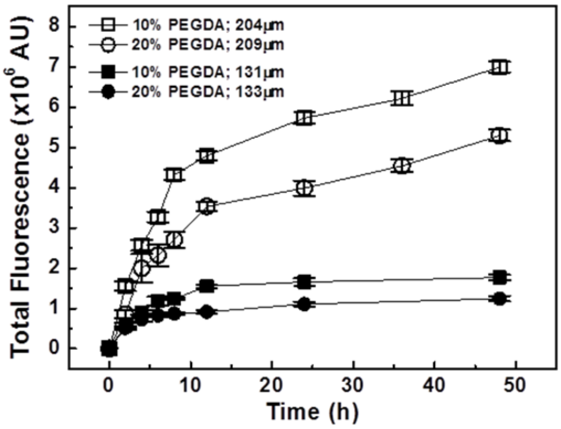

Figure A4.8. R-PE conjugation kinetics with different-sized microspheres via SPAAC reaction for 48 h. Small microspheres; 131 μm and 133 μm diameters (solid squares and circles respectively), and large microspheres; 204 μm and 209 μm diameters (open squares and circles respectively). Error bars represent standard deviation from five microspheres per each condition.

A4.9 Estimated Number of Conjugation Sites in Microspheres

To examine my hypothesis on abundant protein conjugation sites in the small (131 μm diameter) 10% PEGDA microspheres, the number of conjugation sites was estimated, and compared with the maximum number of R-PEs that can be packed in the microsphere, as shown in Figure A4.9. First, since the chitosan's primary amines in the microsphere are activated with ADIBO molecules for protein conjugation, I estimated the number of primary amines as the conjugation sites by utilizing chitosan incorporation ratio (Figure A4.9a). The chitosan incorporation results (Figure 5.4d) show that ~10% of chitosans (η=0.1) in the prepolymer droplet are incorporated in the large 10% PEGDA microspheres, and the result in Figure A4.8 suggests this incorporation ratio is also retained in the small ones. The droplet volume is equivalent to that of the micromold (V_{M}=1.20 nL for small microspheres). Thus, the number of incorporated chitosans in the small 10% PEGDA microsphere can be estimated as follows:

$$N_{\mathrm{CS}} = V_{\mathrm{M}} \times C_{\mathrm{CS}} \times \eta \times \frac{1}{\mathrm{MW_{CS}}} = 1.20\ \mathrm{nL} \times \frac{0.5\ \mathrm{g}}{100\ \mathrm{mL}} \times 0.1 \times \frac{\mathrm{moles}}{5000\ \mathrm{g}}$$

$$= 1.20\ \times 10^{-13}\ \mathrm{moles}$$

where C_{CS} and $\mathrm{MW_{CS}}$ represent concentration (0.5% w/v) and molecular weight (5 kDa) of the chitosan in the droplet, respectively.

The number of the primary amines per chitosan with 90% deacetylation is:

$$n_{\mathrm{Am}} = \frac{\mathrm{MW_{CS}}}{\mathrm{MW_{R-CS}}} \times 0.9 = \frac{5000}{161} \approx 27$$

where $\mathrm{MW_{R-CS}}$ represents molecular weight (161 Da) of the glucosamine repeating unit of the chitosan.

Thus, the number of the primary amines (i.e. conjugation sites) in the microsphere is:

$$\underline{\boldsymbol{N_{\mathrm{Am}}}} = N_{\mathrm{CS}} \times n_{\mathrm{Am}} = \underline{\mathbf{3.24\ \times 10^{-12}\ moles}}$$

I note that not all of these conjugation sites should be equally accessible for the protein conjugation partly due to steric hindrance resulting from multiple amines existing in a close proximity on a chitosan backbone.

Next, I estimated the maximum number of R-PEs that can be packed in the microsphere with assumptions that the R-PEs are hard spheres with 5.6 nm radius (i.e. hydrodynamic radius),[184] and densely packed in a face-centered cubic (FCC) structure. To simplify this estimation, I also assume that the number of the packed R-PEs in the microsphere is equivalent to that in an imaginary cube whose volume is the same with that of the microsphere (Figure A4.9b).

The volume of the microsphere and also the imaginary cube is:

$$V_{\mathrm{SP}} = V_{\mathrm{IC}} = \frac{4}{3} \times \pi \times {r_{\mathrm{SP}}}^3 = 1.18 \text{ nl}$$

where r_{SP} represents radius (65.6 μm) of the microsphere.

The FCC unit cell volume consisting of four R-PEs[211] is:

$$V_{\mathrm{FCC}} = 16 \times {r_{\mathrm{R-PE}}}^3 \times \sqrt{2} = 3.97 \times 10^{-12} \text{ nl}$$

where $r_{\mathrm{R-PE}}$ represents radius (5.6 nm) of the R-PE.

Thus, the maximum number of R-PEs packed via FCC configuration in the imaginary cube (i.e. microsphere) is:

$$\underline{\boldsymbol{N}_{\mathbf{R-PE}}} = \frac{V_{\mathrm{IC}}}{V_{\mathrm{FCC}}} \times 4 \times \frac{\text{moles}}{6.02 \times 10^{23}} = \underline{\mathbf{1.97 \times 10^{-12}\ moles}}$$

I note that this value is an estimated one under ideal conditions (i.e. tightly packed in the empty space). In other words, the number of R-PEs conjugated in the microsphere should be much less than this estimated maximum value due to excluded volume in the microsphere by polymer networks and the R-PEs conjugated along the incorporated chitosans rather than tightly packed.

Overall, the estimation results in Figure A4.9 show that a 10% PEGDA microsphere could possess roughly 1.6-fold more conjugation sites (i.e. chitosan's amines) than the maximum number of R-PEs that can be packed in the microsphere under ideal conditions. This suggests that there exist sufficient sites for protein conjugation in the microsphere, while the sites may not be equally available or accessible due to steric hindrance.

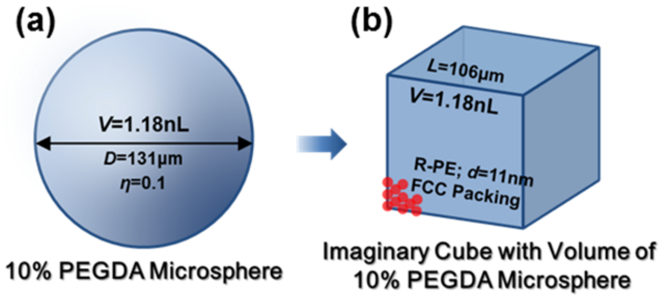

Figure A4.9. Schematic diagrams of (a) the 10% PEGDA microsphere, and (b) an imaginary cube possessing the same volume with the 10% PEGDA microsphere and filled with the R-PEs in compact face-centered cubic (FCC) structure.

BIBLIOGRAPHY

[1] Appleyard, D. C.; Chapin, S. C.; Srinivas, R. L.; Doyle, P. S. *Nature Protocols* **2011**, *6*, 1761.

[2] Helwa, Y.; Dave, N.; Froidevaux, R.; Samadi, A.; Liu, J. W. *ACS Applied Materials & Interfaces* **2012**, *4*, 2228.

[3] Chen, K.; Merkel, T. J.; Pandya, A.; Napier, M. E.; Luft, J. C.; Daniel, W.; Sheiko, S.; DeSimone, J. M. *Biomacromolecules* **2012**, *13*, 2748.

[4] Jha, A. K.; Yang, W. D.; Kirn-Safran, C. B.; Farach-Carson, M. C.; Jia, X. Q. *Biomaterials* **2009**, *30*, 6964.

[5] Wei, J.; Ju, X. J.; Zou, X. Y.; Xie, R.; Wang, W.; Liu, Y. M.; Chu, L. Y. *Advanced Functional Materials* **2014**, *24*, 3312.

[6] Chung, B. G.; Lee, K. H.; Khademhosseini, A.; Lee, S. H. *Lab on a Chip* **2012**, *12*, 45.

[7] Khademhosseini, A.; Langer, R. *Biomaterials* **2007**, *28*, 5087.

[8] Helgeson, M. E.; Chapin, S. C.; Doyle, P. S. *Current Opinion in Colloid & Interface Science* **2011**, *16*, 106.

[9] Gokmen, M. T.; Du Prez, F. E. *Progress in Polymer Science* **2012**, *37*, 365.

[10] Peppas, N. A.; Hilt, J. Z.; Khademhosseini, A.; Langer, R. *Advanced Materials* **2006**, *18*, 1345.

[11] Choi, C. H.; Jeong, J. M.; Kang, S. M.; Lee, C. S.; Lee, J. *Advanced Materials* **2012**, *24*, 5078.

[12] Lewis, C. L.; Choi, C. H.; Lin, Y.; Lee, C. S.; Yi, H. *Analytical Chemistry* **2010**, *82*, 5851.

[13] Seiffert, S.; Thiele, J.; Abate, A. R.; Weitz, D. A. *Journal of the American Chemical Society* **2010**, *132*, 6606.

[14] Thornton, P. D.; Mart, R. J.; Webb, S. J.; Ulijn, R. V. *Soft Matter* **2008**, *4*, 821.

[15] Chen, K.; Xu, J.; Luft, J. C.; Tian, S. M.; Raval, J. S.; DeSimone, J. M. *Journal of the American Chemical Society* **2014**, *136*, 9947.

[16] Dunn, S. S.; Tian, S. M.; Blake, S.; Wang, J.; Galloway, A. L.; Murphy, A.; Pohlhaus, P. D.; Rolland, J. P.; Napier, M. E.; DeSimone, J. M. *Journal of the American Chemical Society* **2012**, *134*, 7423.

[17] Hermanson, G. T. *Bioconjugate Techniques*; Elsevier Science: Burlington, 2008.

[18] Welsch, N.; Lu, Y.; Dzubiella, J.; Ballauff, M. *Polymer* **2013**, *54*, 2835.

[19] Lewis, M. R.; Kao, J. Y.; Anderson, A. L. J.; Shively, J. E.; Raubitschek, A. *Bioconjugate Chemistry* **2001**, *12*, 320.

[20] Yi, H.; Wu, L. Q.; Bentley, W. E.; Ghodssi, R.; Rubloff, G. W.; Culver, J. N.; Payne, G. F. *Biomacromolecules* **2005**, *6*, 2881.

[21] Karver, M. R.; Weissleder, R.; Hilderbrand, S. A. *Bioconjugate Chemistry* **2011**, *22*, 2263.

[22] Karver, M. R.; Weissleder, R.; Hilderbrand, S. A. *Angewandte Chemie International Edition* **2012**, *51*, 920.

[23] Xi, W. X.; Scott, T. F.; Kloxin, C. J.; Bowman, C. N. *Advanced Functional Materials* **2014**, *24*, 2572.

[24] Cruise, G. M.; Scharp, D. S.; Hubbell, J. A. *Biomaterials* **1998**, *19*, 1287.

[25] Engberg, K.; Frank, C. W. *Biomedical Materials* **2011**, *6*, 055006.

[26] Beck, R. E.; Schultz, J. S. *Science* **1970**, *170*, 1302.

[27] Jung, S.; Yi, H. *Biomacromolecules* **2013**, *14*, 3892.

[28] Zubtsov, D. A.; Ivanov, S. M.; Rubina, A. Y.; Dementieva, E. I.; Chechetkin, V. R.; Zasedatelev, A. S. *Journal of Biotechnology* **2006**, *122*, 16.

[29] Zubtsov, D. A.; Savvateeva, E. N.; Rubina, A. Y.; Pan'kov, S. V.; Konovalova, E. V.; Moiseeva, O. V.; Chechetkin, V. R.; Zasedatelev, A. S. *Analytical Biochemistry* **2007**, *368*, 205.

[30] Kusnezow, W.; Hoheisel, J. D. *Journal of Molecular Recognition* **2003**, *16*, 165.

[31] Wulfkuhle, J. D.; Liotta, L. A.; Petricoin, E. F. *Nature Reviews Cancer* **2003**, *3*, 267.

[32] Baker, K. N.; Rendall, M. H.; Patel, A.; Boyd, P.; Hoare, M.; Freedman, R. B.; James, D. C. *Trends in Biotechnology* **2002**, *20*, 149.

[33] Bronze, M. S.; Greenfield, R. A. *Drug Discovery Today* **2003**, *8*, 740.

[34] Uttamchandani, M.; Neo, J. L.; Ong, B. N. Z.; Moochhala, S. *Trends in Biotechnology* **2009**, *27*, 53.

[35] Rusmini, F.; Zhong, Z. Y.; Feijen, J. *Biomacromolecules* **2007**, *8*, 1775.

[36] Walt, D. R. *Lab on a Chip* **2014**, *14*, 3195.

[37] de la Rica, R.; Stevens, M. M. *Nature Nanotechnology* **2012**, *7*, 821.

[38] Ellington, A. A.; Kullo, I. J.; Bailey, K. R.; Klee, G. G. *Clinical Chemistry* **2010**, *56*, 186.

[39] Templin, M. F.; Stoll, D.; Schrenk, M.; Traub, P. C.; Vohringer, C. F.; Joos, T. O. *Trends in Biotechnology* **2002**, *20*, 160.

[40] Wilson, R.; Cossins, A. R.; Spiller, D. G. *Angewandte Chemie-International Edition* **2006**, *45*, 6104.

[41] Peppas, N. A.; Hoffman, A. S. Hydrogels. In *Biomaterials Science: An Introduction to Materials in Medicine* 3rd ed.; Ratner, B. D.,Hoffman, A. S.,Schoen, F. J.,Lemons, J. E., Eds.; Academic Press: Boston, 2013.

[42] Slaughter, B. V.; Khurshid, S. S.; Fisher, O. Z.; Khademhosseini, A.; Peppas, N. A. *Advanced Materials* **2009**, *21*, 3307.

[43] Andrzejewska, E. *Progress in Polymer Science* **2001**, *26*, 605.

[44] Ward, J. H.; Peppas, N. A. *Macromolecules* **2000**, *33*, 5137.

[45] Decker, C. *Progress in Polymer Science* **1996**, *21*, 593.

[46] Goff, G. C. L.; Srinivas, R. L.; Hill, W. A.; Doyle, P. S. *European Polymer Journal* **2015**, http://dx.doi.org/10.1016/j.eurpolymj.2015.02.022.

[47] Odian, G. *Principles of Polymerization*; Wiley: Hoboken, 2004.

[48] Dendukuri, D.; Panda, P.; Haghgooie, R.; Kim, J. M.; Hatton, T. A.; Doyle, P. S. *Macromolecules* **2008**, *41*, 8547.

[49] Park, S.; Kim, D.; Ko, S. Y.; Park, J. O.; Akella, S.; Xu, B.; Zhang, Y.; Fraden, S. *Lab on a Chip* **2014**, *14*, 1551.

[50] Fotin, A. V.; Drobyshev, A. L.; Proudnikov, D. Y.; Perov, A. N.; MIrzabekov, A. D. *Nucleic Acids Research* **1998**, *26*, 1515.

[51] Sorokin, N. V.; Chechetkin, V. R.; Pan'kov, S. V.; Somova, O. G.; Livshits, M. A.; Donnikov, M. Y.; Turygin, A. Y.; Barsky, V. E.; Zasedatelev, A. S. *Journal of Biomolecular Structure and Dynamics* **2006**, *24*, 57.

[52] Gervais, T.; Jensen, K. F. *Chemical Engineering Science* **2006**, *61*, 1102.

[53] Appleyard, D. C.; Chapin, S. C.; Doyle, P. S. *Analytical Chemistry* **2011**, *83*, 193.

[54] Wang, J. T.; Wang, J.; Han, J. J. *Small* **2011**, *7*, 1728.

[55] Meiring, J. E.; Schmid, M. J.; Grayson, S. M.; Rathsack, B. M.; Johnson, D. M.; Kirby, R.; Kannappan, R.; Manthiram, K.; Hsia, B.; Hogan, Z. L.; Ellington, A. D.; Pishko, M. V.; Willson, C. G. *Chemistry of Materials* **2004**, *16*, 5574.

[56] Lee, W.; Choi, D.; Kim, J. H.; Koh, W. G. *Biomedical Microdevices* **2008**, *10*, 813.

[57] Ye, B. F.; Zhao, Y. J.; Li, T. T.; Xie, Z. Y.; Gu, Z. Z. *Journal of Materials Chemistry* **2011**, *21*, 18659.

[58] Chapin, S. C.; Appleyard, D. C.; Pregibon, D. C.; Doyle, P. S. *Angewandte Chemie-International Edition* **2011**, *50*, 2289.

[59] Gates, B. D.; Xu, Q. B.; Stewart, M.; Ryan, D.; Willson, C. G.; Whitesides, G. M. *Chemical Reviews* **2005**, *105*, 1171.

[60] Qin, D.; Xia, Y. N.; Whitesides, G. M. *Nature Protocols* **2010**, *5*, 491.

[61] Rinaudo, M.; Pavlov, G.; Desbrieres, J. *Polymer* **1999**, *40*, 7029.

[62] Sorlier, P.; Denuziere, A.; Viton, C.; Domard, A. *Biomacromolecules* **2001**, *2*, 765.

[63] Varum, K. M.; Ottoy, M. H.; Smidsrod, O. *Carbohydrate Polymers* **1994**, *25*, 65.

[64] Dash, M.; Chiellini, F.; Ottenbrite, R. M.; Chiellini, E. *Progress in Polymer Science* **2011**, *36*, 981.

[65] Wang, W.; Xu, D. S. *International Journal of Biological Macromolecules* **1994**, *16*, 149.

[66] Sletten, E. M.; Bertozzi, C. R. *Angewandte Chemie-International Edition* **2009**, *48*, 6974.

[67] Lang, K.; Chin, J. W. *Acs Chemical Biology* **2014**, *9*, 16.

[68] Lallana, E.; Riguera, R.; Fernandez-Megia, E. *Angewandte Chemie-International Edition* **2011**, *50*, 8794.

[69] Lallana, E.; Sousa-Herves, A.; Fernandez-Trillo, F.; Riguera, R.; Fernandez-Megia, E. *Pharmaceutical Research* **2012**, *29*, 1.

[70] Steinmetz, N. F.; Evans, D. J. *Organic & Biomolecular Chemistry* **2007**, *5*, 2891.

[71] Singh, P.; Gonzalez, M. J.; Manchester, M. *Drug Development Research* **2006**, *67*, 23.

[72] Douglas, T.; Young, M. *Science* **2006**, *312*, 873.

[73] Fischlechner, M.; Donath, E. *Angewandte Chemie-International Edition* **2007**, *46*, 3184.

[74] Douglas, T.; Young, M. *Advanced Materials* **1999**, *11*, 679.

[75] Gazit, E. *Febs Journal* **2007**, *274*, 317.

[76] Nanduri, V.; Sorokulova, I. B.; Samoylov, A. M.; Simonian, A. L.; Petrenko, V. A.; Vodyanoy, V. *Biosensors and Bioelectronics* **2007**, *22*, 986.

[77] Goldman, E. R.; Pazirandeh, M. P.; Mauro, J. M.; King, K. D.; Frey, J. C.; Anderson, G. P. *Journal of Molecular Recognition* **2000**, *13*, 382.

[78] Nanduri, V.; Bhunia, A. K.; Tu, S. I.; Paoli, G. C.; Brewster, J. D. *Biosensors and Bioelectronics* **2007**, *23*, 248.

[79] Charlton, K.; Harris, W. J.; Porter, A. J. *Biosensors and Bioelectronics* **2001**, *16*, 639.

[80] Mao, C. B.; Liu, A. H.; Cao, B. R. *Angewandte Chemie-International Edition* **2009**, *48*, 6790.

[81] Sapsford, K. E.; Soto, C. M.; Blum, A. S.; Chatterji, A.; Lin, T. W.; Johnson, J. E.; Ligler, F. S.; Ratna, B. R. *Biosensors and Bioelectronics* **2006**, *21*, 1668.

[82] Soto, C. M.; Blum, A. S.; Vora, G. J.; Lebedev, N.; Meador, C. E.; Won, A. P.; Chatterji, A.; Johnson, J. E.; Ratna, B. R. *Journal of the American Chemical Society* **2006**, *128*, 5184.

[83] Namba, K.; Pattanayek, R.; Stubbs, G. *Journal of Molecular Biology* **1989**, *208*, 307.

[84] Bruckman, M. A.; Kaur, G.; Lee, L. A.; Xie, F.; Sepulvecla, J.; Breitenkamp, R.; Zhang, X.; Joralemon, M.; Russell, T. P.; Emrick, T.; Wang, Q. *ChemBioChem* **2008**, *9*, 519.

[85] Yin, Z. J.; Nguyen, H. G.; Chowdhury, S.; Bentley, P.; Bruckman, M. A.; Miermont, A.; Gildersleeve, J. C.; Wang, Q.; Huang, X. F. *Bioconjugate Chemistry* **2012**, *23*, 1694.

[86] Yi, H.; Nisar, S.; Lee, S. Y.; Powers, M. A.; Bentley, W. E.; Payne, G. F.; Ghodssi, R.; Rubloff, G. W.; Harris, M. T.; Culver, J. N. *Nano Letters* **2005**, *5*, 1931.

[87] Yi, H.; Rubloff, G. W.; Culver, J. N. *Langmuir* **2007**, *23*, 2663.

[88] Jung, S.; Yi, H. *Langmuir* **2012**, *28*, 17061.

[89] Tan, W. S.; Lewis, C. L.; Horelik, N. E.; Pregibon, D. C.; Doyle, P. S.; Yi, H. M. *Langmuir* **2008**, *24*, 12483.

[90] Rego, J. M.; Yi, H. Viruses as Self-Assembled Templates. In *Supramolecular Chemistry: From Molecules to Nanomaterials*; Steed, J. W.,Gale, P. A., Eds.; Wiley: Hoboken, 2012.

[91] Zaitlin, M. Aab Descriptions of Plant Viruses (Tobacco Mosaic Virus). http://www.dpvweb.net/dpv/showdpv.php?dpvno=370 (accessed April 2, 2015).

[92] Rego, J. M.; Lee, J. H.; Lee, D. H.; Yi, H. *Biotechnology Journal* **2013**, *8*, 237.

[93] Blackburn, W. H.; Dickerson, E. B.; Smith, M. H.; McDonald, J. F.; Lyon, L. A. *Bioconjugate Chemistry* **2009**, *20*, 960.

[94] Champion, J. A.; Katare, Y. K.; Mitragotri, S. *Journal of Controlled Release* **2007**, *121*, 3.

[95] Dendukuri, D.; Pregibon, D. C.; Collins, J.; Hatton, T. A.; Doyle, P. S. *Nature Materials* **2006**, *5*, 365.

[96] Panda, P.; Ali, S.; Lo, E.; Chung, B. G.; Hatton, T. A.; Khademhosseini, A.; Doyle, P. S. *Lab on a Chip* **2008**, *8*, 1056.

[97] Merkel, T. J.; Herlihy, K. P.; Nunes, J.; Orgel, R. M.; Rolland, J. P.; DeSimone, J. M. *Langmuir* **2010**, *26*, 13086.

[98] Zhao, X. M.; Xia, Y. N.; Whitesides, G. M. *Journal of Materials Chemistry* **1997**, *7*, 1069.

[99] Koev, S. T.; Dykstra, P. H.; Luo, X.; Rubloff, G. W.; Bentley, W. E.; Payne, G. F.; Ghodssi, R. *Lab on a Chip* **2010**, *10*, 3026.

[100] Kolhe, P.; Kannan, R. M. *Biomacromolecules* **2003**, *4*, 173.

[101] Hudak, J. E.; Barfield, R. M.; de Hart, G. W.; Grob, P.; Nogales, E.; Bertozzi, C. R.; Rabuka, D. *Angewandte Chemie-International Edition* **2012**, *51*, 4161.

[102] Kim, C. H.; Axup, J. Y.; Dubrovska, A.; Kazane, S. A.; Hutchins, B. A.; Wold, E. D.; Smider, V. V.; Schultz, P. G. *Journal of the American Chemical Society* **2012**, *134*, 9918.

[103] Lallana, E.; Fernandez-Megia, E.; Riguera, R. *Journal of the American Chemical Society* **2009**, *131*, 5748.

[104] Bolisay, L. D.; Culver, J. N.; Kofinas, P. *Biomacromolecules* **2007**, *8*, 3893.

[105] Rasband, W. S. *Imagej*; U. S. National Institutes of Health: Bethesda, 1997-2014.

[106] Shuler, M. L.; Kargi, F. *Bioprocess Engineering: Basic Concepts*; Prentice Hall: New Jersey, 2002.

[107] Wu, L. Q.; Yi, H. M.; Li, S.; Rubloff, G. W.; Bentley, W. E.; Ghodssi, R.; Payne, G. F. *Langmuir* **2003**, *19*, 519.

[108] Lee, S. J.; Kim, S. S.; Lee, Y. M. *Carbohydrate Polymers* **2000**, *41*, 197.

[109] Wade, L. G. *Organic Chemistry*; Pearson Education: Upper Saddle River, 2003.

[110] El-Sherbiny, I. M. *European Polymer Journal* **2009**, *45*, 199.

[111] Sabaa, M. W.; Mohamed, N. A.; Mohamed, R. R.; Khalil, N. M.; El Latif, S. M. A. *Carbohydrate Polymers* **2010**, *79*, 998.

[112] Pavinatto, F. J.; Caseli, L.; Oliveira, O. N. *Biomacromolecules* **2010**, *11*, 1897.

[113] Yi, H. M.; Wu, L. Q.; Ghodssi, R.; Rubloff, G. W.; Payne, G. F.; Bentley, W. E. *Analytical Chemistry* **2004**, *76*, 365.

[114] Padmavathi, N. C.; Chatterji, P. R. *Macromolecules* **1996**, *29*, 1976.

[115] Pregibon, D. C.; Doyle, P. S. *Analytical Chemistry* **2009**, *81*, 4873.

[116] El-Sherbiny, I. M.; Smyth, H. D. C. *Carbohydrate Research* **2010**, *345*, 2004.

[117] El-Sherbiny, I. M.; Smyth, H. D. C. *Carbohydrate Polymers* **2010**, *81*, 652.

[118] Wu, W.; Shen, J.; Banerjee, P.; Zhou, S. Q. *Biomaterials* **2010**, *31*, 8371.

[119] Bostic, H. E.; Smith, M. D.; Poloukhtine, A. A.; Popik, V. V.; Best, M. D. *Chemical Communications* **2012**, *48*, 1431.

[120] Canalle, L. A.; van der Knaap, M.; Overhand, M.; van Hest, J. C. M. *Macromolecular Rapid Communications* **2011**, *32*, 203.

[121] Meagher, R. J.; Won, J. I.; McCormick, L. C.; Nedelcu, S.; Bertrand, M. M.; Bertram, J. L.; Drouin, G.; Barron, A. E.; Slater, G. W. *Electrophoresis* **2005**, *26*, 331.

[122] Russell, R. J.; Axel, A. C.; Shields, K. L.; Pishko, M. V. *Polymer* **2001**, *42*, 4893.

[123] Watkins, A. W.; Anseth, K. S. *Macromolecules* **2005**, *38*, 1326.

[124] Braga, P. C.; Ricci, D. *Atomic Force Microscopy: Biomedical Methods and Applications*; Humana Press: New Jersey, 2004; Vol. 242.

[125] Getz, E. B.; Xiao, M.; Chakrabarty, T.; Cooke, R.; Selvin, P. R. *Analytical Biochemistry* **1999**, *273*, 73.

[126] Canalle, L. A.; van Berkel, S. S.; de Haan, L. T.; van Hest, J. C. M. *Advanced Functional Materials* **2009**, *19*, 3464.

[127] Kusnezow, W.; Jacob, A.; Walijew, A.; Diehl, F.; Hoheisel, J. D. *Proteomics* **2003**, *3*, 254.

[128] Arenkov, P.; Kukhtin, A.; Gemmell, A.; Voloshchuk, S.; Chupeeva, V.; Mirzabekov, A. *Analytical Biochemistry* **2000**, *278*, 123.

[129] Krishhan, V. V.; Khan, I. H.; Luciw, P. A. *Critical Reviews in Biotechnology* **2009**, *29*, 29.

[130] Falipou, S.; Chovelon, J. M.; Martelet, C.; Margonari, J.; Cathignol, D. *Bioconjugate Chemistry* **1999**, *10*, 346.

[131] Anaspec, Inc. Home Page. http://www.anaspec.com/products/product.asp?id=29041 (accessed April 2, 2015).

[132] George, P. S. Chemical and Proteolytic Modification of Antibodies. In *Making and Using Antibodies: A Practical Handbook*; Howard, G. C.,Kaser, M. R., Eds.; CRC Press: New York, 2006.

[133] MacColl, R.; Eisele, L. E.; Williams, E. C.; Bowser, S. S. *Journal of Biological Chemistry* **1996**, *271*, 17157.

[134] Mallis, R. J.; Hamann, M. J.; Zhao, W.; Zhang, T. Q.; Hendrich, S.; Thornas, J. A. *Biological Chemistry* **2002**, *383*, 649.

[135] Kuzmin, A.; Poloukhtine, A.; Wolfert, M. A.; Popik, V. V. *Bioconjugate Chemistry* **2010**, *21*, 2076.

[136] Lee, A. G.; Arena, C. P.; Beebe, D. J.; Palecek, S. P. *Biomacromolecules* **2010**, *11*, 3316.

[137] Orski, S. V.; Sheppard, G. R.; Arumugam, S.; Arnold, R. M.; Popik, V. V.; Locklin, J. *Langmuir* **2012**, *28*, 14693.

[138] Contreras-Martel, C.; Martinez-Oyanedel, J.; Bunster, M.; Legrand, P.; Piras, C.; Vernede, X.; Fontecilla-Camps, J. C. *Acta Crystallographica Section D-Biological Crystallography* **2001**, *57*, 52.

[139] Madej, T.; Addess, K. J.; Fong, J. H.; Geer, L. Y.; Geer, R. C.; Lanczycki, C. J.; Liu, C. L.; Lu, S. N.; Marchler-Bauer, A.; Panchenko, A. R.; Chen, J.; Thiessen, P. A.; Wang, Y. L.; Zhang, D. C.; Bryant, S. H. *Nucleic Acids Research* **2012**, *40*, D461.

[140] Oates, M. R.; Clarke, W.; Marsh, E. M.; Hage, D. S. *Bioconjugate Chemistry* **1998**, *9*, 459.

[141] Moorthy, J.; Burgess, R.; Yethiraj, A.; Beebe, D. *Analytical Chemistry* **2007**, *79*, 5322.

[142] Dagnolo, E.; Rizzo, R.; Paoletti, S.; Murano, E. *Phytochemistry* **1994**, *35*, 693.

[143] Suh, S. K.; Chapin, S. C.; Hatton, T. A.; Doyle, P. S. *Microfluidics and Nanofluidics* **2012**, *13*, 665.

[144] Lee, C. S.; Kim, B. G. *Biotechnology Letters* **2002**, *24*, 839.

[145] Wan, J. D.; Thomas, M. S.; Guthrie, S.; Vullev, V. I. *Annals of Biomedical Engineering* **2009**, *37*, 1190.

[146] Sharma, S.; Johnson, R. W.; Desai, T. A. *Langmuir* **2004**, *20*, 348.

[147] Nguyen, K. T.; West, J. L. *Biomaterials* **2002**, *23*, 4307.

[148] Rubina, A. Y.; Dementieva, E. I.; Stomakhin, A. A.; Darii, E. L.; Pan'kov, S. V.; Barsky, V. E.; Ivanov, S. M.; Konovalova, E. V.; Mirzabekov, A. D. *Biotechniques* **2003**, *34*, 1008.

[149] Floyd, R. A.; Carney, J. M. *Annals of Neurology* **1992**, *32*, S22.

[150] Pattison, D. I.; Davies, M. J. *Experientia Supplementum* **2006**, 131.

[151] Manjappa, A. S.; Chaudhari, K. R.; Venkataraju, M. P.; Dantuluri, P.; Nanda, B.; Sidda, C.; Sawant, K. K.; Murthy, R. S. R. *Journal of Controlled Release* **2011**, *150*, 2.

[152] Jang, S.; Sachin, K.; Lee, H. J.; Kim, D. W.; Lee, H. S. *Bioconjugate Chemistry* **2012**, *23*, 2256.

[153] Rissin, D. M.; Kan, C. W.; Campbell, T. G.; Howes, S. C.; Fournier, D. R.; Song, L.; Piech, T.; Patel, P. P.; Chang, L.; Rivnak, A. J.; Ferrell, E. P.; Randall, J. D.; Provuncher, G. K.; Walt, D. R.; Duffy, D. C. *Nature Biotechnology* **2010**, *28*, 595.

[154] Brault, N. D.; Sundaram, H. S.; Huang, C. J.; Li, Y. T.; Yu, Q. M.; Jiang, S. Y. *Biomacromolecules* **2012**, *13*, 4049.

[155] Ma, H. W.; He, J. A.; Liu, X.; Gan, J. H.; Jin, G.; Zhou, J. H. *ACS Applied Materials & Interfaces* **2010**, *2*, 3223.

[156] Hu, W. H.; Liu, Y. S.; Lu, Z. S.; Li, C. M. *Advanced Functional Materials* **2010**, *20*, 3497.

[157] Qin, W.; Song, Z.; Fan, C.; Zhang, W.; Cai, Y.; Zhang, Y.; Qian, X. *Analytical Chemistry* **2012**, *84*, 3138.

[158] Miller, R. A.; Presley, A. D.; Francis, M. B. *Journal of the American Chemical Society* **2007**, *129*, 3104.

[159] Lee, L. A.; Nguyen, H. G.; Wang, Q. *Organic & Biomolecular Chemistry* **2011**, *9*, 6189.

[160] Sebra, R. P.; Masters, K. S.; Bowman, C. N.; Anseth, K. S. *Langmuir* **2005**, *21*, 10907.

[161] Haun, J. B.; Devaraj, N. K.; Hilderbrand, S. A.; Lee, H.; Weissleder, R. *Nature Nanotechnology* **2010**, *5*, 660.

[162] Wilson, A. N.; Guiseppi-Elie, A. *Advanced Healthcare Materials* **2013**, *2*, 520.

[163] Stenekes, R. J.; De Smedt, S. C.; Demeester, J.; Sun, G.; Zhang, Z.; Hennink, W. E. *Biomacromolecules* **2000**, *1*, 696.

[164] Hernandez, M.; Hu, Y.; Kim, J. R. *Chemical Communications* **2013**, *49*, 10712.

[165] Dong, H. F.; Lei, J. P.; Ding, L.; Wen, Y. Q.; Ju, H. X.; Zhang, X. J. *Chemical Reviews* **2013**, *113*, 6207.

[166] Mader, A.; Riehle, U.; Brandstetter, T.; Stickeler, E.; zur Hausen, A.; Ruhe, J. *Analytical and Bioanalytical Chemistry* **2010**, *397*, 3533.

[167] Grallert, H.; Leopoldseder, S.; Schuett, M.; Kurze, P.; Buchberger, B. *Nature Methods* **2011**, *8*, iii.

[168] Karlsson, R.; Michaelsson, A.; Mattsson, L. *Journal of Immunological Methods* **1991**, *145*, 229.

[169] Wetmur, J. G. *Critical Reviews in Biochemistry and Molecular Biology* **1991**, *26*, 227.

[170] Giljohann, D. A.; Mirkin, C. A. *Nature* **2009**, *462*, 461.

[171] Lima, A. C.; Custodio, C. A.; Alvarez-Lorenzo, C.; Mano, J. F. *Small* **2013**, *9*, 2487.

[172] Pan, H. M.; Beyer, S.; Zhu, Q. D.; Trau, D. *Advanced Functional Materials* **2013**, *23*, 5108.

[173] Shenoy, R.; Tibbitt, M. W.; Anseth, K. S.; Bowman, C. N. *Chemistry of Materials* **2013**, *25*, 761.

[174] Boots, H. M. J.; Kloosterboer, J. G.; Serbutoviez, C.; Touwslager, F. J. *Macromolecules* **1996**, *29*, 7683.

[175] Kwok, A. Y.; Prime, E. L.; Qiao, G. G.; Solomon, D. H. *Polymer* **2003**, *44*, 7335.

[176] Guo, S.; Yao, T.; Ji, X. B.; Zeng, C. F.; Wang, C. Q.; Zhang, L. X. *Angewandte Chemie International Edition* **2014**, *53*, 7504.

[177] Chern, C. S. *Progress in Polymer Science* **2006**, *31*, 443.

[178] Pacios, I. E.; Molina, M. J.; Gomez-Anton, M. R.; Pierola, I. F. *Journal of Applied Polymer Science* **2007**, *103*, 263.

[179] Reinhart, C. T.; Peppas, N. A. *Journal of Membrane Science* **1984**, *18*, 227.

[180] Ju, L. K.; Ho, C. S. *Biotechnology and Bioengineering* **1989**, *34*, 1221.

[181] Nelson, D. L.; Lehninger, A. L.; Cox, M. M. *Lehninger Principles of Biochemistry*; W. H. Freeman: New York, 2008.

[182] Tanaka, T.; Sakai, R.; Kobayashi, R.; Hatakeyama, K.; Matsunaga, T. *Langmuir* **2009**, *25*, 2956.

[183] Hatti-Kaul, R. Aqueous Two-Phase Systems: Methods and Protocols. In *Methods in Biotechnology*; Hatti-Kaul, R., Ed.; Humana Press: Totowa, 2000; Vol. 11.

[184] Goulian, M.; Simon, S. M. *Biophysical Journal* **2000**, *79*, 2188.

[185] Santos, N. C.; Castanho, M. A. R. B. *Biophysical Journal* **1996**, *71*, 1641.

[186] Jung, S.; Yi, H. *Langmuir* **2014**, *30*, 7762.

[187] Choi, N. W.; Kim, J.; Chapin, S. C.; Duong, T.; Donohue, E.; Pandey, P.; Broom, W.; Hill, W. A.; Doyle, P. S. *Analytical Chemistry* **2012**, *84*, 9370.

[188] Badu-Tawiah, A. K.; Lathwal, S.; Kaastrup, K.; Al-Sayah, M.; Christodouleas, D. C.; Smith, B. S.; Whitesides, G. M.; Sikes, H. D. *Lab on a Chip* **2015**, *15*, 655.

[189] Schweitzer, B.; Roberts, S.; Grimwade, B.; Shao, W. P.; Wang, M. J.; Fu, Q.; Shu, Q. P.; Laroche, I.; Zhou, Z. M.; Tchernev, V. T.; Christiansen, J.; Velleca, M.; Kingsmore, S. F. *Nature Biotechnology* **2002**, *20*, 359.

[190] Sebra, R. P.; Masters, K. S.; Cheung, C. Y.; Bowman, C. N.; Anseth, K. S. *Analytical Chemistry* **2006**, *78*, 3144.

[191] de Jager, W.; te Velthuis, H.; Prakken, B. J.; Kuis, W.; Rijkers, G. T. *Clinical and Diagnostic Laboratory Immunology* **2003**, *10*, 133.

[192] Yang, B. D.; Lu, Y. C.; Luo, G. S. *Industrial & Engineering Chemistry Research* **2012**, *51*, 9016.

[193] Righetti, P. G.; Brost, B. C. W.; Snyder, R. S. *Journal of Biochemical and Biophysical Methods* **1981**, *4*, 347.

[194] Liu, Q. S.; Singh, A.; Lalani, R.; Liu, L. Y. *Biomacromolecules* **2012**, *13*, 1086.

[195] Xiao, D. Q.; Zhang, H.; Wirth, M. *Langmuir* **2002**, *18*, 9971.

[196] Cringus-Fundeanu, I.; Luijten, J.; van der Mei, H. C.; Busscher, H. J.; Schouten, A. J. *Langmuir* **2007**, *23*, 5120.

[197] Ensikat, H.-J.; Maximilian, W. *Microscopy and Analysis* **2013**, *27*, 7.

[198] Hyam, P. Understanding and Maintaining the Cryostat. In *A Practical Guide to Frozen Section Technique*; Peters, S. R., Ed.; Springer: New York, 2010.

[199] Erdman, N.; Campbell, R.; Asahina, S. *Microscopy Today* **2006**, *14*, 22.

[200] Hiemenz, P. C.; Rajagopalan, R. *Principles of Colloid and Surface Chemistry, Third Edition, Revised and Expanded*; Taylor & Francis: 1997.

[201] Crank, J. *The Mathematics of Diffusion*; Clarendon Press: 1979.

[202] Debets, M. F.; van Berkel, S. S.; Schoffelen, S.; Rutjes, F. P. J. T.; van Hest, J. C. M.; van Delft, F. L. *Chemical Communications* **2010**, *46*, 97.

[203] Jewett, J. C.; Sletten, E. M.; Bertozzi, C. R. *Journal of the American Chemical Society* **2010**, *132*, 3688.

[204] McNitt, C. D.; Popik, V. V. *Organic & Biomolecular Chemistry* **2012**, *10*, 8200.

[205] Miron, T.; Wilchek, M. *Analytical Biochemistry* **1982**, *126*, 433.

[206] Click Chemistry Tools Home Page. https://www.clickchemistrytools.com/wp-content/uploads/2012/10/A124.pdf (accessed April 2, 2015).

[207] Koo, H.; Lee, S.; Na, J. H.; Kim, S. H.; Hahn, S. K.; Choi, K.; Kwon, I. C.; Jeong, S. Y.; Kim, K. *Angewandte Chemie-International Edition* **2012**, *51*, 11836.

[208] Yi, H.; Wu, L. Q.; Sumner, J. J.; Gillespie, J. B.; Payne, G. F.; Bentley, W. E. *Biotechnology and Bioengineering* **2003**, *83*, 646.

[209] Kaul, A. The Phase Diagram. In *Methods in Biotechnology*; Hatti-Kaul, R., Ed.; Humana Press: Totowa, NJ, 2000; Vol. 11.

[210] Fahmy, T. M.; Fong, P. M.; Goyal, A.; Saltzman, W. M. *Materials Today* **2005**, *8*, 18.

[211] Callister, W. D. *Materials Science and Engineering: An Introduction*; John Wiley & Sons, Incorporated: Hoboken, 2006.